U N I V E R S I T Y O F L I V E R P O O L

DEPARTMENT OF CIVIL ENGINEERING

Wave Loading on Offshore Structures: A Probabilistic Approach

Thesis submitted in accordance with
the requirements of the University of Liverpool
for the degree of Doctor in Philosophy

by

R. Burrows, B. Eng.

May, 1982

BEST COPY

AVAILABLE

Variable print quality

SUMMARY

The objective of the work presented here is to develop a description of the structural response of offshore structures, of the steel lattice type, to the loading induced by the random waves experienced during a lifetime of exposure in the ocean.

Application is restricted to structures which do not respond dynamically to the induced fluid loading. The main emphasis of the approach is the necessity for retention of the non-linearity of the loading in the analysis for these structures where the effects of fluid drag are significant. Probability theory is adopted as the most appropriate approach to the problem and the description of loading is developed from the known statistics of the short-term wave field (representing a stationary sea state) using Morison's Equation. The long-term description of loading is then obtained by convolution of this model with the wave climate, representing the complete population of sea states at the site of interest.

The behaviour of the probabilistic model, which does not account for the presence of uni-directional currents or the intermittency of loading in the splash zone, is investigated in terms of the probability distributions of load, which is non-Gaussian in form, and its narrow-band peak and extreme peak variates. Various member and sea state conditions are considered and the significance of full retention of the non-linear drag component of loading is demonstrated by comparison with a model employing a linearised loading mechanism, yielding results equivalent to those produced by spectral analysis, which is shown to considerably under-estimate extreme wave loads. The significance of the spectral model chosen for description of the surface elevation and the form of treatment of the wave climate description are also demonstrated and the problem of computational requirements is discussed.

The probabilistic description of structural response, based on linear behaviour of the structure, is developed from that of individual member loading in terms of the statistics of the wave field for short-term conditions. Convolution with the wave climate again produces the long-term properties. It is the probabilistic properties of response, either

displacements or internal stresses, rather than individual member loading which are of most direct value in the design against fatigue and first excursion failure.

In the model it is necessary to idealise the distributed fluid loading on the structure by lumped load components at a finite number of locations. These elemental random loads are distributed in space but are correlated with each other and the probabilistic procedure fully accounts for the varying degrees of correlation. The computational requirements of this model are considerable and it has proved practicable to investigate simple systems of only two load components due to run-time limitations. However, from this study it is shown that the probability distribution of response is of the same non-Gaussian form as that of the underlying loading. This distribution is fully defined by its second and fourth order statistical moments and expressions for these statistics for the response variate are developed, again in terms of the statistics of the short-term wave field.

There is still a computational problem with this approach imposing a ceiling on system complexity dependent upon the run-time limitations imposed. Using 30-minute run times on the ICL 1906S computer at Liverpool, systems of up to 35 load components can be analysed. However, an important refinement to the model has yet to be realised and as a consequence the accuracy of the present model for systems exceeding 12 load components is uncertain.

Finally, application of the model is demonstrated for a number of simple test structures under the action of short-term sea state conditions and the results are compared with those obtained using time-series simulation.

ACKNOWLEDGEMENTS

The author would like to thank his supervisor Professor P. Holmes and Mr. R. G. Tickell, both colleagues in the Department of Civil Engineering and co-investigators in the OSFLAG 5 Research Project, for their help and guidance throughout the course of study leading to this Thesis.

The contribution of the Department of Industry in funding the author for two years on the OSFLAG 5 Research Contract is greatly appreciated.

Finally, thanks are also due to Christine Cope and Barbara Cotgreave for their diligence in producing the typescript and drawings.

CONTENTS

NOTATION

The following notation is comprehensive for the main text only. Where notation differs in the Appendices (notably Appendices I and II) parameters are defined where they first appear and the text may be read in isolation from the main report.

a_i, a_2	coefficients of conditional expectations, Eq. (5.4.23)
a_j	abscissa coefficients in Gaussian Quadrature, Eq. (5.6.1)
A	constant coefficient in Pierson-Moskowitz spectrum, Eq. (2.3.23)
	or constant in Weibull distribution, Chapter Four and Appendix Two only
A'	standardised wave amplitude, Eq. (2.3.13)
[A]	transformation matrix, Eq. (5.2.7)
A_k	coefficients of Chebyshev-Hermite quadrature, Eq. (3.5.1)
A_r	member area projected perpendicular to flow, Eq. (2.1.1)
b_i	coefficients of conditional expectations, Eq. (5.4.37)
B	constant coefficient in Pierson-Moskowitz spectrum, Eq. (2.3.23)
B_ℓ	coefficients of Chebyshev-Laguerre quadrature
c_{ij}	co-factors of [M], Eq. (5.3.2)
{c}	vector of coefficients of conditional expectations, Eq. (5.4.42)
cdf.	cumulative distribution function
C_D	'Morisons' drag coefficient
C_M	'Morisons' inertia coefficient
d	water depth
D	diameter of cylindrical member
D'	structural damage, Eq. (2.3.62)
Det[ ]	determinant
exp	exponential
E{ }	expected value operator, see Appendix One
$E\{N^+(0)\}_1$	long-term mean rate of zero-up crossings of force, type 1 peak model, Section 3.3
$E\{\eta^+(0)\|H_{1/3_i}\}$, $E\{N_o^+\|H_{1/3_i}\}$	mean rate of zero-upcrossings of swl. under sea state $H_{1/3_i}$
E1 → E23	abbreviations for expectations, Section 5.4

f	linearised 'Morison' wave force, Eq. (3.1.2)
$f(\ )$	function
F	wave force
F_D	drag component of force
F_{DN}	drag component of force normal to member axis, Eq. (2.1.3)
F_{Dx}, F_{Dy}, F_{Dz}	components of F_{DN} in co-ordinate directions
$\{F_e\}$	vector of nodal forces, Eq. (5.2.7)
F_i	force components
F_I	inertia component of force
F_{IN}	inertia component of force normal to member axis, Eq. (2.1.7)
F_x, F_y, F_z	components of F in co-ordinate directions
g	gravitational acceleration
$g(\ )$	function
G_i	functions of d, L and H in Stokes Wave Theories
H	wave height
$H_{1/3}$	$H_S \equiv$ 'significant' wave height - average height of largest (1/3) of waves
H_{rms}	'root mean square' value of wave height = $\sqrt{E\{H^2\}}$
H_j	weighting coefficients, Gaussian Quadrature, Eq. (5.6.1)
$H_n(\ )$	Chebyshev-Hermite polynomial
i	variable
I_{max}	annual maximum sea state intensity
I_{T_r}	sea state intensity of T_r year return period
j	variable
k	wave number, $2\pi/L$ or variable, Section 5.4
k_D	drag coefficient, Eq. (2.3.46)
k_I	inertia coefficient, Eq. (2.3.46)
$[K]$	structural stiffness matrix, Eq. (5.2.8)
ℓ	variable
ℓn; $\log_e$	natural logarithm
L	wave length
L_D	time duration (years)
L_0	deep water wave length = $gT^2/2\pi$
m	integer constant
m_i	i-th moment of spectrum of surface elevation $= \int_0^\infty \omega^i S_{\eta\eta}(\omega)\, d\omega$
$[M]$	matrix of cross-covariances (cross-correlations), Eq. (3.3.6)

M_n	n-th order statistical moment
M(t)	bending moment, Section 5.6.1
MPPV	most probable peak (extreme) value, Section 3.4.1
n	integer constant
N_1	number of waves per year
$N^+(\gamma)$	rate of up-crossing of level γ with positive slope, Eq. (2.3.58)
$N(H_{1/3_i}, T_{z_j})$	total number of peaks in sea state (i, j) during period of exposure, t_e, Eq. (3.4.12)
p( )	probability density function
pdf.	probability density function
p_H( )	Pierson-Holmes pdf, Eq. (2.3.47)
P( )	cumulative distribution function, cdf, see Appendix One
P_H( )	Pierson-Holmes cdf.
P_{p_1}( )	cdf. of positive peak values, type 1, Eq. (2.3.58)
P_{p_2}( )	cdf. of positive peak values, type 2, Eq. (2.3.60)
P_{EP}( )	cdf. of extreme values, Eq. (2.3.70)
P/H	'Pierson-Holmes'
P-M($H_{1/3}$)	Pierson-Moskowitz spectrum defined through $H_{1/3}$
P-M(T_z)	Pierson-Moskowitz spectrum defined through T_z
P-M(DNV)	Det Norske Veritas modification to Pierson-Moskowitz spectrum
$Q(\alpha)$	$\int_{\alpha}^{\infty} Z(\lambda)\, d\lambda$
Q(t)	shear force, Section 5.6.1
r; $r_{x_1x_2}$	correlation coefficient, see Appendix One
r.v.	random variable
$R_{x_ix_j}(\tau)$	cross-correlation function between random variables x_i and x_j with time lag τ
$R_{x_ix_j}$; R_{ij}	cross-correlation between x_i and x_j (τ = 0), Section 2.3.5
s	wave steepness parameter, Eq. (3.2.2)
swl.	still water level
S( )	spectral density function
[S]	'influence' or flexibility matrix, Eq. (5.2.9)
S_i, S_{ij}	influence or flexibility coefficients
t	time
t_e	period of exposure
T	wave period or time duration, Appendix One
T_z	mean zero-upcrossing wave period, Eq. (2.3.22)

$\overline{T_z^{-1}}$	'long-term mean period factor', Eq. (2.3.32)
T_r	'return period'
u	horizontal component of water particle velocity in direction of wave advance
$\dot{u}$	du/dt, water particle acceleration
U_w	wind speed
v	vertical component of water particle velocity
$\dot{v} = dv/dt$	vertical component of water particle acceleration
V_N	instantaneous resultant velocity vector normal to axis of inclined member
V_o	member volume
V_R	instantaneous resultant velocity vector = $\sqrt{u^2 + v^2}$
w_{ij}	number of occurrences in scatter diagram class (i, j)
w	$\sum_{\text{all } i,j} \sum w_{ij}$
	$\sum_{\text{all } T_z} \sum w_{ij}$
$W(H_{1/3i})$	$\sum_{j} w_{ij}$, Eq. (4.6)
x	horizontal cartesian co-ordinate
	or variable, Section 3.4
	or random variable Appendix One
x(t)	random variable
x_f	fetch length in Jonswap Spectrum, Eq. (3.2.15)
X_i	mean-zero Gaussian random variables, functions of u, $\dot{u}$, Eq. (5.2.2)
y	horizontal cartesian co-ordinate
	or random variable, Appendix One
{Y}	vector of nodal responses, Eq. (5.2.9)
z	vertical cartesian co-ordinate measured +ve upwards from sea bed
$Z(\alpha)$	$\frac{1}{\sqrt{2\pi}} \exp\{-\frac{1}{2}\alpha^2\}$
α	coefficient in Jonswap Spectrum, Eq. (3.2.12)
β	kurtosis, Eq. (2.3.53)
γ	random variable
γ_p	coefficient in Jonswap Spectrum, Eq. (3.2.12)
$\delta(.)$	dirac delta function
ϵ	spectral band width, Appendix One, Section I.2.2.3
η	water surface elevation relative to still water level

Θ	direction of advance of wave component in 3-D random sea
Θ_v	angle of inclination of instantaneous velocity vector in x-z plane, Section 2.1.
μ	skewness
ρ	fluid density
σ	standard deviation
σ^2	variance
σ_a, σ_b	coefficients in Jonswap Spectrum, Eq. (3.2.12)
τ	time-lag
ϕ	random phase, Eq. (2.3.1)
ϕ_p	velocity potential, Section 2.2
Φ	angle of inclination, Fig. 2.1.2
χ^2	chi-square distribution, Appendix Four
ψ	angle of inclination, Fig. 2.1.2
ψ_1, ψ_2	mean-zero 'Gaussian' random variables, Eq. (2.3.54)
ψ_x^2	mean square value of r.v. x
ω	wave frequency, $2\pi/T$
ω_0	g/U_w, Eq. (2.3.23)
ω_p	frequency at peak of Jonswap Spectrum, Eq. (3.2.12)

Symbols

$(\bar{\ })$	mean value
$(\dot{\ })$	time derivative
$(\ddot{\ })$	second time derivative

C H A P T E R O N E

INTRODUCTION

Current emphasis on offshore development is aimed primarily at the exploitation of oil and gas reserves in coastal and offshore locations within the continental shelves throughout the world. The North Sea not only represents one of the most intense areas of activity in this respect at the present time, but is also subject to some of the most hostile environmental conditions encountered for such exploitation. As a result, the available technology associated with the extraction of oil and gas has been found to be lacking in many areas including the structural design of production platforms.

The existing generation of fixed production structures are founded on the sea bed in water depths notionally up to 200m. with legs supporting a deck, located above the level of storm waves, which houses all mechanical and electrical plant. Structures installed in the North Sea at present are either of the 'jacket' or 'gravity' types. The former are steel lattice structures, consisting of vertical legs and cross-bracing members of tubular section, supported by piles driven into the sea bed. The gravity structures are usually of reinforced concrete, with large diameter legs and a base designed to spread the loading over large areas of the sea bed, relying on bearing pressures for stability.

It is likely that even after the development of the 'new generation' of production structures, including tethered buoyant platforms and sub-sea facilities which will inevitably be required as exploration ventures into water depths in excess of 200m, the present generation of fixed structures will still be employed as new fields are discovered and exploited in relatively shallower waters.

The major loads exerted upon these fixed structures result from the particle motions associated with the passage of wind generated waves over the sea surface, these being far in excess of potential wind or 'live' (working) loadings. The mechanism giving rise to this random oscillatory wave loading is not fully understood and must be expressed by semi-empirical formulae. These differ in form between the two types

of structure, for the generally small diameter members associated with steel platforms both viscous drag and inertia effects are significant whilst on the larger diameter legs of concrete gravity structures, the drag effects are negligible.

Structures installed offshore must resist these loads for periods of exposure of possibly 30 or more years depending on the design life of the facility. They must not only be sufficiently strong to resist the loading exerted by the passage of the largest wave likely to be encountered but must also retain their integrity against fatigue resulting from the stress reversals associated with the passage of each wave, when there may be of the order of five million waves per year.

Platforms have been installed for many years in the oilfields in the Gulf of Mexico and the majority have endured the wave loading over their design lifetimes without significant signs of structural distress. However, these structures are located at generally shallower water depths than the typical 150m. of the Northern North Sea and are subject to wind generated seas of only moderate intensity, the most potentially dangerous loading conditions resulting from the chance occurrence of tropical hurricanes which tend to recur in the area about once every five or six years. Consequently, the success of the structural design of platforms in this area offers limited assurance to the adequacy of current design methods for structures at Northern North Sea locations where sea states are of a much increased severity, with the possibility of waves in excess of 30m. in height.

In the Northern North Sea fixed structures have only been installed for a small part of their design lives and no evidence of damage resulting from either the loading of individual waves or from fatigue has been reported to date. In contrast, a number of structures installed in the gas fields of the Southern North Sea for longer periods, but still short of their design lives, in relatively calmer and shallower waters have already shown signs of damage from fatigue.

The methods of structural design employed to date are largely deterministic relying on subjective procedures for the estimation of wave loading. The typical procedure is to check the structure for strength and stability against a single design wave chosen to represent the most severe loading

condition anticipated. The form of this wave, being approximately sinusoidal, bears little resemblance to the form of real large waves in random seas. Furthermore, such a technique permits no reliable assessment to be made of the risks of this loading being exceeded during the structure's lifetime even if the risk of exceedence of the associated wave height is known.

Fatigue problems were not fully envisaged until fairly recently and current techniques for the estimation of fatigue damage make similar assumptions to those applied to extreme load prediction. Typically, the relationship between the required stress range and wave height is based on space frame analysis of the structure under several idealised regular waves of different height with associated frequency of occurrence assumed to represent the entire frequency distribution of wave heights in the real sea.

Even if it is proved to be the case that structures based on the current design methods and installed in the hostile waters of the Northern North Sea fulfill their functions without any sign of damage no quantifiable indication of possible structural overdesign will be feasible until more thorough and physically realistic techniques of wave load prediction are developed. This must be of some concern since the financial penalties of such overdesign are likely to be severe with single production platforms costing in excess of £100m.

The information essential for the realistic estimation of extreme wave loading, and its associated risks of exceedence, required for first excursion failure analyses and the number of cycles associated with each stress range, resulting from the wave loading, necessary in fatigue analyses may be provided by the long-term probability distribution of wave loading. However, this cannot be reliably ascertained from idealisations of the random sea surface in terms of a discrete number of approximately sinusoidal regular waves. A thorough analysis must preserve the randomness associated with the waves throughout the transformations from the description of the wave field to the description of wave load and the resulting structural responses, such as internal stresses or displacements. Both probabilistic and spectral analyses would satisfy these requirements. The former method is the most favourable since it can fully account for the non-linearities inherent in the above transformations, due to the presence of viscous drag,

yielding the complete probability structure of loading or response. Spectral methods can only yield a limited statistical description of the loading thus requiring an approximation for the probability structure which cannot retain the full effects of the non-linearities.

The behaviour of the random wave field has been investigated for many years, primarily by oceanographers, and there exists today a considerable depth of understanding of its statistical properties and probability structure, although there still remain some significant limitations in the mathematical descriptions of the phenomenon. The most notable contributions in this field are summarised by Draper[1].

Significant advances in the description of random wave loading have been made over the last fifteen years. The probability structure of loading on individual members submerged beneath ocean waves has been developed using various techniques by Pierson and Holmes[2], Borgman[3] and Bretschneider[4]. The allied effects of the superimposition of unidirectional currents onto the wave motion and the intermittency of loading experienced by members located near the water surface within the splash zone have been investigated more recently by Tung[5,6]. However, all these applications have been limited to the prediction of loading in the short-term, over a period of several hours, when the random variation of the water surface may be assumed to be statistically stationary.

An extension of the above procedures was proposed by Holmes and Tickell at the University of Liverpool to account for the variations in the sea state intensity present in typical long-term wave climates at offshore locations. This technique follows an analogous application in the wave height domain proposed by Battjes[7] and also in the prediction of wave loading on marine vessels by Söding[8].

Even incorporating the above extension, the long-term probability distributions of loading on single members are of limited practical value. The probability distributions of wave loading or structural response at critical locations on complete structures is required by the designer. Penzien[9] has gone some way towards solving the problem using spectral methods which yield the frequency spectra of total load or response for structures idealised into a number of load components, a procedure which may also account for the presence of dynamic response.

However, as discussed previously, spectral methods cannot fully account for the non-linearity of the loading mechanism, when transformed to the required descriptions in the probability domain, which may be of considerable importance for structures where the non-linear effects of viscous drag are significant. In these situations, which apply to most structures of the steel lattice type, it can be inferred from the description of loading on single members[2] that failure to retain the non-linearities may result in considerable underestimation of the loading or response.

In view of the above comments the major pre-requisites for the improvement of current methods of structural design are:

i) the combination of the short-term probability distributions of loading with descriptions of the long-term wave climate to yield the long-term wave load distributions; and

ii) the extension of these probabilistic techniques from applications on single members to complete structures.

The need for further research along these lines, and into wave loading in general, was identified by the British Government and the Offshore Structures Fluid Loading Advisory Group (OSFLAG) was formed by the Department of Industry (later transferred to the Department of Energy). The group identified ten research topics and the National Maritime Institute (formerly the National Physical Laboratory) were appointed as the main contractor although many of the projects were undertaken by other organisations.

In October 1974 the author was appointed as a Research Assistant on the OSFLAG 5 project awarded to Professor Holmes at the University of Liverpool, the research undertaken by the author under this contract forming the bulk of the contents of this Thesis. The objective of the OSFLAG 5 research programme was to provide a method of calculating a statistical or probabilistic description of long-term wave loading on members of offshore structures based on short-term and long-term probabilistic descriptions of wave conditions. The background to the problem was stated in the original OSFLAG 5 proposal as follows:

'Regulations concerning the long-term integrity of offshore structures which will be subjected to wave action over several tens of years are of obvious importance. For such regulations and in corresponding design computations a unified method is required to estimate the lifetime loading conditions imposed by waves.

For particular wave conditions the load on a member can be estimated by computations based on a single wave - said to represent a given sea state - or by calculations based on the probabilistic properties of that sea state, using known relationships between wave kinematics and load and accepting the limitations thereof.

The former method leads to a deterministic description of the load, the latter to a probability distribution of the load which has been shown to give good agreement with measurements in the Gulf of Mexico and the North Sea.

It is then possible to accumulate 'short-term' descriptions based on the second method given above according to 'long-term' wave behaviour. Although this behaviour is in need of further research, it is considered that the Weibull probability distribution for wave heights forms a viable basis on which predictions of long-term wave loading can be based.

There is an urgent need to formalise this computational process giving loading on a single member in terms of magnitude and number of cycles per annum.

This computation then needs to be extended to entire structures. This is a significantly more complex problem because of the spatial relationships between wave lengths and structural geometry. Techniques are available for dealing with such correlations and the problem of cyclic loading of complex structures is of such importance as to warrant an investigation of their use, leading to viable design procedures.'

This theoretical, computer based project aimed primarily at loading in the drag/inertia regime on steel lattice structures was split into two parts; the first involving estimation of the long-term loading on single structural elements and the second part involving an extension of the methods to include complete structures.

This Thesis describes the results of work undertaken by the author on the above topic. Some of the material included here has been presented within the OSFLAG report and associated reports and publications[10-20]. The study has involved no physical experimentation, although some reference is made to both model scale and full-scale wave load and response measurements taken by others. The remainder of this Chapter summarises the contents of the Thesis.

Chapter Two develops the background theory relevant to the probabilistic description of long-term random wave loading. It proceeds with an outline of the generally accepted, semi-empirical, 'Morison' wave load model[21] which is applicable to short sections of submerged objects with dimensions such that viscous drag and inertial effects are significant. This is followed by a brief outline of the most commonly employed wave theories for relatively deep water conditions, which are typical of the sites for offshore installations in the North Sea. The linear (or Airy or first order) wave theory and Stokes' finite amplitude theories for the description of the particle motions beneath regular waves are summarised, the particle kinematics of which define the wave loading through the 'Morison' model. The significance of the orientation of cylindrical members in relation to the direction of the waves is reviewed and modifications to the Morison loading model are presented.

Both short and long-term statistical descriptions of the wave field are summarised and the use of such information for deterministic wave load estimation is discussed. Limitations in these design methods are identified and the case is made for more rigorous non-deterministic techniques. Spectral and probabilistic methods are considered in this respect and the latter is shown to be favourable for the purposes of load prediction in first excursion and fatigue analyses. Models yielding the long-term probability distributions of wave load and its peak and extreme values are then developed from the probability structure of the wave field through transformations involving the Morison loading model and first order wave theory.

The theoretical procedures described in Chapter Two form the basis of the work described herein and are almost entirely the results of previous work by others, as may be inferred from the references made within the text.

Chapter Three describes the results of work carried out by the author in the application of the techniques for long-term wave load prediction. Long-term probability distributions of loading and its peak and extreme values are presented and discussed and it is demonstrated that linearisation of the loading mechanism, inherent in existing spectral techniques, and as proposed in some probabilistic approaches to simplify analysis, leads to a considerable underestimation of extreme loading for small diameter members, typical of steel structures, where the effects of

viscous drag are predominant. The significance of various theoretical spectral models, used to describe the short-term wave field, on the wave load prediction is also investigated. Computing requirements for the implementation of the probabilistic techniques are considered and since these are likely to exceed the facilities available in most design offices a useful hand-computation procedure is outlined.

Chapter Four examines the significance of the wave climate data used as input to the probabilistic analyses. The basic requirement that the data should cover a complete number of years, preferably greater than one year, is identified. The need for extrapolation of the measured climate, to account for severe sea states not experienced, before incorporation in the long-term wave load computations is discussed. A method of extrapolation is proposed, based on the fitting of the significant wave height recordings from the data to a theoretical probability distribution.

Chapter Five extends the probability theory from application on single members to entire structures where the total loading or associated structural responses are idealised to result from the combination of a large number of individual, correlated, random load components. This extension, applied to short-term conditions where the wave climate is statistically stationary, is shown to be impractical, due to computer limitations, for systems of greater than two load components and is, therefore, inadequate for modelling all but the simplest of structural members. However, by assuming that total load or structural response possess the same probability structure as the elemental loading, a postulation supported from analysis of model and prototype data, only the second and fourth statistical moments are required for definition of this probability structure. Mathematical expressions for these moments are developed in terms of the known statistics of the wave field and the resulting short-term probability distributions of load may be convoluted with the long-term wave climate to yield long-term probability distributions, in the same way as applied to loading on single elemental members. The results of these procedures are applied to idealised systems of load components to demonstrate the use of the techniques and are compared with those obtained from mathematical time-series simulation techniques. The computing requirements for the estimation of the short-term statistical moments are still considerable although using this approach the probability structure for systems up to 35 load components may be determined.

Chapter Six contains a summary of the conclusions drawn from the research and Chapter Seven presents recommendations for future work.

Finally, a comment should be made on the form of computation used in this study. In the course of the research reported herein a large number of computer programs were developed by the author and it would be impractical to include listings of the programs here. Consequently, no details other than program names (see Appendix Six) are given in the Thesis. A document[22] containing the listings of all programs has been compiled separately. Multiple comment statements are included to obviate the need for detailed flow charting. Fortran IV programming language was used throughout for operation on the ICL 1906S computer at the University of Liverpool and the ICL CDC 7600 computer at the University of Manchester Regional Computer Centre.

CHAPTER TWO

THEORY DESCRIBING WAVE LOADING AND ITS PREDICTION

2.1 WAVE INDUCED LOADING ON SUBMERGED RIGID CYLINDRICAL MEMBERS

Application of the work described herein is intended primarily for the structural analysis of the steel lattice, or jacket, type of offshore structures against wave loading, for which the diameters of the majority of the cylindrical members are less than 20% of the largest wavelengths to be encountered. Under these circumstances the loading is in the drag/inertia regime as demonstrated in Fig. 2.1.1 taken from Hogben[23].

The most generally accepted method for the estimation of loading in the drag/inertia regime has developed from an investigation into ocean wave loading on vertical cylindrical members by Morison et al[21]. The method is semi-empirical and is based on the assumption that the total force exerted by the fluid is equal to the sum of a drag component due to the water particle velocity and an inertia component due to the water particle acceleration, the two forces being assumed to develop without interaction.

The horizontal force may thus be expressed by 'Morison's Equation' as:

$$F = F_D + F_I = \frac{1}{2} C_D \rho A_r u|u| + C_M \rho V_o \dot{u} \qquad (2.1.1)$$

where F_D and F_I are the drag and inertia components, respectively;

u is the horizontal component of the water particle velocity;

$\dot{u} = \frac{du}{dt}$ is the horizontal component of the water particle acceleration;

V_o is the volume of the member;

A_r is the area projected perpendicular to u;

ρ is the fluid density; and

C_D and C_M are empirical drag and inertia coefficients.

The water particle kinematics u and $\dot{u}$ are the values that would be present in the flow field at the location of the centroid of the member in its absence. It is assumed in Eq. (2.1.1) that spatial variations in these kinematics are negligible over the space taken up by the member. The

modulus sign is included to preserve the direction of the drag component of loading which is a function of velocity squared.

The absolute validity of the linear combination of the two force components in Eq. (2.1.1) is open to question since, as discussed by Wiegel[24], the underlying assumptions for the derivation of the inertia component are violated by the presence of the effects of drag, interaction effects, therefore, being significant. However, from an engineering point of view the model may be deemed to be satisfactory, in the absence of a more precise model, in applications to wave loading since it has been shown to yield reasonable results.

In their original work Morison et al were concerned only with the loading on vertical cylindrical members for which the total horizontal load per unit length is:

$$F = \frac{1}{2} C_D \rho D u|u| + \rho \frac{\pi D^2}{4} C_M \dot{u} \qquad (2.1.2)$$

Little attention has been given to the loading mechanism resulting from wave-induced fluid motion around non-vertical members, Eq. (2.1.1) being strictly applicable only to a short section of a vertical member, although some writers have assumed that the load in any particular direction may be derived using only the components of the water particle motions in that direction[25,26], as may be implied from Eq. (2.1.1).

A more thorough representation of the loading mechanism for inclined members lying in a plane parallel to the wave crests was developed by the author in association with his colleagues[18] for application to a North Sea oil production platform. This representation follows the cross-flow principle, recommended by Hogben et al[27], and is in agreement with previous work by Borgman[28] on members of arbitrary orientation with respect to the waves.

Consider a unit length section of cylindrical member submerged beneath the water surface at location (x_0, y_0, z_0), as shown in Fig. 2.1.2. The x-y plane is horizontal and the member is inclined at an angle ψ to the y axis in the y-z plane. Regular long-crested waves are assumed to advance in the positive x-direction.

At a particular instant of time the resultant velocity vector at location (x_0, y_0, z_0) will be inclined at an angle Θ_V to the horizontal, as indicated in Fig. 2.1.2, where Θ_V varies between 0 and 2π during the passage of each wave. Furthermore, the resultant velocity vector, giving rise to the drag component of loading, is out of phase with the resultant acceleration vector, giving rise to the inertial component of loading, and thus the total force at any instant must be evaluated using vector addition of these two components.

In the super and post-critical flow regimes[27] the contribution of skin friction to the total drag will be negligible and the total force may then be assumed to be determined essentially by the pressure difference across the cylinder. Consequently, it acts normal to the member axis in the direction of V_N (the normal component of the resultant water-particle velocity V_R) and may be written:

$$F_{DN} = \frac{1}{2} \rho C_D D [u^2 + (v \cos \psi)^2] \qquad (2.1.3)$$

The drag components in the co-ordinate directions are:

$$F_{Dx} = F_{DN} \cos \Phi = \frac{1}{2} \rho C_D D u|\sqrt{u^2 + (v \cos\psi)^2}| \qquad (2.1.4)$$

$$F_{Dy} = F_{DN} \sin \Phi \cos \psi = \frac{1}{2} \rho C_D D v|\sqrt{u^2 + (u \cos \psi)^2}|\cos^2\psi \qquad (2.1.5)$$

$$F_{Dz} = - F_{DN} \sin \Phi \sin \psi = - F_{Dy} \tan \psi \qquad (2.1.6)$$

The inertia loading may be estimated in a similar way if it is assumed that only accelerations in a plane normal to the member axis are significant[29], yielding:

$$F_{IN} = \rho \frac{\pi D^2}{4} C_M[(\dot{u})^2 + (\dot{v} \cos \psi)^2]^{1/2} \qquad (2.1.7)$$

Reducing this force to its components in the co-ordinate directions and adding the appropriate drag force gives the components of the total force as:

$$F_x = \frac{1}{2} \rho C_D Du \left|\sqrt{u^2 + (v \cos \psi)^2}\right| + \rho \frac{\pi D^2}{4} C_M \dot{u} \qquad (2.1.8)$$

$$F_z = [\frac{1}{2}\rho C_D Dv|\sqrt{u^2 + (v \cos \psi)^2}| + \rho \frac{\pi D^2}{4} C_M \dot{v}] \cos^2\psi \qquad (2.1.9)$$

$$F_y = - F_z \tan \psi \qquad (2.1.10)$$

For a vertical member $\psi = 90°$ and F_x simplifies to Eq. (2.1.2) with $F_y = F_z = 0$. Note that in this special case of the general condition the vertical member is still subject to the application of the cross-flow principle since the resultant water-particle velocity vector is rotating in a vertical plane normal to the wave fronts and, therefore, is perpendicular to the member axis under wave crests and troughs only.

In contrast, a horizontal member with its axis parallel to the wave crests represents a condition in which the resultant rotating velocity vector is always perpendicular to the member axis, obviating the need to apply the cross-flow principle. For such a member $\psi = 0$ and F_x simplifies to:

$$F_x = \frac{1}{2} \rho C_D D u |\sqrt{u^2 + v^2}| + \rho \frac{\pi D^2}{4} C_M \dot{u} \qquad (2.1.11)$$

A similar expression exists for the vertical loading but with the roles of u and v reversed. Obviously, in this situation F_y is zero.

Whilst the values of C_M may be the same for a horizontal member using Eqs. (2.1.1) and (2.1.11) a larger value of C_D is required in the former equation if the same forces are to be predicted.

Although the above procedure is supported by Borgman[28] and Hogben[27], the U.S. Army Coastal Engineering Research Centre[30] indicate that from experimental work the expressions associated with application of the cross-flow principle may not be conservative. They suggest instead the use of the actual resultant velocity and acceleration magnitudes in the direction of the normal to the member axis in applications using the cross-flow principle. As a result of these uncertainties it is recommended in the Shore Protection Manual[30] that the force per unit length on an inclined cylindrical member be taken as the horizontal force per unit length on an equivalent vertical pile at the same location.

It is probably justifiable to say that any of the methods of load estimation outlined so far would prove acceptable for engineering applications by appropriate choice of C_M and C_D. At this stage it should be re-emphasised that the basic loading model and the modified forms developed above, as combinations of drag and inertia components without interaction, are essentially semi-empirical approximations to the actual loading mechanism relying on the choice of C_M and C_D values to yield a

reasonably close approximation to the actual loading behaviour. In view of this uncertainty and the flexibility available in any of the models considered, by virtue of the presence of the empirical coefficients, the approximations made by assuming the loading in any direction to be of the Morison form, developed from Eq. (2.1.1), may well be acceptable for engineering purposes.

Much effort has been directed towards the evaluation of C_M and C_D values in recent years[27,31]. However, most investigations have suffered from considerable scatter, typical values for the coefficients are in the range 0.5-1.5 for C_D and 1.0-2.5 for C_M, possibly reflecting the inadequacies and inaccuracies of the wave and loading models.

However, in order to use the methods of load prediction correctly, and thereby reduce the uncertainties, the coefficients chosen in any application should be compatible with the form of computation adopted. For example, if Morison's equation together with Stokes' 5th order wave theory is to be used to estimate the vertical loading on a horizontal member, then the coefficients C_M and C_D should ideally correspond to values obtained from vertical load analysis on horizontal members using the same wave and load models. Similarly in non-deterministic investigations the coefficients chosen should be the result of statistical analyses not values selected for use with deterministic waves.

In the work described herein only loading of the Morison form is considered in detail, the interpretation being that Morison's equation is applicable for loading in any direction on members of any member orientation conditional on the appropriate choice of empirical coefficients C_M and C_D.

2.2 THEORIES OF PERIODIC WAVES

There exist a large number of wave theories which describe the form and motion of periodic gravity waves, some being more suited than others to particular water depth regions.

Waves may be classified by the depth of water in which they travel, d, relative to their wavelength, L, as follows:

Deepwater	$d/L > 0.5$
Intermediate water	$0.5 > d/L > 0.04$
Shallow water	$d/L < 0.04$

Since, in the work described here, attention will be centred on conditions tending towards, and into, deep water the most applicable wave theories[32], and the only ones considered here, are the linear wave theory (Lamb[33], 1945) and the Stokes finite amplitude theories (Stokes[34], 1880).

Consider the co-ordinate system shown in Fig. 2.2.1 describing the irrotational motion of oscillatory non-viscous water waves of constant height and of infinite extent perpendicular to the direction of propagation ('long-crested' waves).

Linear wave theory and some finite amplitude wave theories can be developed by the introduction of a velocity potential, ϕ_p, such that the water particle velocity components at location (x, z) are given by:

$$u = \frac{\partial \phi_p}{\partial x} \text{ and } v = \frac{\partial \phi_p}{\partial z} \qquad (2.2.1)$$

with the requirement that:

i) the continuity (Laplace) equation; and
ii) the energy (dynamical, 'Bernoulli') equation, are satisfied for the body of the fluid.

In addition, the boundary conditions to be satisfied are:

i) particles on the bed remain on the bed; and
ii) particles in the free surface remain in the free surface, where the pressure must be atmospheric.

In practice it does not prove possible to satisfy the free surface boundary conditions exactly, the 'goodness of fit' has been used to measure the accuracy of the theory by Dean[32] and others.

2.2.1 Linear Wave Theory

Linear (first order or Airy) wave theory makes the linearising assumption that the surface boundary condition applies at $z = d$ rather than $z = d + \eta$, the method only strictly being applicable to waves of infinitesimal height and of small steepness. For this theory the water surface elevation at location x and time t is given by[24]:

$$\eta(x, t) = \frac{H}{2} \cos(kx - \omega t) \qquad (2.2.2)$$

where H = wave height

k = wave number = $2\pi/L$

L = wave length

ω = wave frequency = $2\pi/T$

T = wave period

and

$$\omega^2 = gk \tanh kd \qquad (2.2.3)$$

d = water depth

g = gravitational acceleration.

The water particle kinematics are expressed as follows. The component velocities are:

$$u(x, z, t) = \omega \frac{H}{2} \left[\frac{\cosh kz}{\sinh kd}\right] \cos(kx - \omega t) \qquad (2.2.4)$$

$$v(x, z, t) = \omega \frac{H}{2} \left[\frac{\sinh kz}{\sinh kd}\right] \sin(kx - \omega t) \qquad (2.2.5)$$

and the component accelerations are:

$$\dot{u}(x, z, t) = \frac{\partial u}{\partial t} = \omega^2 \frac{H}{2} \left[\frac{\cosh kz}{\sinh kd}\right] \sin(kx - \omega t) \qquad (2.2.6)$$

$$\dot{v}(x, z, t) = \frac{\partial v}{\partial t} = -\omega^2 \frac{H}{2} \left[\frac{\sinh kz}{\sinh kd}\right] \cos(kx - \omega t) \qquad (2.2.7)$$

which are 90° out of phase with their respective velocity components.

In deep water (d/L > 0.5) the wave characteristics become independent of the depth. For first order wave theory the surface motion is sinusoidal and symmetrical about still water level. Furthermore, it can be easily shown that the water particles move in closed elliptical orbits, becoming circular in deep water, as indicated in Fig. 2.2.2, returning to their original position at the end of each wave cycle.

2.2.2 Stokes' Finite Amplitude Wave Theories

In the finite amplitude wave theories the velocity potential is expanded, as described by Wiegel[24], which yields a symmetrical wave form with larger and more peaky crests than troughs conforming more closely to the

observed form of steep periodic gravity waves. Particle orbits resulting from the passage of each wave are no longer closed, but the particles exhibit a gradual forward motion or 'mass transport' effect.

The solution of the 3rd order approximation[35] results in the following expressions for surface elevation and horizontal velocity:

$$\eta(x, t) = G_1 \cos(kx - \omega t) + G_2 \cos 2(kx - \omega t) + G_3 \cos 3(kx - \omega t) \quad (2.2.8)$$

$$u(x, z, t) = G_4 \cosh(kz) \cos(kx - \omega t) + G_5 \cosh(2kz).$$

$$\cos 2(kx - \omega t) + G_6 \cosh(3kz) \cos 3(kx - \omega t) \quad (2.2.9)$$

where G_i are functions of d, L and H.

Expressions of a similar form involving 5 terms are developed for Stokes' 5th order approximation[36].

2.2.3 Utility of Linear Wave Theory

The 3rd and 5th order solutions are used extensively to describe particle motions for deterministic estimation of wave loading on members of offshore structures. With precise values of wave amplitude and period the higher order (non-linear) theories provide more accurate estimates of the wave profile, and the velocity, acceleration and pressure fields, than can the linear theory. However, it is suggested[30] that when estimates of wave height and period are obtained from empirical data the uncertainties about the choice of parameters leads to greater uncertainty about the final answer than does neglecting the non-linearities, hence questioning the justification for the extra effort involved in the higher order theories.

Linear wave theory has been compared with Stokes' 5th order theory by the British Ship Research Association[31] for elevations up to the surface of large steep waves, although the linear theory should strictly only be applied for waves of low steepness and at elevations up to still-water-level. It was found that the deviation between the particle kinematics and total wave induced force on a typical member, estimated by the two theories differed by at most 10%, the values derived from the linear theory being larger.

Milgram[26] has stated that most ocean waves are of relatively low steepness, for which the relative differences between the surface profiles, and presumably particle motions, derived by the linear and higher order theories are small. As a result of its reasonable approximation to the behaviour of regular waves of realistic steepnesses the first order theory has become the basis for much of the wave loading work in ocean engineering. The major advantage of linear theory is that it is wholly linear so that any number of waves, of any height, period or direction, can be simply added together to form a realistic sea condition. Also, any wave forces which are expressible as linear operations on the sea surface are given by the sum of the component forces. These properties form the basis of the non-deterministic methods of wave load prediction discussed later.

2.3 PREDICTION OF LOADING INDUCED BY RANDOM WAVES

The theory outlined so far enables the estimation of loading exerted on structural members by particle motions beneath regular waves of constant height and period. However, the actual form of the ocean surface is confused. Waves are short-crested of differing height and period and travel in various directions, the variation of the surface elevation in both space and time being of a random nature.

Under these conditions, it is no longer possible to predict accurately the value of the surface elevation, or associated particle motions, at any point in space at a particular instant of time, as is the case for regular waves, and the most complete description of the phenomenon is provided in terms of its statistical properties.

2.3.1 Description of the Random Wave Field

The usual method of describing the random behaviour of the ocean surface is to consider the sea state to consist of an infinite sum of infinitesimal linear waves, each having a random height, period, direction of advance and phase. With reference to Eq. (2.2.2) the surface elevation may be expressed as[37]:

$$\eta(x,y,t) = \sum_{n=1}^{\infty} \frac{H_n}{2} \cos(k_n x \cos \Theta_n + k_n y \sin \Theta_n - \omega_n t + \phi_n) \quad (2.3.1)$$

where x, y are orthogonal co-ordinate axes in the horizontal plane,

ϕ is a random phase uniformly distributed between 0 and 2π, and

Θ_n is the direction of advance measured relative to the x-axis.

The wave height components, H_n, are distributed such that in each small rectangular element ($\Delta\omega\ \Delta\Theta$) of the frequency, ω, and direction, Θ, space:

$$\sum_{(\Delta\omega\ \Delta\Theta)} \left(\frac{H_n}{2}\right)^2 = S_{\eta\eta}(\omega, \Theta)\Delta\omega\ \Delta\Theta \qquad (2.3.2)$$

where the summation is over the whole of the infinitesimal rectangle. $S_{\eta\eta}(\omega, \Theta)$ is the bivariate spectral density of the sea surface at frequency $\omega(> 0)$ and direction Θ. The summation may be interpreted as the variance of the sea surface elevations for a confused sea obtained by addition of all wave components with frequency and direction of travel in the rectangle ($\Delta\omega\ \Delta\Theta$) centred at point ($\omega$, Θ). The spectral density, therefore, describes the distribution of the total variance of the surface elevation over the (ω, Θ) space. Also as the wave energy per unit area is proportional to the variance of the sea surface then $S_{\eta\eta}(\omega, \Theta)$ can also be considered to represent the distribution of wave energy.

If the spectral density function is known for a particular sea state, and noting that k_n and ω_n are related through Eq. (2.2.3), the time variation in surface elevation at location (x, y) can be described using Eq. (2.3.1) as:

$$\eta(x,y,t) = \sum_{\omega=0}^{\infty} \sum_{\Theta=0}^{2\pi} \sqrt{2S_{\eta\eta}(\omega,\Theta)\Delta\omega\Delta\Theta}\ \cos(kx\cos\Theta + ky\sin\Theta - \omega t + \phi) \qquad (2.3.3)$$

In a similar manner expressions for the particle motions can be developed with reference to Eqs. (2.2.4) to (2.2.7).

Although the directional distribution of the waves is a significant feature of the description of ocean waves, the directional spectrum has not been widely used in design computations, partly as a result of the lack of reliable measurements. Theoretical models have been developed[37], and the subject is receiving much attention at the present time. However, since most measurements of wave climate do not include information in the Θ domain, it is common practice to consider the uni-directional spectrum $S_{\eta\eta}(\omega)$ in engineering applications, where:

$$S_{\eta\eta}(\omega) = \sum_{\Theta=0}^{2\pi} S_{\eta\eta}(\omega, \Theta)\ \Delta\Theta \qquad (2.3.4)$$

This approximation assumes all waves to be long-crested in the predominant wave direction yielding, in that direction, a more severe condition as a result of the concentration of energy at each frequency component from Eq. (2.3.4). Only the long-crested situation is considered herein.

Using this model the motion of the random wave field may be expressed as follows, using Eqs. (2.2.3)-(2.2.7):

$$\eta(x, t) = \sum_{\omega=0}^{\infty} \sqrt{2S_{\eta\eta}(\omega)\ \Delta\omega}\ \cos(kx - \omega t + \phi) \qquad (2.3.5)$$

and

$$u(x, z, t) = \sum_{\omega=0}^{\infty} \omega \frac{\cosh kz}{\sinh kd} \sqrt{2S_{\eta\eta}(\omega)\ \Delta\omega}\ \cos(kx - \omega t + \phi)$$

$$= \sum_{\omega=0}^{\infty} \sqrt{2S_{uu}(\omega)\ \Delta\omega}\ \cos(kx - \omega t + \phi) \qquad (2.3.6)$$

and

$$S_{uu}(\omega) = \left[\omega \frac{\cosh kz}{\sinh kd}\right]^2 S_{\eta\eta}(\omega) \qquad (2.3.7)$$

is the horizontal particle velocity spectral density.

Similarly:

$$\dot{u}(x,z;t) = \sum_{\omega=0}^{\infty} \omega^2 \frac{\cosh kz}{\sinh kd} \sqrt{2S_{\eta\eta}(\omega)\ \Delta\omega}\ \sin(kx - \omega t + \phi) \qquad (2.3.8)$$

$$= \sum_{\omega=0}^{\infty} \sqrt{2S_{\dot{u}\dot{u}}(\omega)\ \Delta\omega}\ \sin(kx - \omega t + \phi)$$

where $S_{\dot{u}\dot{u}}(\omega) = \left[\omega^2 \frac{\cosh kz}{\sinh kd}\right]^2 S_{\eta\eta}(\omega) = \omega^2\ S_{uu}(\omega)$ (2.3.9)

Expressions for particle kinematics in the vertical direction follow in the same way with (cosh kz) replaced by (sinh kz).

2.3.2 Statistical and Probabilistic Properties of the Random Sea Surface

2.3.2.1 Short-term

In the short-term, over a period of several hours, the sea state intensity can be assumed to be constant. Under these conditions the surface elevation spectrum is of constant form and it can be shown that in the limit as $\Delta\omega \to 0$, by the central limit theorem, the randomly varying surface elevation is statistically stationary following a mean-zero Gaussian probability distribution[38]. (A summary of statistical and probabilistic concepts is given in Appendix One).

The probability density function (pdf.) of η is, (see Eq. (I.32), Appendix One):

$$p(\eta) = \frac{1}{\sqrt{2\pi}\,\sigma_\eta} \exp\left\{-\frac{1}{2}\left(\frac{\eta - \bar{\eta}}{\sigma_\eta^2}\right)^2\right\} \tag{2.3.10}$$

where $\bar{\eta} = E\{\eta\} = 0$ = mean value of η (2.3.11)

$$\sigma_\eta^2 = E\{(\eta - \bar{\eta})^2\} = \int_0^\infty S_{\eta\eta}(\omega)\, d\omega \tag{2.3.12}$$

= variance of η

and

$E\{.\}$ is the expected value operator

Furthermore, with reference to Eqs. (2.3.6) - (2.3.9), it is clear that the water particle kinematics are also mean-zero Gaussian distributed random variables with variances obtained as the area beneath their respective spectral density functions. This follows both by analogy to the above comments and also as a result of the linear transformations between η and the particle kinematics given that Gaussian input to linear systems produces Gaussian output, a property which can be easily proved.

The pdf. of wave amplitude, i.e., the heights of the crests above still-water level and troughs below, may be expressed as[39]:

$$p(A') = \frac{1}{\sqrt{2\pi}}.\varepsilon \exp\left(-\frac{A'^2}{2\varepsilon^2}\right) + A'(1-\varepsilon^2)^{1/2} \exp\left(-\frac{A'^2}{2}\right) \int_{-\infty}^{\frac{A'}{\varepsilon}(1-\varepsilon^2)^{1/2}} \exp\left(-\frac{\alpha^2}{2}\right) d\alpha \tag{2.3.13}$$

where $A' = \eta_{max}/\sigma_\eta$ or η_{min}/σ_η
and ε = spectral bandwidth (see Section I.2.2.3, Appendix One).

For a <u>narrow band spectrum</u>, $\varepsilon = 0$ and:

$$p(A') = A' \exp\left(-\frac{A'^2}{2}\right)$$

which is a Rayleigh pdf. (see Section I.3.1.6, Appendix One).

For a <u>wideband spectrum</u>, $\varepsilon = 1$ and:

$$p(A') = \frac{1}{\sqrt{2\pi}} \exp\left(-\frac{A'^2}{2}\right)$$

which is a Gaussian pdf.

Spectra can be considered to be of narrow band if the frequency width over which the ordinates of $S_{\eta\eta}(\omega)$ are significant is substantially less than the central frequency within the band. Although most ocean wave spectra are not narrow band in this sense, results for a narrow band spectrum are still applicable for engineering purposes when primarily concerned with extremal statistics[26]. This proposition follows from the work of Ochi[40], who investigated the statistics of extreme wave amplitudes, which showed that there was little dependence on ϵ in the range $0 < \epsilon < 0.8$. This range includes nearly all sea spectra[26] as demonstrated for the 'Famita' wave environment in the North Sea by Draper and Driver[41] and Saetre[42].

Employing the narrow band model, the pdf. of wave height, H, defined as $(\eta_{max} - \eta_{min})$ between two successive upcrossings of the mean-water-level, is a Rayleigh pdf. given by

$$p(H) = \frac{H}{4\sigma_\eta^2} \exp[-\frac{H}{8\sigma_\eta^2}] \qquad (2.3.14)$$

and the mean wave height is:

$$\overline{H} = \sqrt{2\pi}\,\sigma_\eta \qquad (2.3.15)$$

also the root-mean-square wave height may be shown to be:

$$H_{rms} = \sqrt{E\{H\}^2} = 2\sqrt{2}\,\sigma_\eta \qquad (2.3.16)$$

and the average height of the highest (1/n)-th of the waves, $H_{1/n}$, is[39]:

$$H_{1/n} = H_{rms}[\sqrt{\ell n\ n} + \frac{n}{2}\sqrt{\pi}(1 - \text{erf}\ \sqrt{\ell n\ n})] \qquad (2.3.17)$$

where ℓn is the natural logarithm; and
erf is the error function

The <u>significant wave height</u> corresponds to a value n = 3, hence:

$$H_s = H_{1/3} = 4\sigma_\eta \qquad (2.3.18)$$

$$p(H) = \frac{4H}{H_{1/3}^2} \exp[-\frac{2H^2}{H_{1/3}^2}] \qquad (2.3.19)$$

and the cumulative distribution function, cdf. (see Section I.3.1.2, Appendix One) is:

$$P(H) = 1 - \exp[-\frac{2H^2}{H_{1/3}{}^2}] \qquad (2.3.20)$$

Substituting Eq. (2.3.12) into (2.3.18):

$$H_{1/3} = 4\sqrt{m_0} \qquad (2.3.21)$$

where m_0 is the zeroth moment of the surface elevation spectrum (see Section I.2.2.2, Appendix One).

The significant wave height is one parameter used to characterise the short-term behaviour of the ocean surface and is obtained from analysis of surface elevation records. The other commonly used parameter defining the wave intensity is the mean zero-upcrossing period, T_z, the reciprocal of the mean number of still-water-level crossings per unit time with positive slope, given by (see Section I.3.4.2, Appendix One):

$$T_z = 2\pi\sqrt{\frac{m_0}{m_2}} \qquad (2.3.22)$$

where m_2 is the second moment of $S_{\eta\eta}(\omega)$.

The probabilistic properties of wave period, T, are more complex than those for wave height, the pdf. of T^2 being found to be Rayleigh, and are little used in practice.

The parameters $H_{1/3}$ and T_z are sufficient to define both the probabilistic and spectral descriptions of short-term sea states using the most commonly employed existing models. The probabilistic description of η obtained through Eqs. (2.3.10)-(2.3.12) is the one parameter mean-zero Gaussian process defined by σ_η using (2.3.18). The spectral density functions of the wind driven sea surface may usually be defined in terms of $H_{1/3}$ or T_z or both parameters. For example, the much used Pierson-Moskowitz spectrum[43], obtained from analysis by curve fitting of a large number of measured spectra for fully developed sea states over a particular range of wind speeds, may be expressed as a function of wind speed, U_w, as:

$$S_{\eta\eta}(\omega) = \frac{Ag^2}{\omega^5} \exp\{- B[\frac{\omega_0}{\omega}]^4\} \qquad (2.3.23)$$

where $A = 0.0081$

$B = 0.74$

$\omega_0 = g/U_w$

and applying Eqs. (2.3.21) and (2.3.22) the link between wind speed and sea state parameters is formed.

$$H_{1/3} = \frac{2U_w^2}{g} (\frac{A}{B})^{1/2} \qquad (2.3.24)$$

and

$$T_z = \frac{2\pi U_w}{g} (\frac{1}{B\pi})^{1/4} \qquad (2.3.25)$$

2.3.2.2 Long-term

The long-term description of the wave climate describes the distribution of wave intensities over periods of typically six months or 'one-year' durations. Recordings of surface elevation are often taken for approximately 15 minute durations every three hours. Each record can thereby be considered to represent a sample from a short-term stationary sea state, analysis yielding values of $H_{1/3}$ and T_z, together with other significant statistical parameters.

Long-term data is often represented in the form of a scatter diagram, or bivariate histogram, giving the proportion of the time for which the values of $H_{1/3}$ and T_z fell within certain classes, as shown in Fig. 2.3.1.

This figure shows results obtained from wave recordings, taken in the above manner, from one winter's operation, between October, 1969 and March, 1970, by shipborne wave recorder placed on m.v. 'Famita', a Norwegian rescue and meteorological vessel stationed,as shown in Fig. 2.3.2,in the Northern North Sea in 73m. of water. Also included in Fig. 2.3.1 is a prediction of a corresponding scatter diagram for a six-month summer period and a summation yielding a predicted one-year scatter diagram. The need for extension of the wave climate description is expounded in Chapter Four, the one-year Famita scatter diagram being used as input in all long-term computations described herein.

2.3.2.3 The long-term distribution of significant wave height

The marginal distribution (see Appendix One) of $H_{1/3}$ is obtained from the bivariate pdf. of $H_{1/3}$ and T_z as:

$$p(H_{1/3}) = \int_0^\infty p(H_{1/3}, T_z)\, dT_z \qquad (2.3.26)$$

and

$$P(H_{1/3}) = \int_0^{H_{1/3}} p(H_{1/3})\, dH_{1/3} \qquad (2.3.27)$$

In the discrete form of the scatter diagram, we have:

$H_{1/3i}$ = mid-point of the i-th class interval, i = 1, ..., n
$\Delta H_{1/3}$ = class width of $H_{1/3}$
T_{zj} = mid-point of the j-th class interval, j = 1, ..., m
ΔT_z = class width of T_z
w_{ij} = number of occurrences in the scatter diagram class (i, j)

Eq. (2.3.27) may now be approximated as:

$$P(H_{1/3I} + \frac{\Delta H_{1/3}}{2}) = \sum_{i=1}^{I}\sum_{j=1}^{m} w_{ij} \Big/ \sum_{i=1}^{n}\sum_{j=1}^{m} w_{ij} \qquad (2.3.28)$$

However, since this expression assigns an incorrect probability of 1.0 to the upper limit of $H_{1/3}$ in the wave data, preventing the upper-most data class from being plotted on probability paper, a standard modification is applied, as described in Appendix Two, where:

$$P(H_{1/3I} + \frac{\Delta H_{1/3}}{2}) = \sum_{i=1}^{I}\sum_{j=1}^{m} w_{ij} \Big/ \left(\sum_{i=1}^{n}\sum_{j=1}^{m} w_{ij} + 1\right) \qquad (2.3.29)$$

This enables all data points to be plotted and has an insignificant effect on the cumulative probabilities associated with the other data points when the total number of occurrences in the scatter diagram is large.

2.3.2.4 The long-term distribution of individual wave height

The short-term distribution of individual wave height, H, is given by Eq. (2.3.20) but since this is conditional on the sea state intensity, defined through $H_{1/3}$ and T_z, it is more correct to re-write the equation as a conditional cdf. (See Appendix One):

$$P(H|H_{1/3}, T_z) = 1 - \exp[-2\frac{H^2}{H_{1/3}^2}] \qquad (2.3.30)$$

The long-term distribution may be obtained, as derived by Battjes[7] as a weighted sum, or convolution, of the above short-term Rayleigh distributions:

$$P(H) = 1 - \frac{1}{\overline{T_z^{-1}}} \int_0^\infty \int \frac{p(H_{1/3}, T_z)}{T_z} \exp\{-2 \frac{H^2}{H_{1/3}^2}\} \, dH_{1/3} \, dT_z \qquad (2.3.31)$$

$$\text{where } \overline{T_z^{-1}} = \int_0^\infty \int \frac{p(H_{1/3}, T_z)}{T_z} \, dH_{1/3} \, dT_z \qquad (2.3.32)$$

The division by T_z for each short-term condition of $H_{1/3}$, T_z reflects the transformation necessary in converting time, given by the scatter diagram, into number of waves.

In discrete form, Eq. (2.31) becomes:

$$P(H) = 1 - \frac{1}{\overline{T_z^{-1}}} \sum_{i=1}^{n} \left[\exp\{-2 \frac{H^2}{H_{1/3i}^2}\} . \sum_{j=1}^{m} \frac{w_{ij}}{T_{zj}} \right] \qquad (2.3.33)$$

$$\text{where } \overline{T_z^{-1}} = \sum_{i=1}^{n} \sum_{j=1}^{m} \frac{w_{ij}}{T_{zj}} \qquad (2.3.34)$$

This cdf. is plotted for the Famita wave climate in Fig. 2.3.3. The plot is made on Weibull paper and it is clear that the tail of the distribution is reasonably straight indicating that the cdf. of H may be approximated quite well by the theoretical Weibull distribution, which follows with reference to Appendix Two.

2.3.3 Deterministic Methods of Wave Load Prediction and their Limitations

The 'design wave' approach is the most commonly used method for the design of structures and structural members submerged beneath ocean waves. The objective of the method is to design against first excursion failure, to ensure that structural members can resist the greatest load likely to occur during a period of exposure in the wave environment.

In deterministic methods the random behaviour of the loading induced by waves is ignored and the greatest load is assumed to result from the passage of the largest wave. This wave is then assumed to take the form of a single 'regular' wave, having the characteristics developed for the motion of regular waves of the same height and period. Wave kinematics are, therefore, developed using an appropriate wave theory, as outlined in Section 2.2, yielding wave loading on structural elements using Morison's equation. If the structure is modelled as comprising of a large number of loaded elements a quasistatic structural analysis may be

performed to estimate total imposed loads and moments, internal stresses and structural deformations, etc.

The height of the design wave is often chosen to correspond to a certain 'design' return period, Tr, typically 50 or 100 years. This represents the height of a wave which is equalled or exceeded on average only once in Tr years. Since wave data covering such periods is not available, the magnitude of the wave height must be extrapolated from measurements covering much shorter periods, possibly using the long-term distribution of individual wave heights as introduced in the previous section.

For example, from the 'one-year' Famita wave climate data the 50 year wave height could be estimated using Fig. 2.3.3 as follows:

Long-term mean number of waves per second = $\overline{T_z^{-1}} = .1511$

Number of waves per year, $N_1 = 4.765 \times 10^6$

Number of waves in 50 years = 23.8×10^6

Prob $(H < H_{50}) = P(H_{50}) = 1 - \frac{1}{23.8 \times 10^6} = 0.9999999958$

and extrapolating from the figure, $H_{50} \simeq 26m$.

It must be appreciated in the design wave method that there is always a risk associated with the adoption of any design wave height (or design return period, Tr) as there is a possibility that a wave larger than the design wave will occur during the period of exposure of the structure. It can be shown that if all waves are assumed to be independent and if N represents the number of waves in one year then for a structure of design life L years, the probability that the largest wave will exceed the design wave, H_{Tr}, is:

$$\text{Prob}(H_{max} > H_{Tr}) = 1 - \left(1 - \frac{1}{(Tr \times N_1)}\right)^{LxN_1} \qquad (2.3.35)$$

and since $(Tr \times N_1)$ will be large:

$$\text{Prob}(H_{max} \geq H_{Tr}) \simeq 1 - \left[\exp\{-\frac{1}{(Tr \times N_1)}\}\right]^{LxN_1}$$

$$\simeq 1 - \exp\{-\frac{L}{Tr}\} \qquad (2.3.36)$$

For example, if the design return period Tr was chosen to be equal to the structure's design lifetime there would be greater than a 63% chance of the design wave height being exceeded.

Design should generally proceed, therefore, from an assessment of the maximum tolerable risk of failure, substitution of which in Eq. (2.3.36) would yield the return period to be used as a basis for design.

Having determined the height of the design wave it remains to estimate a wave period to be associated with it. The usual approach appears to be to choose a wave profile of near maximum steepness, as measured by the ratio of wave height to wave length, the latter being expressible in terms of wave period for regular waves, for example through Eq. (2.2.3) for linear wave theory. Theoretically, the maximum wave steepness is approximately 1/7 although analysis of wave data by Howard[44] indicates a limit of 1/12.

As a general rule in design it is often assumed that, for a given wave height, reduction in wave period increases the induced loading. However, this is only strictly true for members located close to the water surface as a result of the hyperbolic decay of the water particle kinematics with depth. This effect is demonstrated by the author in reference 20, for deep water conditions and using linear wave theory. Hence, although the design wave may result in the maximum induced loading on some members of a structure, it would not have the optimum period to maximise the loading on all other members.

In view of the above comments, the inherent idealisation of the form of the design wave and the non-linearity of the loading mechanism there must be some doubt regarding the transformation from a 'risk of wave height exceedence' criterion to a 'risk of failure' or 'wave load exceedence'. It does not follow that the 100-year design wave will necessarily yield the '100-year' design load or stress. To obtain a more acceptable method of assessing risks of failure the long-term probabilistic behaviour of the wave loading and structural response is required. This must be developed from the probability structure of the random wave environment taking into account all non-linearities in the transformations.

From experience gained with existing offshore installations, it would appear that the current design methods yield structures which are sufficiently strong to resist the extreme loads imposed. Unfortunately, in the absence of the more rigorous probabilistic analyses, the efficiency of the designs, as measured by the departure between the

accepted design risk of failure and the risk associated with the deterministic loading assessment, is unknown.

Fatigue failure of structural members, following periods of exposure to the oscillating loads induced by the passage of millions of waves, is of great concern to the designers of steel lattice structures. A thorough probabilistic description of the peak loading distribution, for transformation into the stress range distribution, is essential for fatigue analysis, as described by Lin[45] and outlined later. In the absence of probabilistic descriptions of load or stress, deterministic design rules, and more recently more thorough spectral methods[46], have been developed, the performance of which need to be investigated by the development of probabilistic analyses for the non-linear loading situation.

2.3.4 Non-deterministic Methods of Wave Load Prediction

From the discussion in the previous Section it is clear that deterministic methods cannot be used to adequately describe random wave loading for structural design. Random phenomena may be most thoroughly described using their statistical properties in association with either time history simulation analyses (in the time domain), spectral analyses (in the frequency domain) or probabilistic analyses (in the amplitude domain) as summarised in Appendix One and dealt with in detail by Bendat and Piersol[47].

Simulation techniques, considered briefly in Chapter Five, are extremely demanding in computer run times and consequently are only really feasible for application to short-term conditions. Spectral techniques have the advantage over probabilistic methods in that they can be applied to analysis of structures which respond dynamically to the wave loading[9,48] although it would appear that many marine structures are relatively rigid for which such effects are thought to be negligible.

The advantage of the probabilistic approach is that first excursion and fatigue damage analyses for structural design involve the use of probabilistic descriptions of load or response. Consequently, the results of spectral analyses must be transposed to yield the statistical parameters necessary to define the relevant probability distributions. However, existing (linear) spectral techniques can only develop the second order statistical moment, or variance of mean zero processes, while the probabilistic description of non-linear loading of the Morison

form' requires knowledge of up to the fourth order moment, as described later.

Statistical moments higher than the second order may only be obtained using spectral techniques by extension of the concepts to include higher order spectra[49,50]. For example, the bispectrum would be related to the third order statistical moment and the trispectrum to the fourth moment. However, although higher order spectra have received some attention in applications to ship behaviour[51,52], they are far from being sufficiently well understood for inclusion in design procedures.

Consequently, with the limitations imposed by analysis based on first order spectra, the usual design procedure is to derive the spectrum of load or response and compute the corresponding variances. The probability structure of load or response are then assumed to be Gaussian distributed and hence may be fully defined by their variance when the behaviour is mean-zero. This assumption indirectly implies that the loading mechanism can be linearised which will be shown in the following Chapter to considerably underestimate the loading, or response, under conditions where the effects of drag are significant.

For these reasons probabilistic analysis forms the most complete and direct approach for the structural design of offshore installations for which dynamic response is insignificant and loading is within the drag/inertia regime.

2.3.5 Statistical and Probabilistic Properties of the Water Particle Kinematics Beneath Random Waves

The short-term properties of water particle kinematics at particular locations are required as an intermediate step in the transformation from a description of the ocean surface to the description of wave loading, developed as explained earlier using linear wave theory and Morison's equation.

In Section 2.3.2.1 it was demonstrated that the particle kinematics, u, $\dot{u}$, v and $\dot{v}$, at a particular location are all mean-zero Gaussian distributed random variables, defined by their variances which are obtained as the areas beneath their respective spectral density functions.

The relationship between certain pairs of the kinematics are required for the development of the probability structure of wave load, for example between u and $\dot{u}$ or v and $\dot{v}$, as demonstrated in the following Section. More generally, the relationship describing the behaviour of pairs of the kinematics at different space locations is required when considering the multi-variate loading domain, covered in Chapter Five, where the probabilistic properties of the sum of a number of single 'Morison' load components is under investigation.

The cross-covariance expressions are of prime importance in this respect although these degenerate to the cross-correlation expressions for mean-zero variables (see Appendix One). The correlation functions relating the value of particle kinematics at location (x_1, z_1) to those at location (x_2, z_2) measured τ time units later have been derived by Foster[53], from expressions of the form of Eqs. (2.3.6) and (2.3.8), as follows:

$$R_{u_1u_2}(\tau) = R_{u_2u_1}(-\tau) = E\{u_1(t)\, u_2(t+\tau)\}$$

$$= \int_0^\infty \omega^2\, S_{\eta\eta}(\omega)\, d\omega.\, \frac{\cosh kz_1 \cosh kz_2}{\sinh^2 kd} \cos(k(x_1 - x_2) + \omega\tau) \qquad (2.3.37)$$

$$R_{u_1v_2}(\tau) = -\int_0^\infty \omega^2\, S_{\eta\eta}(\omega)\, d\omega.\, \frac{\cosh kz_1 \sinh kz_2}{\sinh^2 kd} \sin(k(x_1 - x_2) + \omega\tau) \qquad (2.3.38)$$

$$R_{v_1u_2}(\tau) = \int_0^\infty \omega^2\, S_{\eta\eta}(\omega)\, d\omega.\, \frac{\sinh kz_1 \cosh kz_2}{\sinh^2 kd} \sin(k(x_1 - x_2) + \omega\tau) \qquad (2.3.39)$$

$$R_{v_1v_2}(\tau) = \int_0^\infty \omega^2\, S_{\eta\eta}(\omega)\, d\omega.\, \frac{\sinh kz_1 \sinh kz_2}{\sinh^2 kd} \cos(k(x_1 - x_2) + \omega\tau) \qquad (2.3.40)$$

Also:

$$R_{u_1\dot{v}_2}(\tau) = -R_{\dot{u}_1v_2}(\tau) = \frac{\partial}{\partial\tau}\,[R_{u_1v_2}(\tau)] \qquad (2.3.41)$$

and

$$R_{\dot{u}_1\dot{v}_2}(\tau) = -\frac{\partial^2}{\partial\tau^2}\,[R_{u_1v_2}(\tau)] \qquad (2.3.42)$$

etc.

The cross-correlation, or values of the cross-correlation function at $\tau = 0$, are required in probability analysis.

For kinematics at a single point (i.e., $x_1 = x_2$, $z_1 = z_2$) the cross-correlations degenerate as follows, omitting the subscripts:

$$R_{uu} = \sigma_u^2; \quad R_{vv} = \sigma_v^2; \quad R_{\dot{u}\dot{u}} = \sigma_{\dot{u}}^2; \; R_{\dot{v}\dot{v}} = \sigma_v^2 \tag{2.3.43}$$

and

$$R_{uv} = R_{vu} = R_{u\dot{u}} = R_{v\dot{v}} = 0 \tag{2.3.44}$$

which shows that the two velocity components at a point are uncorrelated and hence statistically independent (see Appendix One) as are the velocity and acceleration kinematics in either co-ordinate direction.

2.3.6 Probabilistic Methods for the Prediction of Wave Load and Associated Structural Response

The prediction of wave loading considered herein is restricted, as mentioned in Section 2.1, to loading mechanisms of the 'Morison' form on members which do not respond dynamically and will be limited for convenience to a treatment of loading, in the horizontal direction only, from long-crested waves.

Thus, restating Eq. (2.1.2), the horizontal load per unit length of member is:

$$F = k_I \dot{u} + k_D \, u|u| \tag{2.3.45}$$

$$\text{where } k_I = C_M \rho \frac{\pi D^2}{4} \quad \text{and} \quad k_D = \frac{1}{2} C_D \rho D \tag{2.3.46}$$

The effects of uni-directional currents and the intermittency of loading in the splash zone are not included here, but are discussed in the OSFLAG reports[10,11].

2.3.6.1 Short-term

In the short-term the statistical properties of the wave field remain constant, conditional on the values of $H_{1/3}$ and T_z as discussed in Section 2.3.2.1, and the random variations in the surface elevation and particle kinematics all follow mean-zero Gaussian probability distributions.

Probability distribution of the basic force variate

With reference to Eq. (2.3.45) it is seen that the loading is a zero-memory non-linear transformation of the mean-zero bivariate Gaussian process involving the statistically stationary and independent random variables u and $\dot{u}$. The probability structure of F may be obtained from

the bivariate pdf. of (u, $\dot{u}$) by applying the method of transformation of random variables (see Sections I.3.2.9 and I.3.3.1, Appendix One), yielding:

$$p_H(F) = \frac{1}{2\pi K_I \sigma_{\dot{u}} \sigma_u} \int_{-\infty}^{\infty} \exp\{-\frac{1}{2}[\frac{u^2}{\sigma_u^2} + \frac{\dot{u}^2}{\sigma_{\dot{u}}^2}]\} du \qquad (2.3.47)$$

where $\dot{u} = (F - k_D u|u|)/k_I$ from Eq. (2.3.45).

The above expression was developed by Holmes and Tickell[54], the pdf. having been derived previously in a different form by Pierson and Holmes[2], both expressions requiring numerical integration for solution. An alternative expression was developed by Borgman[3] which involves tabulated 'parabolic cylinder functions'.

The pdf. given by Eq. (2.3.47) will hereafter be referred to as the Pierson/Holmes, or P/H, distribution. It forms the basis of much of the work reported herein and is a mean-zero symmetrical function with all odd statistical moments being zero:

$$M_n = E\{F^n\} = 0 \qquad n = \text{odd integer} \qquad (2.3.48)$$

and, as will be shown later, is fully defined by its second and fourth order statistical moments:

$$M_2 = k_I^2 \sigma_{\dot{u}}^2 + 3k_D^2 \sigma_u^4 \qquad (2.3.49)$$

$$M_4 = 3k_I^4 \sigma_{\dot{u}}^4 + 18k_I^2 k_D^2 \sigma_{\dot{u}}^2 \sigma_u^4 + 105k_D^4 \sigma_u^8 \qquad (2.3.50)$$

Solving the above equations:

$$k_D = \left[\frac{M_4 - 3M_2^2}{78\sigma_u^8}\right]^{1/4} \qquad (2.3.51)$$

$$k_I = \left[\frac{M_2 - 3k_D^2 \sigma_u^4}{\sigma_{\dot{u}}^2}\right]^{1/2} \qquad (2.3.52)$$

These expressions can be used for the statistical evaluation of the drag and inertia coefficients in Morison's equation, C_M and C_D, from analysis of records of surface elevation and force, as described by Pierson and Holmes[2].

The ratio of M_4 to M_2^2 is referred to as the kurtosis, β, and measures the peakiness of the pdf.

$$\beta = M_4/M_2^2 \tag{2.3.53}$$

This parameter may be used to measure the departure of $p_H(F)$ from the Gaussian form, which takes the value $\beta = 3.0$.

Standardised notation for the Pierson/Holmes pdf.

There is evidence that the distributions of structural response show a similar probabilistic behaviour to that of the wave load[55], a proposition to be investigated further in Chapter Five. It is, therefore, appropriate to represent the P/H pdf. in a general form directly applicable to either loading or response variables. Also, since the pdf. applies to short-term stationary sea state conditions it should be considered to be conditional on the values of $H_{1/3}$ and T_z.

In standardised form Eq. (2.3.47) for random variable γ becomes[14,17]:

$$p_H(\gamma|H_{1/3}, T_z) = \frac{1}{2\pi\,\sigma_{\psi_1}\,\sigma_{\psi_2}} \int_{-\infty}^{\infty} \exp\{-\frac{1}{2}\,[\frac{\psi_1^2}{\sigma_{\psi_1}^2} + \frac{\psi_2^2}{\sigma_{\psi_2}^2}]\}\, d\psi_1 \tag{2.3.54}$$

where $\psi_2 = \gamma - \psi_1|\psi_1$ (2.3.55)

$$\sigma_{\psi_1}^2 = \left|\frac{E\{\gamma^4|H_{1/3}, T_z\} - 3(E\{\gamma^2\}H_{1/3}, T_z\})^2}{78}\right|^{1/4} \tag{2.3.56}$$

$$\sigma_{\psi_2}^2 = E\{\gamma^2|H_{1/3}, T_z\} - 3\sigma_{\psi_1}^4 \tag{2.3.57}$$

Eq. (2.3.54) describes the mechanism giving rise to γ where ψ_1 and ψ_2 are statistically independent mean-zero Gaussian random variables. Clearly, when considering wave load $\gamma = F$, $\psi_1 = \sqrt{k_D}\,u$ and $\psi_2 = k_I\,\dot{u}$. It is also apparent that the pdf. of γ is defined by its second and fourth moments, $E\{\gamma^2|H_{1/3}, T_z\}$ and $E\{\gamma^4|H_{1/3}, T_z\}$, respectively.

The P/H distribution is plotted in the standardised form in Fig. 2.3.4, taken from Reference 17, prepared by the author on Gaussian paper such that the Gaussian pdf. ($\beta = 3.0$) plots as a straight line (note that $\sigma^2 \equiv E\{\gamma^2|H_{1/3}, T_z\}$). This graph clearly demonstrates how the probability of occurrence of high levels of γ can be underestimated by Gaussian assumptions.

Probability distribution of peak values of random variables following the P/H pdf.

In design applications it is the probabilistic descriptions of the peak and extreme values of either load or response, rather than the basic variate, that are of most importance. Distributions of peak values may be transformed into the pdf.s of stress range required in fatigue analyses to check the long-term integrity of structures and they also form the input to the distribution of extreme values necessary for the assessment of risk of first excursion failure.

The peak and extreme distributions of Gaussian distributed linear wave loading, generally applicable to members of large cross-sectional area where the loading is inertial, see Fig. 2.1.1, have been investigated for short-term conditions by Ochi[40] and for long-term conditions by Söding[8]. In the past wave loading of the non-linear Morison form, where drag effects are significant, has been linearised to an equivalent Gaussian process to facilitate investigations into the distribution of peak and extreme loading. However, these assumptions may lead to considerable under-estimation[12], as will be demonstrated in Chapter Three.

The theory covering the probability structure of the peaks of random variables is given by Lin[45] and Bendat[56] and is summarised in Section I.3.4 Appendix One, the important results being presented below for variables γ having a narrow band spectrum.

The narrow band assumption for wave loading or response would appear to be reasonably well founded since the sea surface acting as the input to the system generating γ is often considered to be narrow banded, as discussed in Section 2.3.2.1. This proposition is supported by Tickell[55] from analysis of prototype data.

For the narrow band (type-1) process, (see Section I.3.4, Appendix One) the cdf. of positive peak values (maxima) is:

$$P_{p1}(\gamma|H_{1/3}, T_z) = 1 - \frac{E\{N^+(\gamma)|H_{1/3}, T_z\}}{E\{N^+(0)|H_{1/3}, T_z\}} \qquad (2.3.58)$$

$$E\{N^+(\dot{\gamma})\,|H_{1/3},\ T_z\} = \int_0^\infty \dot{\gamma}\ p(\gamma,\ \dot{\gamma}|H_{1/3},\ T_z)\ d\dot{\gamma} \qquad (2.3.59)$$

and $E\{N^+(0)\,|H_{1/3},\ T_z\}$ is the expected rate of up-crossing of the mean level, $\gamma = 0$, with positive slope.

If γ and $\dot{\gamma}$ are assumed to be statistically independent a simplified expression results, termed the type-2 peak cdf:

$$P_{p2}(\gamma|H_{1/3},\ T_z) = 1 - \frac{p_H(\gamma|H_{1/3},\ T_z)}{p_H(0|H_{1/3},\ T_z)} \qquad (2.3.60)$$

and, from Eq. (I.82), Appendix One:

$$E\{N^+(\dot{\gamma})\,|H_{1/3},\ T_z\} = p_H(\gamma|H_{1/3},\ T_z) \int_0^\infty \dot{\gamma}\ p(\dot{\gamma}|H_{1/3},\ T_z)\ d\dot{\gamma} \qquad (2.3.61)$$

The great advantage of the type 2 approximation is that it represents a considerable reduction in computational effort over the type 1 approach, requiring only the P/H probability densities for its evaluation. The performance and relative merits of these two approaches are discussed in Chapter Three and have been reported in Reference 12.

A standardised plot of the type-2 peak distributions of γ is made in Fig. 2.3.5 which show similar characteristics to Fig. 2.3.4. In the case of Fig. 2.3.5 the plots are made on Rayleigh paper since the narrow-band Gaussian process ($\beta = 3.0$) has peak values following the Rayleigh pdf.

Expected fatigue damage

The expected value of damage per unit time, D', associated with γ may be expressed, for the type 2 peak distribution, as[6,45]:

$$E\{D'|H_{1/3},\ T_z\} = c^{-1}\ E\{N^+(0)\,|H_{1/3},\ T_z\} \int_{-\infty}^{\infty} \gamma^b\ p_{p2}(\gamma|H_{1/3},\ T_z)\ d\gamma \qquad (2.3.62)$$

where c^{-1} and b are constants representing the characteristics of the fatigue properties of the structural material according to the Palmgrem-Miner criterion[57]. A value of unity for the expected damage represents the failure condition.

2.3.6.2 Long-term

Basic variate

The long-term cdf. of γ is obtained by convolution of the short-term distributions with the long-term wave climate data, in the form of a bivariate pdf. of $(H_{1/3}, T_z)$:

$$P(\gamma) = \int_0^\infty \int_0^\infty P_H(\gamma|H_{1/3}, T_z)\, p(H_{1/3}, T_z)\, dH_{1/3}\, dT_z \qquad (2.3.63)$$

For the discrete scatter diagram representation of wave climate this equation becomes, with reference to Section 2.3.2.3:

$$P(\gamma) = \sum_{i=1}^{n} \sum_{j=1}^{m} \left[P_H(\gamma|H_{1/3_i}, T_{z_j}) \frac{w_{ij}}{w}\right] \qquad (2.3.64)$$

where $w = \sum_{i=1}^{n} \sum_{j=1}^{m} w_{ij}$

Peak variate

Convolution of short-term peak cdf.s with the wave climate proceeds in the same manner as previously described for individual wave height in Section 2.3.2.4. In this case the transformation from the time domain into the number of cycle domains is provided by $E\{N^+(0)|H_{1/3}, T_z\}$ as follows, for the type 2 process:

$$P_{p2}(\gamma) = \int_0^\infty \int_0^\infty P_{p2}(\gamma|H_{1/3}, T_z) \frac{E\{N^+(0)|H_{1/3}, T_z\}}{E\{N^+(0)\}} p(H_{1/3}, T_z)\, dH_{1/3}\, dT_z \qquad (2.3.65)$$

$$\text{where } E\{N^+(0)\} = \int_0^\infty \int_0^\infty E\{N^+(0)|H_{1/3}, T_z\}\, p(H_{1/3}, T_z)\, dH_{1/3}\, dT_z \qquad (2.3.66)$$

An approximation, supported by Söding[8], reduces the computational effort by assuming that the mean zero-crossing rate of γ is the same as that for surface elevation given by the reciprocal of T_z, thus:

$$E\{N^+(0)|H_{1/3}, T_z\} \simeq 1/T_z \qquad (2.3.67)$$

and

$$E\{N^+(0)\} \simeq \overline{T_z^{-1}}$$

The wave climate weightings are, therefore, assumed to be identical to those applied in the convolution of wave heights and for discrete wave climate data:

$$P_{p2}(\gamma) = \frac{1}{T_z - T} \sum_{i=1}^{n} \sum_{j=1}^{m} [P_{p2}(\gamma | H_{1/3i}, T_{zj}] . \frac{w_{ij}}{T_{zj}} \qquad (2.3.69)$$

The implications of this approximation are discussed in Chapter Three.

Extreme variate

The distribution of extreme values may be derived from the distribution of the peaks by applying the theory of Gumbel[58]. If all peaks of γ are assumed to be independent, the cdf. of the greatest or extreme value in N peaks is given by:

$$P_{EP}(\gamma) = [P_p(\gamma)]^N \qquad (2.3.70)$$

This distribution may be used to assess the risk of exceedence of a particular level of γ during a period of exposure equivalent to the passage of N cycles for application in first excursion failure analyses.

Expected Fatigue Damage

The expected short-term fatigue damage per unit time given by Eq. (2.3.62) may be convoluted with the wave climate to produce the estimate of mean long-term damage in time t:

$$E\{D'\} = t \int_0^\infty \int_0^\infty E\{D | H_{1/3}, T_z\}\, p(H_{1/3}, T_z)\, dH_{1/3}\, dT_z \qquad (2.3.71)$$

A less justifiable but more convenient representation may be obtained using the long-term peak pdf. in the basic damage formula[59], which is not strictly applicable to the non-stationary long-term behaviour:

$$E\{D'\} = t\, E\{N^+(0)\}\, c^{-1} \int_{-\infty}^{\infty} \gamma^b\, P_{p2}(\gamma)\, d\gamma \qquad (2.3.72)$$

FIG. 2.1.1. LOADING REGIMES FOR CYLINDRICAL MEMBERS AT FREE SURFACE IN DEEPWATER UNDER LINEAR WAVES (Cm = 2·0, Cd = 0·6)

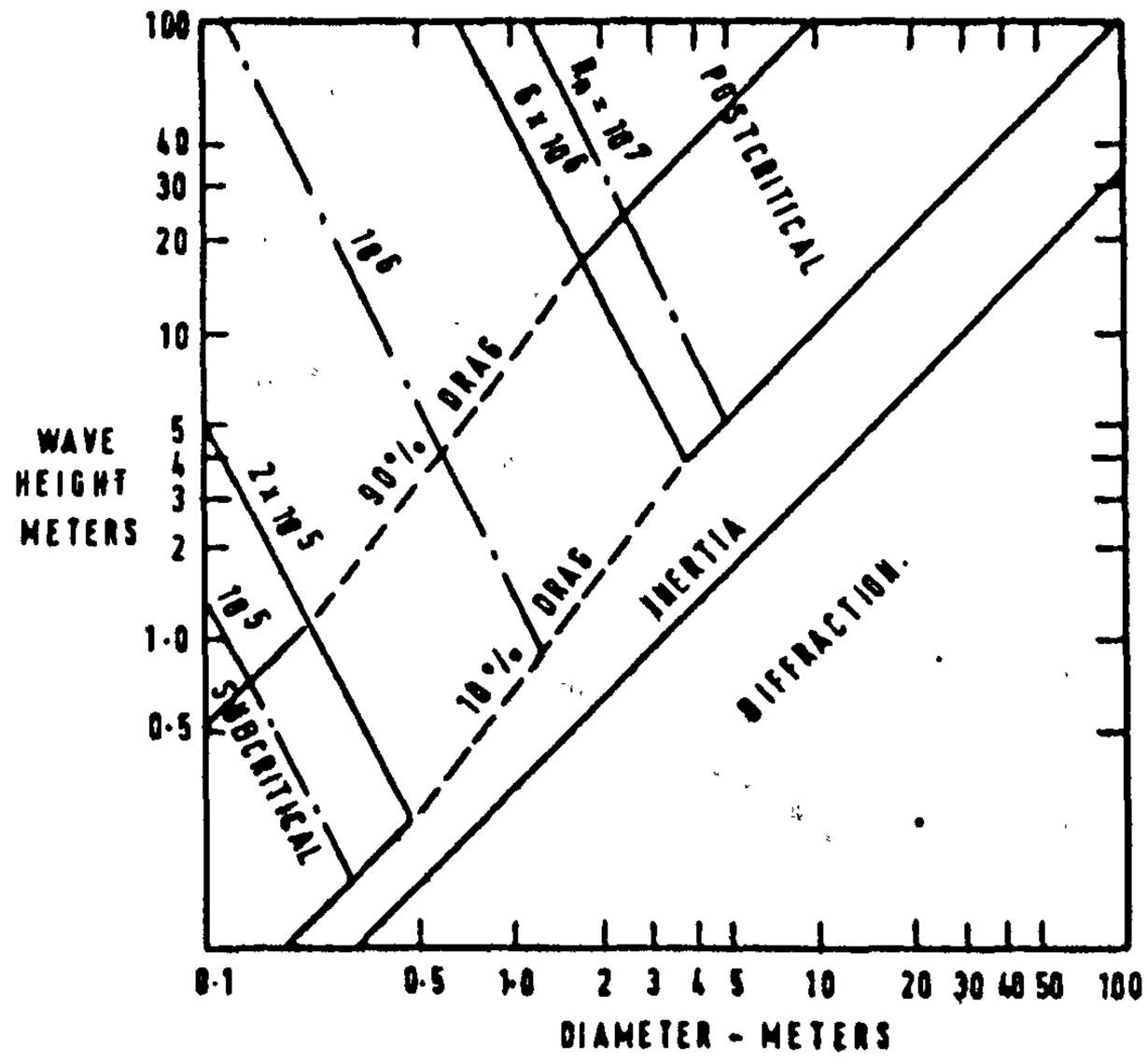

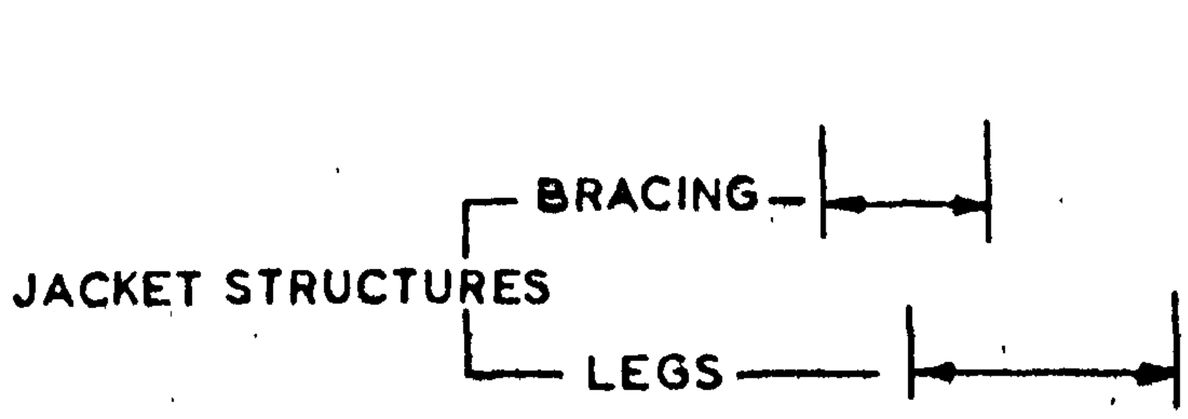

FIG. 2.1.2. INSTANTANEOUS WATER PARTICLE VELOCITY VECTORS AT THE CENTROID OF A SHORT SECTION OF CYLINDRICAL MEMBER INCLINED IN A PLANE PERPENDICULAR TO THE WAVE MOTION.

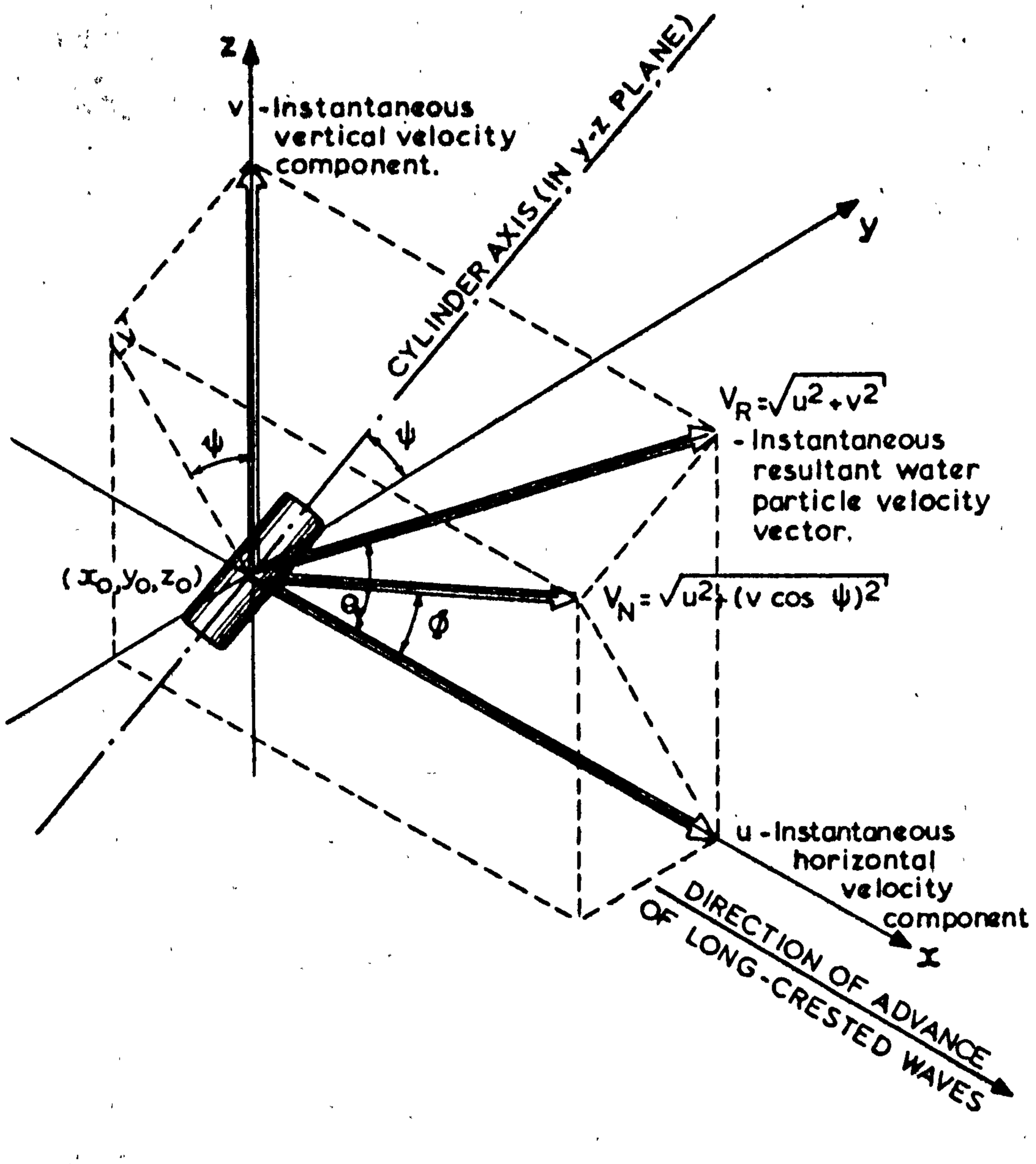

FIG. 2.2.1. DEFINITION OF TERMS - ELEMENTARY, SINUSOIDAL, PROGRESSIVE WAVE.

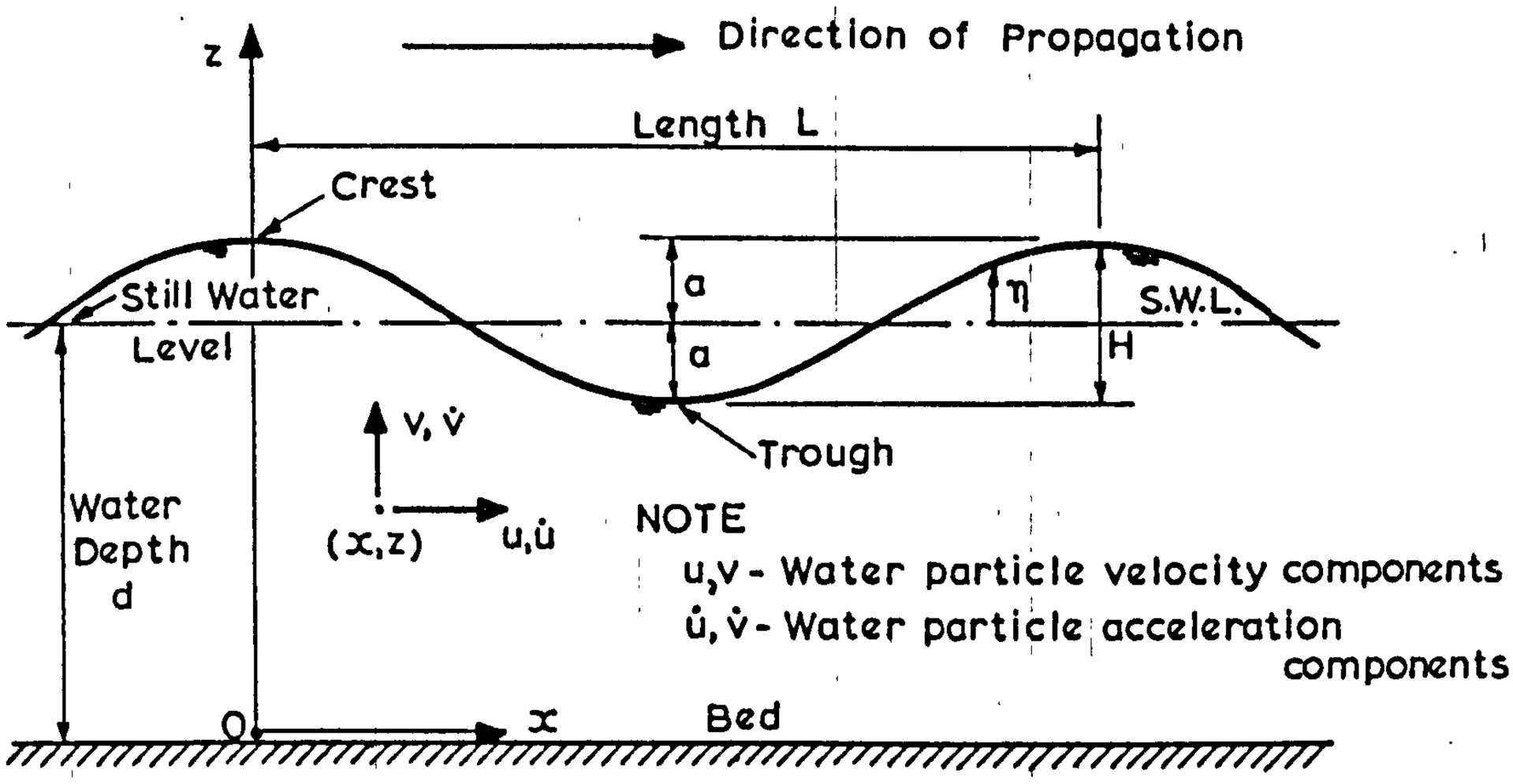

FIG. 2.2.2. WATER PARTICLE DISPLACEMENTS FROM MEAN POSITION FOR SHALLOW-WATER AND DEEPWATER WAVES FOR FIRST ORDER WAVE THEORY.

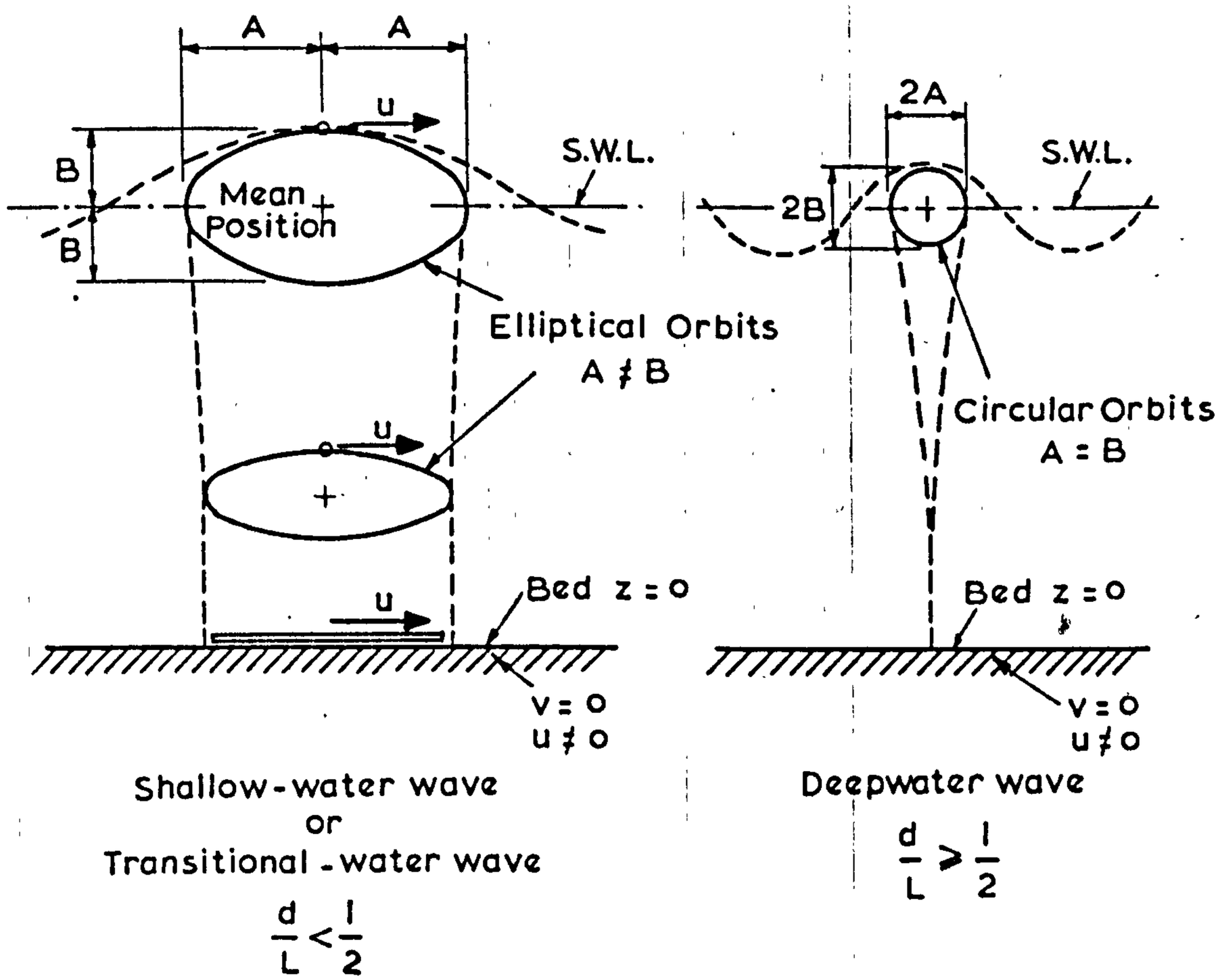

FIG. 2.3.1. SCATTER DIAGRAMS M.V. FAMITA.

WINTER (MEASURED)

PERIOD, T_z (SECONDS)

$H_{1/3(m)}$	4·5	5·5	6·5	7·5	8·5	9·5	10·5	11·5	12·5	13·5
0·3		3	2							
0·9	21	36	33	14						
1·5	2	45	89	30	6					
2·1		24	71	45	11	1				
2·7		4	74	39	16					
3·3		6	36	55	19	1				
3·9		1	18	54	34	4				
4·5			5	18	28	9	2	1		
5·1			5	12	13	12	1			
5·7			1	9	4	6	3			
6·3				2	2	4	2			2
6·9					1	3	7			
7·5				1	1		4		2	
8·1					2					
8·7						2	2			
9·3										2

PARTS PER 962·0

SUMMER (PREDICTED)

PERIOD, T_z (SECONDS)

4·5	5·5	6·5	7·5	8·5	9·5	10·5
14	37	32	8			
43	123	102	26	4		
16	58	75	48	18	2	
6	29	55	50	22	6	1
	15	29	33	25	8	2
	3	10	16	12	2	1
		5	9	4	2	1
		1	2	3	1	
			1	2		

PARTS PER 952·0

ONE YEAR (PREDICTED)

PERIOD, T_z (SECONDS)

4·5	5·5	6·5	7·5	8·5	9·5	10·5	11·5	12·5	13·5
14	40	34	8						
64	159	135	40	4					
18	103	164	78	24	2				
6	53	126	95	33	7	1			
	19	103	72	41	8	2			
	9	46	71	31	3	1			
	1	23	63	38	6	1			
		6	20	31	10	2	1		
		5	13	15	12	1			
		1	9	4	6	3			
			2	2	4	2			2
				1	3	7			
			1	1		4		2	
				2					
					2	2			
									2

PARTS PER 1924·0

FIG. 2.3.2. RESCUE AND WEATHERSHIP m/v "FAMITA" AT LOCATION 57° 30' N, 3° 00' E.

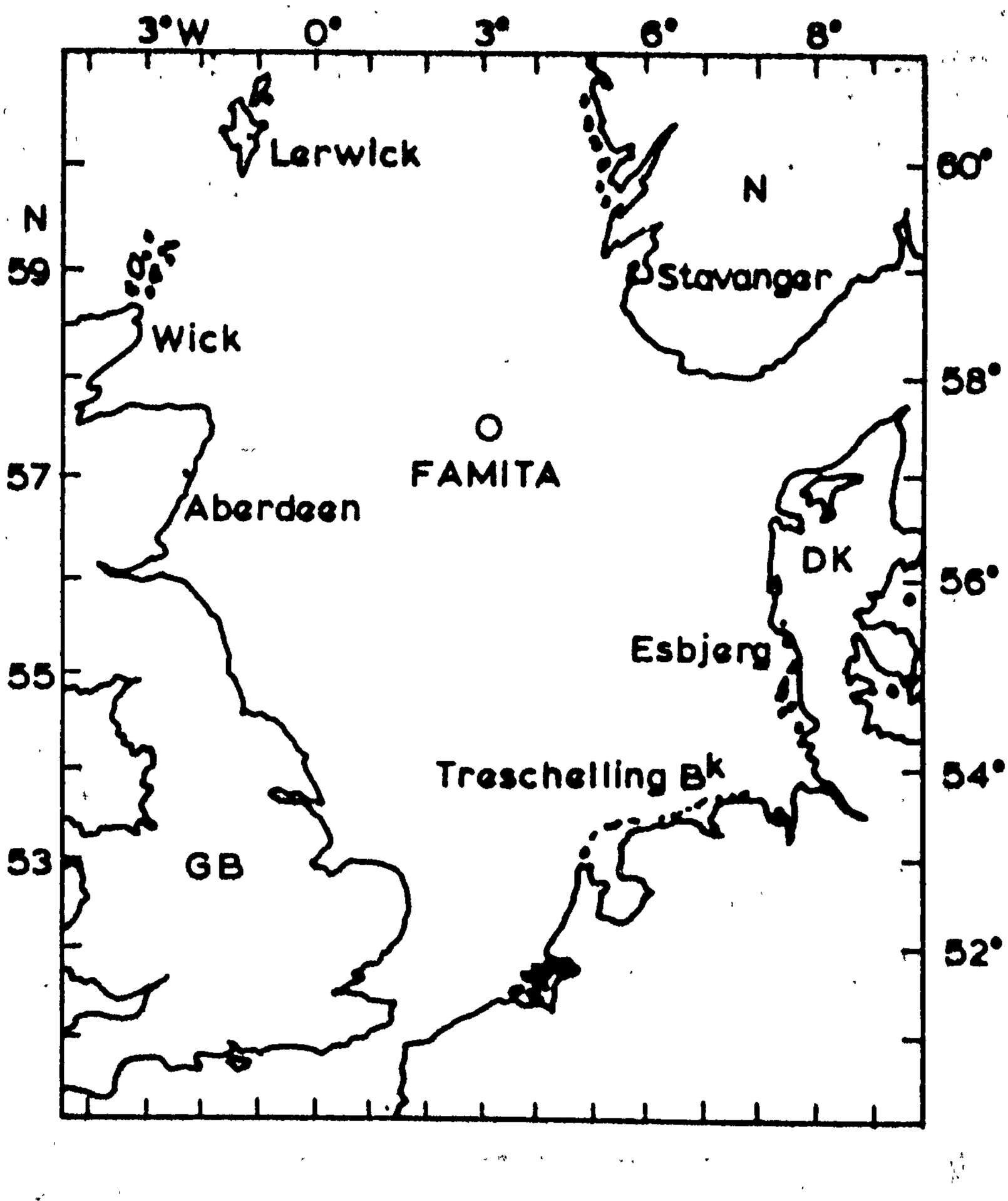

FIG. 2.3.3. LONG TERM MARGINAL PROBABILITY DISTRIBUTION OF INDIVIDUAL WAVE HEIGHT, H

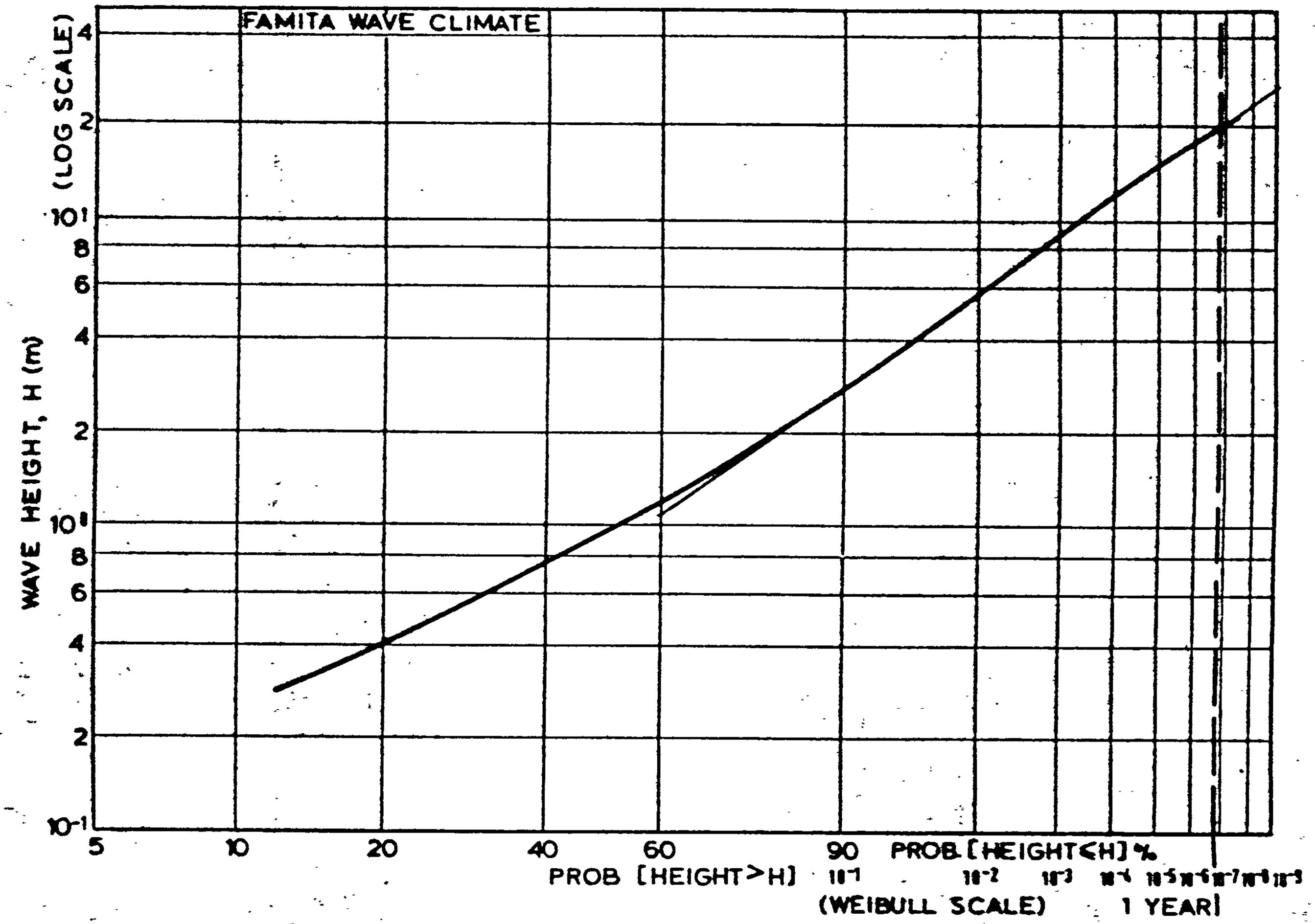

FIG. 2.3.4. STANDARDISED PIERSON/HOLMES CUMULATIVE DISTRIBUTION FUNCTIONS (c d f 's), P (χ)

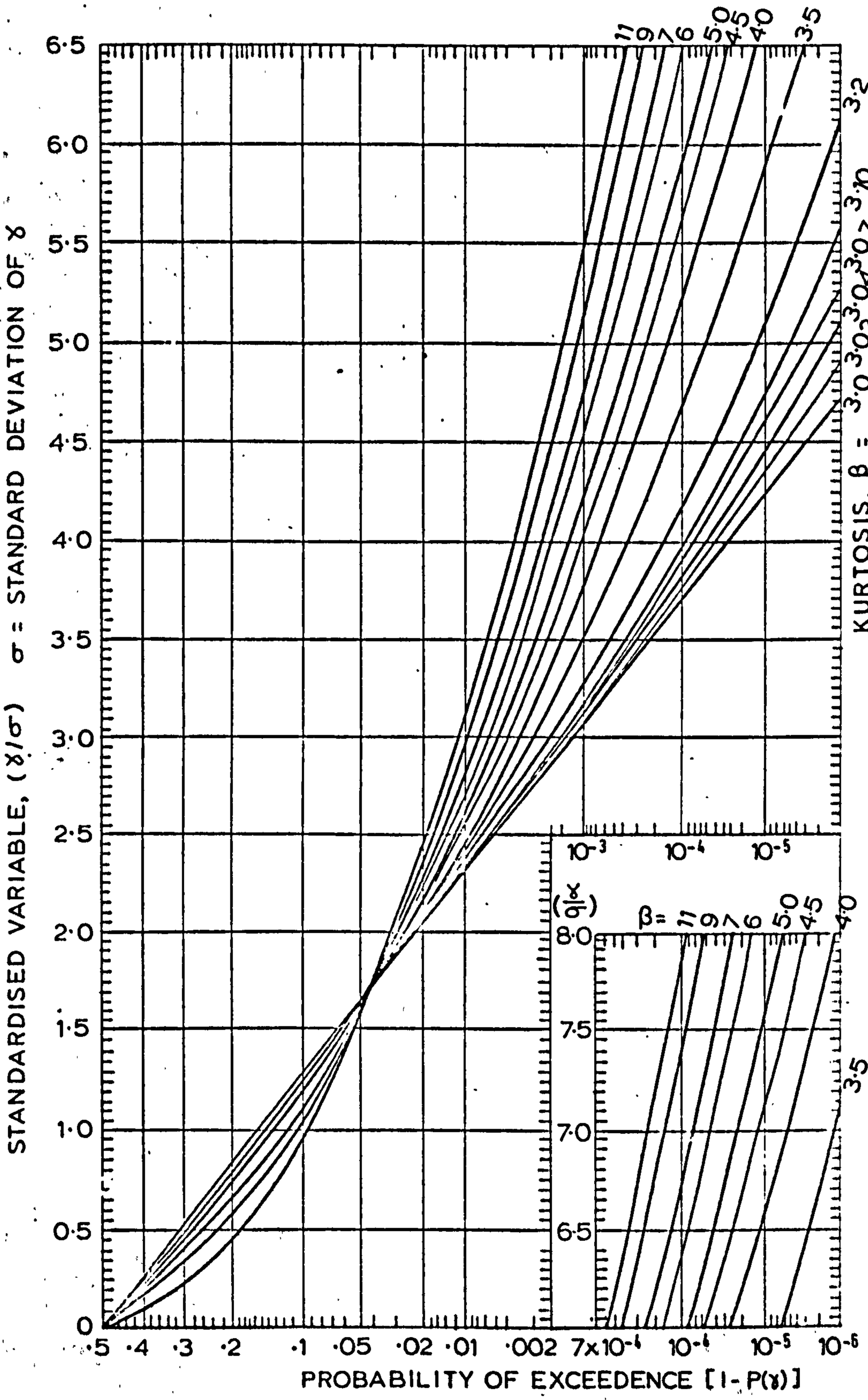

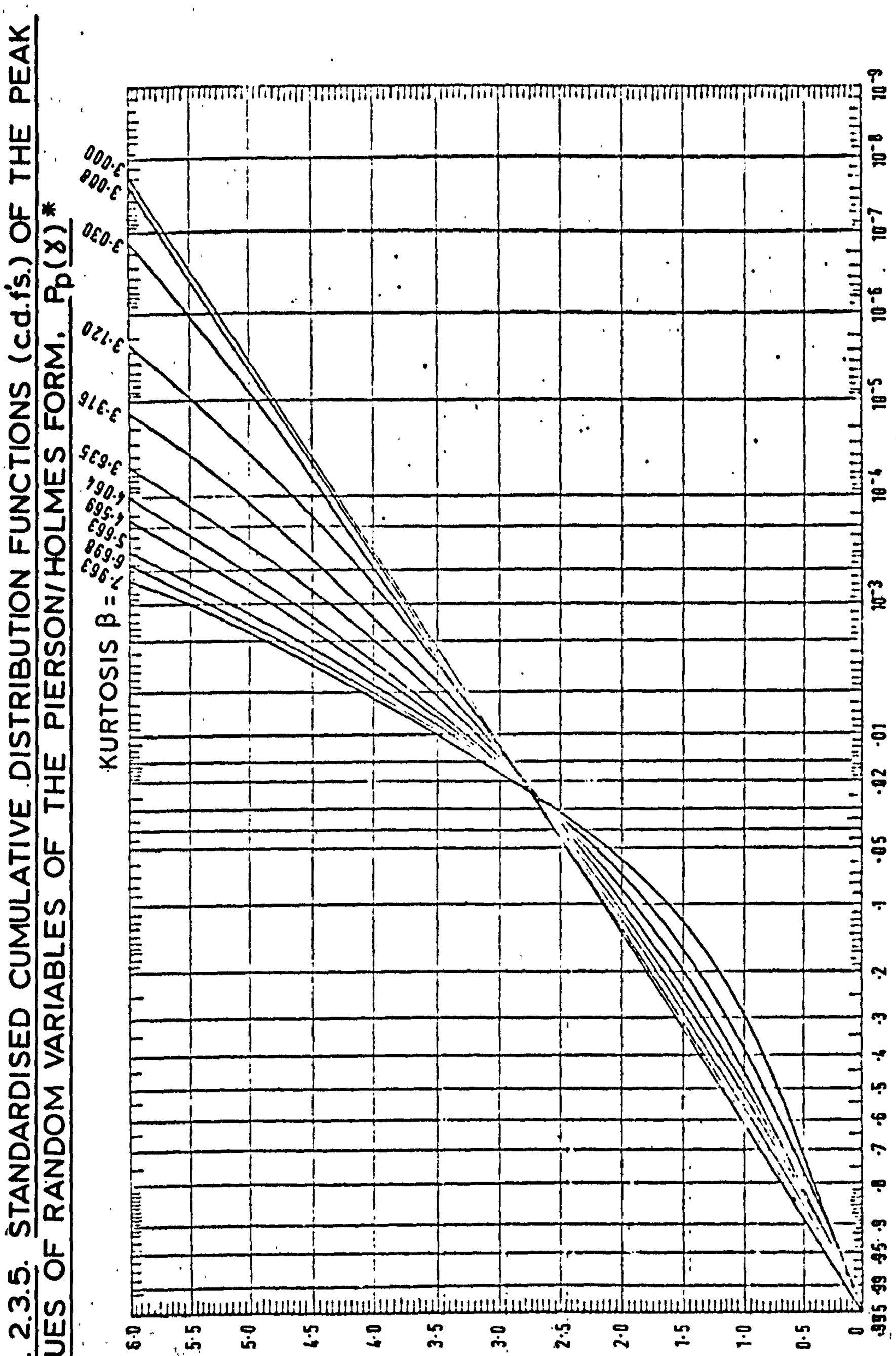

FIG. 2.3.5. STANDARDISED CUMULATIVE DISTRIBUTION FUNCTIONS (c.d.f's.) OF VALUES OF RANDOM VARIABLES OF THE PIERSON/HOLMES FORM, $P_b(\chi)$*

* - Variable assumed to follow narrow-band behaviour, statistically independent of its first time derivative
- Narrow-band type 2 distribution.

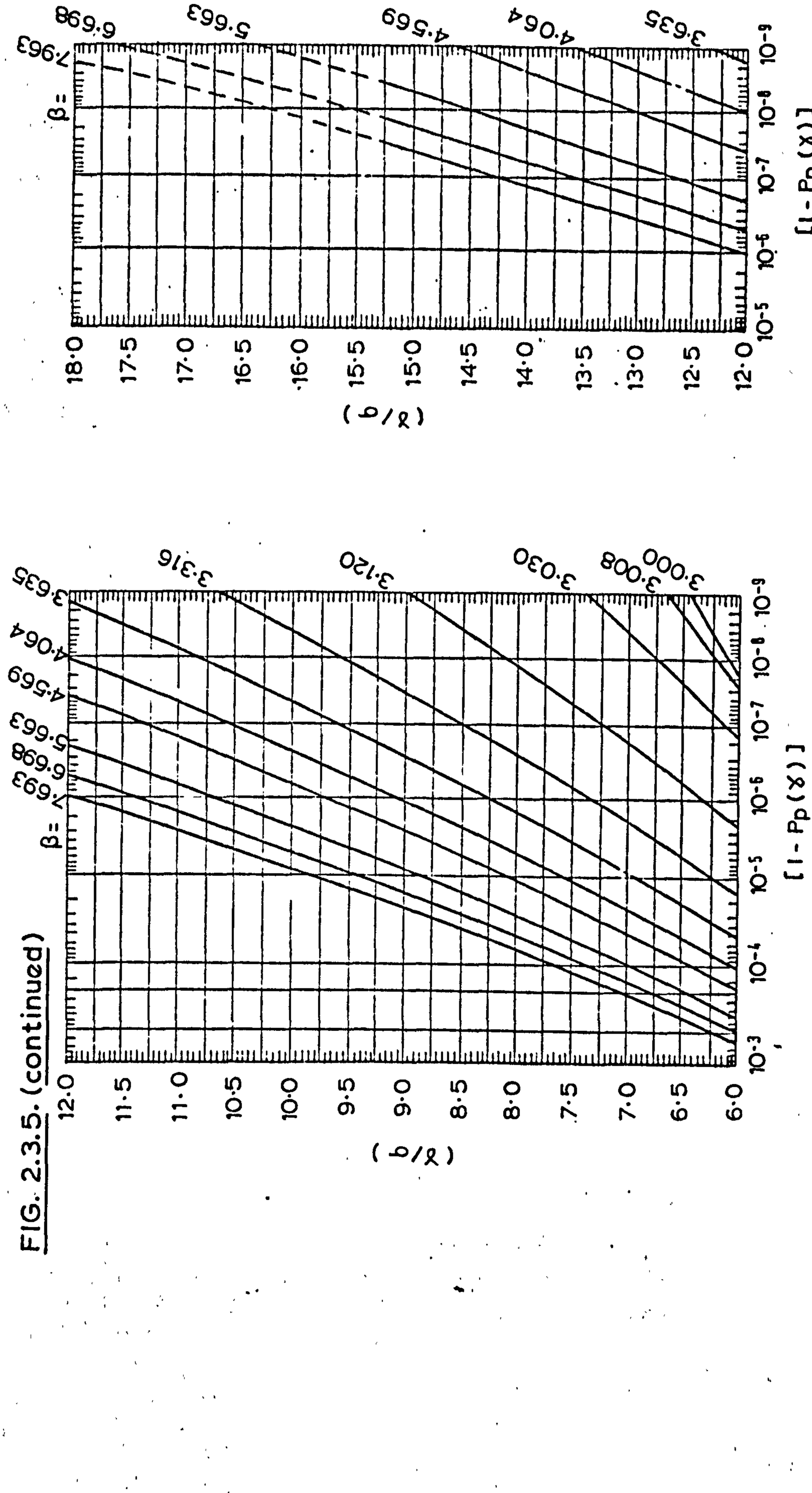

FIG. 2.3.5. (continued)

C H A P T E R T H R E E

PROBABILISTIC WAVE LOADING ON SINGLE MEMBERS

In the following investigation into wave loading on unit length sections of cylindrical members application is restricted to locations beneath the 'splash-zone', or region of surface wave activity. Within the splash zone members are only submerged for a proportion of the time and the loading is, therefore, of an intermittent nature. This effect has been examined by the author and is reported in Reference 11. A further restriction imposed is that the wave field is considered to act on still water. The effects of uni-directional currents on the random wave characteristics and the resulting fluid loading have also been considered by the author and are also reported in Reference 11. In this latter study a number of inadequacies were found in existing theory which have now been resolved by the author and his colleagues at Liverpool.[59]

Before proceeding it should be emphasised that the long-term wave load predictions made in this Chapter are for comparison purposes only. The reason for this restriction is that, in all the computations performed herein, the long-term wave climate is assumed to be represented by the Famita scatter diagrams of Fig. 2.3.1. In Chapter Four it will be shown that for the prediction of extreme events it is necessary to extrapolate the wave climate prior to convolution into long-term descriptions of wave height and wave load. For this reason most of the long-term distributions of wave load presented in the following sections will be truncated at the 'one-year'probability level (the probability associated with a wave load which recurs, or is exceeded, on average once per year).

3.1 THE EFFECT OF NON-LINEARITY IN THE WAVE LOADING ON ITS PROBABILISTIC PROPERTIES

The objective of this Section is to investigate the departures between the long-term probability distributions of the non-linear 'Morison' wave loading, given by the P/H pdf., Eq. (2.3.47), and a linearisation of the loading mechanism, which yields a Gaussian pdf. of wave loading, for typical member and sea state conditions.

Linearised methods of analysis have been applied satisfactorily in the past by Naval Architects for the response of ships to ocean waves. They are also applied, as indicated in Section 2.3.4, in linear spectral analysis techniques[9,25]. Procedures for the prediction of the extreme values of Gaussian random variables are well established and are attractive for use in load prediction by virtue of their relative simplicity[8,40]. It is, therefore, desirable to demonstrate the necessity or otherwise of including the non-linearities in the procedures under certain conditions.

3.1.1 The Linearised Wave Loading Mechanism

The basic 'Morison' wave load expression, Eq. (2.3.45), may be linearised as shown by Borgman[60] by the supposition that:

$$u|u| \simeq u(\sigma_u \sqrt{\frac{8}{\pi}}) \tag{3.1.1}$$

which results from minimisation of the 'mean-square' error in a statistical sense.

The force may now be expressed as:

$$f = k_I \dot{u} + \sqrt{\frac{8}{\pi}}\, k_D\, \sigma_u\, u \tag{3.1.2}$$

Clearly, this approximation over-estimates the loading when u is small and underestimates it when u is large.

In the short-term, f follows the Gaussian pdf. since it is now a linear combination of the Gaussian variables u and $\dot{u}$. Also, since u and $\dot{u}$ are both mean-zero and are statistically independent, for a sea state defined by $H_{1/3}$ and T_z, we obtain:

$$\sigma_f^2 = \frac{8}{\pi} k_D^2\, \sigma_u^4 + k_I^2\, \sigma_{\dot{u}}^2 \tag{3.1.3}$$

and the pdf. is:

$$p(f) = \frac{1}{\sqrt{2\pi}\,\sigma_f} \exp\{-\frac{1}{2}\frac{f^2}{\sigma_f^2}\} \tag{3.1.4}$$

The long-term distributions of this linearised loading follow in the same manner as described for the non-linear loading in Section 2.3.6.2 where Eqs. (3.1.3) and (3.1.4) are strictly conditional on the values of $H_{1/3}$ and T_z.

3.1.2 Methods of Computation and Range of Conditions Considered

Computer program OSF2 (see Appendix Six for a list of computer programs) was developed for the computation of both short and long-term probability distributions of non-linear wave loading using a scatter diagram representation of the wave climate. In all applications considered herein the 'one-year' scatter diagram for Famita given in Fig. 2.3.1 has been used. The program is essentially a refinement of an existing program developed by others based on the original Pierson/Holmes expression for the wave load pdf.[2] referred to in Section 2.3.6.1 and it has been presented in documented form in Reference 10.

Computer program OSF3 was developed for the linearised loading, it being similar in form to OSF2 but with the algorithm for estimation of the short-term P/H pdf. replaced by the Gaussian pdf, Eq. (3.1.4). This program has also been documented in Reference 10.

In both procedures the surface elevation spectrum describing the sea state intensity is of the Pierson-Moskowitz form given in Eq. (2.3.23) defined in terms of $H_{1/3}$ through Eq. (2.3.24). This is the model most often adopted in current practice. The effects of the use of different spectral forms on the long-term distributions of loading are investigated in the following section.

Computations have been carried out for four typical member diameters (0.5, 1.0, 2.0, 5.0m.) at various depths of immersion below the water surface in 150m. of water. This water depth is comparable with that at the locations of existing offshore structures although the effects of an increase in water depth have been briefly considered.

To avoid the effects of intermittency of member submergence in the 'splash-zone' a minimum depth of immersion of 7.5m. has been considered here. This represents greater than 3 standard deviations of the water surface variation under the most intense condition present in the Famita data and hence the member will be submerged for greater than 99.7% of the

time under this sea state and for practically all the time under the less severe sea conditions which predominate in the wave climate.

The majority of the loading computations have been performed with Morison coefficients of $C_M = 2.0$ and $C_D = 1.0$, these values being within the acceptable range referred to in Section 2.1. The effect of change in the coefficients has also been investigated.

3.1.3 Short-term Conditions

The departures between load predictions from the non-linear and linearised methods for sea states present in the Famita data are demonstrated in Figs. 3.1.1 and 3.1.2.

With reference to Eqs. (2.3.49) and (3.1.3) it is apparent that the linearised procedure underestimates the variance of loading by:

$$[\sigma_F^2 - \sigma_f^2] = (3\pi - 8)\, K_D^2\, \sigma_u^4/\pi \qquad (3.1.5)$$

where $\sigma_F^2 = M_2$ is the variance of the non-linear loading.

The magnitude of this underestimation is shown in Fig. 3.1.1. The effect increases as the sea state intensity, defined by $H_{1/3}$ here, increases and as member diameters and depths of immersion decreases. This results from the increased weighting attached to the drag component in the loading equations under these circumstances. For the most drag dependent loading considered the underestimation is seen to be in excess of 10%. However, variation in the long-term standard deviation of load is only marginal as may be inferred from Fig. 3.1.1.

For the linearised method the Gaussian loading is represented in Fig. 3.1.2 by a value of kurtosis of 3.0. The non-linear loading following the P/H pdf. has a kurtosis given by Eqs. (2.3.53), (2.3.49) and (2.3.50) as:

$$\beta = \frac{3k_I^4\,\sigma_{\dot{u}}^4 + 18k_I^2\,k_D^2\,\sigma_{\dot{u}}^2\,\sigma_u^4 + 105k_D^4\,\sigma_u^8}{(k_I^2\,\sigma_u^2 + 3k_D^2\,\sigma_u^4)^2}$$

$$= 3 + \{78/(3 + \frac{k_I^2\,\sigma_{\dot{u}}^2}{k_D^2\,\sigma_u^4})^2\} \qquad (3.1.6)$$

Hence, for <u>inertia dominated loading</u> $k_I^2 \sigma_{\dot{u}}^2 >> k_D^2 \sigma_u^4$

and $\beta \rightarrow 3.0$

For <u>drag dominated loading</u> $k_D^2 \sigma_u^4 >> k_I^2 \sigma_{\dot{u}}^2$

and $\beta \rightarrow 11.67$

From Fig. 3.1.2 it can be seen that for the sea state and member conditions considered here values of kurtosis in excess of eight are obtained. The kurtosis measures the importance of the drag component of loading and increases under the same conditions which were shown above to increase the underestimation of load variance in the linearised model.

The significance of the differences in variance and kurtosis obtained from the two procedures on predictions of wave loading may be appreciated with reference to Fig. 2.3.4 which shows the standardised P/H cdf. for various values of kurtosis. On this figure the cdf. of non-linear wave loading may be represented by the curve with the appropriate value of kurtosis from Fig. 3.1.2. The linearised loading distribution is represented on this figure by the straight line with ordinates reduced below the line corresponding to $\beta = 3.0$ by an amount given by the square root of the values from Fig. 3.1.1, representing the underestimation of the standard deviation of load.

For example, for a 0.5m. diameter member at a depth of immersion of 7.5m. under a sea state with $H_{1/3} = 9.3$m. the linearisation underestimates loading at a probability of exceedence of 10^{-3} by approximately 41% and at a probability of 10^{-4} by 50%, the underestimate increasing rapidly at lower probabilities of exceedence. For a 2.0m. diameter member under the same conditions the underestimate is 13% at the 10^{-4} probability level.

The departures between the distributions of peak loading from the non-linear and linearised procedures show similar characteristics to the basic loading at low probabilities of exceedence with reference to Fig. 2.3.5.

However, at probabilities of exceedence greater than about 0.02 the linearised procedures predict loads in excess of those from the non-linear

method, the effect increasing as the kurtosis increases. This behaviour implies that linearisation of the loading overestimates fatigue damage associated with the small waves.

3.1.4 Long-term Conditions

The long-term cdf.s of non-linear loading are obtained from Eq. (2.3.64) for the basic variate and Eq. (2.3.69) for the narrow-band 'type 2' peak variate. The distribution of peak values is of most practical value in design, forming the input in both fatigue and extreme value analyses and attention is, therefore, concentrated on this variate.

For the situation where the short-term conditions are defined by $H_{1/3}$ only, as considered here, Eqs. (2.3.64) and (2.3.69) reduce to:

$$P(F) = \sum_{i=1}^{n} [P_H(F|H_{1/3i}) \sum_{j=1}^{m} \frac{w_{ij}}{w}]; \; w = \sum_{i=1}^{n} \sum_{j=1}^{m} w_{ij} \qquad (3.1.7)$$

$$P_{p2}(F) = \sum_{i=1}^{n} \left[\left\{1 - \frac{P_H(F|H_{1/3i})}{P_H(0|H_{1/3i})}\right\} \frac{1}{T_z^{-1}} \sum_{j=1}^{m} \frac{w_{ij}}{T_{zj}}\right] \qquad (3.1.8)$$

For the linearised method the P/H probability densities are replaced by the Gaussian values in Eqs. (3.1.7) and (3.1.8).

In Fig. 3.1.3 short-term cdf.s of peak non-linear loading are plotted for a typical member for the conditions present in the Famita wave climate. Superimposed on the figure is the long-term cdf. resulting from convolution of the short-term values by the wave climate according to Eq. (3.1.8).

Figs. 3.1.4 to 3.1.6 show the long-term cdf.s of both non-linear and linearised peak loading for different member conditions, a more detailed presentation being given in Reference 10. These plots demonstrate that the characteristics observed in the short-term properties of loading are retained in the long-term properties. In Fig. 3.1.4 for the smallest diameter member where drag effects are most pronounced, there is only a marginal difference between the peak loads predicted at low levels of load (or high probabilities of exceedence). For members of larger diameter the differences tend to zero as apparent from Figs. 3.1.5 to 3.1.6 since the drag effects are less significant. At low probabilities of exceedence the linearised method considerably underestimates the loading. For example, at a probability of 2.2×10^{-7}, corresponding to the 'one-

year' condition, the underestimation is approximately 48%, 40% and 15% for the 0.5, 1.0 and 2.0m. diameter members, there being negligible differences in the case of the 5.0m. diameter member.

Linearisation of the loading results in considerable saving in computing costs by virtue of run-time requirements of approximately 10% of those required for the non-linear loading computations. This follows because the basic loading pdf. is Gaussian in the short-term and hence its values can be obtained directly, from Eq. (3.1.4), whereas for non-linear loading the P/H pdf., Eq. (2.3.47), requires numerical integration for its solution.

3.1.5 Variation in Morison Coefficients

Fig.3.1.7 shows the effect of changes in the Morison coefficients for a 1.0m. diameter member at an immersion of 15.0m. The pairs of coefficients considered for C_M and C_D, respectively, are (2.0, 1.0), (2.0, 0.5), (1.5, 1.0) and (1.5, 0.5), these values being representative of a range of design values. From the distributions of the non-linear method it is clear that at extreme values the drag coefficient is critical, changes in the inertia coefficient being significant in the lower range. In the linearised method, the changes in drag coefficient are less critical, as expected, due to the suppression of the drag term under the large waves which produce high particle velocities.

3.1.6 Variation in Water Depth

An increase in water depth from 150m. to 250m. has been considered for the 0.5 and 5.0m. diameter members. At the 'one-year' probability level this change causes only a slight reduction in the non-linear load predictions of approximately (1.1, 1.5, 1.9%) and (0.3, 0.4, 0.7%), respectively, at depths of immersion of (7.5, 15.0, 22.5m.). This indicates that the majority of sea conditions considered were in 'deep-water' and suggests also that the results presented here, and those presented in subsequent sections for the 150m. water depth, are applicable to depths of water in excess of 150m.

3.2 EFFECT OF THE CHOICE OF WAVE SPECTRA ON LOAD PREDICTION

The objective of this Section is to demonstrate how the choice of spectral form describing the variation of surface elevation affects the prediction of long-term wave loading.

3.2.1 Spectral Models Considered

The wave spectra investigated here are all based on the Pierson-Moskowitz (P-M) spectrum defined in Eq. (2.3.23), the general shape of which is shown in Fig. 3.2.1. This spectrum was developed as an 'average' curve fitting measured spectra from fully developed wind generated sea states over a limited range of wind speeds. In existing practise the basic P-M spectrum is the most widely accepted model for the description of short-term sea conditions in non-deterministic analyses. Although other spectral forms exist, for example those given by Neumann[61], Darbyshire[62] and Bretschneider[63], they are little used in engineering applications and have, therefore, been omitted here.

3.2.1.1 Basic Pierson-Moskowitz spectra

The spectrum, in its basic form, is a function of wind speed U_w as shown in Fig. 3.2.1. However, from the properties of the spectral moments, U_w is related to the statistical parameters used to describe the short-term sea state, $H_{1/3}$ and T_z, through Eqs. (2.3.24) and (2.3.25). With reference to these equations it is evident that U_w may be derived from either $H_{1/3}$ or T_z. Consequently, with wave climate data in the form of a scatter diagram, for any particular short-term sea state condition, representing a single class in this diagram, there will in general be two distinct P-M spectra developed from the characterising parameters unless the values of $H_{1/3}$ and T_z yield the same wind speed in Eqs. (2.3.24) and (2.3.25). For this condition, $H_{1/3}$ and T_z are related as follows:

$$T_z^2 = \frac{2\pi^2 H_{1/3}}{g(A\pi)^{1/2}}$$

$$T_z = 3.55 \sqrt{H_{1/3}} \qquad \text{in S.I. units} \qquad (3.2.1)$$

This relationship, superimposed on Fig. 2.3.1, should be satisfied for all sea states if the actual surface elevation spectrum is of the P-M form. In practice, sea states deviate from this theoretical form yielding the characteristic scatter in the bi-variate relationship between $H_{1/3}$ and T_z.

Defining the 'characteristic' wave steepness, s, to be the ratio of $H_{1/3}$ to a deep water wave length, $L_0 = gT_z^2/2\pi$, we obtain:

$$s = H_{1/3}/1.56T_z^2 \qquad (3.2.2)$$

Eq. (3.2.1), therefore, represents a wave steepness of 1/19.67 whilst the maximum value present in the Famita scatter diagram is 1/11.6. From analysis of seven stations around the British Isles, Battjes[7] found the steepness limit to lie between 1/16 and 1/20, with only infrequent recordings exceeding these limits. These constants would appear to also be satisfied for the Famita location with reference to Fig. 2.3.1.

The significance of the above discussion is the observation that the vast majority of the data points in scatter diagrams from any offshore location will represent steepnesses much lower than those required to satisfy Eq. (3.2.1). Consequently, wind speed predictions for short-term scatter diagram classes based on T_z will on average exceed the values predicted by $H_{1/3}$.

For practical purposes it is essential to obtain a unique spectrum for each class of the scatter diagram to enable the generation of long-term descriptions of surface elevation or the resulting wave load variations.

One approach to this problem is to consider only one of the parameters $H_{1/3}$ or T_z for the definition of each sea state condition yielding spectra referred to as P-M ($H_{1/3}$) or P-M (T_z). Such an approach was applied in the previous section, using the former, and is considered to be the most appropriate choice, although, from the comments made above it is likely to underestimate sea state severity relative to the latter procedure, as discussed below.

An alternative to the above procedures, which retains the basic P-M model, uses Eqs. (2.3.24) and (2.3.25) to yield the wind speed as a function of the ratio of $H_{1/3}$ and T_z:

$$U_w = \left\{\frac{\pi^3 B}{A^2}\right\}^{1/4} \frac{H_{1/3}}{T_z} = 24.32 \frac{H_{1/3}}{T_z} \qquad (3.2.3)$$

The surface spectrum now becomes a two parameter function of $H_{1/3}$ and T_z which permits a more complete description of the wave climate to be

developed from the scatter diagram. This approach, would appear to have little physical justification since the same spectrum is predicted from, for example, a sea state with $H_{1/3}$ = 4.0m. and T_z = 5.0secs. as from $H_{1/3}$ = 8.0m, T_z = 10secs. Consequently, it is not pursued further here.

The implication of the adoption of any of the above P-M models in preference to the others is illustrated in Fig. 3.2.2 showing the cdf. of wind speed developed from the Famita scatter diagrams from Eq. (2.3.34) for the P-M ($H_{1/3}$) approach and Eq. (2.3.25) for the P-M (T_z) approach. From the figure it is clear that the use of T_z for wave climate description predicts wind speeds in excess of those predicted by the other methods. Furthermore, sea state intensity may be measured by the variances of surface elevation given by the area under $S_{\eta\eta}(\omega)$, which for the P-M spectrum is obtained from Eqs. (2.3.12) and (2.3.23) as:

$$\sigma_{\eta\eta}^2 = \frac{Ag^2}{4B\ \omega_0^4} = 0.00274\ \frac{U_w^4}{g^2} \qquad (3.2.4)$$

Consequently, departures in wind speed predictions from the above procedures are considerably magnified in the resulting statistical descriptions of sea state intensity which form the input into wave loading computations.

3.2.1.2 DNV modification to the Pierson-Moskowitz spectrum

Det Norske Veritas[64] in their design rules for offshore structures utilise the complete wave climate information for the description of wave conditions by recommending a modification to the P-M spectrum, referred to here as P-M (DNV), given by:

$$S_{\eta\eta}(\omega) = \frac{H_{1/3}^2\ T_z}{8\pi^2} \left[\frac{T_z\omega}{2\pi}\right]^{-5} \exp\{-\frac{1}{\pi}\left[\frac{T_z\omega}{2\pi}\right]^{-4}\} \qquad (3.2.5)$$

It is instructive to compare this function with the basic P-M expression by expressing both spectra in the form:

$$S_{\eta\eta}(\omega) = \frac{a}{\omega^5} \exp\{-\frac{b}{\omega^4}\} \qquad (3.2.6)$$

where a and b are constants thus demonstrating that both spectra are of the same shape.

Concentrating firstly on the argument of the exponent, for the P-M expression:

$$b = B\,\omega_0^{\,4} = B\,\frac{g^4}{U_W^{\,4}} \tag{3.2.7}$$

and substituting from Eq. (2.3.25):

$$b = B.\frac{1}{B\pi}\left[\frac{2\pi}{T_z}\right]^4 = \frac{1}{\pi}\left[\frac{2\pi}{T_z}\right]^4 \tag{3.2.8}$$

This expression is identical to the value given in P-M (DNV).
Constant coefficient, a, in P-M (DNV) is:

$$a = \left[\frac{H_{1/3}^2}{T_z^{\,4}}.4\pi^3\right] \tag{3.2.9}$$

Substituting again from Eq. (2.3.25) for T_z:

$$a = \left[\frac{H_{1/3}^2}{4}.\frac{B}{U_W^{\,4}}\,g^4\right] \tag{3.2.10}$$

and substituting for $H_{1/3}$ from Eq. (2.3.24) yields:

$$a = Ag^2 \tag{3.2.11}$$

which is the coefficient in the P-M spectrum.

It may, therefore, be inferred that P-M (DNV) is identical to the basic P-M spectrum when the values of $H_{1/3}$ and T_z satisfy Eq. (3.2.1). It can also be easily shown that the spectral densities, and hence the values of $\sigma_{\eta\eta}^{\,2}$, from P-M (DNV) will be less than those derived from P-M (T_z) for classes within the scatter diagram for which the significant wave height is less than that satisfying Eq. (3.2.1). Since this condition on the value of $H_{1/3}$ is satisfied for the majority of the classes, as discussed earlier, it follows that the P-M (DNV) approach will on average predict sea state intensities less severe than P-M (T_z) but greater than P-M ($H_{1/3}$).

3.2.1.3 JONSWAP spectrum

The JONSWAP program of research[65,66] demonstrated the existance of a significant departure in the spectral shape from the P-M form for fetch limited sea states. This condition results from situations where the generating wind has not blown over a sufficient distance for the fully

developed state to be reached. In fully developed seas the energy contained in each frequency band possesses a maximum 'equilibrium' value, further energy input increases wave steepnesses causing wave breaking and return to the equilibrium condition.

To account for fetch dependence a modification to the P-M spectrum was developed, the main characteristic of which is an enhanced spectral peak, as shown in Fig. 3.2.1. The JONSWAP spectrum is a five parameter function, expressible as:

$$S_{\eta\eta}(\omega) = [\frac{\alpha g^2}{\omega^5} \exp\{-\frac{5}{4}(\frac{\omega}{\omega_p})^{-4}\}] \gamma_p^{\exp[-\frac{(\omega-\omega_p)}{2\sigma^2\omega_p}]} \qquad (3.2.12)$$

where $\sigma = \sigma_a$ if $\omega \leq \omega_p$

$= \sigma_b$ if $\omega > \omega_p$

and ω_p is the frequency at the spectral peak

In Eq. (3.2.12) the term in square brackets is the P-M spectrum modified by the inclusion of a variable parameter α replacing A = 0.0081 to describe the 'constant' in Phillips equilibrium range[67]. The argument of the exponential function is unchanged since by differentiation of the P-M spectral density:

$$\omega_p = \omega_0(\frac{4B}{5})^{1/4}; \quad [= 0.88\omega_0] \qquad (3.2.13)$$

Parameters γ_p, σ_a and σ_b describe the shape of the spectral peak as shown in Fig. 3.2.1. These were found to show no definite trend with variation in fetch and constant values are recommended[65]:

$$\gamma_p = 3.3; \quad \sigma_a = 0.07; \quad \sigma_b = 0.09 \qquad (3.2.14)$$

The remaining parameters defining the JONSWAP spectrum are fetch dependent, the best estimates being[65]:

$$\omega_p = (\frac{2\pi g}{U_w}).3.5\left\{\frac{gx_f}{U_w^2}\right\}^{-0.33} \qquad (3.2.15)$$

and

$$\alpha = 0.076\{g\frac{x_f}{U_w^2}\}^{-0.22} \qquad (3.2.16)$$

where x_f = fetch, distance of open sea in the direction of the wind available for wave generation.

In the engineering applications of interest here wave climate description includes the variation of $H_{1/3}$ and T_z only, no information covering wind speeds and corresponding fetches being available. However, the JONSWAP spectral form can be included in the procedures using a relationship obtained as a regression fit to data[68]:

$$\alpha = 5.78\left(H_{1/3}\left[\frac{\omega_p}{2\pi}\right]^2\right)^{2.036}\left(1.0 - 0.298\ln(\gamma_p)\right) \qquad (3.2.17)$$

Using this expression the JONSWAP spectrum can be generated for each short-term sea state through the value of $H_{1/3}$ as explained below.

The procedure, referred to hereafter as JONSWAP ($H_{1/3}$), is iterative since for a given value of $H_{1/3}$ values of α and ω_p must be obtained which satisfy Eq. (3.2.17) and which specify the spectrum, producing an estimate of $H_{1/3}$ (from the area beneath $S_{\eta\eta}(\omega)$, using Eqs. (2.3.12) and (2.3.18)) which is in agreement with the original value. The algorithm developed in this study for specification of the spectrum for a given value of $H_{1/3}$ is as follows:

i) initial estimate of peak frequency, $\omega_p = 1.1\omega_{pP\text{-}M}$, where $\omega_{pP\text{-}M}$ is obtained from Eqs. (3.2.13) and (2.3.24);

ii) calculate α from Eq. (3.2.17);

iii) calculate spectrum and integrate to obtain $\sigma_{\eta\eta}^2$;

iv) if $\left|1 - \frac{4\sigma_{\eta\eta}}{H_{1/3}}\right| \leq 0.01$, spectrum satisfactory since it yields an estimate of $H_{1/3}$ within 1% of the true value;

v) if (iv) not satisfied obtain a second estimate of peak frequency from Eq. (3.2.17) (assuming α to remain unchanged):

$$\omega_{p2} = \omega_{p1}\left[\frac{4\sigma_{\eta\eta}}{H_{1/3}}\right]^{4.072};$$

vi) repeat (i) to (v) until convergence is achieved.

With reference to Fig. 3.2.1 the JONSWAP spectrum derived in this way will result from the P-M spectrum corresponding to a wind speed less than that developed directly from the P-M ($H_{1/3}$) approach, by virtue of the additional area contained beneath the spectral peak, unless the value of α departs considerably from A = 0.0081 when the reverse may be true. The purpose of the above comment is to show that the JONSWAP spectral densities may be shifted bodily in the frequency domain relative to the significant frequency range in the equivalent P-M ($H_{1/3}$) spectra.

By analogy to the comments made with respect to the P-M spectrum a similar procedure could be formulated for the JONSWAP spectrum based on T_z rather than $H_{1/3}$. However, in the absence of an equivalent expression of the form of Eq. (3.2.17) relating T_z to α and ω_p based on data analysis such an approach is impractical and is not considered further.

3.2.2 Transformations from Surface Elevation to Particle Kinematics

Wave field input to the probabilistic description of loading takes the form of short-term estimates of σ_u^2 and $\sigma_{\dot{u}}^2$, the variances of water particle velocity and acceleration, as described in Eq. (2.3.47) and discussed in the Section 3.1. These variances are obtained as the area beneath the respective spectra, developed from $S_{\eta\eta}(\omega)$ by the transformations of Eqs. (2.3.7) and (2.3.9). Examples of the transfer functions for 'deep-water' conditions are sketched in Fig. 3.2.3.

For the 150m. water depth considered herein the 'deep-water' limit of $d/L = 0.5$ is represented in the figure by a frequency of $\omega \simeq 0.45$ radians/sec, values of ω greater than this representing 'deep-water' conditions. With reference to Fig. 3.2.1, for wind speeds up to about 15m/s. for P-M spectra there is little energy (or a negligible portion of the total variance of η) contained outside the 'deep-water' frequency range. Furthermore, since from Fig. 3.2.2 between 80 and 95% of sea states are likely to satisfy this constraint on wind speed, most conditions considered here are 'deep-water' as suggested in Section 3.1.6.

Although wave properties for the most severe conditions will correspond to intermediate water depths, the 'deep-water' transfer functions sketched in Fig. 3.2.3 are sufficient for demonstration purposes and their use in conjunction with Fig. 3.2.1 provides an appreciation of the process of transformation between $S_{\eta\eta}(\omega)$ and $S_{uu}(\omega)$ and $S_{\dot{u}\dot{u}}(\omega)$.

Excluding from consideration here the transfer functions for elevations within the splash zone, in line with the comments made at the beginning of this Chapter, all functions are convergent. Those for acceleration are shifted to a higher frequency range than those for velocity. The functions decay in magnitude approximately exponentially with depth and since most peak frequencies are below $\omega = 1.0$ the magnitude of the peaks for velocity are greater than for acceleration due to the ω^2 multiplier.

This departure in magnitudes combined with the significant frequency shift gives rise to a varying relationship between σ_u^2 and $\sigma_{\dot{u}}^2$ with change in depth of immersion and also wind speed as the significant frequency range of $S_{\eta\eta}(\omega)$ varies with U_w as demonstrated by the plot of the P-M peak frequencies, ω_p, on Fig. 3.2.3.

From the comments made in Section 3.1, and with reference to Eq. (3.1.6), variation in the variances of u and $\dot{u}$ cause changes in the relative magnitudes of the drag and inertia loading components thereby modifying the form of the loading distribution through change in kurtosis. A detailed investigation into the significance of changes in wind speed and member elevation on the relationship between drag and inertia loading components is not pursued here. However, these effects are illustrated in the following account of the consequences of the use of the different spectral forms on long-term wave load prediction.

3.2.3 Wave Load Predictions from Different Spectral Models

The results described here were obtained from computer programs OSF2 for P-M ($H_{1/3}$), OSF4 for P-M (T_z), OSF8 for P-M (DNV), OS10 for P-M ($H_{1/3}$, T_z) and OS22 for JONSWAP ($H_{1/3}$).

All programs are based on OSF2 which was used in Section 3.1 and is documented in Reference 10, the only differences being in the algorithms defining $S_{\eta\eta}(\omega)$ for each short-term condition considered and the weightings applied to these conditions in the wave climate convolution for long-term predictions.

Program OSF2 in its documented form conforms to the P-M ($H_{1/3}$) approach, short-term conditions being defined by $H_{1/3}$ only and long-term convolution for wave loading taking the form of Eqs. (3.1.7) and (3.1.8). An identical procedure is followed for the JONSWAP ($H_{1/3}$) approach. The convolution for P-M (T_z) follows by analogy as:

$$P(F) = \sum_{j=1}^{m} \left[P_H(F|T_{zj}) \sum_{i=1}^{n} \frac{w_{ij}}{w}\right. \tag{3.2.18}$$

and

$$P_{p2}(F) = \sum_{j=1}^{m} \left[\left\{1 - \frac{p_H(F|T_{zj})}{p_H(0|T_{zj})}\right\} \frac{1}{T_{zj}} \sum_{i=1}^{n} \frac{w_{ij}}{w}\right] \tag{3.2.19}$$

where the short-term distribution of loading is defined by, and hence conditional on, only the value of T_z.

In the P-M (DNV) approach short-term conditions are defined in terms of both $H_{1/3}$ and T_z and consequently each class of the scatter diagram represents a unique sea state and the long-term cdf.s of wave loading are obtained from the general expressions, Eqs. (2.3.64) and (2.3.69).

The variances of velocity and acceleration at a 7.5m. depth of immersion were studied for each short-term sea state according to the P-M ($H_{1/3}$), P-M (T_z), P-M (DNV) and JONSWAP ($H_{1/3}$) approaches. The first observation from the study was that the JONSWAP ($H_{1/3}$) approach yields variances in close agreement with P-M ($H_{1/3}$) for all but the lower intensity sea states. This is not unexpected since the value of α from Eq. (3.2.17) corresponding to $\gamma = 3.3$, takes a value of approximately 0.005 showing little variation with $H_{1/3}$. Therefore, following the comments made in Section 3.2.1.3, the area of the P-M spectral shape generating the JONSWAP spectrum is reduced by the ratio of $A = 0.0081$ to 0.005 from the equivalent P-M spectrum. However, if this reduction in area is of a similar magnitude to the area contained in the peak enhancement, Fig. 3.2.1, the value of ω_p for JONSWAP ($H_{1/3}$) will be close to that for P-M ($H_{1/3}$) and both spectra will cover the same range of frequencies.

This implies that both approaches will cover the same range of frequencies in the transfer functions, Fig. 3.2.3, and the departures in the resulting variances of u and $\dot{u}$ will be small unless the peak frequency of the transfer functions falls within the region of significant spectral density close to the peak of $S_{\eta\eta}(\omega)$. This latter condition exists for the lower intensity sea states, with reference to Figs. 3.2.1 and 3.2.3. The transformations are, therefore, more sensitive to variations in $S_{\eta\eta}(\omega)$ due to the rapid variation the magnitude of the transfer functions in this vicinity and consequently more significant departures in σ_u^2 and $\sigma_{\dot{u}}^2$ result from the two approaches.

The measure of agreement in the estimates of σ_u^2 and $\sigma_{\dot{u}}^2$ from P-M ($H_{1/3}$) and JONSWAP ($H_{1/3}$) was also reflected in the values of variance and kurtosis of short-term wave loading on both 0.5m. and 5.0m. diameter members. The long-term cdf.s of peak loading plotted in Figs. 3.2.4 and 3.2.5 also retain the agreement with load predictions differing by less than 5%, JONSWAP ($H_{1/3}$) resulting in the higher values.

Having compared JONSWAP ($H_{1/3}$) with P-M ($H_{1/3}$) it is convenient and appropriate to compare the remaining approach with the results from P-M ($H_{1/3}$). Concentrating firstly on P-M (T_z) an impression of the effects of its adoption in wave load prediction in place of P-M ($H_{1/3}$) may be obtained from the distribution of the wind speed predictions in Fig. 3.2.3. The plots in this figure show that more severe conditions for the long-term wave climate result from P-M (T_z). This leads to a prediction of generally larger waves yielding greater and more drag dependent loading since members are correspondingly smaller with respect to the waves. This is illustrated in the corresponding long-term wave load cdf.s as shown in Figs. 3.2.4 and 3.2.5. The departure between predictions is less significant for large diameter members as a result of the relative insignificance of drag effects. For the 0.5m. member P-M (T_z) predicts peak forces at the 'one-year' probability level in excess of those from P-M ($H_{1/3}$) by more than 77% whilst for the 5.0m. member this figure is reduced to 24%.

Use of P-M (DNV) in place of P-M ($H_{1/3}$) is found to produce lower mean values of force variance and higher values of kurtosis for most classes of $H_{1/3}$ in the scatter diagram. This results in the long-term standard deviation of force, included in Figs. 3.2.4 and 3.2.5, from P-M (DNV) underestimating the estimate from P-M ($H_{1/3}$) by about 9% in both cases of member diameter.

From the long-term distribution of peak loading on the 0.5m. diameter member in Fig. 3.2.4 the slight increase in kurtosis combined with the slight reduction in variance from P-M (DNV) produces a cdf. showing only marginal departure from that for P-M ($H_{1/3}$). However, for the 5.0m. diameter member, Fig. 3.2.5, the departure is more significant with P-M (DNV) predicting loading approximately 12% greater than P-M ($H_{1/3}$) at the 'one-year' probability level. This difference in behaviour between drag dominated and inertia dominated conditions is probably caused primarily by the changes brought about in the kurtosis of the short-term loading conditions. Small increases in kurtosis in the region of the Gaussian limit, where the kurtosis takes the value $\beta = 3.0$, represented here by all short-term sea states for the 5.0m. diameter member, cause a significant change in the shape of the cdf. resulting in an increased skewness of the tail of the distribution. For conditions of initially high kurtosis, on the other hand, represented by many of the sea states

for the 0.5m. diameter member, changes in kurtosis of a similar magnitude have only a marginal effect on the cdf. as illustrated in Fig. 2.3.4.

3.2.4 Critical Assessment of the Spectral Models

Of the models considered those based on short-term sea state description in terms of $H_{1/3}$ only are favoured since they are considered to be the most reliable, and acceptable for use in wave load prediction in engineering design. This statement is justified by the following comments.

1. Models of this form are in general use for the prediction of the long-term distributions of individual wave height as demonstrated in Section 2.3.2.4 by Eq. (2.3.30), representing the Rayleigh cdf. of short-term wave height defined by $H_{1/3}$ only. This short-term cdf. could equally well be expressed in terms of σ_η^2 using Eq. (2.3.14) developed from the surface spectrum defined by T_z, in the manner of that applied in the P-M (T_z) approach. Furthermore, with reference to the results of the wave load prediction it may be presumed that such a technique would considerably increase the predicted wave heights. However, wave climate description in the marginal T_z domain has received little attention and from the apparently satisfactory performance of the existing techniques for wave height prediction based on the marginal $H_{1/3}$ description of wave climate it may be surmised that the predictions of wave loading based on P-M (T_z) are probably over-conservative.

2. In many applications the wave climate data, in the form of the scatter diagram, may be considered to be inadequate for reliable long-term predictions to be made, necessitating an extrapolation of the data. Such an extrapolation in the bivariate $H_{1/3}$, T_z domain, required for the P-M (DNV) procedure, is too complex to be attempted with any degree of confidence using the present state of knowledge. Much effort has, however, been directed to the long-term distribution of $H_{1/3}$ with attempts to mathematically model its behaviour from extensive data analysis. As a result, acceptable procedures for wave climate extrapolation in the $H_{1/3}$ domain have been developed, as discussed in detail in Chapter Four. No such emphasis has been placed on the long-term description of T_z and thus little reliability could be placed on data extrapolations in the absence of an extensive program of wave climate analysis in the T_z domain.

3. Additional computational effort is required for the P-M (DNV) procedures over that required for P-M ($H_{1/3}$) or JONSWAP ($H_{1/3}$) as a result of the greater number of short-term sea state conditions considered in the long-term convolutions, as may be deduced from the form of Eqs. (2.3.64) and (2.3.69) in comparison with Eqs. (3.1.7) and (3.1.8). The computer run-times required are directly proportional to the number of short-term conditions and thus if P-M ($H_{1/3}$) and JONSWAP ($H_{1/3}$) represent 16 units then P-M (DNV) requires 72 units while P-M (T_z) requires only 10 units. This considerable increase in computing costs and the reasonable measure of agreement between P-M (DNV) and P-M ($H_{1/3}$) for drag dependent members cast doubts on the practicality of the use of P-M (DNV) for such circumstances.

From the results presented it would appear that the differences in wave load predictions resulting from the P-M ($H_{1/3}$) and JONSWAP ($H_{1/3}$) are sufficiently small for both approaches to be considered as being equally acceptable. However, since the P-M form is the most commonly applied in engineering practice at present, this is used as the basis of all remaining computations.

3.3 COMPARISON OF NARROW-BAND MODELS TYPES 1 AND 2 FOR LONG-TERM PEAK WAVE LOAD PREDICTION

The 'type 1' and 'type 2' models for narrow-band peak wave load prediction were introduced in Section 2.3.6.1 and are derived in Appendix One, Section I.3.4. The 'type 1' model accounts for the correlation that may exist between load, F, and its first time derivative, $\dot{F}$, whilst the 'type 2' model assumes statistical independence between these two random variables.

The great disadvantage of the more rigorous 'type 1' model is that it makes demands on computational effort far in excess of the 'type 2' model yielding itself impractical for extensive usage in engineering applications. However, it is instructive to investigate the deviations between results predicted from the two models. Tickell[55] has recently compared the distributions of the above models with a wide-band model (see Section I.3.4.3, Appendix One) for the short-term peak wave loading covering a practical range of loading non-linearity, described by kurtosis in the range 3.3-8.3. From these results it was found that the simple 'type 2' model predicts lower forces than the 'type 1' model, which in

turn was in close agreement with the wide-band model. The level of underestimation increases with kurtosis, being negligible in the lower range but representing values of up to approximately 30% at some probability levels for the most non-linear situations. Nevertheless, Tickell shows that the 'type 2' model for structural response resulting from wave loading compares favourably with observed values, as will be further demonstrated in Chapter Five.

The purpose of this section is to extend the comparison of the narrow band models from the short-term wave environment to long-term conditions. All the foregoing applications have been made with the 'type 2' model and it is intended here to illustrate the implications of the inherent simplifications in this preferred model on the long-term peak wave load distributions.

3.3.1 Derivation of the Short-term Type 1 cdf. of Peak Loading

The short-term cdf. of narrow-band peak load may be expressed, from Eq. (2.3.58) as:

$$P_{p1}(F|H_{1/3}, T_z) = 1 - \frac{E\{N^+(F)|H_{1/3}, T_z\}_1}{E\{N^+(0)|H_{1/3}, T_z\}_1} \qquad (3.3.1)$$

and

$$E\{N^+(F)|H_{1/3}, T_z\}_1 = \int_0^\infty \dot{F}p(F, \dot{F}|H_{1/3}, T_z)\, d\dot{F} \qquad (3.3.2)$$

is the mean rate of upcrossing of the force level, F.

The bi-variate pdf. of F and $\dot{F}$ may be derived as follows:

From Morison's equation, Eq. (2.3.45):

$$F = k_I \dot{u} + k_D u|u|$$

hence:

$$\dot{F} = \frac{dF}{dt} = k_I \ddot{u} + 2k_D|u|\dot{u} \qquad (3.3.3)$$

where $\ddot{u} = d\dot{u}/dt$.

Using the method of Appendix One, Section I.3.2.9 (with $y_1 \equiv F$; $y_2 \equiv \dot{F}$ and defining arbitrary variable $y_3 = u$), to enable transformation from the known probability domain of u, $\dot{u}$ and $\ddot{u}$ (equivalent to x_1, x_2, x_3 in Appendix One), we obtain:

$$p(F, \dot{F}, u) = p(u, \dot{u}, \ddot{u})/k_I^2 \tag{3.3.4}$$

and integrating out u:

$$p(F, \dot{F}) = \frac{1}{k_I^2} \int_{-\infty}^{\infty} p(u, \dot{u}, \ddot{u})\, du \tag{3.3.5}$$

Substituting for the trivariate Gaussian pdf. of particle kinematics from Appendix One, Section I.3.3.1:

$$p(F, \dot{F}) = \frac{1}{(2\pi)^{3/2}\, k_I^2 \sqrt{Det[M]}} \int_{-\infty}^{\infty} \exp[-\frac{1}{2}\, \{U\}\, [M]^{-1}\, \{U\}^T]\, du \tag{3.3.6}$$

where $\{U\} = (u, \dot{u}, \ddot{u})$

$[M]$ is the matrix of cross-covariances

$$= \begin{vmatrix} R_{uu} & 0 & -R_{\dot{u}u} \\ 0 & R_{\dot{u}\dot{u}} & 0 \\ -R_{\dot{u}u} & 0 & R_{\ddot{u}\ddot{u}} \end{vmatrix}$$

with $R_{uu} = \sigma_u^2 = \int_0^{\infty} S_{uu}(\omega)\, d\omega$

$$R_{\dot{u}\dot{u}} = \sigma_{\dot{u}}^2 = \int_0^{\infty} S_{\dot{u}\dot{u}}(\omega)\, d\omega = \int_0^{\infty} \omega^2 \cdot S_{uu}(\omega)\, d\omega$$

$$R_{\ddot{u}\ddot{u}} = \sigma_{\ddot{u}}^2 = \int_0^{\infty} S_{\ddot{u}\ddot{u}}(\omega)\, d\omega = \int_0^{\infty} \omega^4\, S_{uu}(\omega)\, d\omega \tag{3.3.7}$$

and

$S_{uu}(\omega)$ is obtained from Eq. (2.3.7).

$$Det[M] = \sigma_{\dot{u}}^2(\sigma_u^2\, \sigma_{\ddot{u}}^2 - \sigma_{\dot{u}}^4)$$

is the determinant of [M].

Expanding the argument of the exponential function in Eq. (3.3.6) and substituting in Eq. (3.3.2):

$$E\{N^+(F)\,|H_{1/3}, T_Z\}_1 = \frac{1}{(2\pi)^{3/2}\, k_I^2 \sqrt{Det[M]}} \cdot \int_0^{\infty} \dot{F} \int_{-\infty}^{\infty} \exp[-\frac{1}{2}\, (\ell_{11}\, u^2 + 2\ell_{13}\, u\ddot{u} + \ell_{22}\, \dot{u}^2 + \ell_{33}\, \ddot{u}^2)]\, du\, d\dot{F} \tag{3.3.8}$$

where $\dot{u} = (F - k_D\, u|u|)/k_I$

$\ddot{u} = (\dot{F} - 2k_D|u|\dot{u})/k_I$

$$\ell_{11} = \sigma_{\ddot{u}}^2/(\sigma_u^2\,\sigma_{\ddot{u}}^2 - \sigma_{\dot{u}}^4)$$

$$\ell_{13} = \sigma_{\dot{u}}^2/(\sigma_u^2\,\sigma_{\ddot{u}}^2 - \sigma_{\dot{u}}^4)$$

$$\ell_{22} = 1/\sigma_{\dot{u}}^2$$

$$\ell_{33} = \sigma_u^2/(\sigma_u^2\,\sigma_{\ddot{u}}^2 - \sigma_{\dot{u}}^4)$$

and the above variances are strictly conditional on the values of $H_{1/3}$ and T_z which define $S_{\eta\eta}(\omega)$.

3.3.2 Long-term 'Type 1' cdf. of Peak Loading

For the discrete scatter diagram description of wave climate the long-term cdf. of peak loading may be obtained, according to the procedure of Section 2.3.6.2, as:

$$P_{pl}(F) = \sum_{i=1}^{n}\sum_{j=1}^{m}\left[P_{pl}(F|H_{1/3i},\,T_{zj}).E\{N^+(O)|H_{1/3i},\,T_{zj}\}_1\,\frac{w_{ij}}{w}.\frac{1}{E\{N^+(O)\}_1}\right] \tag{3.3.9}$$

and the mean rate of zero-upcrossings of force, $E\{N^+(O)\}_1$, is given by:

$$E\{N^+(O)\}_1 = \sum_{i=1}^{n}\sum_{j=1}^{m}\left[E\{N^+(O)|H_{1/3i},\,T_{zj}\}\,\frac{w_{ij}}{w}\right] \tag{3.3.10}$$

Consequently, the departures between the 'type 1' and 'type 2' models for long-term peak wave load cdf.s given by Eqs. (3.3.9) and (2.3.69) are two-fold. There is firstly the difference between the short-term peak distributions, as investigated by Tickell, and secondly, of more concern here, the difference resulting from changes in the weighting attached to the short-term conditions in the long-term convolution. The latter arises from the departure between the estimates of zero-upcrossing rates for force applied in the procedures, namely $E\{N^+(O)|H_{1/3},\,T_z\}_1$ given by Eq. (3.3.8) for the 'type 1' model and the approximation, applied herein for the 'type 2' model, that $E\{N^+(O)|H_{1/3},\,T_z)\}$ is equal to the rate for surface elevation upcrossings, from Eq. (2.3.67), referred to here as $E\{\eta^+(O)|H_{1/3},\,T_z\}$. It is, therefore, important to investigate the relationship between these two estimates as well as the force upcrossing rate for the 'type 2' distribution from Eq. (2.3.61) referred to as $E\{N^+(O)|H_{1/3},\,T_z\}_2$.

3.3.3 Method of Computation

Computer program OSF6 was developed for the prediction of short and long-term distributions of narrow band 'type 1' peak wave loading according to the above procedures. The program follows the same general form and notation as program OSF2, referenced earlier. In view of the findings of the previous section, the P-M ($H_{1/3}$) approach has been used and, therefore, short-term conditions are considered as a function of $H_{1/3}$ only.

Eq. (3.3.8) is solved in the computer routine by constant step numerical integration. In line with the procedure used for OSF2, a range of force from zero to 8 standard deviations of the most severe short-term condition was considered with 10 steps per standard deviation. To ensure stability of the numerical integrations in the u and $\dot{F}$ domains it was found necessary to integrate the former between limits of $\pm 5\sigma_u$ with steps of $0.1\sigma_u$ and the latter from zero to $5\sigma_{\dot{F}}$ with $0.1\sigma_{\dot{F}}$ step width, where:

$$\sigma_{\dot{F}}^2 = k_I^2 \, \sigma_{\ddot{u}}^2 + 4k_D^2 \, \sigma_u^2 \, \sigma_{\dot{u}}^2$$

since $\dot{F}$ is mean zero and random variables u, $\dot{u}$ and $\ddot{u}$, $\ddot{u}$ are statistically independent.

In consistency with Sections 3.1 and 3.2 only member elevations beneath the splash zone have been considered here, with the minimum depth of immersion taken as 7.5m. However, at this location under the most intense short-term conditions the estimate of $\sigma_{\ddot{u}}^2$ is sensitive to variation in the upper frequency truncation applied on $S_{\eta\eta}(\omega)$ due to the ω^6 multiplier in the transformation as demonstrated in Fig. 3.3.1. This arises because moments of $S_{\eta\eta}(\omega)$ greater than the fourth are divergent and at locations near the free surface the depth transforms in the transposition to the spectra of particle kinematics do not restrict this behaviour. Under the most severe sea state with $H_{1/3}$ = 9.3m, it is found that using a frequency truncation of $8\omega_0$ yields estimates of $\sigma_{\ddot{u}}^2$ approximately 14% greater than for a truncation at $2.75\omega_0$. At greater depths of immersion the rapid convergence of the depth transformations, which may be deduced from Fig. 3.2.3, reduces the effect of the spectral tails and there is negligible difference in the computed variances.

Fig. 3.3.1 also shows that the spectral truncation has a marginal effect on the estimate of $\sigma_{\dot{u}}^2$ at the 7.5m. depth of immersion, represented by a 3% variation from the above truncation points for $H_{1/3}$ = 9.3m. Similarly, the corresponding departure in σ_u^2 was found to be less than 0.5%. However, these departures in σ_u^2, $\sigma_{\dot{u}}^2$ have no discernible effect on the results given in the preceding Sections and spectral truncation are not, therefore, significant for those situations, the $8.0\omega_0$ upper truncation being used throughout.

There seems to be no rational basis on which to truncate $S_{\eta\eta}(\omega)$ when divergence occurs and in this Section an upper frequency cut-off at $2.75\omega_0$ is adopted. This value was chosen following a trial and error procedure to retain a consistent trend in kurtosis for variation in depth of immersion up to still-water-level, indicated on Fig. 3.1.2. This value has no theoretical justification but is considered to be appropriate since it retains the significant spectral mass of $S_{\eta\eta}(\omega)$ but prevents 'distortion' of the variances of particle kinematics which would result from the transformed spectra due to the probable inadequacies in both the theoretical models for $S_{\eta\eta}(\omega)$ and the first order wave theory transformations in the high frequency range.

3.3.4 Results of Computations

Fig. 3.3.2 shows the cdf.s of short-term peak loading produced from the 'type 1' and 'type 2' models for the most severe conditions of wave load non-linearity, represented by a 0.5m. diameter member at a depth of immersion of 7.5m, where the wave load kurtosis is 7.936. From the plots it is seen that a high levels of load the two distributions become parallel and the most extreme departure between load predictions, in percentage terms, occurs for probabilities in the region of 0.9 to 0.95 and is of the order of 30%. This behaviour is identical to that shown by Tickell's results[55].

The long-term peak distributions are plotted on Fig. 3.3.3 for both 0.5m. and 2.0m. diameter members at a 7.5m. depth of immersion. For the small member the departures between the short-term 'type 1' and 'type 2' cdf.s for the high intensity sea states are retained in the long-term descriptions. The departures decrease with reduction in the non-linearity of loading, there being only small differences for the 2.0m. diameter member indicated and negligible difference for a 5.0m. member. Increase in the depth of immersion reduces the departures.

The absence of any apparent departures between the two distributions for the inertia dominated loading implies that F and $\dot{F}$ are statistically independent which is to be expected since in the limit F is a function of $\dot{u}$ only, $\dot{F}$ is a function of $\ddot{u}$, and $\dot{u}$ and $\ddot{u}$ are statistically independent. Furthermore, the agreement also implies that the variations in the short-term mean zero-upcrossing rates, $E\{N^+(0)|H_{1/3}\}_1$ and $E\{\eta^+(0)|H_{1/3}\}$, have negligible effect on the cdf.s.

Short-term mean zero-upcrossing rates for the entire range of conditions considered here are plotted on Fig. 3.3.4. The values for surface elevation used in the 'type 2' procedures are represented by $E\{\eta^+(0)|H_{1/3}\}_{FAMITA}$ whilst the values obtained from the moments of the P-M spectra for given values of $H_{1/3}$ are represented by $E\{\eta^+(0)|H_{1/3}\}_{P-M}$. The differences between these values arise from the departure of the real sea states from the theoretical P-M form as discussed in more detail in Section 3.2.

The short-term values of $E\{N^+(0)|H_{1/3}\}_1$ are seen to decrease with increase in sea state intensity (or $H_{1/3}$) and decrease in both member diameter and depth of immersion. This behaviour can be understood by considering the frequency spectrum of force since the estimates of zero-upcrossing rate can be obtained from Eq. (I.71), Appendix One, as:

$$E\{N^+(0)|H_{1/3}\} = \frac{1}{2\pi}\sqrt{\frac{m_2}{m_0}} \tag{3.3.11}$$

where m_0 and m_2 are the zeroth and second moments of the force spectrum (Section I.2.2.2, Appendix One). It is not necessary to develop the force spectrum, as it is sufficient to appreciate that a shift in the significant frequency range covered by the spectrum affects $E\{N^+(0)|H_{1/3}\}$, a positive shift (to higher frequencies) increasing the ratio m_2/m_0 and thereby increasing the zero-upcrossing rate. The relevant frequency range can be deduced from that of the spectra of u, $\dot{u}$ and $\ddot{u}$, which in turn can be inferred from Figs. 3.2.1 and 3.2.3.

The zero-upcrossing rates for force based on the 'type 2' approach have not been investigated directly. An estimate has been made based on the assumption of linearity of the loading since for such a Gaussian process we obtain, from Section I.3.4.2, Appendix One:

$$E\{N^+(0)|H_{1/3}\}_2 = \frac{1}{2\pi}\left\{\frac{\sigma_{\dot{F}}}{\sigma_F}\right\} \tag{3.3.12}$$

This expression has been evaluated for the most non-linear loading condition and is compared with the 'type 1' estimates in Table 3.3.1. From the table it is seen that the difference between the estimates is only marginal. It may, therefore, be inferred that statistical dependence between F and $\dot{F}$ has negligible effect on the zero-upcrossing rates since it might be expected that the correct value of $E\{N^+(0)|H_{1/3}\}_2$, from Eq. (2.3.61), which retains the non-linearity in the loading, would lie between the two estimates considered above.

Returning to Fig. 3.3.4, it is evident that the Famita estimate of surface elevation zero-upcrossings lies within the 'band' of the force zero-upcrossing for almost the entire range of short-term conditions demonstrating the acceptability of the simplifying assumption in the 'type 2' approach. The only significant departures are in the lowest intensity conditions which have negligible effect on the long-term load distributions. As mentioned previously, from the apparent coincidence between the 'type 1' and 'type 2' models for inertia dominated loading it can be concluded that the long-term peak load distributions are insensitive to moderate changes in the short-term zero-upcrossing rates and, therefore, the most appropriate model for practical application is that requiring the minimum amount of computation effort, namely $E\{\eta^+(0)|H_{1/3}\}$.

It should be appreciated that interpretation of the peak cdf.s does vary slightly with the model adopted for the upcrossing rates as may be deduced from the probabilities assigned to the 'one exceedence per year' condition indicated in Fig. 3.3.4. However, variation in load predictions due to this effect is unlikely to be of significance.

3.4 PREDICTION OF EXTREME WAVE LOADS

Design against first excursion failure requires the consideration of probability distributions of the extreme value of wave loading to be experienced during the period of exposure of the structure. The cdf. of extreme positive peak wave loading may be obtained directly from that of the positive peak loading from Eq. (2.3.70) under the assumption that the peak loads are independent:

$$P_{EP}(F) = [P_p(F)]^N \qquad (3.4.1)$$

where N is the number of force peaks expected during the period of exposure.

For a period of exposure, t_e, we have, for a narrow-band 'type 1' process:

$$N = t_e \, E\{N^+(0)\}_1 \tag{3.4.2}$$

where the long-term mean rate of zero-upcrossings of force, $E\{N^+(0)\}_1$ is obtained from Eq. (3.3.10).

For the 'type 2' processes applied herein, the zero-upcrossing rates of surface elevation have been used, as discussed in Section 3.3, and thus:

$$N = t_e \, E\{\eta^+(0)\} = t_e \, \overline{T_z^{-1}} \tag{3.4.3}$$

where $\overline{T_z^{-1}}$ is defined in Eq. (2.3.34).

Since the underlying distributions of wave loading are symmetrical the probability distributions of negative peak and extreme values will be identical to those of the positive values considered herein. In many applications of first excursion analysis it is the absolute value of force which is required and thus, if the positive and negative peaks are assumed to be independent, Eq. (3.4.1) becomes:

$$P_{EP}(|F|) = [P_p(F)]^{2N} \tag{3.4.4}$$

where 2N now represents the total number of extrema.

In this Section the extreme values of positive loading are developed from the distributions of peak loading derived from some of the models investigated in the previous Sections of this Chapter.

Before proceeding it should again be emphasised that the results of this study are for comparison purposes only. Wave climate description used here is in the form of the Famita scatter diagrams of Fig. 2.3.1. In any real application the wave climate should be extrapolated to cover a period in excess of the period of exposure under investigation, as discussed in detail in Chapter Four. In this study it is assumed that the long-term distributions of peak force derived previously represent

the complete long-term behaviour in the absence of the arbitrary truncation at the 'one-year' level applied in the foregoing graphical presentations.

3.4.1 Behaviour of the Wave Loading Models of Sections 3.1 to 3.3 in the Prediction of Extremes

The probability distributions of extreme wave load have been investigated for a range of member diameters and depths of immersions. A summary of the results for the 0.5m. and 5.0m. diameter members at a 7.5m. depth of immersion is presented in Tables 3.4.1 and 3.4.2 and the pdf.s for the drag dominated condition are plotted on Figs. 3.4.1. Variation in the properties of extreme loading due to change in depth of immersion or member diameter reflect the behaviour observed in the high load regions of the distributions of the peak variate discussed previously and are, therefore, omitted here.

In the tables three levels of extreme force are included for description of the properties of its probability distribution. Each estimate of force is associated with a different probability of being exceeded in a particular period of exposure. The estimates are as follows:

(a) The Most Probable Peak Value (MPPV) representing the force at the mode (or maxima) of the pdf. From Eq. (3.4.1) the pdf. of extreme force is given by:

$$p_{EP}(F) = \frac{dP_{EP}(F)}{dF} = N[P_p(F)]^{N-1}\, p_p(F)$$

and the mode is obtained as the solution to:

$$\frac{d\, p_{EP}(F)}{dF} = 0, \text{ yielding } \quad \frac{d}{dF}\{p_p(F)\} = (N-1)[p_p(F)]^2/P_p(F)$$

This expression cannot be solved analytically since the mathematical form of $p_p(F)$ and $P_p(F)$ are not known explicitly. However, it is found that the most probable peak force is, not surprisingly, in agreement with the load prediction abstracted from the cdf. of peak loading at the relevant probability level. This follows since for F = MPPV the peak probability is given by $P_p(F = MPPV) = 1 - \frac{1}{N}$ where N is the number of waves. Substitution into Eq. (3.4.1) yields $P_{EP}(F = MPPV) = \exp(-1) = 0.3679$

and this is satisfied from the discrete cdf.s computed herein for both 0.5 and 5.0m. diameter members at depths of immersion of 7.5, 15.0 and 22.5m. With reference to Eq. (II.4), Appendix Two, it may, therefore, be implied that the cdf.s of extreme values follow the Gumbel distribution as demonstrated later.

(b) The expected extreme force, $E\{F_{MAX}\}$, is obtained as:

$$E\{F_{MAX}\} = \int_0^\infty F p_{EP}(F)\, dF \qquad (3.4.5)$$

and, therefore, represents the centroid of the pdf, corresponding to a force in excess of the MPPV value due to the positive skewness of the pdf. demonstrated in Fig. 3.4.1.

(c) With reference to Fig. (3.4.1) it is apparent that there is a high probability that the MPPV and $E\{F_{MAX}\}$ estimates will be exceeded. It is, therefore, desirable to predict an extreme value with only a small probability, α, of being exceeded. In Tables 3.4.1 and 3.4.2 a level of $\alpha = 0.01$ is taken which may be described as the probability that one member in 100 members, all exposed to statistically identical environments, will sustain a load greater than the value quoted.

The periods of exposure considered here, and previously reported in Reference 12, are 'one-year', 'six months summer' and 'six months winter', each of which was applied in conjunction with the relevant scatter diagrams in Fig. 2.3.1. As a further consideration a period of exposure of 50 years has been investigated based on the 'one-year' data set.

The distributions of extreme force for the 'one-year' data set are identical to those for the six winter month period because summer conditions ($H_{1/3} < 5.4$m.) never reach sea state intensities sufficient to cause peak forces of a magnitude comparable with those in the winter distributions.

In Tables 3.4.1 and 3.4.2 it is seen that the departures between the 'type 1' and 'type 2' narrow band models follow the behaviour at high force levels in the peak cdf.s. This is as expected in view of the correlation between MPPV and the 'return-period' estimates from the peak cdf.s as mentioned above.

Instability was experienced in the extreme pdf.s derived from the 'type 1' model in the upper force range considered. The force range covered in the computations extended from zero to 15 standard deviations of force for the most intense short-term condition as opposed to only eight standard deviations employed for the basic and peak cdf.s. The inaccuracy in the computations results from the errors inherent in the numerical integrations required for the removal of $\dot{F}$ and u, as explained in Section 3.3. Unfortunately the errors could not be suppressed by increase in the precision of the integration (through reduction in step lengths and expansion of the range of the variables covered) due to computer run-time limitations thus further emphasising the impracticality of the 'type 1' model.

The comments relating to the spectral forms in Sections 3.2 are also reflected in the extreme value statistics as demonstrated here by results for the P-M (DNV) approach in tables 3.4.1 and 3.4.2.

The linearised method of Section 3.1 underestimates extreme values with respect to the non-linear procedure at the MPPV and $E\{F_{MAX}\}$ levels by amounts in close agreement with the values quoted in Section 3.1.4. These values were measured from the peak cdf.s and correspond to approximately 48% for the 0.5m. member under the 'one-year' wave climate. However, it is seen in Fig. 3.4.1 that the linearised method gives density functions which are much narrower than the non-linear method for the conditions where drag is important. The change in shape of the pdf. is important in the consideration of force estimates at the $\alpha = 0.01$ level. From Table 3.4.1 the under-estimation is 58%, a further 21% on that at the MPPV level due to the extended tail in the non-linear distributions.

3.4.2 Long-term Extreme Force Distributions From the Short-term Extremes

The agreement between extreme load estimates from the winter and 'one-year' data sets implies that lower intensity sea states have negligible effect in the prediction of extreme values.

The significance of particular short-term conditions on the extremes may be assessed by expansion of Eq. (3.4.1) as follows:

For the general narrow band condition, substituting from Eqs. (3.3.9) and (3.3.1) into (3.4.1):

$$P_{EP}(F) = \left[\sum_{i=1}^{n} \sum_{j=1}^{m} \left\{ \left[1 - \frac{E\{N^+(F) \,|H_{1/3i}, T_{zj}\}}{E\{N^+(O) \,|H_{1/3i}, T_{zj}\}} \right] \frac{E\{N^+(O) \,|H_{1/3i}, T_{zj}\}}{E\{N^+(O)\}} \frac{w_{ij}}{w} \right\} \right]^N$$

$$= \left[1.0 - \frac{1}{E\{N^+(O)\}} \sum_{i=1}^{n} \sum_{j=1}^{m} E\{N^+(F) \,|H_{1/3i}, T_{zj}\} \frac{w_{ij}}{w} \right]^N \qquad (3.4.6)$$

In the study of extremes high levels of force are of primary importance, where the mean upcrossing rate of threshold level F, $E\{N^+(F) \,|H_{1/3}, T_z\}$, for the highest intensity sea state is much less than the long-term mean zero-upcrossing rate, $E\{N^+(O)\}$, and is, therefore, even smaller for the lower intensity conditions. Consequently, it follows that the summation in Eq. (3.4.6) will be much less than the denominator for the significant range of forces in the pdf. of extremes and hence Eq. (3.4.6) is of the form:

$$P_{EP}(F) = [1.0 - x]^N \qquad x << 1 \qquad (3.4.7)$$

which may be approximated by:

$$[1.0 - x]^N \simeq [\exp\{- x\}]^N = \exp\{- Nx\} \qquad (3.4.8)$$

Using Eq. (3.4.2):

$$P_{EP}(F) = \exp\left\{ - t_e \sum_{i=1}^{n} \sum_{j=1}^{m} [E\{N^+(F) \,|H_{1/3i}, T_{zj}\} \frac{w_{ij}}{w}] \right\} \qquad (3.4.9)$$

$$= \prod_{\text{all } i,j} [\exp -\left\{ t_e \, E\{N^+(F) \,|H_{1/3i}, T_{zj}\} \right\} \frac{w_{ij}}{w}] \qquad (3.4.10)$$

where $\prod_{\text{all } i,j}[\ ]$ represents the product of all short-term values of the argument.

Rearranging this equation using Eq. (3.4.8):

$$P_{EP}(F) = \prod_{\text{all } i,j} \left[\left\{ 1.0 - \frac{E\{N^+(F) \,|H_{1/3i}, T_{zj}\}}{E\{N^+(O) \,|H_{1/3i}, T_{zj}\}} \right\}^{N(H_{1/3i}, T_{zj})} \right] \qquad (3.4.11)$$

where $N(H_{1/3i}, T_{zj}) = t_e \, E\{N^+(O) \,|H_{1/3i}, T_{zj}\} \frac{w_{ij}}{w}$ (3.4.12)

= total number of peaks occurring in sea state given by $(H_{1/3i}, T_{zj})$ during period of exposure.

Hence:

$$P_{EP}(F) = \prod_{\text{all } i,j} P_{EP}(F|H_{1/3i}, T_{zj}) \tag{3.4.13}$$

and

$$P_{EP}(F|H_{1/3i}, T_{zj}) = [P_p(F|H_{1/3i}, T_{zj})]^{N(H_{1/3i},T_{zj})} \tag{3.4.14}$$

The probability distribution of the extreme value of force may thus be expressed as the product of the short-term extreme distributions. Furthermore, as only high levels of force are of interest (large compared with the standard deviation of force for the highest intensity sea state) the value of $P_{EP}(F|H_{1/3}, T_z)$ will be unity for many of the lower intensity sea states since for these conditions all the short-term peaks will be lower than the thresholds of force considered. For example, suppose in the investigation of extremes, $F > F_{EMIN}$ then for a particular sea state denoted by $(H_{1/3I}, T_{zJ})$:

$$P_p(F_{EMIN}|H_{1/3I}, T_{zJ}) \simeq 1.0$$

as observed from Fig. 2.3.5 and similarly for sea states of lesser intensity, hence Eq. (3.4.13) becomes:

$$P_{EP}(F) = \prod_{i>I,j>J} P_{EP}(F|H_{1/3i}, T_{zj}) \tag{3.4.15}$$

For the 'type 2' process considered here and considering the P-M ($H_{1/3}$) approach, the short-term extreme distribution, Eq. (3.4.14), simplifies to:

$$P_{EP}(F|H_{1/3i}) = \left[1.0 - \frac{p_H(F|H_{1/3i})}{p_H(0|H_{1/3i})}\right]^{N(H_{1/3i})} \tag{3.4.16}$$

where $N(H_{1/3i}) = t_e\, E\{\eta^+(0)|H_{1/3i}\} \sum_{j=1}^{m} \frac{w_{ij}}{w}$ (3.4.17)

and from Fig. 3.3.4, the mean zero-upcrossing rate associated with $H_{1/3i}$ for the Famita data is:

$$E\{\eta^+(0)|H_{1/3i}\} = \sum_{j=1}^{m} \left(\frac{w_{ij}}{T_{zj}}\right) \Big/ \sum_{j=1}^{m} w_{ij} \tag{3.4.18}$$

Values of $N(H_{1/3})$ for the 'one-year' Famita data are derived in Table 3.4.3 according to Eqs. (3.4.17) and (3.4.18) with a one-year period of exposure. The resulting short-term pdf.s of extreme peak force

on a 0.5m. diameter member from Eq. (3.4.16) are plotted in Fig. 3.4.2 for $H_{1/3}$ in the range 4.5 to 9.3m. Also included in the figure is the long-term pdf. of extreme peak force for a one-year period based on the 'one-year' wave climate.

The cumulative probability for these distributions at any level of force is represented by the area contained beneath the pdf. up to that force level and the cdf.s are plotted for the short-term conditions in Fig. 3.4.3 . For long-term distributions the cumulative probability is the product of the short-term values at each force level considered, also plotted on Fig. 3.4.3. From inspection of Figs. 3.4.2 and 3.4.3 it is seen that the significant force range of the long-term distribution represents cumulative probabilities of effectively unity for sea states of $H_{1/3}$ = 4.5m. and below.

Fig. 3.4.3 is plotted on Gumbel paper and the straightness of the cdf.s implies that the extreme forces for both long and short-term conditions follow the Gumbel distribution (see Appendix Two). However, this does not permit a simplification in the procedure for derivation of the extreme cdf.s since an estimate of the variance of extreme values in addition to the mode (given by the MPPV obtained from the peak cdf.) is required for specification of the Gumbel distribution.

An important observation to be made from Figs. 3.4.2 and 3.4.3 is the fact that it is inadequate to estimate extreme values from the properties of only the highest intensity short-term condition, a concept which is not always fully appreciated.

3.5 COMPUTATIONAL CONSIDERATIONS: USE OF QUADRATURE METHODS FOR RUN-TIME MINIMISATION AND A TECHNIQUE OF HAND CALCULATION

3.5.1 Approximate Integration Using Quadrature Methods

In the preceding Sections of this Chapter it has been shown that retention of the non-linearity of the Morison wave load equation implies considerable increase in computation effort due to the numerical integration required for solution of the probability densities of short-term wave loading (Eq. (2.3.47)). Furthermore, if the 'type 1' model for narrow band peak load is considered a further level of numerical integration is required (Eqs. (3.3.1) and (3.3.8)). For this latter method numerical instability in the solutions are experienced in the

prediction of extreme values due to errors inherent in the constant step integration procedures employed, the sensitivity of the discretisation being limited by computer run-time limitations.

As an attempt to reduce the computer run-time requirements for the non-linear probabilistic methods and to improve the accuracy of computation for the 'type 1' peak cdf.s, the viability of using quadrature techniques of approximate integration of Eqs. (2.3.47) and (3.3.8) was investigated. The relevant quadrature formulae are of the 'Gaussian-Hermite' and 'Gaussian-Laguerre' types[69].

For Gaussian-Hermite Quadrature

$$\int_{-\infty}^{\infty} e^{-x^2} f(x)\, dx \simeq \sum_{k=1}^{n} A_k^{(n)}\, f(x_k^{(n)}) \qquad (3.5.1)$$

the integral is approximated by a summation of terms where (x_k, A_k) are the function point and coefficient respectively of the Chebyshev-Hermite polynomial of degree n. The quadrature yields an exact solution whenever f(x) is expressible as a polynomial of degree $\leq(2n - 1)$.

Similarly for Gaussian-Laguerre Quadrature

$$\int_{0}^{\infty} x^a e^{-x} f(x)\, dx \simeq \sum_{\ell=1}^{m} B_\ell^{(m)}\, f(x_\ell^{(m)}) \qquad (3.5.2)$$

where (x_ℓ, B_ℓ) are the function point and coefficient, respectively, of Chebyshev-Laguerre polynomials of degree n.

3.5.1.1 Application for solution of Pierson-Holmes probability densities of wave load, Eq. (2.3.47)

Eq. (2.3.47) can be expressed in the form of Eq. (3.5.1), yielding:

$$p_H(F) \simeq \frac{1}{\sqrt{2\pi}\, k_I\, \sigma_{\dot{u}}} \sum_{k=1}^{n} A_k^{(n)}\, f(x_k^{(n)}) \qquad (3.5.3)$$

where $x = u/\sqrt{2}\sigma_u$

and

$$f(x) = \exp\left\{-\frac{1}{2k_I^2\, \sigma_{\dot{u}}^2} (F - 2k_D\, \sigma_u^2\, x|x|)^2\right\} \qquad (3.5.4)$$

For the computations performed herein, using the constant step procedure developed by Pierson and Holmes and summarised in Reference 2, a total of

201 points were considered in the numerical integration and hence if values of n in Eq. (3.5.3) less than this are satisfactory the quadrature should produce savings in computer costs (run-times).

The values of (x_k, A_k) are tabulated for polynomials of degree up to n = 20 and some examples are given in Table 3.5.1. However, for the purposes of this study values were computed for polynomials up to n = 42 using the following relationships.

Chebyshev-Hermite polynomials of degree n, $H_n(x)$, are derived by induction from:

$$H_0(x) = 1$$

and

$$H_n(x) = 2x\, H_{n-1}(x) - \frac{d}{dx}\{H_{n-1}(x)\} \tag{3.5.5}$$

The function points $x_k^{(n)}$ correspond to the roots of $H_n(x) = 0$ and the coefficients are given by:

$$A_k^{(n)} = \frac{2^{n+1} n! \sqrt{\pi}}{[\frac{d}{dx}\{H_n(x_k^{(n)})\}]^2} \tag{3.5.6}$$

The cdf.s of peak loading resulting from inclusion of the quadrature, computed using program OSF7, are shown in Fig. 3.5.1 for the most drag-dependent short-term conditions investigated. The oscillations present in the plots illustrate the numerical instability inherent in the approximate integration. Although this behaviour decays with increase in n it is evident that f(x) cannot be accurately approximated by a polynomial of degree 83 corresponding to n = 42. As drag effects, and hence wave load kurtosis, are reduced by increase in member diameter and depth of immersion or by reduction in sea state intensity through decrease in $H_{1/3}$, these effects diminish. This is not surprising since these conditions lead to reduced significance attached to the second term in the argument of the exponent in Eq. (3.5.4). In the limit this term is negligible, the loading being wholly inertial, and f(x) becomes invariant in which case it may be exactly fitted by a polynomial of degree 1.

The above comments may be illustrated by considering various force levels $F = j\,\sigma_F$ where j is, for convenience, taken as an integer constant. From Eq. (3.1.6):

$$\frac{k_D^2 \sigma_u^4}{k_I^2 \sigma_{\dot{u}}^2} = \frac{1}{\sqrt{\frac{78}{\beta-3}} - 3} \qquad (3.5.7)$$

and substituting in Eq. (3.5.4):

$$f(x) = \exp\left\{-\frac{1}{2}\left[\left(\frac{1}{1 - 3\sqrt{\frac{\beta-3}{78}}}\right)(j - 2[\frac{\beta-3}{78}]^{1/4} x|x|)^2\right]\right\} \qquad (3.5.8)$$

For inertial, Gaussian distributed, loading the kurtosis $\beta = 3.0$ and $f(x)$ is constant for each level of force (j) considered. The quadrature is, therefore, unnecessary since the integration from Eq. (3.5.1) may be performed analytically, as represented by the procedure applied in the linearised probabilistic method discussed in Section 3.1.

The functions $f(x)$ are plotted on Fig. 3.5.2 for $\beta = 5.0$ at various levels of force (j) and are seen to become more peaky at the high force levels, taking significant values over only a narrow region of the x axis. This behaviour is amplified for larger values of β. Function points $x_k^{(n)}$ for the quadratures are distributed, reasonably uniformly, over a range of x in excess of ten centred at $x = 0$ for quadrature with $n > 18$. It is, therefore, reasonable to suppose that for low levels of force the functions $f(x)$ in Fig. 3.5.2 might be accurately approximated by polynomials of degree up to 83. However, it is unlikely that this will be true of the narrow peaky functions remote from the centre of the quadrature range representing the high levels of force. Thus errors resulting from the fitted polynomials are likely to increase as the force is increased yielding the divergent oscillations in Fig. 3.5.1.

From the above comments it follows that the instabilities are less significant in long-term distributions, as demonstrated in Fig. 3.5.3, and the cdf.s for the most precise quadrature ($n = 42$) may well be sufficiently accurate for most applications. Use of this approximation leads to computer run-time savings over the constant step procedure of about 70%. The degree n of the approximation necessary to contain the oscillations in the cdf.s to acceptable levels reduces as the effects of drag diminish and may, therefore, permit additional savings in computer costs, over that quoted above, for larger diameter members.

3.5.1.2 Application for solution of the 'type 1' distribution of peak wave loading, Eqs. (3.3.1) and (3.3.8)

In this section, the formulation for solution of Eq. (3.3.8), and hence Eq. (3.3.1) using quadrature is summarised. No attempt has been made here to employ this approximate integration in view of the preference for 'type 2' peak loading models, as expressed in Section 3.2.

Eq. (3.3.8) may be rearranged into a form expressible in terms of both Gaussian-Hermite and Gaussian-Laguerre quadrature, as:

$$E\{N^+(F)\,|H_{1/3},\ T_z\}_1 \simeq \frac{1}{(2\pi)^{3/2}\ell_{33}\sqrt{\frac{\ell_{11}}{2}\,\mathrm{Det}[M]}} \sum_{\ell=1}^{m}\sum_{k=1}^{n} B_\ell^{(m)}\, A_k^{(n)}\, f(x_k^{(n)}, y_\ell^{(m)}) \qquad (3.5.9)$$

where $x = \sqrt{\frac{\ell_{11}}{2}}\,u$

$$y = \frac{\ell_{33}}{2}\,\frac{\dot{F}^2}{k_I^{\,2}}$$

$$f(x,y) = \exp[-\tfrac{1}{2}A]$$

$$A = \Bigg[2\ell_{13}\sqrt{\frac{2}{\ell_{11}}}\,x\left(\sqrt{\frac{2}{\ell_{33}}}\,y^{1/2} - \frac{2k_D F}{k_I^{\,2}}\sqrt{\frac{2}{\ell_{11}}}|x| + \frac{2k_D^{\,2}}{k_I^{\,2}}\left(\frac{2}{\ell_{11}}\right)^{3/2}x^3\right)$$

$$+ \ell_{22}\left(\frac{F}{k_I} - \frac{2k_D}{k_I}\,\frac{x|x|}{\ell_{11}}\right)^2 + 8\ell_{33}\left(\frac{k_D^{\,2}F^2x^2}{k_I^{\,2}\ell_{11}} + \frac{4k_D^{\,4}}{k_I^{\,4}}\,\frac{x^6}{\ell_{33}^3}\right)$$

$$+ 8\ell_{33}\left[\frac{2k_D^{\,2}}{k_I^{\,2}}\,\frac{y^{1/2}x^3}{\sqrt{\ell_{33}\ell_{11}^3}} - \frac{k_D}{k_I^{\,2}}\,\frac{F|x|y^{1/2}}{\sqrt{\ell_{33}\ell_{11}}} - \frac{4k_D^{\,3}Fx^3|x|}{k_I^{\,4}\ell_{11}^2}\right)\Bigg]$$

and for the Gaussian-Laguerre quadrature a = 0. In the constant step integration 101 steps were used in integration over the $\dot{F}$ and u domains. Consequently, if sufficient accuracy can be obtained with values of n and m such that:

$$n \times m < (101)^2$$

then savings in computer run-times should result.

3.5.2 Wave Load Prediction by Hand Computation

The object of this Section is to illustrate how the long-term distributions of the wave loading and its peak ('type 2') and extreme values can be developed without recourse to the complex computer routines developed for the solution herein. The procedure, reported in Reference 17, is based on the standardised cdf.s of Pierson-Holmes distributed random variables in Figs. 2.3.4 and 2.3.5. The only essential computing facility is a standard scientific hand calculator although a programmable desk top calculator would normally be required for the derivation and integration of the spectra of particle kinematics for each short-term condition considered. The method is described by means of an example as follows.

Problem

To derive the long-term distributions of basic load, positive peak load and positive extreme load, for a one-year period of exposure in the 'one-year' wave climate given in Fig. 2.3.1, on a unit length component of a vertical cylindrical member, 0.5m. in diameter, submerged 7.5m. beneath the surface in a 150m. depth of water.

Assume

i) the wave force to be given by Morison's Equation, Eq. (2.3.45), with $C_M = 2.0$; $C_D = 1.0$ and $\rho = 10^3 Kg/m^3$; and

ii) the sea surface spectrum is of the Pierson/Moskowitz form given by Eqs. (2.3.23) and (2.3.24) defined by $H_{1/3}$ only (P-M ($H_{1/3}$) approach).

Applying (i) and (ii) in the manner described in Section 2.3.6 for each short-term condition produces the second and fourth moments of wave load which yield values of σ_F and β necessary in the use of figures 2.3.4 and 2.3.5. These values are included in Table 3.4.3.

The long-term distributions of basic and peak force can be built up considering a range of values of force and carrying out the summations in Eqs. (3.1.7) and (3.1.8) by hand. The wave climate weightings for use in these equations are given in Table 3.4.3 and the short-term probabilities, $P_H(F|H_{1/3})$ and $P_p(F|H_{1/3})$ are taken from Figs. 2.3.4 and 2.3.5 for each force level considered. In practice the hand calculation

is less prone to error accumulation if P(F) and $P_p(F)$ are evaluated indirectly as, from Eq. (3.1.7):

$$1 - P(F) = \sum_{i=1}^{n} [\{1 - P_H(F|H_{1/3i})\}. \sum_{j=1}^{m} \frac{w_{ij}}{w}] \qquad (3.5.10)$$

and likewise for $P_p(F)$ from Eq. (3.1.8).

The probabilities of non-exceedence are computed, at three force levels, in Table 3.5.2 and are shown to be in close agreement with the values obtained by computer. This is further illustrated on Fig. 3.1.3.

The probability of non-exceedence of three levels of extreme force are derived using Fig. 2.3.5, Eq. (3.4.16) and values of $N(H_{1/3})$ from Table 3.4.3. The computations are performed in Table 3.5.3 and again the estimates are in close agreement with those from the computer solution.

The precision of the hand computation procedure decreases for low levels of force as a result of the increase in the number of short-term conditions making significant contributions to the probabilities, each of which represents a possible error in reading off values from Figs. 2.3.4 and 2.3.5.

It is anticipated that the primary application of these hand computation procedures would be in the prediction of extreme values for use in first excursion analysis. A possible reservation regarding the application to peak values for subsequent fatigue analysis is that it is the low levels of force which cause most fatigue damage. In this range computational effort is high as most short-term conditions contribute with the possibility of error accumulation.

T A B L E 3 . 3 . 1

MEAN ZERO UP CROSSING RATES FOR FORCE ON 0.5M DIAMETER MEMBER

AT 7.5M DEPTH OF IMMERSION

$H_{1/3}$.(m)	.9	2.1	3.3	4.5	5.7	6.9	8.1	9.3
$E\{N^+(0)\|H_{1/3}\}_1$ (s^{-1})	.2207	.1725	.1517	.1386	.1292	.1219	.1160	.1109
$E\{N^+(0)\|H_{1/3}\}_2$ (s^{-1})	.2208	.1732	.1531	.1403	.1306	.1227	.1161	.1105

T A B L E 3 . 4 . 1

LEVELS OF EXTREME PEAK FORCE PER UNIT LENGTH OF A VERTICAL CYLINDRICAL MEMBER; *FAMITA* WAVE CLIMATE, MEMBER DIAMETER 0.5m, DEPTH OF IMMERSION 7.5m, $C_M = 2.0$, $C_D = 1.0$

Period of Exposure	Type of probability distribution	Most probable peak force kN/m.	Expected peak force kN/m.	Peak Force with 1% probability of exceedance, kN/m.
One year or Six Months Winter	Type 1 P-M ($H_{1/3}$)	4.05	4.15	5.80
	Type 2 P-M ($H_{1/3}$)	3.22	3.45	5.02
	Type 2: linearised P-M ($H_{1/3}$)	1.70	1.74	2.09
	Type 2 P-M (DNV)	3.28	3.49	5.03
Six Months Summer	Type 1 P-M ($H_{1/3}$)	1.50	1.60	2.20
	Type 2 P-M ($H_{1/3}$)	1.35	1.43	2.02
	Type 2: linearised P-M ($H_{1/3}$)	0.87	0.90	1.07
	Type 2 P-M (DNV)	1.33	1.42	2.01
50 Years	Type 2 P-M ($H_{1/3}$)	4.71	4.95	6.57
	Type 2: linearised P-M ($H_{1/3}$)	2.03	2.07	2.38
	Type 2 P-M (DNV)	4.75	4.95	6.57

T A B L E 3 . 4 . 2

LEVELS OF EXTREME PEAK FORCE PER UNIT LENGTH OF A VERTICAL CYLINDRICAL MEMBER; *FAMITA* WAVE CLIMATE, MEMBER DIAMETER 5.0m, DEPTH OF IMMERSION 7.5m, C_M = 2.0, C_D = 1.0

Period of Exposure	Type of probability distribution	Most probable peak force kN/m.	Expected peak force kN/m.	Peak force with 1% probability of exceedance, kN/m.
One Year or Six Months Winter	Type 1 P-M ($H_{1/3}$)	94.9	98.1	115.7
	Type 2 P-M ($H_{1/3}$)	94.9	97.6	115.5
	Type 2: linearised P-M ($H_{1/3}$)	94.7	97.0	114.1
	Type 2 P-M (DNV)	106.9	109.1	130.0
Six Months Summer	Type 1 P-M ($H_{1/3}$)	69.9	72.1	84.9
	Type 2 P-M ($H_{1/3}$)	69.9	71.9	84.6
	Type 2: linearised P-M ($H_{1/3}$)	69.8	71.8	84.6
	Type 2 P-M (DNV)	70.9	73.1	87.2
50 Years	Type 2 P-M ($H_{1/3}$)	112.5	114.7	131.2
	Type 2 linearised P-M ($H_{1/3}$)	112.3	113.5	128.9
	Type 2 P-M (DNV)	127.3	129.3	147.8

T A B L E 3 . 4 . 3

SHORT-TERM WAVE STATISTICS FOR ONE-YEAR *FAMITA* DATA AND ASSOCIATED FORCE STATISTICS FOR 0.5m. DIAMETER MEMBER AT 7.5m. DEPTH OF IMMERSION (C_M = 2.0, C_D = 1.0)

(1) $H_{1/3}$	(2) $E\{\eta^+(0)\|H_{1/3}\}$ Eq. (3.4.18) c.p.s	(3) $\sum_{j=1}^{m} \frac{w_{ij}}{w}$	(4) $\frac{E\{\eta^+(0)\|H_{1/3}\}}{E\{\eta^+(0)\}} \cdot \sum_{j=1}^{m} \frac{w_{ij}}{w}$	(5) $N(H_{1/3})$ Eq. (3.4.17)*	(6) σ_F Eq. (2.3.49) (kN)	(7) β Eq. (2.3.53)
0.3	0.17376	0.04990	0.05738	273.4×10^3	0.0032	3.000
0.9	0.17339	0.20894	0.23978	1142.5×10^3	0.0322	3.000
1.5	0.15782	0.20218	0.21119	1006.3×10^3	0.0621	3.003
2.1	0.14871	0.16684	0.16421	782.4×10^3	0.0884	3.030
2.7	0.14186	0.12734	0.11956	569.7×10^3	0.1128	3.120
3.3	0.13812	0.08368	0.07650	364.5×10^3	0.1368	3.316
3.9	0.13119	0.06861	0.05957	283.9×10^3	0.1612	3.635
4.5	0.12238	0.03638	0.02947	140.4×10^3	0.1867	4.064
5.1	0.12230	0.02391	0.01935	92,217	0.2135	4.569
5.7	0.11920	0.01195	0.00943	44,921	0.2417	5.113
6.3	0.10514	0.00624	0.00434	20,690	0.2714	5.663
6.9	0.10001	0.00572	0.00378	18,040	0.3025	6.196
7.5	0.09899	0.00416	0.00272	12,986	0.3350	6.698
8.1	0.11765	0.00104	0.00081	3,859	0.3690	6.162
8.7	0.10025	0.00208	0.00138	6,576	0.4042	7.584
9.3	0.07407	0.00104	0.00051	2,429	0.4406	7.963
	(8) $E\{\eta^+(0)\}$ = 0.15109 see Fig. 3.3.4, c.p.s.					

*Period of exposure, t_e = 1 year = 31,536,000 secs.

Note: (a) w_{ij} is the number of occurrences in the scatter diagram in class ($H_{1/3i}$, T_{zj}) and w is the total number of occurrences, as defined in Section 2.3.2.3.

(b) Column (4) represents weighting applied to short-term distributions in convolution for long-term distributions of positive peak force, see Eq. (3.1.8).

T A B L E 3 . 5 . 1

GAUSSIAN-HERMITE QUADRATURE FUNCTION POINTS AND COEFFICIENTS

$x_k^{(n)}$	$A_k^{(n)}$
n = 1	
0.00000 00000 00000	1.77245 38509 055
n = 2	
0.70710 67811 86548	0.88622 69254 528
n = 3	
0.00000 00000 00000	1.18163 59006 037
1.22474 48713 91589	0.29540 89751 509
n = 4	
0.52464 76232 75290	0.80491 40900 055
1.65068 01238 85785	(-1)0.81312 83544 725
n = 5	
0.00000 00000 00000	0.94530 87204 829
0.95857 24646 13819	0.39361 93231 522
2.02018 28704 56086	(-1)0.19953 24205 905
n = 10	
0.34290 13272 23705	0.61086 26337 353
1.03661 08297 89514	0.24013 86110 823
1.75668 36492 99882	(-1)0.33874 39445 548
2.53273 16742 32790	(-2)0.13436 45746 781
3.43615 91188 37738	(-5)0.76404 32855 233
n = 15	
0.00000 00000 0000	0.56410 03087 264
0.56506 95832 5558	0.41202 86874 989
1.13611 55852 1092	0.15848 89157 959
1.71999 25751 8649	(-1)0.30780 03387 255
2.32573 24861 7386	(-2)0.27780 68842 913
2.96716 69279 0560	(-3)0.10000 44412 325
3.66995 03734 0445	(-5)0.10591 15547 711
4.49999 07073 0939	(-8)0.15224 75804 254

The $A_k^{(n)}$ and $x_k^{(n)}$ are symmetric with respect to x = 0 and the tables give only the values corresponding to $0 \leq x_k^{(n)}$.

A number in parenthesis before a value of a coefficient is the power of 10 by which the tabulated value must be multiplied; for example, (-1)0.8131 . . . means that the coefficient is 0.08131 . . .

T A B L E 3 . 5 . 2 A

LONG-TERM PROBABILITIES OF NON-EXCEEDENCE OF VARIOUS LEVELS OF FORCE FOR BOTH BASIC AND PEAK VARIATE

$H_{1/3}$	Force = 0.5kN.				
	(a) $\frac{F}{\sigma_F}$	(b) $P_H(F\|H_{1/3})$	(c) {1-(b)} x(3)†	(d) $P_p(F\|H_{1/3})$	(e) {1.0x(d)} x(4)*
0.3	-				
0.9	15.528				
1.5	8.052	1.0	0	≈1.0	0
2.1	5.656	≈ .9999999	1.67×10^{-8}	0.9999994	9.85×10^{-8}
2.7	4.433	0.999977	2.93×10^{-6}	0.9998	2.39×10^{-5}
3.3	3.655	0.9995	4.18×10^{-5}	0.9971	2.22×10^{-4}
3.9	3.102	0.9975	1.72×10^{-4}	0.988	7.15×10^{-4}
4.5	2.678	0.9933	2.44×10^{-4}	0.972	8.25×10^{-4}
5.1	2.342	0.986	3.35×10^{-4}	0.95	9.68×10^{-4}
5.7	2.069	0.978	2.63×10^{-4}	0.92	7.54×10^{-4}
6.3	1.842	0.968	2.00×10^{-4}	0.888	4.86×10^{-4}
6.9	1.653	0.954	2.63×10^{-4}	0.86	5.29×10^{-4}
7.5	1.493	0.944	2.33×10^{-4}	0.84	4.35×10^{-4}
8.1	1.355	0.932	7.07×10^{-5}	0.825	1.42×10^{-4}
8.7	1.237	0.922	1.62×10^{-4}	0.80	2.76×10^{-4}
9.3	1.135	0.910	9.36×10^{-5}	0.77	1.17×10^{-4}
		$1-P(F)= =2.08\times10^{-}$		$1-P_p(F)= =5.493\times10^{-}$	
		$P(F) = 99.79$		$\underline{P_p(F) = 99.45}$	
	COMP**	$P(F) = 99.80$		$P_p(F) = 99.46$	

† Column (3), Table 3.4.3
* Column (4), Table 3.4.3
** Values from Computer Routines

T A B L E 3 . 5 . 2 B

LONG-TERM PROBABILITIES OF NON-EXCEEDENCE OF VARIOUS LEVELS OF FORCE FOR BOTH BASIC AND PEAK VARIATE

$H_{1/3}$	Force = 1.5kN.		
	$\frac{F}{\sigma_F}$	(d) $P_p(F\|H_{1/3})$	(e) {1.0x(d)} x(4)*
0.3	-		
0.9	-		
1.5	-		
2.1	16.968		
2.7	13.298		
3.3	10.965	≃1.0	0
3.9	9.305	0.99999983	1.01×10^{-8}
4.5	8.034	0.9999952	1.415×10^{-7}
5.1	7.026	0.999955	8.708×10^{-7}
5.7	6.206	0.9998	1.886×10^{-6}
6.3	5.527	0.99935	2.821×10^{-6}
6.9	4.959	0.9986	5.292×10^{-6}
7.5	4.478	0.9977	6.256×10^{-6}
8.1	4.065	0.995	4.05×10^{-6}
8.7	3.711	0.9921	1.09×10^{-5}
9.3	3.404	0.989	5.61×10^{-6}
		$1 - P_p(F) = \Sigma = 3.784 \times 10^{-5}$	
		$\underline{P_p(F) = 0.999962}$	
	COMP**	$P_p(F) = 0.999961$	

* Column (4), Table 3.4.3
** Values from Computer Routines

T A B L E 3 . 5 . 2 C

LONG-TERM PROBABILITIES OF NON-EXCEEDENCE OF VARIOUS LEVELS OF FORCE FOR BOTH BASIC AND PEAK VARIATE

$H_{1/3}$	Force = 3.0kN.				
	(a) $\frac{F}{\sigma_F}$	(b) $p_H(F\|H_{1/3})$	(c) {1-(b)} x(3)†	(d) $P_p(F\|H_{1/3})$	(e) {1.0-(d)} x(4)*
0.3	-				
0.9	-				
1.5	-				
2.1	-				
2.7	-				
3.3	-				
3.9	-				
4.5	16.069			≈1.0	0
5.1	14.052			.9999999973	1.0×10^{-10}
5.7	12.412	≈1.0	0	.9999994	6.0×10^{-10}
6.3	11.053	.99999987	8.0×10^{-10}	.9999993	3.0×10^{-9}
6.9	9.917	.9999982	1.03×10^{-8}	.999996	1.51×10^{-8}
7.5	8.955	.999992	3.33×10^{-8}	.999984	4.35×10^{-8}
8.1	8.130	.999978	2.29×10^{-8}	.99995	4.05×10^{-8}
8.7	7.422	.99994	1.25×10^{-7}	.99987	1.79×10^{-7}
9.3	6.809	.99987	1.352×10^{-7}	.9974	1.33×10^{-7}
		$1-P(F)=\Sigma=3.273 \times 10^{-7}$		$1-P_p(F)=\Sigma=4.15 \times 10^{-7}$	
		$P(F) = 0.99999967$		$\underline{P_p(F) = 0.9999959}$	
	COMP**	$P(F) = 0.99999967$		$P_p(F) = 0.9999960$	

† Column (3), Table 3.4.3
* Column (4), Table 3.4.3
** Values from Computer Routines

TABLE 3.5.3

LONG-TERM PROBABILITIES OF NON-EXCEEDANCE OF VARIOUS LEVELS OF EXTREME FORCE FOR A ONE-YEAR PERIOD OF EXPOSURE

$H_{1/3}$ (m)	Force = 2.51kN.				Force = 2.82kN				Force 5.02kN.			
	(a) $\frac{F}{\sigma_F}$	(b) $P_p(F\|H_{1/3})$	(c) $P_{EP}(F\|H_{1/3})$	(d) $\Pi P_{EP}(F\|H_{1/3})$	(a) $\frac{F}{\sigma_F}$	(b) $P_p(F\|H_{1/3})$	(c) $P_{EP}(F\|H_{1/3})$	(d) $\Pi P_{EP}(F\|H_{1/3})$	(a) $\frac{F}{\sigma_F}$	(b) $P_p(F\|H_{1/3})$	(c) $P_{EP}(F\|H_{1/3})$	(d) $\Pi P_{EP}(F\|H_{1/3})$
0.3												
0.9												
1.5												
2.1												
2.7	22.26											
3.3	18.36				20.61							
3.9	15.57	≃1.0	≃1.0	≃1.0	17.49							
4.5	13.45	≃ .999999999	.99986	.99986	15.10	≃1.0	≃1.0	≃1.0				
5.1	11.76	.99999994	.99448	.99434	13.21	.999999992	.99926	.99926				
5.7	10.39	.9999992	.96469	.95923	11.67	.99999982	.9919	.9917	20.78			
6.3	9.25	.999994	.88330	.84729	10.39	.9999985	.96945	.96089	18.50	≃1.0	≃1.0	≃1.0
6.9	8.30	.999975	.63715	.53985	9.32	.9999925	.87352	.83935	16.60	.99999998	.9999639	.9999639
7.5	7.50	.99991	.31074	.16775	8.42	.999970	.67733	.56832	14.99	.99999995	.999351	.999315
8.1	6.80	.99978	.42800	.(7180	7.64	.999915	.72046	.40960	13.61	.99999988	.999537	.99885
8.7	6.21	.99955	.05190	.00373	6.98	.9998	.26855	.11000	12.42	.9999994	.99606	.99492
9.3	5.70	.9992	.14325	.000534	6.40	.9996	.37855	.04164	11.40	.999998	.99516	.99010
		$P_{EP}(F) = 0.000534$				$P_{EP}(F) = 0.04164$				$P_{EP}(F) = 0.99010$		
	COMP*	$P_{EP}(F) = 0.000501$				$P_{EP}(F) = 0.0432$				$P_{EP}(F) = 0.99066$		

* Values from Computer Routine

FIG. 3.1.1. RATIO OF VARIANCE OF LINEARISED GAUSSIAN WAVE LOAD TO VARIANCE OF PIERSON/HOLMES LOADING, (σ_1^2 / M_2) FOR DIFFERENT MEMBER & SEA STATE CONDITIONS (DEFINED BY $H_{1/3}$)

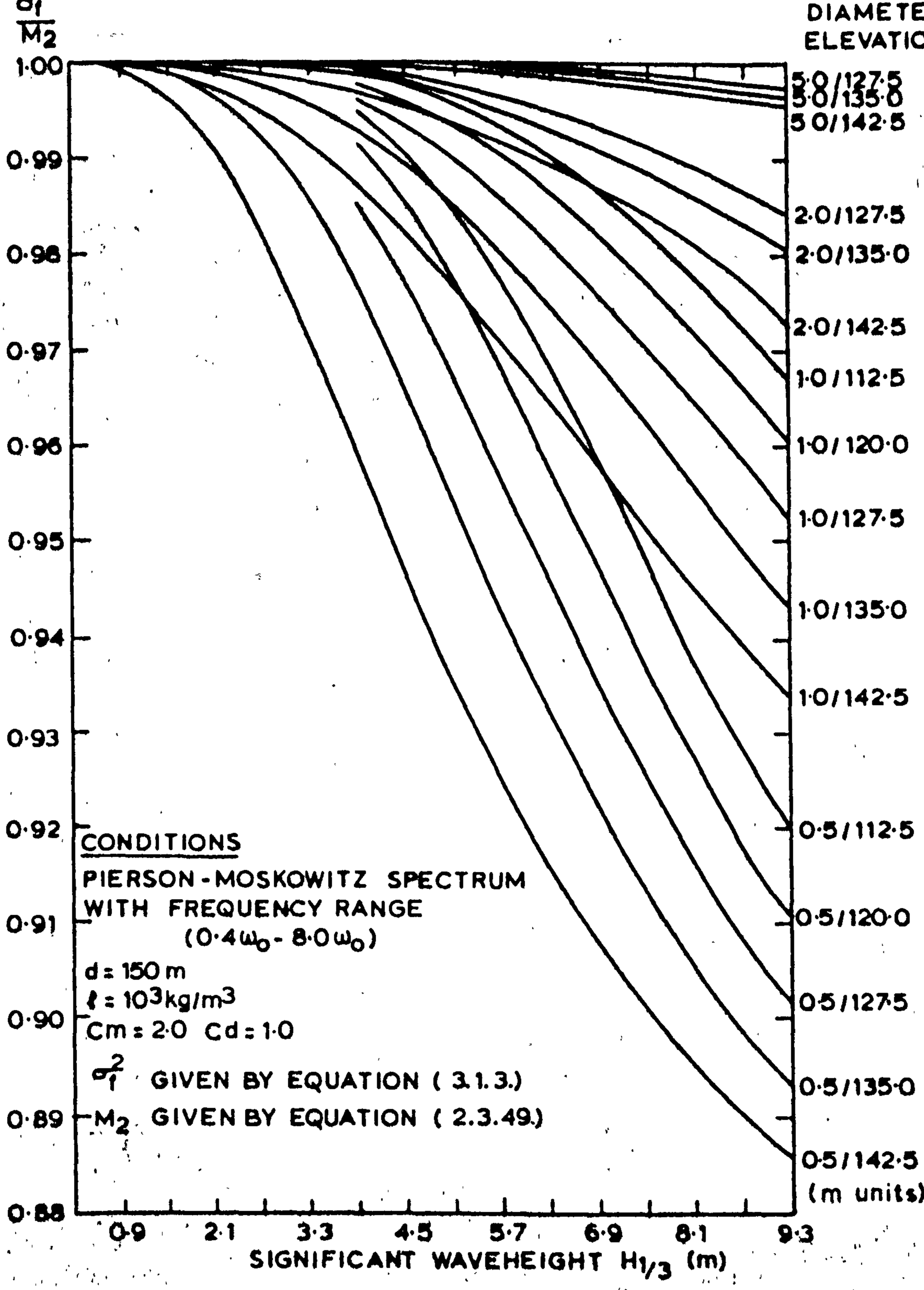

FIG 3.1.2. KURTOSIS OF PIERSON/HOLMES LOADING FOR DIFFERENT MEMBER AND SEA STATE CONDITIONS (DEFINED BY $H_{1/3}$)

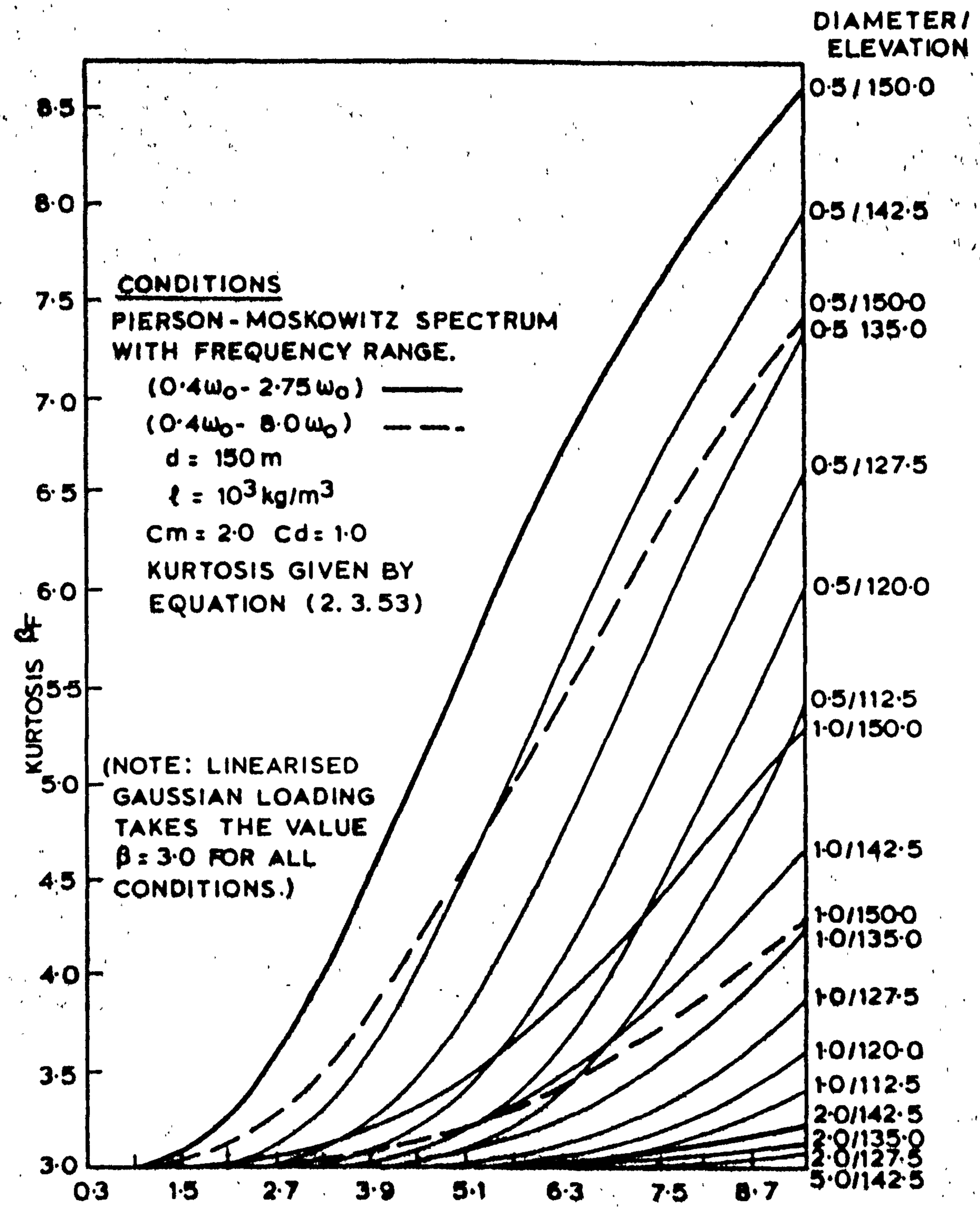

FIG. 3.1.3. SHORT AND LONG-TERM CUMULATIVE DISTRIBUTIONS OF PEAK LOADING $P_p(F/H_{1/3})$ AND $P_p(F)$ RESPECTIVELY

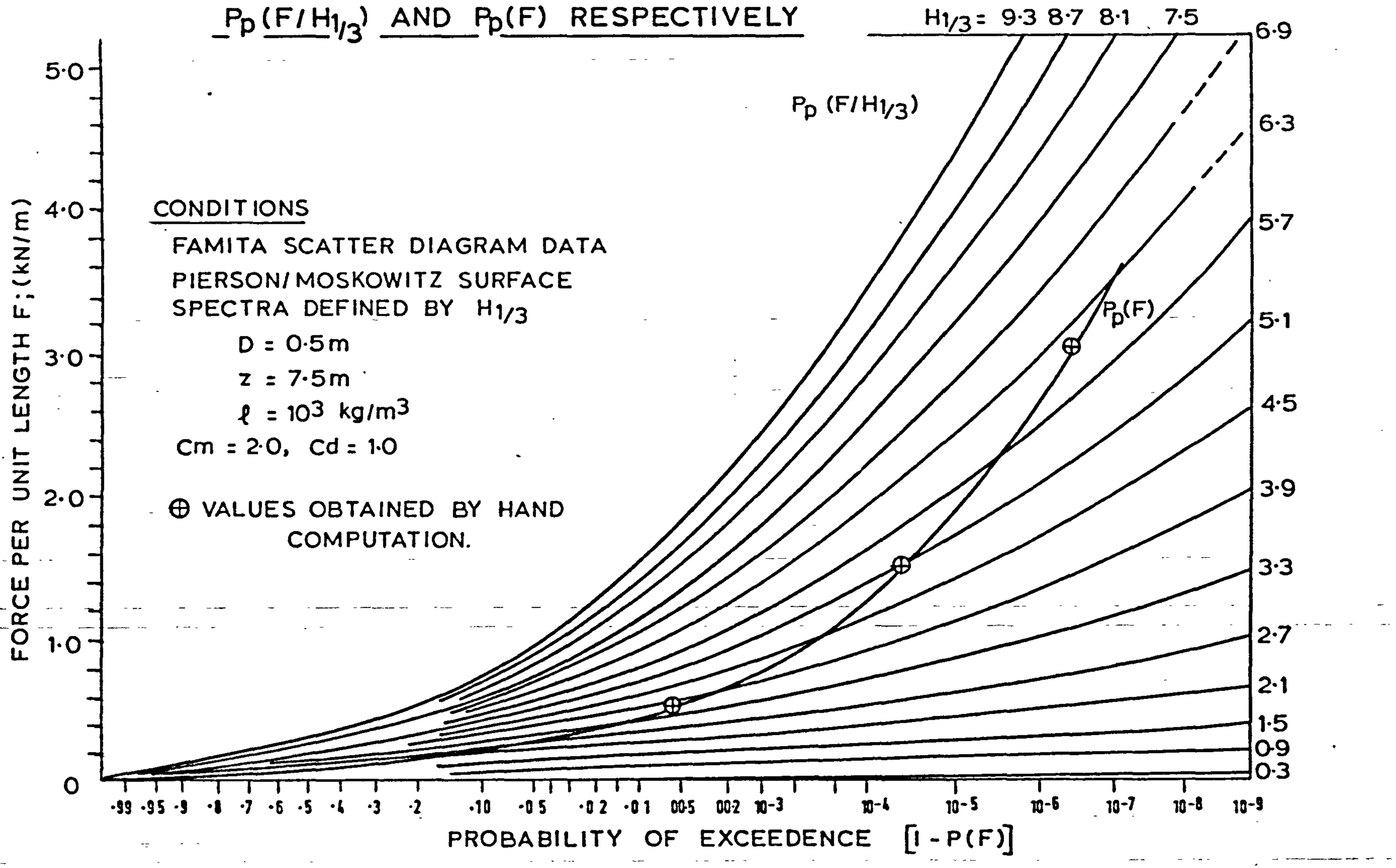

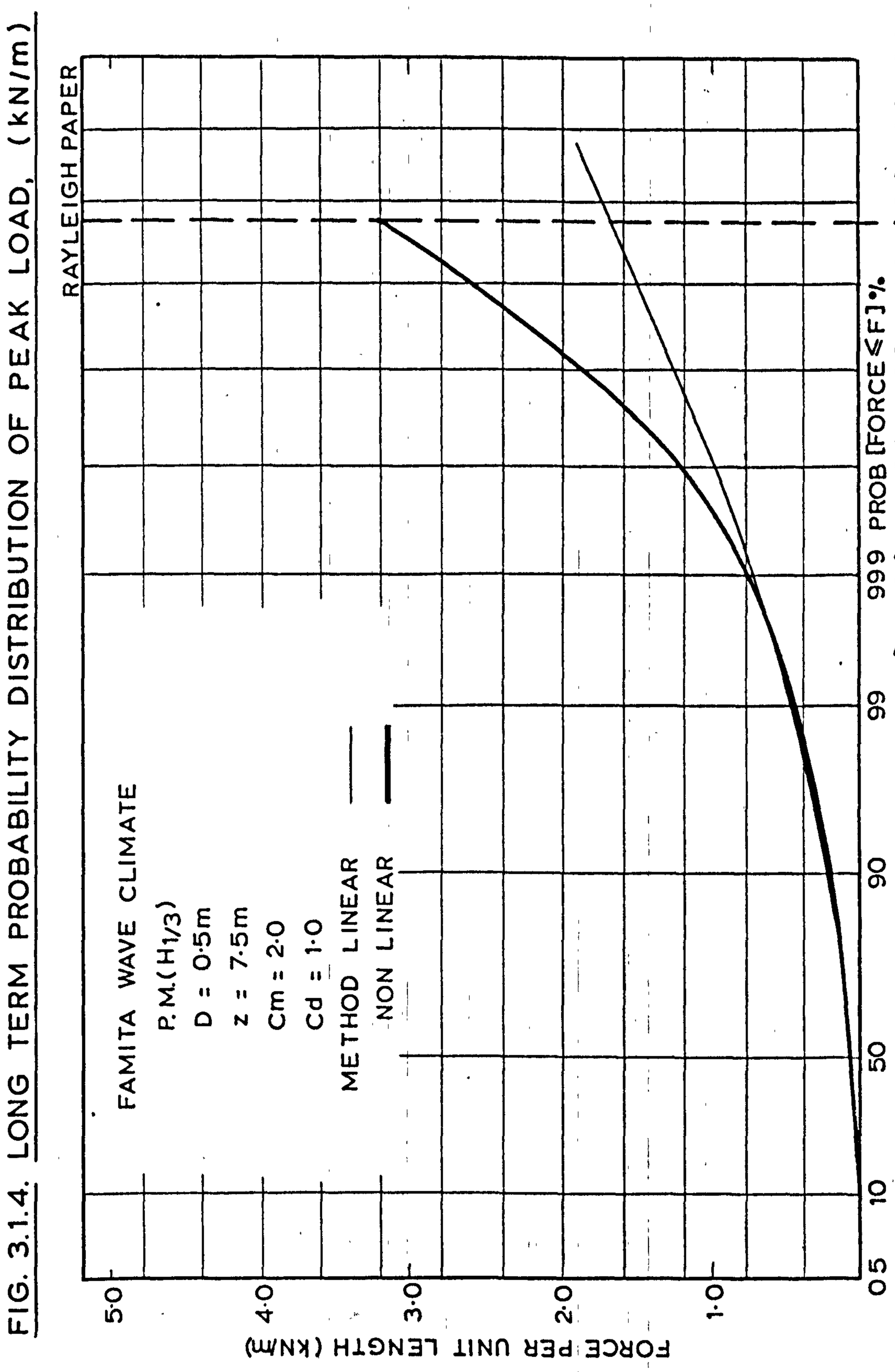
FIG. 3.1.4. LONG TERM PROBABILITY DISTRIBUTION OF PEAK LOAD, (KN/m)
RAYLEIGH PAPER
FAMITA WAVE CLIMATE
P.M.($H_{1/3}$)
D = 0·5m
z = 7·5m
Cm = 2·0
Cd = 1·0
METHOD LINEAR
NON LINEAR
999 PROB [FORCE≤F]%
10-1 10-2 10-3 10-4 10-5 10-6 10-7
1 Year
PROB [FORCE>F]%
99 90 50 10 05
FORCE PER UNIT LENGTH (kN/m)
5·0 4·0 3·0 2·0 1·0

FIG. 3.1.5. LONG TERM PROBABILITY DISTRIBUTION OF PEAK LOAD, (kN/m)

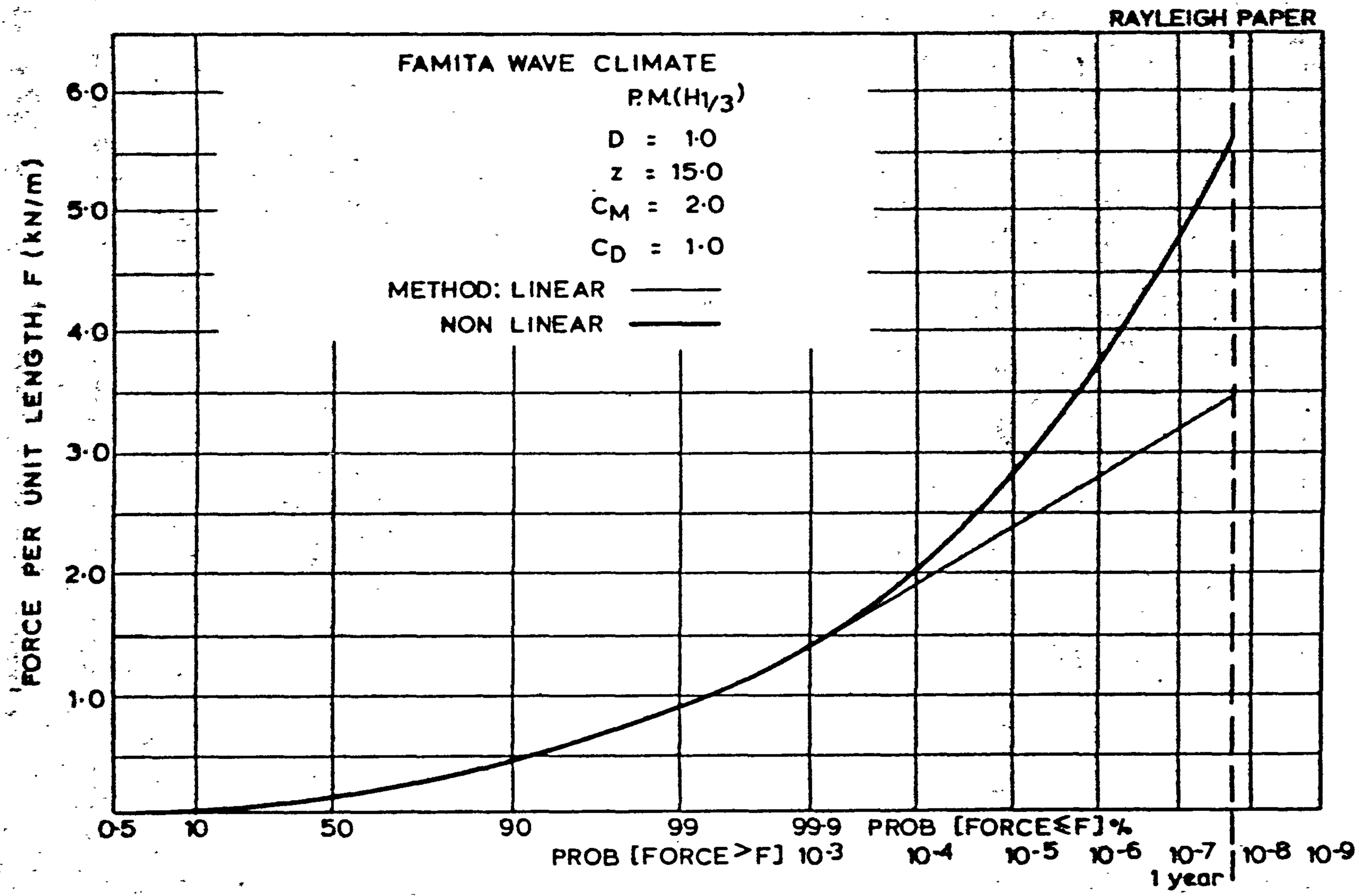

FIG. 3.1.6. LONG TERM PROBABILITY DISTRIBUTION OF PEAK LOAD, (kN/m)

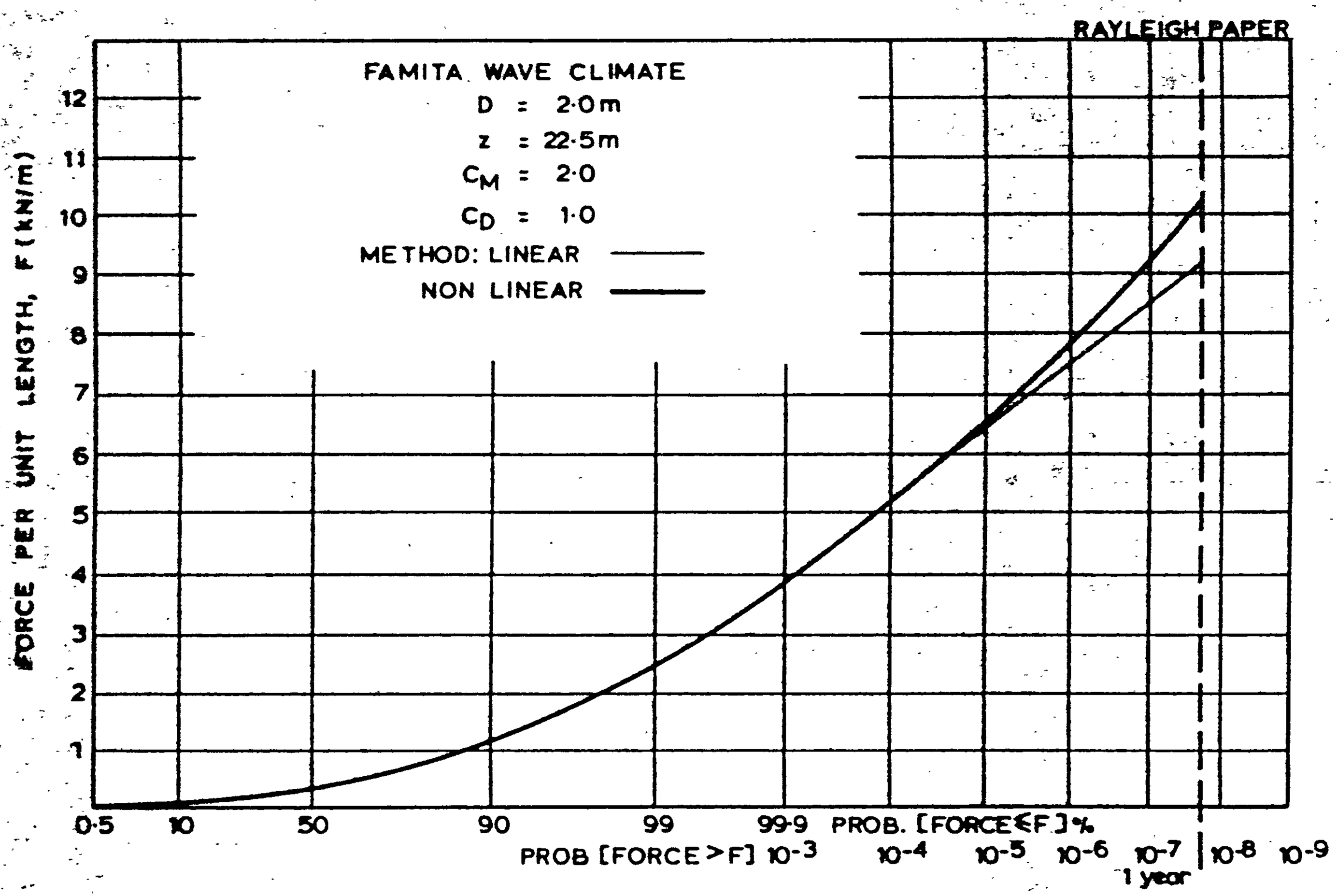

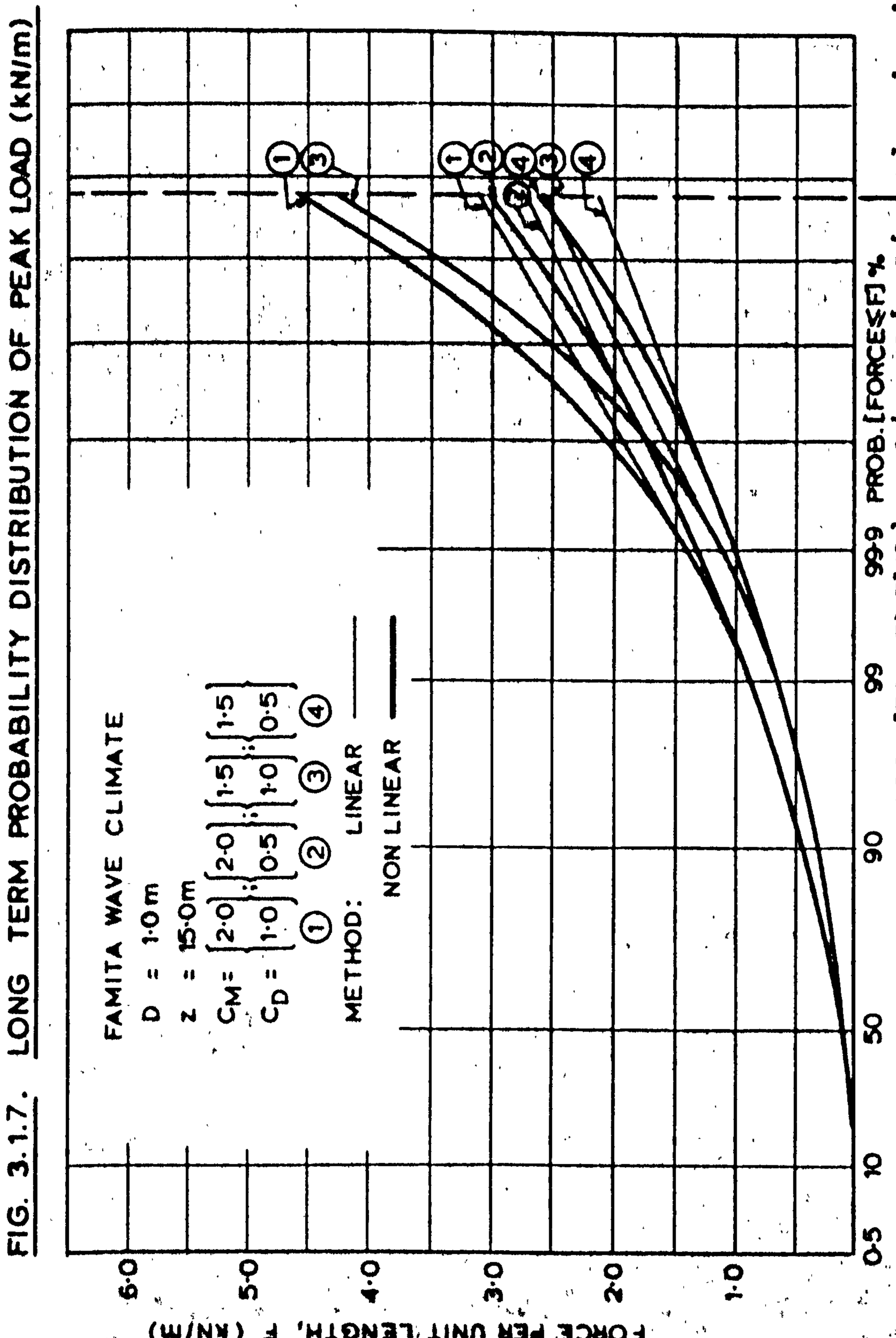
FIG. 3.17. LONG TERM PROBABILITY DISTRIBUTION OF PEAK LOAD
FAMITA WAVE CLIMATE
D = 1·0 m
z = 15·0 m
$C_M = \left\{\begin{matrix}2·0\\1·0\end{matrix}\right\}\left\{\begin{matrix}2·0\\0·5\end{matrix}\right\}\left\{\begin{matrix}1·5\\1·0\end{matrix}\right\}\left\{\begin{matrix}1·5\\0·5\end{matrix}\right\}$
$C_D = \left\{\begin{matrix}1·0\\1·0\end{matrix}\right\}\left\{\begin{matrix}0·5\\0·5\end{matrix}\right\}\left\{\begin{matrix}1·0\\1·0\end{matrix}\right\}\left\{\begin{matrix}0·5\\0·5\end{matrix}\right\}$
① ② ③ ④
METHOD: LINEAR ——— NON LINEAR ———
99·9 PROB.[FORCE≤F] %
PROB [FORCE>F] 10^{-1} 10^{-2} 10^{-3} 10^{-4} 10^{-5} 10^{-6} 10^{-7}
99
90
50
10
0·5
6·0
5·0
4·0
3·0
2·0
1·0
FORCE PER UNIT LENGTH, F (kN/m)

FIG. 3.2.1.

PIERSON - MOSKOWITZ AND JONSWAP SPECTRAL SHAPES.

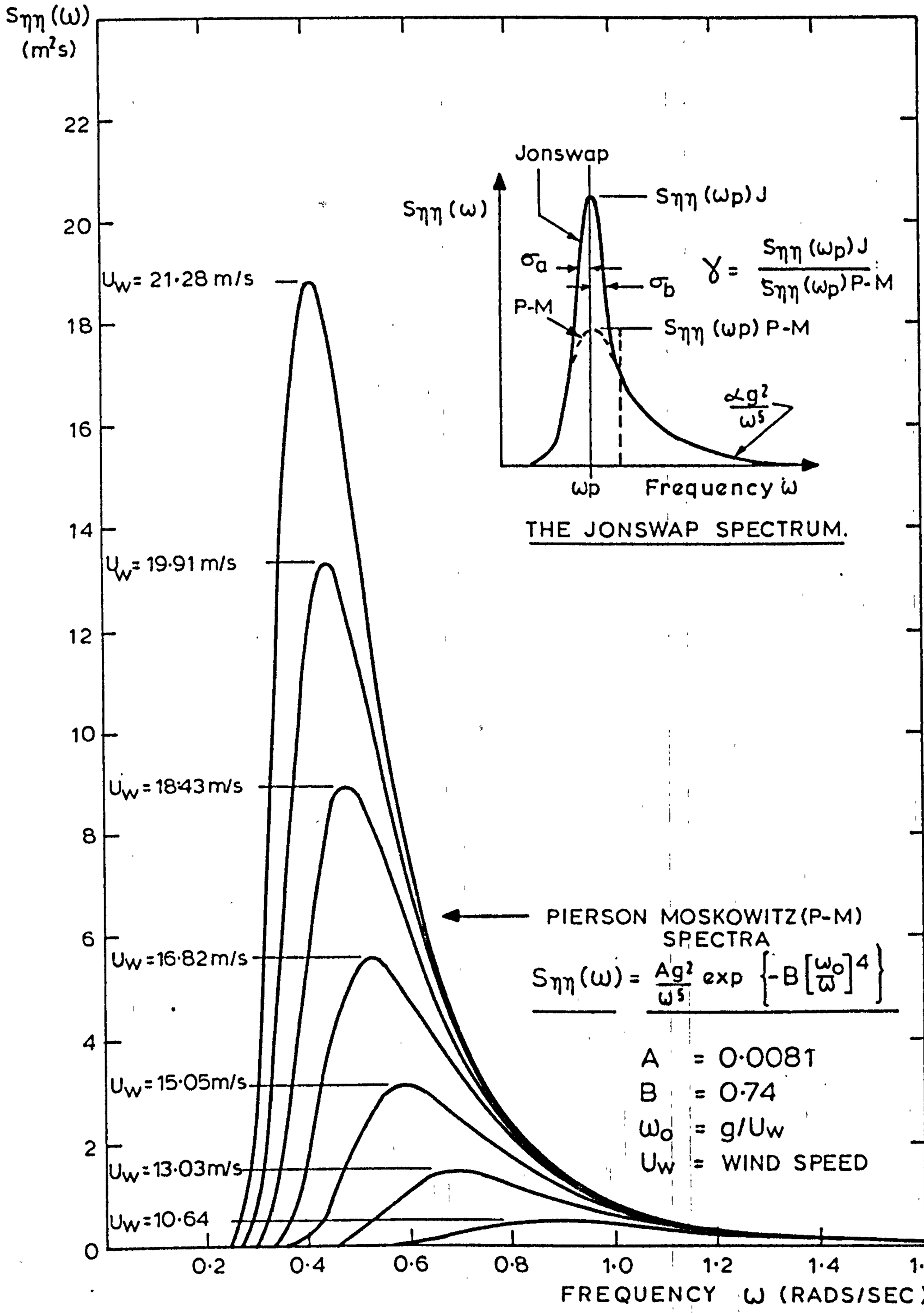

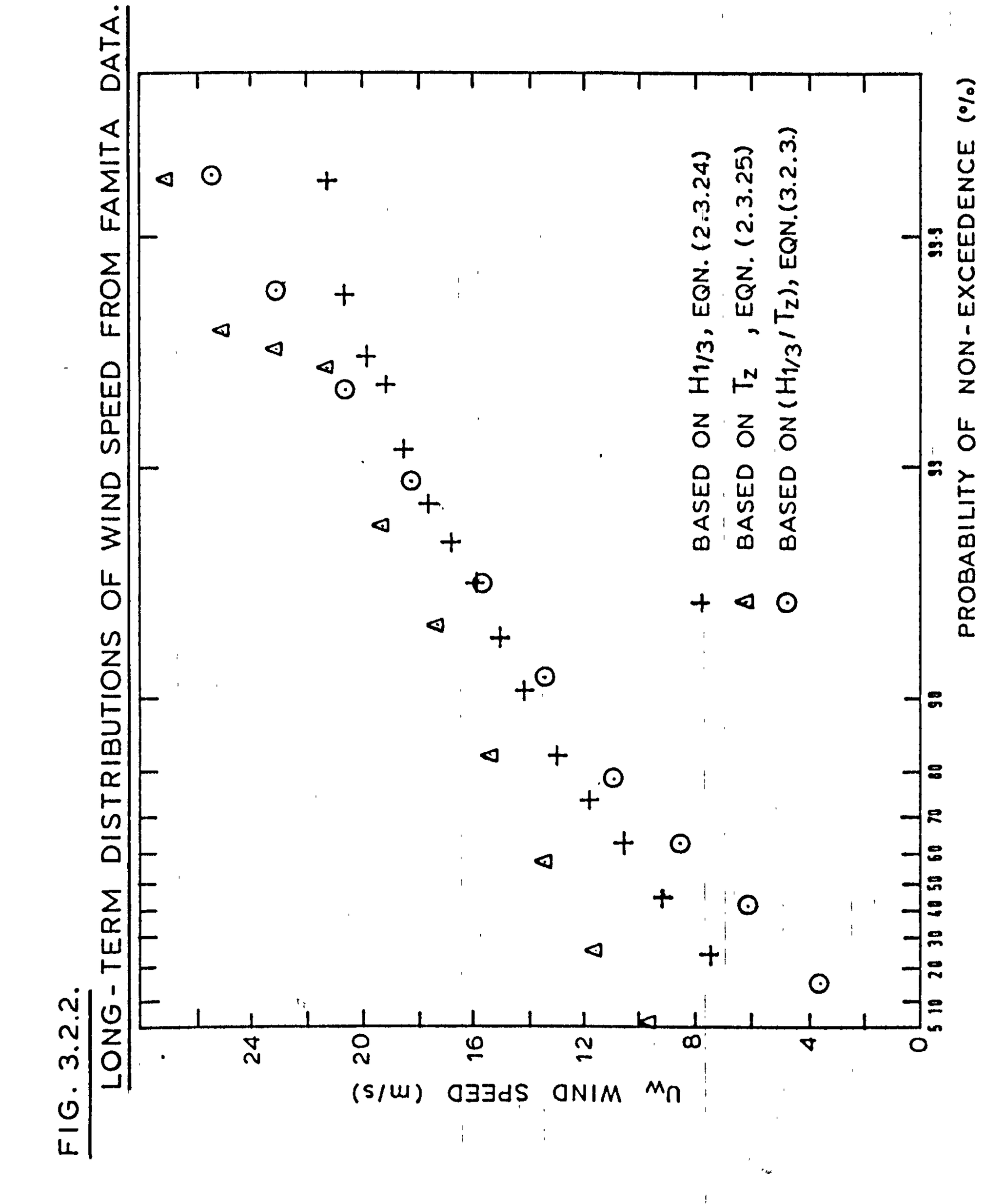
LONG-TERM DISTRIBUTIONS OF WIND SPEED FROM FAMITA DATA.
+ BASED ON H1/3, EQN. (2.3.24)
Δ BASED ON Tz , EQN. (2.3.25)
⊙ BASED ON (H1/3 / Tz), EQN.(3.2.3.)
Uw WIND SPEED (m/s)
0
4
8
12
16
20
24
PROBABILITY OF NON-EXCEEDENCE (%)
5 10 20 30 40 50 60 70 80 90

FIG. 3.2.2.

FIG. 3.2.3. TRANSFER FUNCTIONS APPLIED TO SURFACE ELEVATION SPECTRUM TO PRODUCE SPECTRA OF PARTICLE KINEMATICS IN 'DEEP WATER' CONDITIONS.

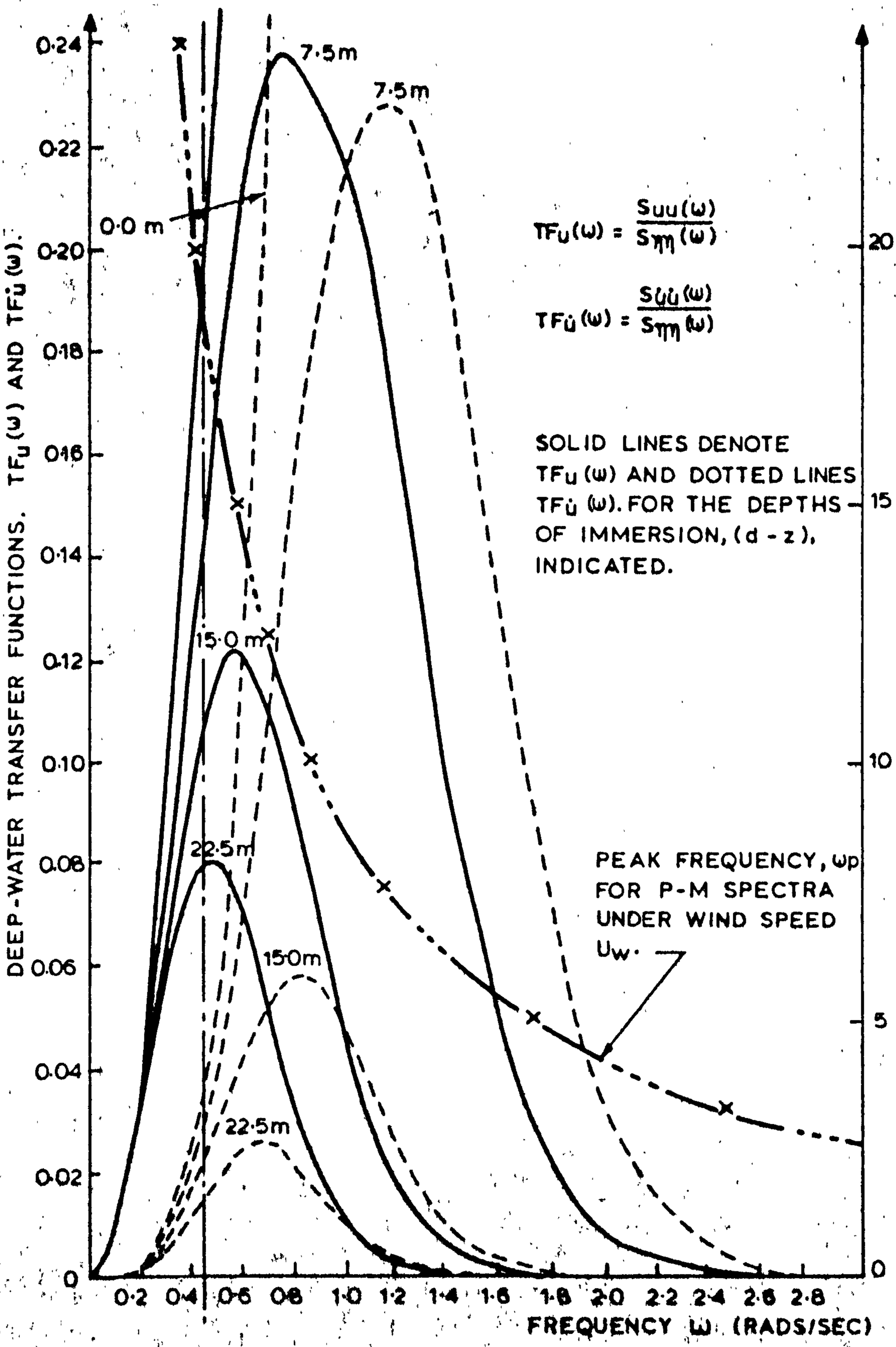

FIG. 3.2.4. LONG-TERM PROBABILITY DISTRIBUTIONS OF PEAK FORCE FOR FAMITA SCATTER DIAGRAM BASED ON SHORT-TERM CONDITIONS DEFINED BY VARIOUS SPECTRAL FORMS

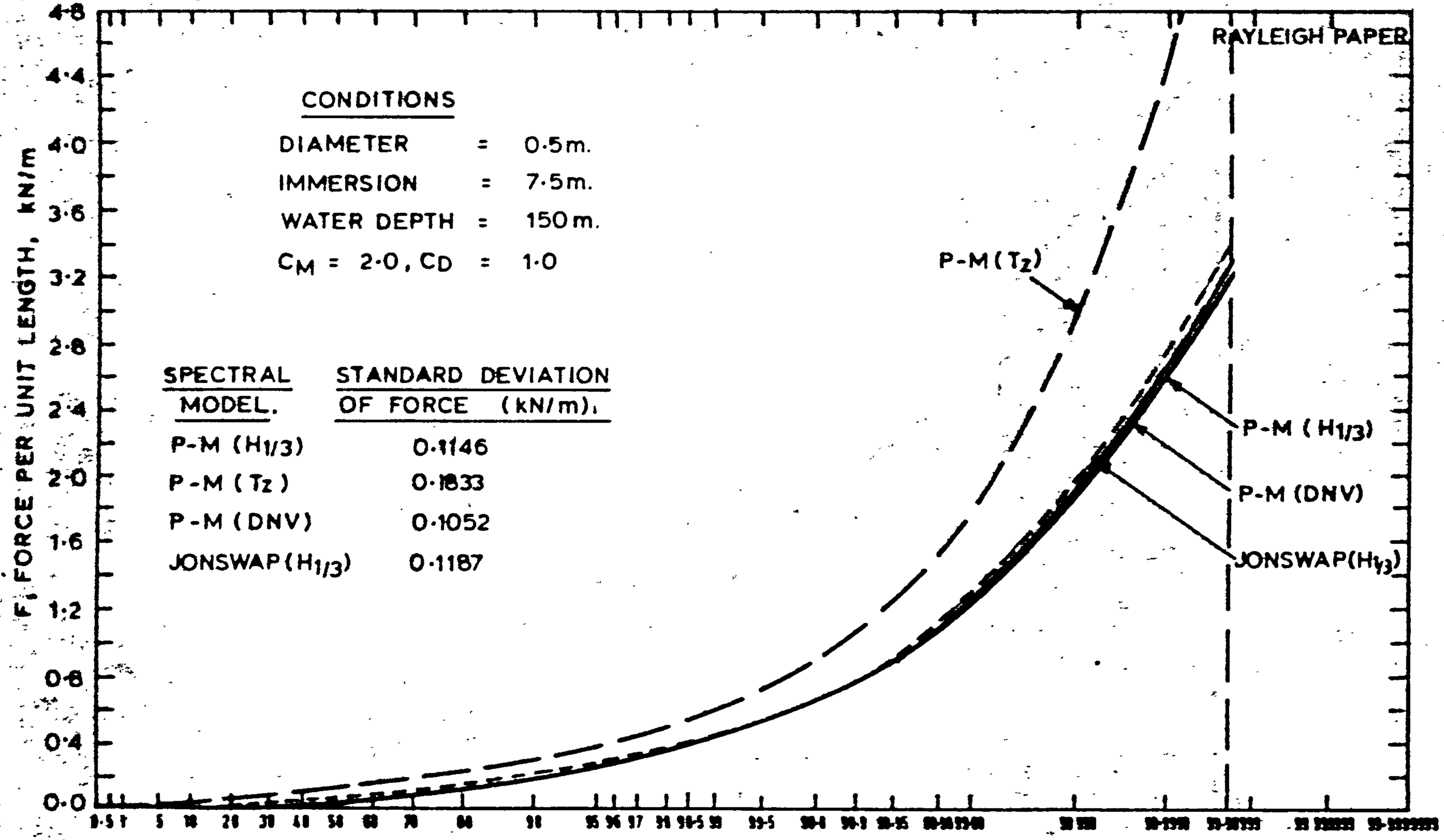

FIG. 3.2.5. LONG-TERM PROBABILITY DISTRIBUTIONS OF PEAK FORCE FOR FAMITA SCATTER DIAGRAM BASED ON SHORT-TERM CONDITIONS DEFINED BY VARIOUS SPECTRAL FORMS.

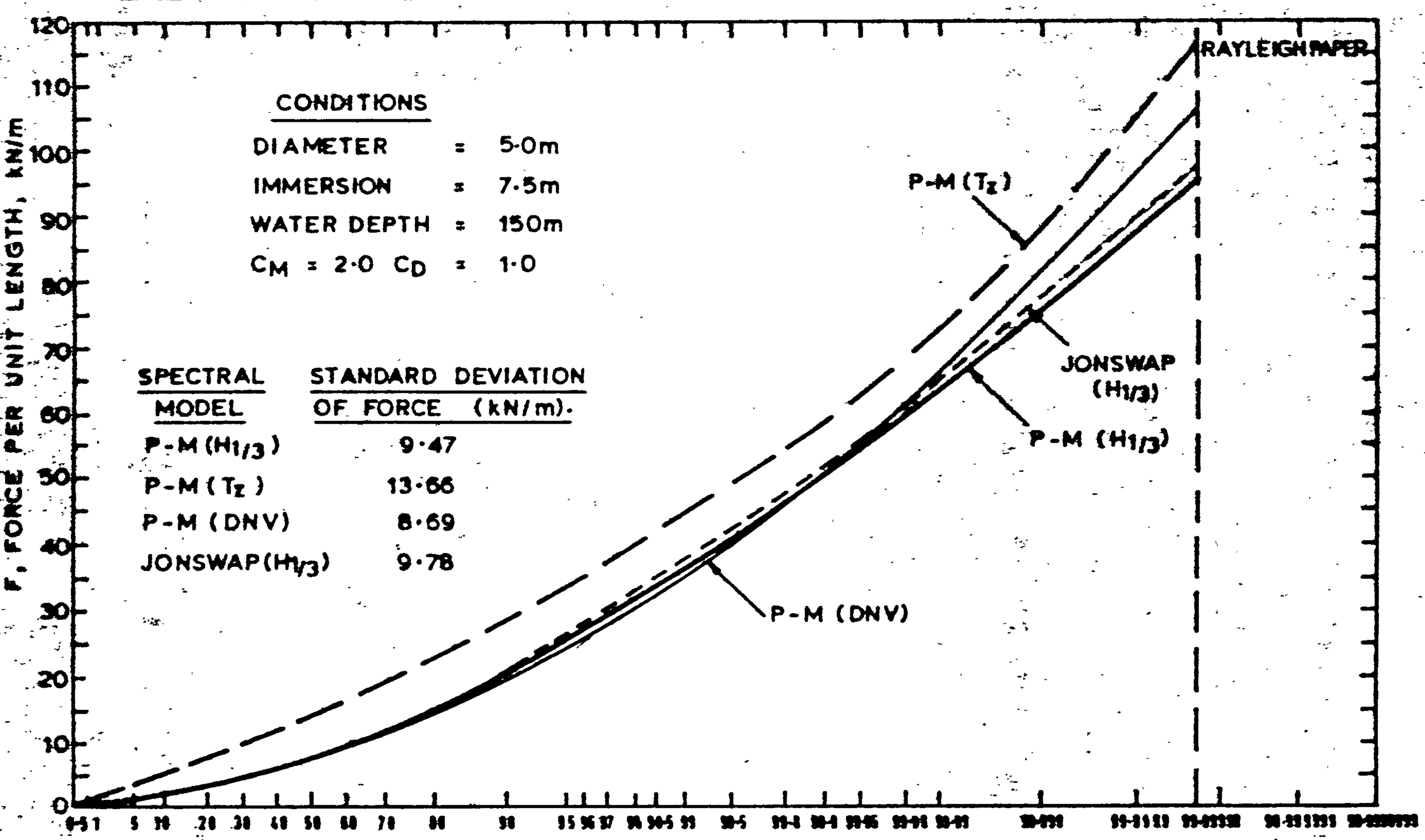

FIG. 3.3.1. EFFECT OF CHANGE IN FREQUENCY RANGE OF $S_{\eta\eta}(\omega)$ ON VARIANCES σ_U^2 AND $\sigma_{\dot{U}}^2$ FOR P-M($H_{1/3}$) SPECTRA.

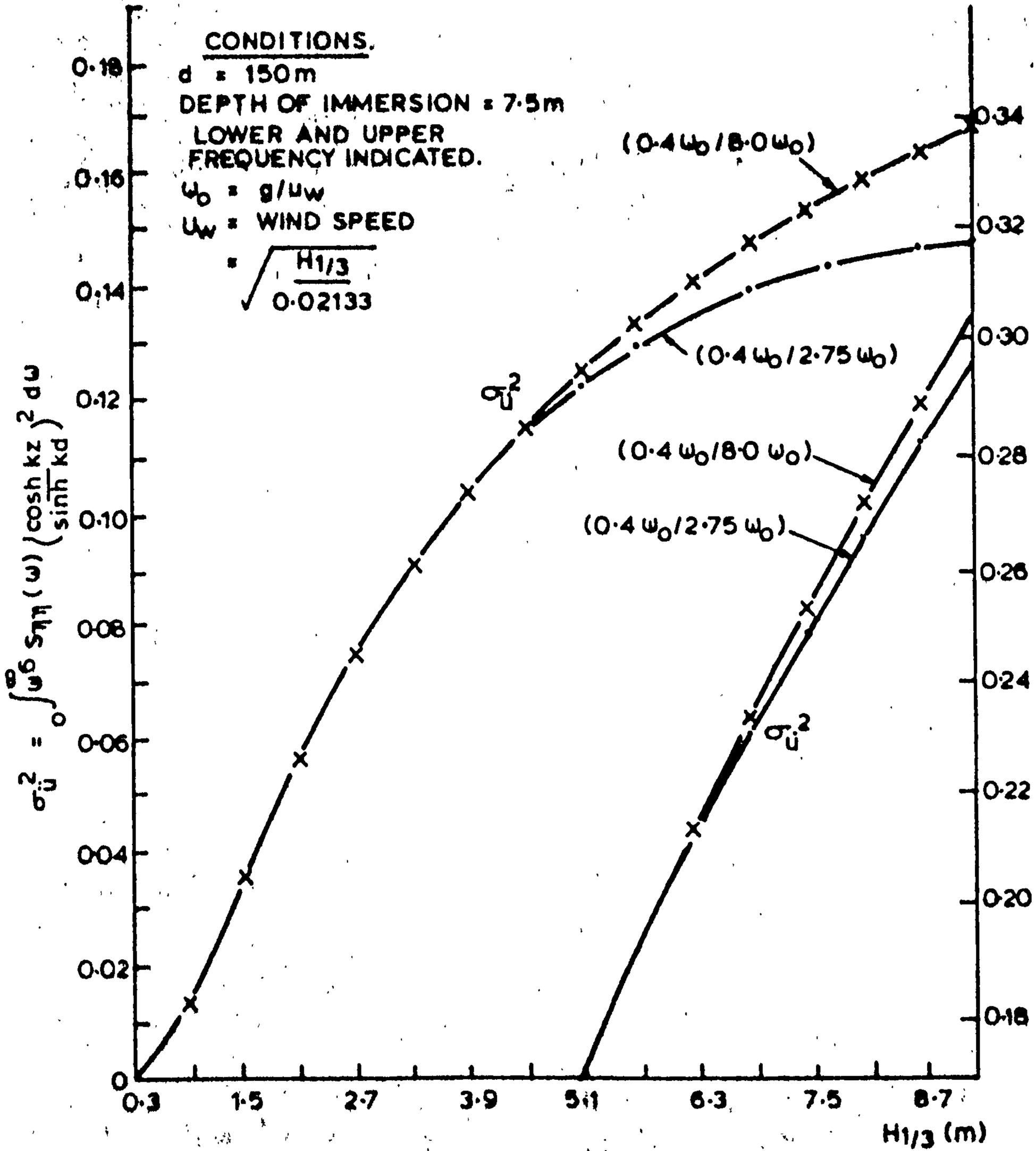

FIG. 3.3.2. SHORT - TERM PEAK FORCE DISTRIBUTION FOR 0·5m DIAMETER MEMBER AT 7·5m DEPTH OF IMMERSION UNDER MOST SEVERE FAMITA SEA STATE.

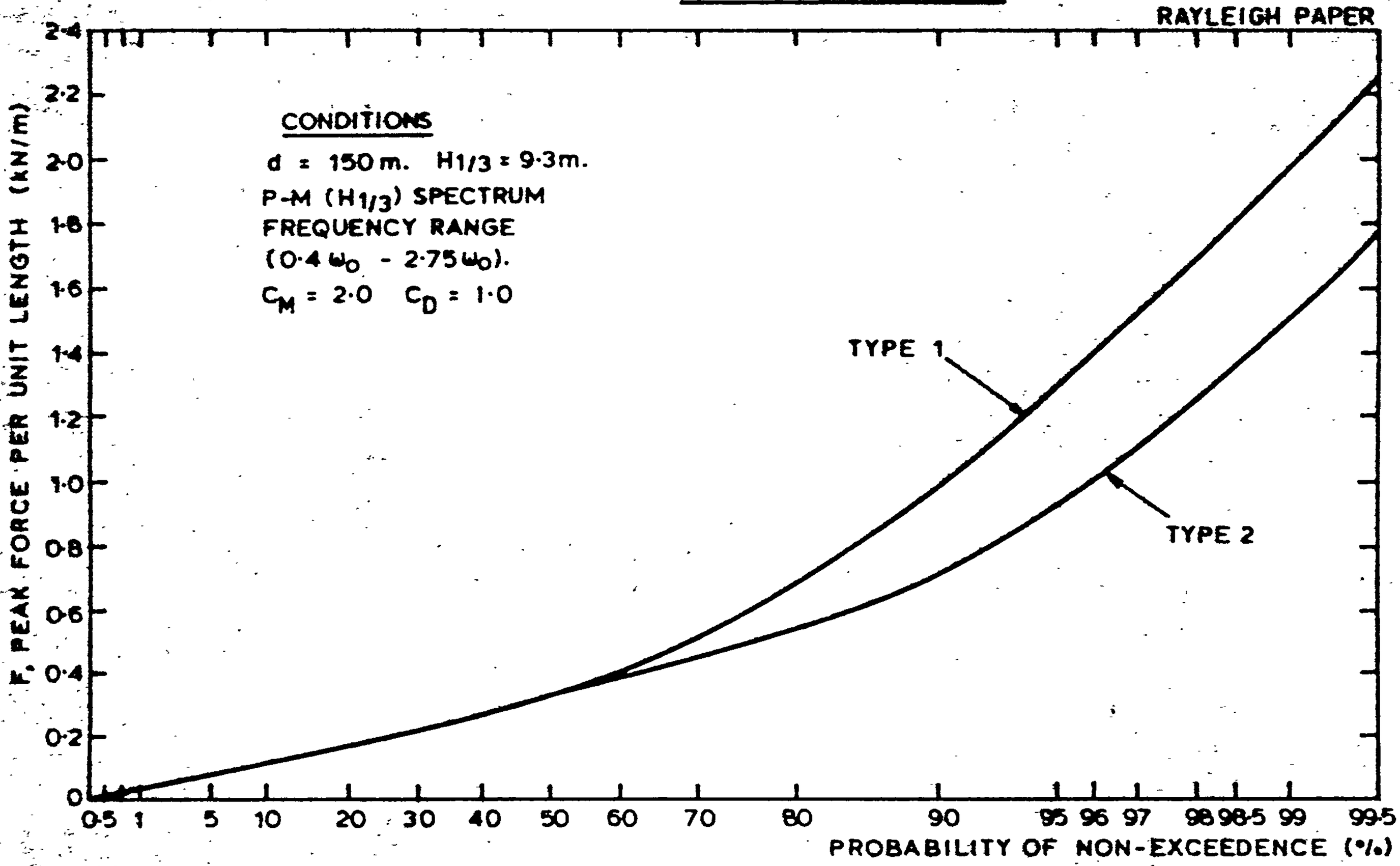

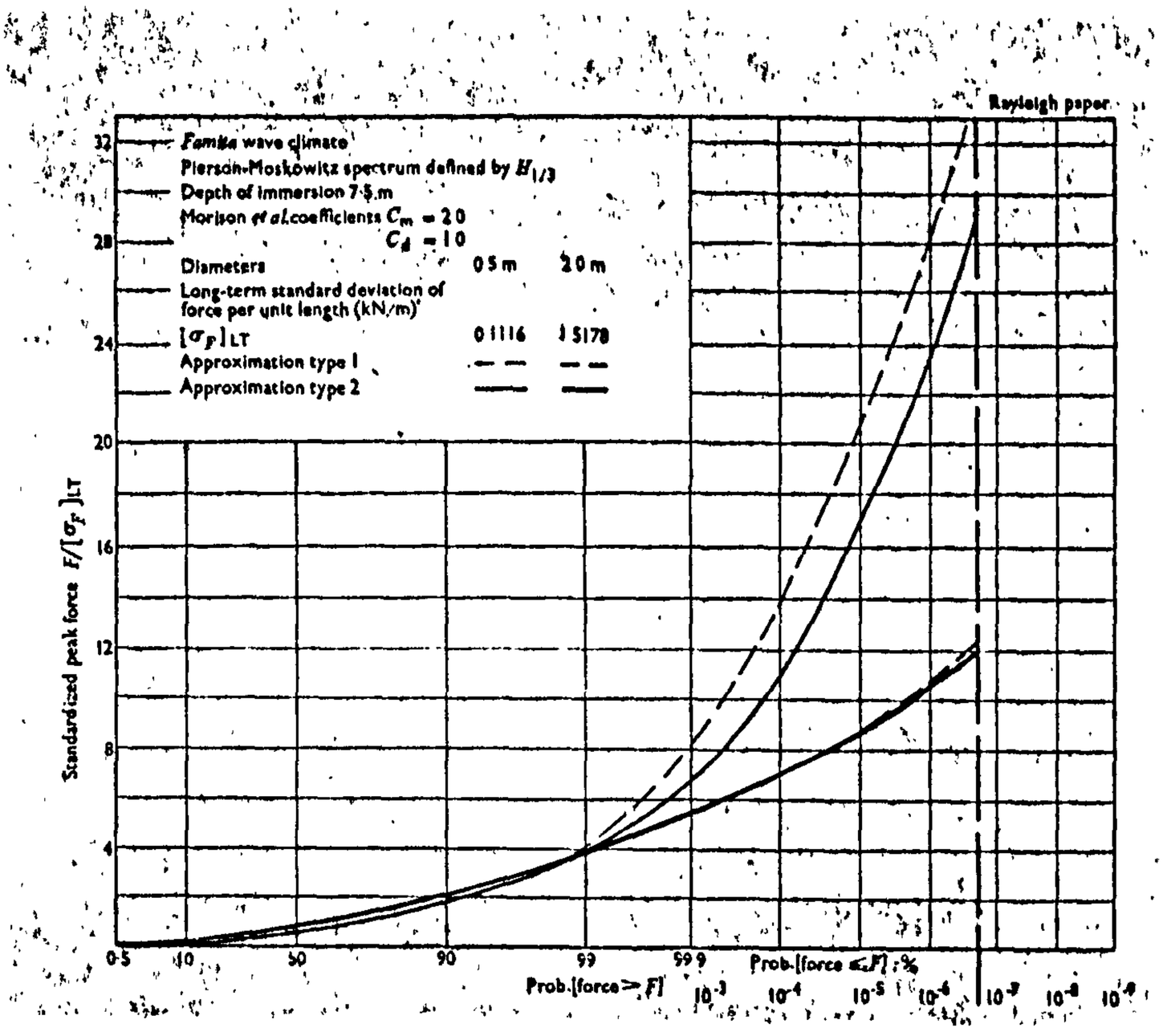

FIG. 3.3.3. LONG-TERM PROBABILITY DISTRIBUTIONS OF PEAK FORCE DERIVED FROM NARROW BAND APPROXIMATIONS TYPES 1 AND 2.

FIG. 3.3.4. SHORT AND LONG-TERM MEAN ZERO-UP CROSSING RATES OF SURFACE ELEVATION AND FORCE FOR VARIOUS MEMBER CONDITIONS BASED ON P-M ($H_{1/3}$)

LONG-TERM (Famita Wave Climate)

$E\{\eta^+(o)\} = \overline{T_z^{-1}} = 0.151 s^{-1}$	ONE-YEAR PROBABILITY* 2.10×10^{-7}	DEPTH OF IMMERSION (m) —
$E\{N^+(o)\}_1 \simeq 0.184 s^{-1}$	1.72×10^{-7}	7.5
$\simeq 0.160$	1.98×10^{-7}	15.0
$\simeq 0.147$	2.16×10^{-7}	22.5
$\simeq 0.140$	2.27×10^{-7}	30.0

* Probability associated with one exceedence per year ≈ 1/(No peaks per year)

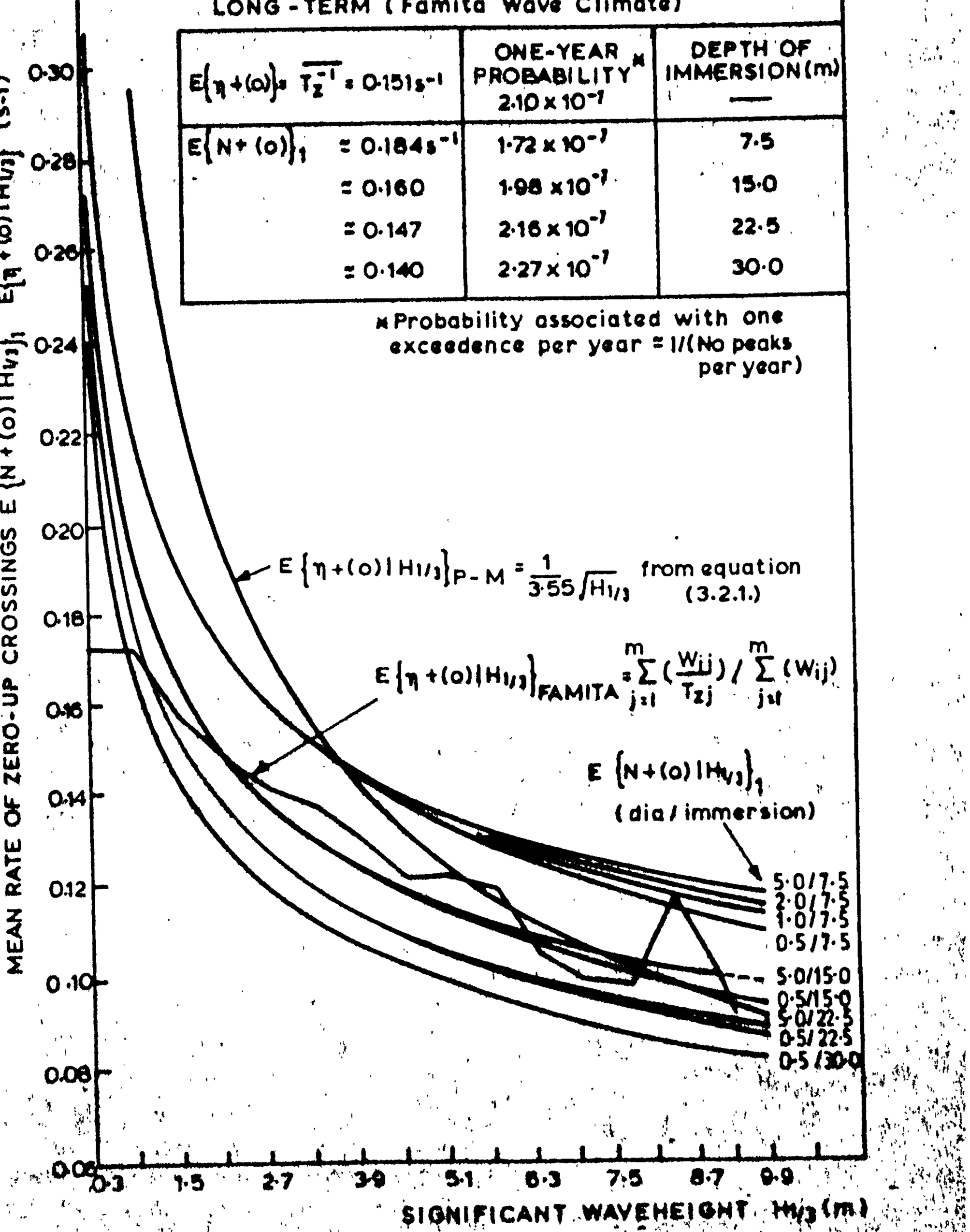

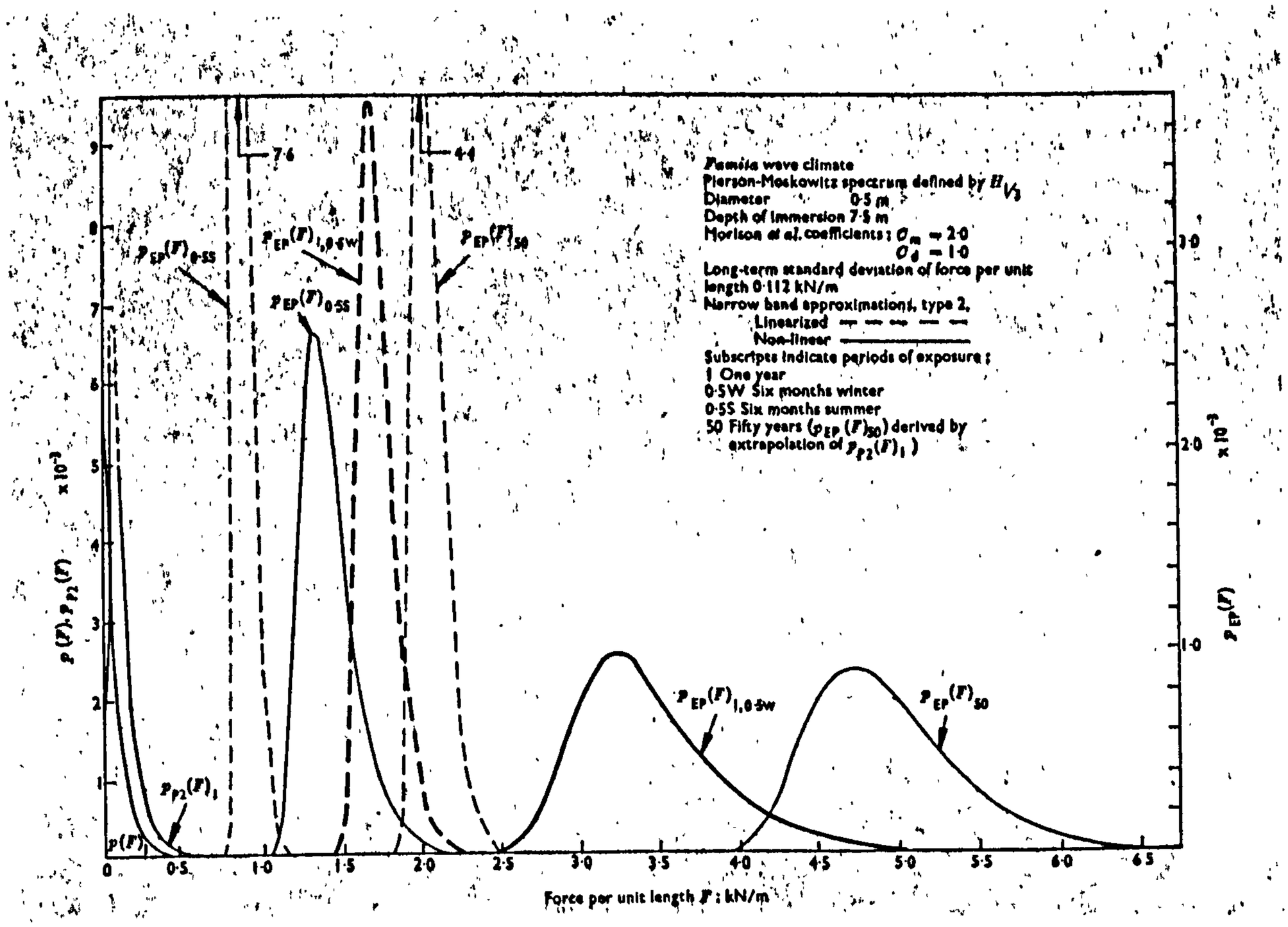

FIG. 3.4.1. LONG-TERM PROBABILITY DENSITY FUNCTIONS OF FORCE $p(F)$. PEAK FORCE $p_{P2}(F)$ AND EXTREME PEAK FORCE $p_{EP}(F)$.

FIG. 3.4.2. PROBABILITY DENSITY FUNCTIONS OF EXTREME PEAK FORCE, CONDITIONAL ON THE SEA STATE INTENSITY (SPECIFIED BY $H_{1/3}$), FOR A PERIOD OF EXPOSURE OF ONE YEAR (FAMITA).

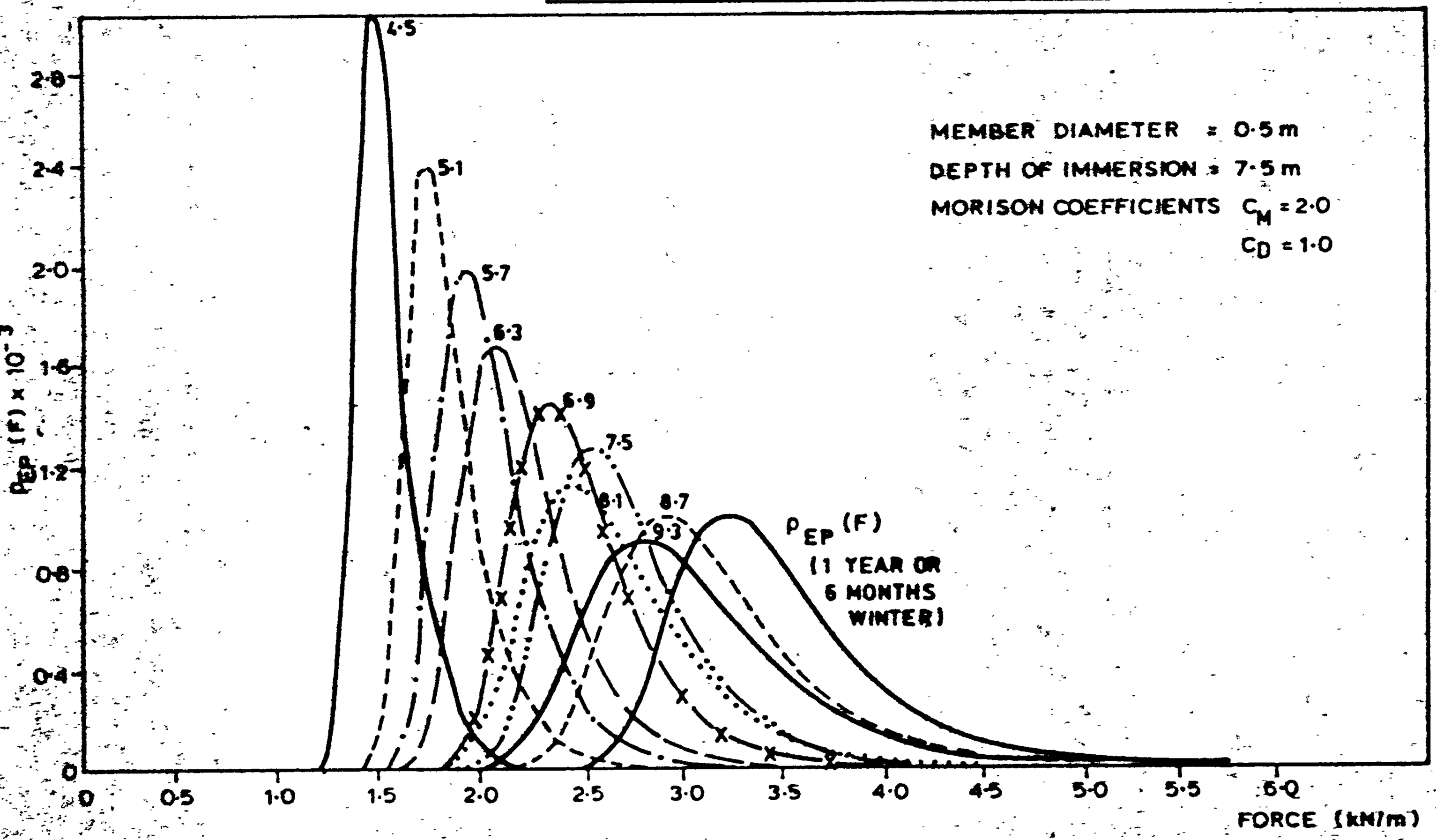

FIG. 3.4.3.
PROBABILITY DISTRIBUTIONS OF EXTREME PEAK FORCE ON 0·5m DIA. MEMBER (UNIT LENGTH) IMMERSED 7·5 m BELOW S.W.L [$C_M = 2{\cdot}0$ $C_D = 1{\cdot}0$] DURING SHORT-TERM STATIONARY CONDITIONS (CONSTANT $H_{1/3}$) FOR ONE YEAR PERIOD OF EXPOSURE AT FAMITA WITH LONG-TERM DISTRIBUTION INCLUDED.

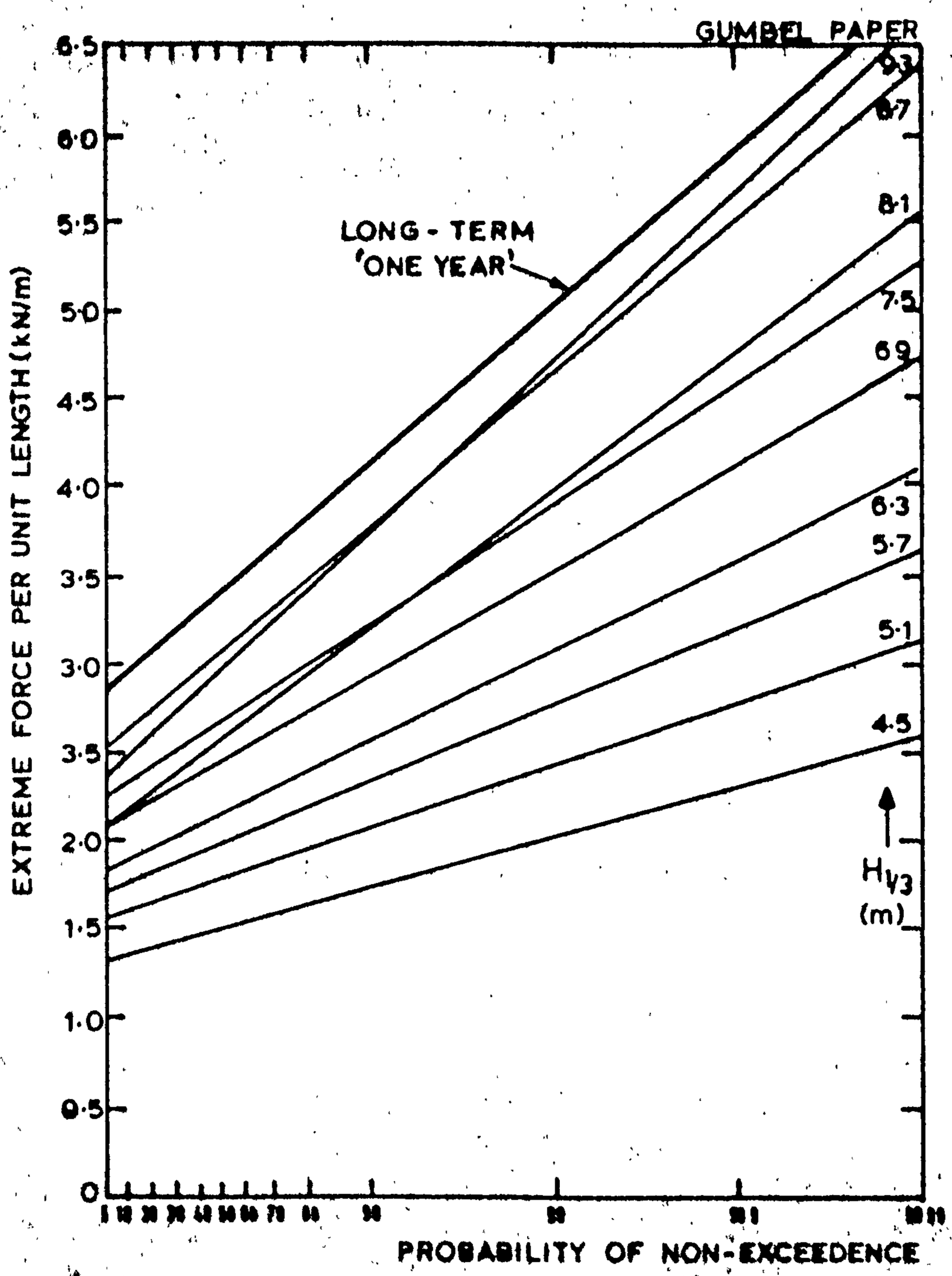

FIG. 3.5.1. SHORT-TERM CDFs OF PEAK FORCE - USING GAUSSIAN-HERMITE QUADRATURE COMPARED WITH THAT OBTAINED BY CONSTANT STEP INTEGRATION OF THE PIERSON-HOLMES PDF.

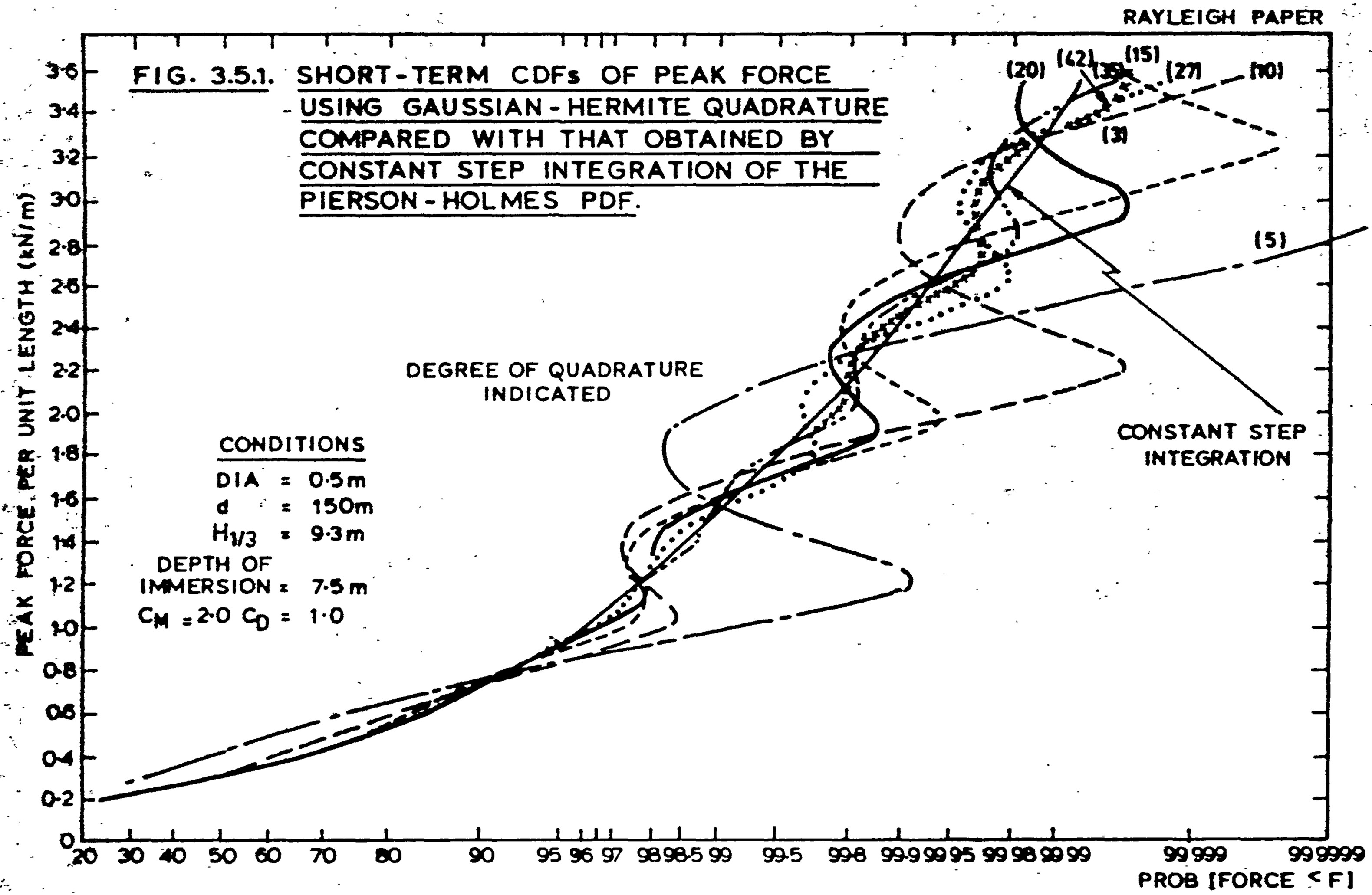

FIG. 3.5.2. VARIATION OF $f(x)$ WITH CHANGE IN FORCE (= $j\sigma_F$) FOR A KURTOSIS OF 5·0

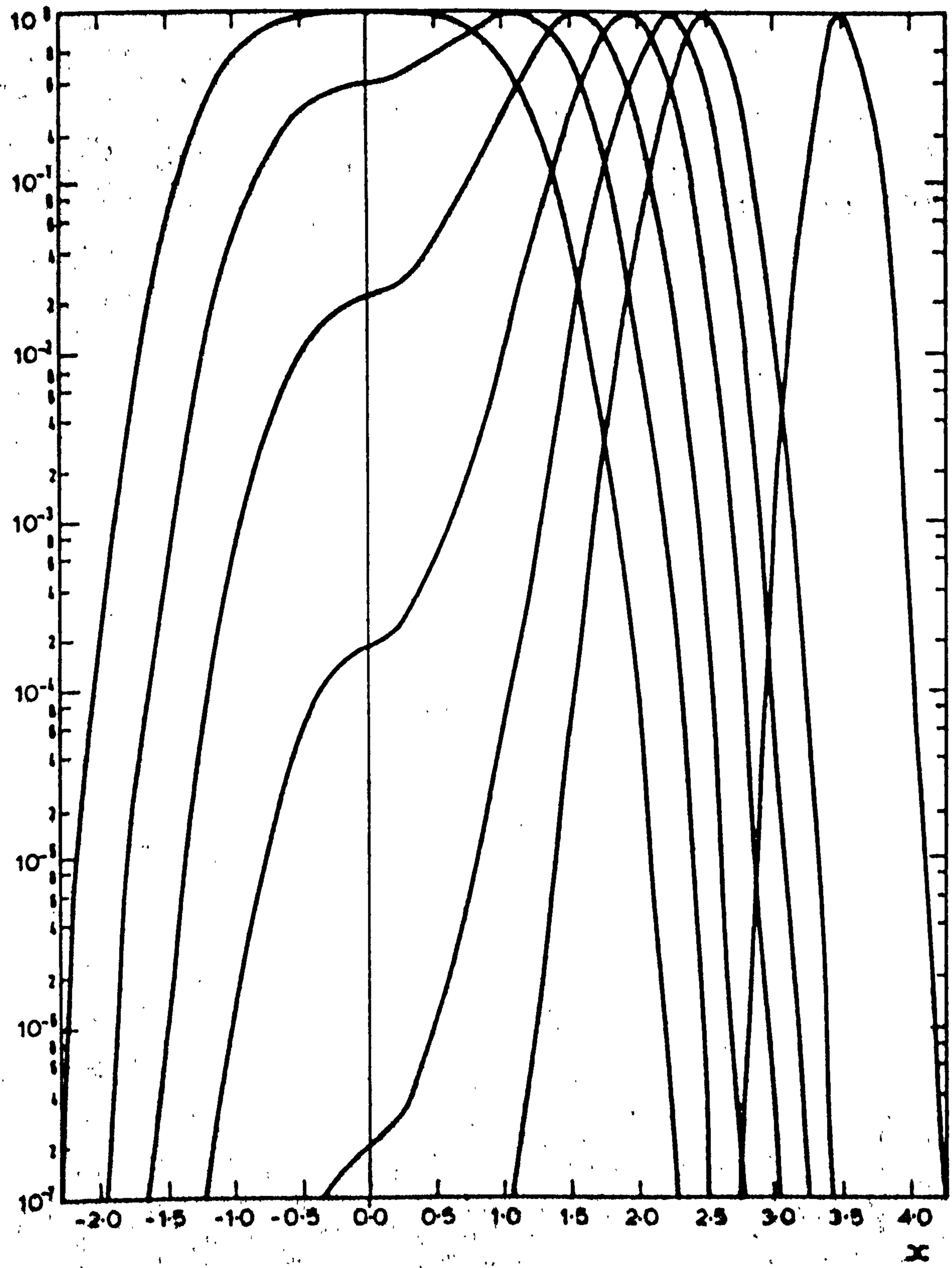

FIG. 3.5.3. LONG-TERM CDF's OF PEAK FORCE USING GAUSSIAN-HERMITE QUADRATURE COMPARED WITH THAT OBTAINED BY CONSTANT STEP INTEGRATION OF THE PIERSON-HOLMES PDF.

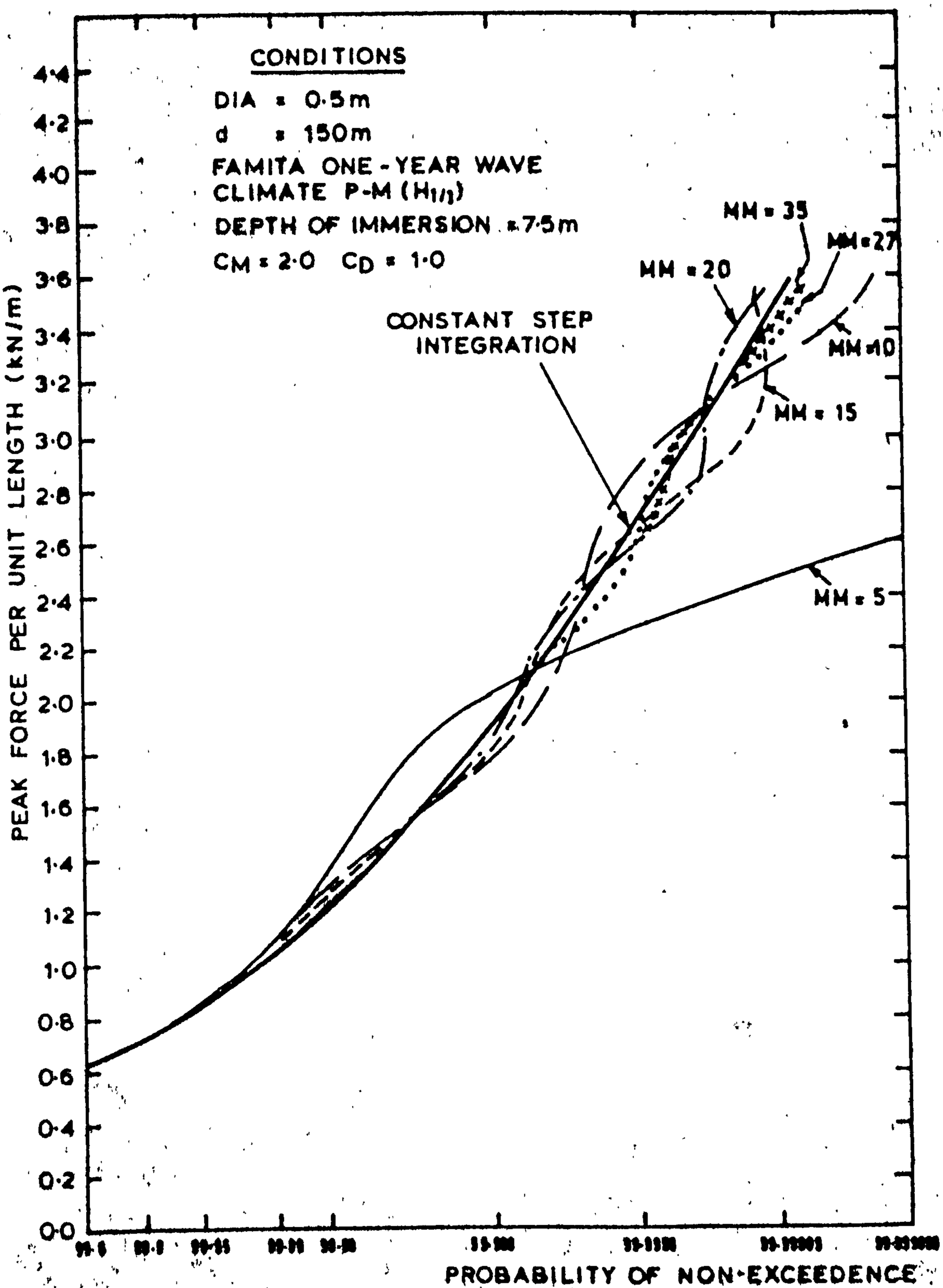

CHAPTER FOUR

THE ROLE OF WAVE CLIMATE IN THE PREDICTION OF LONG-TERM WAVE LOADING

Formulation of the long-term probabilistic descriptions of wave height and the basic and peak variates of wave loading was described in Chapter Two and the techniques have been applied for wave loading in Chapter Three. The long-term distributions result form a convolution of the properties of the stationary, short-term, wave field by the bivariate pdf. of $(H_{1/3}, T_z)$ representing the wave climate, as described by Eqs. (2.3.31), (2.3.63) and (2.3.65).

No theoretical model for the wave climate exists and in real applications the bivariate pdf. of $(H_{1/3}, T_z)$ must be approximated by a histogram of the measured probability structure of these parameters in the form of a scatter diagram. Typically these measurements cover periods rarely in excess of one year and often only covering the most severe period of six Winter months, as described in Section 2.3.2.2 for the Famita data used herein and presented in Fig. 2.3.1.

Accurate assessment of the long-term descriptions of wave height and the induced loading is critically dependent upon the accuracy of the measured sample of wave climate in representing its long-term characteristics.

The objectives of this Chapter are firstly to identify the primary requirements of wave climate data, secondly to describe a method for the extension of the data when the periods covered fall short of the desired requirements and finally to investigate the effects of such extrapolations.

The contents of this Chapter are included in the final OSFLAG 5 report, Reference 11.

4.1 SUPPRESSION OF SEASONAL FLUCTUATIONS IN THE DATA

The primary requirement of the wave climate data, when used as input in procedures for the evaluation of fatigue damage, is that it should cover single, or multiple, complete 12-month periods, to avoid bias resulting from seasonal fluctuations in sea conditions.

In fatigue analyses the accumulative damage is dependent upon the entire range of the distribution of peak loads according to Eq.(2,3.71) and is, therefore, influenced by even the small loads induced by the passage of waves during the generally low intensity sea states present in Summer periods. In fact it may be shown[46] that the major contributions to fatigue damage result from the lower to medium range wave heights, which occur frequently throughout the year. This is in contrast to the investigation of extreme loading, or wave height, necessary for first excursion failure analyses, where lower intensity sea states may be neglected. In this case prediction may be based on data covering only the most severe periods, usually six Winter months.

Two empirical methods of extending seasonally weighted Winter data to simulate conditions covering 'one-year' periods, by the prediction of scatter diagrams for associated Summer periods, have been investigated and a preferred alternative procedure has been developed, as summarised in Appendix III. The results of this latter method are presented in Fig. 2.3.1 which has been used as the basic wave climate input in this and the OSFLAG studies.

The long-term cdf.s of significant and individual wave height developed from the Winter and one-year data sets are plotted on Fig. 4.1, the distribution of $H_{1/3}$ being computed in Table 4.1. Corresponding distributions of wave load are given in Fig. 4.2. Both figures clearly indicate the greater weighting attached to high intensity sea conditions in the Winter data as demonstrated by the increased probability of exceedence of all levels of wave height, or load, from this data.

However, the distributions are not directly comparable. The basic load distribution for the one-year data may be used to predict the proportion of time that a certain load is likely to be equalled or exceeded during any period in excess of one year whereas this application for the Winter data should be restricted to only Winter periods. Although it is easily shown that the time of exceedence estimates for both distributions are the same at high levels of load (at levels never exceeded in corresponding Summer periods), in the middle and lower range the winter data over-estimates times of exceedence if the data is misinterpreted.

4.2 THE NEED TO EXTRAPOLATE WAVE CLIMATE DATA

Estimation of extreme wave heights usually proceeds in the manner developed by Battjes[7] and outlined in Section 2.3.2 where the long-term cdf. of Eq. (2.3.31) is plotted on probability paper for wave climate data covering typically a one-year period. The wave height of design severity, as measured by the required return period or probability of exceedence, is then read off the graph. From the form of Eq. (2.3.65) it is clear that estimation of peak loading can proceed in the same way.

However, there is a fundamental error in applications along these lines since the design condition, which may represent the prediction of the extreme value in 100 years, (as recommended by Det Norske Veritas[29], the Norwegian certifying authority for offshore installations), is extrapolated beyond the duration covered by the wave climate data base. This effect appears to have been overlooked by Battjes and others applying his approach. Pedersen[70] accounted for the discrepancy between the typical scatter diagram sample of wave climate and its true long-term properties, without making specific reference to it, in a technique for long-term wave height prediction. Although Pedersen's approach followed a similar procedure to that of Battjes it failed to account for the necessary transformation from proportions of time to proportion of the number of waves in the scatter diagram weightings, as described in Section 2.3.2.4 and is consequently little used.

The more correct procedure is to extrapolate the wave climate data to cover the complete range of physically feasible sea states, many of which in the extreme range will not have been experienced in the short data sample and which are likely to be assigned incorrect weightings even if observed. The justification for this may be inferred from Eqs. (2.3.31), (2.3.63) and (2.3.65) where the integrals covering the sea state parameters have upper limits of infinity.

There will be a physical limit to the values of $H_{1/3}$ recorded at any location which depends upon the limiting wind speed, and its duration, and the fetch available for the generation of the sea state of extreme severity[30]. Clearly, extrapolation of the wave climate in the $H_{1/3}$ domain beyond such an upper truncation would be meaningless.

In physical terms the original approach, using the available data set only, implies that, in the estimation of extreme conditions during a certain period of exposure covering a number of years, the wave climate is repeated exactly each year. Hence, sea state conditions of greater intensity, and of greater return period, than those measured in the existing data are not accounted for. In contrast the modification, where the data is extrapolated, simulates the presence of these extreme conditions.

In quantitative terms the probability of occurrence of sea state intensities of given return period occurring in a certain period of exposure may be estimated by assuming all sea states to be independent, as follows:

I_{T_r} = sea state intensity of return period T_r
= [function $(H_{1/3}, T_z)$]

Probability that I_{T_r} is equalled or exceeded in one year:

$$\text{Prob}[I_{max} \geq I_{T_r}] = \frac{1}{T_r} \tag{4.1}$$

hence:

$$P_1(I_{T_r}) = \text{Prob}(I_{MAX} < I_{T_r}) = 1 - \frac{1}{T_r} \tag{4.2}$$

and probability that I_{T_r} is not exceeded in L_D years is:

$$P_{L_D}(I_{T_r}) = (1 - \frac{1}{T_r})^{L_D} \tag{4.3}$$

Thus probability that a sea state of intensity I_{T_r} is equalled or exceeded in L_D years is:

$$\text{Prob}_{L_D}(I_{MAX} > I_{T_r}) = 1 - (1 - \frac{1}{T_r})^{L_D} \tag{4.4}$$

This expression is evaluated in Table 4.2 for values of T_r between 1 and 100 years and for durations of 1, 20 and 50 years which shows the probability of occurrence of sea state intensities greater than or equal to I_{T_r} during periods of exposure L_D years.

Relating this information to the prediction of wave height and wave loading from wave climate data it can be seen that L_D = 1 year would correspond to the original procedure applied previously using the basic data. It is evident from Table 4.2 that although there would be a good chance of sea states of return period T_r occurring for example during a 20 year period of exposure (L_D = 20 years), which may be typical for offshore installations, there is generally little chance of these conditions being present in the one year data sample (L_D = 1 year). In contrast, if the data were extrapolated up to, for instance, the equivalent of a 50 year record then there would be a good chance (L_D = 50) that this extrapolated data would account for the presence of all sea conditions likely to be encountered in this 20 year period of exposure.

A one-year scatter diagram data set should not, therefore, be considered to be representative of the long-term wave climate when applied in extreme value analysis of conditions covering periods in excess of one year. Wave conditions omitted by such a procedure would in all probability represent a significant contribution to the convolution of short-term descriptions of wave height and wave load in Eqs. (2.3.31), (2.3.63) and (2.3.65). The effects on the long-term distributions will be pronounced in the extreme regions where omission of the high intensity (high return period) sea states in 'one year' data samples may lead to considerable underestimation of wave heights and wave loads for use in first excursion analyses, as demonstrated for the Famita data later. In contrast the presence of an event of high return period in the data sample can lead to considerable overestimation due to the excessive weighting attached to this event.

In the lower wave height and wave load range of the cdf.s. the effects of the data extrapolation will be less significant, since the data omitted in one-year samples will be the few severe wave conditions whose influence in this range is negligible. Consequently, for fatigue analysis, which has greater dependence upon the lower range of the cdf.s.[46] the effect of wave climate extrapolation will probably be insignificant.

4.3 A METHOD OF WAVE CLIMATE EXTRAPOLATION

Extrapolation of wave data to obtain a reasonable representation of the long-term wave climate requires extension of the scatter diagram. However, the bivariate probability domain of $H_{1/3}$ and T_z is complex and cannot be defined in mathematical terms. In the absence of extensive measurements of the long-term wave climate, the analysis of which might yield such a mathematical description, it is unlikely that attempts at extrapolation in the bivariate domain will be successful.

One practical approach is to consider only the marginal distribution of $H_{1/3}$ in the long-term description of the wave climate together with the corresponding values of the mean rate of zero-crossings obtained from the scatter diagram. Using the notation of Eq.(2.3.28) the mean zero-up-crossing rate associated with significant wave height $H_{1/3i}$ is given by:

$$E\{N_0^+|H_{1/3i}\} = \left(\sum_{j}^{\text{all } T_z} w_{ij}/T_z\right)/W(H_{1/3i}) \tag{4.5}$$

$$\text{where } W(H_{1/3i}) = \sum_{j}^{\text{all } T_z} w_{ij} \tag{4.6}$$

This procedure does not represent a loss of accuracy in the prediction of wave height or peak wave loading when, in developing the statistics of the required parameters of the wave field, the surface elevation spectral form is defined in terms of $H_{1/3}$ only as demonstrated in Chapter Three. This assumption is justified because the most commonly employed spectrum is that of the Pierson-Moskowitz form defined in this way, through Eqs.(2.3.23) and (2.3.24).

In essence the technique of extrapolation is to compare the marginal distribution of $H_{1/3}$, usually in terms of the cumulative histogram from the scatter diagram, with various theoretical probability distributions until a reasonable fit is attained. The distribution of $H_{1/3}$ is then assumed to follow this theoretical distribution from which a discretisation over an extended range of $H_{1/3}$ yields an estimate of the marginal distribution of $H_{1/3}$. The data fitting to theoretical distributions may be performed graphically or mathematically. The former technique entails a plot on probability paper which linearises the theoretical distribution and where the 'best-fit' straight line through the data points, judged by eye, yields the required extension. Mathematical methods involve the estimation of the parameters which define the

theoretical distribution usually performed either by the 'method of moments' or the 'method of least squares'.

The resulting 'fitted' distribution may be discretised into a number of class intervals of the same width as the original data, but covering an increased range, and the probability of occurrence associated with each is then computed. For classes in the extended range of $H_{1/3}$ an estimate of the mean zero-crossing rate is required to provide the correct weightings in the convolution of short-term conditions for prediction of long-term wave height and peak loading. In applications using the Pierson-Moskowitz spectrum, Eqs. (2.3.24) and (2.3.25) may be combined to yield these estimates:

$$E\{N_0^+ | H_{1/3i}\} = \frac{1}{T_z} = \frac{1}{3.55\sqrt{H_{1/3i}}} \qquad (4.7)$$

4.4 ESTIMATION OF THE LONG-TERM DISTRIBUTION OF $H_{1/3}$ FROM MEASUREMENTS COVERING A ONE-YEAR PERIOD AT THE FAMITA LOCATION

From the comments made in Section 4.2 it is clear that measurements of $H_{1/3}$ taken over any finite interval of time are random samples from the complete population of $H_{1/3}$. The objective of this section is, therefore, to estimate the distribution of this population from analysis of the 'one-year' data set. The procedure, as outlined in the previous section, is to assume that the complete population follows a theoretical probability distribution which shows a 'reasonable' fit to the data bearing in mind that the distributions of such short data samples from infinite populations are subject to sampling errors.

4.4.1 A Note on the Interpretation of cdf.s. of $H_{1/3}$ Obtained From the Scatter Diagrams

The Famita scatter diagrams presented in Fig. 2.3.1 indicate the proportion of time for which the values of $H_{1/3}$ and T_z fell within certain classes during the period covered by the measurements. The number of three-hour recordings, representing short-term conditions classified by the mid-class values of $H_{1/3}$ and T_z, are not given by the numbers assigned to each class in the diagrams. The six month winter period covered by the basic data would contain 1456 recordings whereas the total number of occurrences in the winter scatter diagram is 962 and similarly a one year period represents 2920 events not the total of 1924

in the one-year scatter diagram. This consolidation of the data has little effect on the resulting long-term distributions of wave height or wave load as developed previously, but care must be taken in the interpretation of the distribution of $H_{1/3}$ as explained below.

The original Famita recordings were analysed by Draper and Driver[71] and presented as a scatter diagram, included here in Fig. 4.3, with class occurrences as parts per 1000 and crosses representing single recordings which were not retained in the consolidation. The sum of all occurrences in this scatter diagram is 962, neglecting crosses, which indicates that some three-hour recordings were not entered in the scatter diagram since reversing the factorisation on the marginal histogram of $H_{1/3}$ and adding the crosses accounts for only 1427 events. It was stated by Draper and Driver that low intensity sea states (small values of $H_{1/3}$ and T_z) could not be recorded by the instruments and it may, therefore, be inferred that the 29 remaining events may be accounted for in this way as no specific reference was made to other possible causes for omission, such as instrument failure.

A synthetic histogram of $H_{1/3}$ for the 1456 actual measurements may, therefore, be obtained by factoring the marginal histogram of $H_{1/3}$ from Fig. 4.3 by $(\frac{1456}{1000})$, adding the crosses and assuming the missing events to fall within the first class interval ($H_{1/3} < 0.6$m). In this way the cumulative distribution of the three-hour recordings may be plotted as shown in Fig. 4.1, for example:

$$P(H_{1/3} = 31 \text{ ft.} = 9.45\text{m.}) \simeq \frac{1456}{1457} = 0.99931$$

$$P(H_{1/3} = 2 \text{ ft.} = 0.61\text{m.}) \simeq (5 \times \frac{1456}{1000} + 29)/1457 = 0.025$$

The Winter scatter diagram used as the basic input in this study, and in the OSFLAG 5 Project, given in Fig. 2.3.1, is a modification of Fig. 4.3, where a slight redistribution was necessary due to metrication of the diagram and occurrences in each class are assumed to represent parts per 962. This latter simplification ignores single events (crosses) from the original diagram and the missing events and this attaches a slightly increased probability of occurrence to all the classes retained.

From the plots on Fig. 4.1 it is apparent that the modifications have had a negligible effect on the distribution of $H_{1/3}$. However, it must be appreciated that the plots represent three-hourly short-term conditions and the probability of non-exceedence assigned to a significant wave height of one-year return period is approximately $(\frac{1456}{1457})$, according to Eq. (2.3.29) and not $(\frac{962}{963})$.

Similar comments apply to the use of the distribution of $H_{1/3}$ based on the one-year data set of Fig. 2.3.1 where a one-year return period corresponds to a probability of non-exceedence of $(\frac{2920}{2921})$ not $(\frac{1924}{1925})$. Furthermore, an 'n'-year return period is associated with the probability of [1 - 1/2920n].

4.4.2 Graphical Data Fitting using Probability Papers

Probability papers for the Gaussian, log-Gaussian, Rayleigh, Gumbel and Weibull theoretical probability distributions have been constructed according to the procedure outlined in Appendix Two. Each of these distributions has been found from past analyses to reasonably approximate the behaviour of some of the random parameters of the wave field, for example, the surface elevation in the short-term is found to fit the Gaussian distribution quite well and the short-term wave height distribution is approximately Rayleigh distributed. Data which is well approximated by a particular theoretical distribution plots as a straight line on the relevant probability paper.

The long-term distributions of $H_{1/3}$, obtained from the Famita data, are compared with the Rayleigh and Gaussian distributions in Figs. 4.1 and 4.4, respectively. None of the plotted distributions are well approximated by either theoretical distribution as implied by the significant curvature of all plots and measured wave heights in the upper range would exceed those given by a 'best-fitting' straight line through the data plot. It was not anticipated that either of these distributions would provide acceptable fits to the data but the probability plots have been included here for completeness. These probability papers have been used extensively in Chapter Three and comparison of the shapes of the wave height plots, from Figs. 4.1 and 4.4, with those of the other probability paper plots, discussed below, illustrates the differing characteristics of the various theoretical probability distributions.

It has been suggested by Jasper[72] that the logarithm of significant wave height should follow the Gaussian distribution and hence $H_{1/3}$ should plot as a straight line on the log-Gaussian paper. Such a plot is made in Fig. 4.5 which indicates that the inclusion of the logarithmic compression of the wave height scale overcompensates for the 'positive-skewness' exhibited by Fig. 4.4. The result is a negative skewness of the data plot in the upper range for which the theoretical log-Gaussian distribution, as the 'best-fit' straight line, would yield excessive wave height predictions in this range and is, therefore, unacceptable.

The Weibull distribution[73] has been extensively applied[7,70,74,75] to wave data as demonstrated earlier in Fig. 2.3.3 for individual wave height. In this plot the lower limiting value of H, defined by parameter A of the distribution described in Appendix Two and required for the construction of the wave height axis, has been taken as zero and a significant departure of the distribution from a straight line at low wave heights results. This deviation could be removed by the appropriate choice of the value for A. The same comments are applicable to the Weibull plot of $H_{1/3}$ in Fig. 4.6 where the significant departure from the straight line plot is eliminated by the adoption of the lower limiting value $A \simeq 0.37m$, determined graphically. The Weibull distribution given by the best-fit straight line, therefore, yields a satisfactory estimate of the long-term behaviour of significant wave height.

The great disadvantage of the Weibull distribution, when used in analyses based on graphical techniques, is that it compresses large wave heights and gives a more accurate display to the less important lower range data values by virtue of the logarithmic nature of the wave height axis. This effect leads to significant uncertainty in the extraction of wave height/probability information from the probability paper presentation.

A better graphical technique should include a linear wave height scale on the probability paper which gives the same accuracy in plotting to all data points. The Gumbel distribution[58] has this property, as illustrated in Fig. 4.7, and the plot of $H_{1/3}$ shows an extremely good fit to a straight line indicating that the long-term distribution of significant wave height is well approximated by this distribution.

The Gumbel plot forms an ideal basis for the discretisation of the long-term distribution of $H_{1/3}$ into probabilities associated with class intervals. This is demonstrated in Fig. 4.7, the abstracted information being presented in Table 4.3 for an extrapolation of the one-year data to represent conditions of up to '100-year' return period. The limiting value of $H_{1/3}$ is 15.9m. from the Gumbel distribution, obtained as the 'best eye fit' through the data points in Fig. 4.7. The corresponding value from the Weibull plot of Fig. 4.6 is approximately 14.0m. demonstrating that the Gumbel distribution generally predicts wave heights in excess of the Weibull distribution, as confirmed by Saetre[75]. In view of this and the comments made above on the compression of the scales of Weibull plots, the Gumbel distribution is preferred for the description of long-term distributions of significant wave heights for this Famita data.

The Gumbel distribution does not yield a good fit to the distribution of individual wave height, especially in the lower range, as demonstrated by the significant curvature of its plot on Fig. 4.7 and in this case the Weibull distribution may well be preferable.

4.4.3 The Gumbel Fit to $H_{1/3}$ Obtained from the 'Method of Moments'

The Gumbel distribution is a two parameter distribution and is fully defined by the mean and standard deviation, as demonstrated in Appendix Two. The estimates of the mean, $E\{H_{1/3}\}$, and standard deviation, $\sigma_{H_{1/3}}$, for the 'one-year' data set are given in Table 4.1 and have been applied to generate the Gumbel distribution of $H_{1/3}$ given in Table 4.3 and referred to as the 'theoretical' Gumbel distribution which is also plotted on Fig. 4.7.

From the figure it can be seen that the graphical extrapolation of the data obtained by 'eye-fitting' deviates slightly from the 'theoretical' distribution which has a marginally lower slope and predicts a '100-year' significant wave height of 15.6m. compared with 15.9m. from the graphically obtained distribution. In practical terms these differences are likely to be insignificant and either method should be acceptable for the long-term description of significant wave height for this data set. If the method of moments is used it should be stressed that the data must still be plotted on probability paper to confirm that Gumbel fitting is reasonable. The Gumbel fit obtained by the method of moments

is favoured, for reasons which will be discussed in Section 4.4.5, and will be used in all remaining computations.

4.4.4 'Goodness of Fit' of the Gumbel Distribution to $H_{1/3}$

The goodness of fit of the Gumbel distribution to $H_{1/3}$ is further demonstrated, in the probability density histogram plots of Fig. 4.8. The fit is extremely good in the middle range of the data values and the oscillation of the histogram densities in the extreme range of the data, as displayed on the probability plots of the cumulative distributions, is probably the result of sampling variability in the one-year wave climate. Any one-year data set is likely to include extreme conditions which depart from the mean annual wave climate. In this case the extreme condition would appear to represent a return period of less than one-year, since a one-year value of $H_{1/3}$ in excess of 10.2m. is predicted from the Gumbel distributions of Fig. 4.7. However, although the extreme condition, or conditions, in the one-year data set may have a return period slightly less or considerably greater than the period covered by the data measurements, on probability paper this event must correspond to probability of one exceedence per year. The erroneous probabilities which may thus be assigned to the extreme conditions can give rise to distortions in the upper tail of probability paper plots even when the phenomenon under investigation may be known to follow the probability distribution postulated.

In Fig. 4.8, there also appears to be a notable difference in the shape of the density histograms in the lower range of $H_{1/3}$ over the first two class intervals. This is also demonstrated by the application of the 'chi-square goodness of fit test' between the data and the 'theoretical' Gumbel distribution which rejects the fit over the entire $H_{1/3}$ range, as described in Appendix Four. However, over the range of $H_{1/3}$ in excess of 1.2m. the test is satisfied at the 0.05 level of significance which suggests that there is no strong reason to question the hypothesis that $H_{1/3}$ follows the Gumbel distribution over this range. In practical terms the slight deviations over the range of the first two class intervals between the actual distribution of $H_{1/3}$ and the fitted Gumbel distribution will have an insignificant effect on the long-term distributions of wave height or wave load. Consequently the Gumbel distribution may be considered to be satisfactory for the description of $H_{1/3}$ over the entire range of values.

4.4.5 Variations in Annual Wave Climate

The validity of the above procedures for wave climate extrapolation when based on a single year's measurements would be adversely affected by significant variations in annual wave climate.

Saetre[75] has analysed wave measurements covering three successive Winter periods at Famita, including the Winter of 1969-1970 used in this study, and concluded that there is no strong evidence of any significant differences in the extreme wave conditions between the years although his 'Gumbel' plots of $H_{1/3}$, for the three data sets showed notable departures in the extreme range as reproduced here in Fig. 4.9.

The $H_{1/3}$ predictions in Fig. 4.7 are in agreement with those in Saetre's plots for the 1969-1970 data set apart from one data point representing a storm occurrence with $H_{1/3}$ = 12.3m. which was not recorded in the data used here, taken from Draper and Driver[71]. Predictions from Gumbel fits for the one-year data to those obtained by Saetre[75] for the combined three-year data are compared below.

	Return Period	
	10 years	50 years
3-year data: Saetre[15]	14.4m.	16.3m.
1-year data: Graphical 'Gumbel'	13.4m.	15.4m.
Theoretical 'Gumbel'	13.0m.	14.9m.

It is not indicated by Saetre which method of fitting was applied to his Gumbel plots for the generation of the above values and hence no reliable conclusions can be drawn from the above comparisons. The two sets of estimates from the one-year data set demonstrate the variability likely by virtue of the different methods of data fitting. These differences could be exaggerated even further if, in the graphical fitting, the two uppermost data points were neglected, in line with a procedure sometimes applied to account for the uncertainty of the plotting position of these extreme points[76] as discussed earlier. In this way a graphical extrapolation could yield a '10-year' significant wave height of 14.1m. which is much closer to the value quoted by Saetre.

On the basis of Fig. 4.9 it does appear likely that deviations in the predictions of extreme conditions will result from the use of one-year's data. Clearly the uncertainties cannot be assessed from a single year's recordings, which is likely to be the only data available in many practical applications. Reliability in the prediction of long-term distributions of $H_{1/3}$ can only be significantly improved by use of data covering a number of years and every effort should be made to obtain this data before attempting long-term extrapolations. However, whenever possible attempts should be made to assess the typicality of 'short' data sets by performing comparisons between the corresponding wind climate and its long-term behaviour. The results of this exercise may then lead to intuitive adjustments to the distribution of $H_{1/3}$.

The plots in Fig. 4.9 show good agreement in the middle range and only deviate significantly in the extremes as a result of the annual variations in the most severe storm conditions from year to year. Consequently the use of the mathematical techniques of the method of moments, considered here, or 'least squares', for the fitting of the data, which are weighted towards the lower range of data values, would produce less variation in the resulting theoretical Gumbel distributions between the years than graphical fitting, which tends to place more emphasis on the data point in the upper range.

It is, therefore, believed that the effects of annual variations in the extreme sea state conditions on the estimation of the long-term distribution of $H_{1/3}$ will be minimised by fitting the data to the relevant theoretical probability distribution using mathematical methods which are less sensitive to the uncertainties associated with the occurrence of extreme events.

4.4.6 Physical Assessment of the '100-year' Extrapolation of $H_{1/3}$

Before employing an extrapolation of a recorded wave climate as being representative of the long-term climate, steps should be taken to ensure that the extreme conditions are realistic. To this end the fitted distributions of $H_{1/3}$ must be truncated at the physical limit imposed by wind speed, wind duration and fetch limitations. In this study the truncation was initially arbitrarily chosen at the '100-year' value of $H_{1/3} = 15.6$m.

At the Famita location indicated in Fig. 2.3.2 the fetch available for the generation of seas of high intensity is limited to distances between approximately 250 miles and 400 miles for winds in directions other than from the North where the fetch is effectively unlimited. These distances are of sufficient magnitude to discount any likelihood of any directional bias in the wave climate since the vast majority of storm conditions may be generated from any direction.

Employing Bretschneider's empirical curves for wave forecasting[30], a value of $H_{1/3}$ = 15.6m. would require a wind speed of about 29m/s. for a 45 hour duration from the North and greater than 36m/s. for 20 hours from any other direction. On the Beaufort scale[77], the former condition would be described as Force 11, a 'violent storm, very rarely experienced', and the latter would correspond to Force 12, 'hurricane conditions'. From these comments it may be presumed that the extreme condition could feasibly result from storms blowing from any direction, although it is most likely to occur from winds from the North.

In actual recordings at Famita analysed by Saetre[75] a maximum value of $H_{1/3}$ = 12.3m. was observed from only three years of measurements. The storm giving rise to these conditions was from the North-West, over a fetch of approximately 250 miles, having a peak wind speed of 24.2m/s. During the storm, the wind was fairly constant blowing from the North-West and North with an average speed of approximately 20m/s. over a period in excess of 24 hours. On Bretschneider's curves this wave height would require a wind speed of 24m/s. for a 14 hour duration corresponding to hurricane conditions on the Beaufort scale. From this comparison it would appear that for the Famita location Bretschneider's curves predict excessive wind conditions over those actually required for the generation of seas of given $H_{1/3}$ values.

If the extreme sea conditions are fully developed and described by the Pierson-Moskowitz spectrum using Eq.(2.3.23) the value of $H_{1/3}$ associated with the 24.2m/s. recorded wind speed would be 12.4m. compared with the measured value of 12.3m. Similarly the '100-year' sea state of the Pierson-Moskowitz form with $H_{1/3}$ = 15.6m. would require a wind speed of 27m/s. or a Force 10 storm, in a direction where the fetch is sufficient for fully developed conditions to exist. This storm would clearly be feasible under a wind from the North.

In view of the above discussion, the wave climate extrapolation to heights up to $H_{1/3}$ = 15.6m. for Famita is not considered to be physically unrealistic.

4.5 THE EFFECT OF WAVE CLIMATE EXTRAPOLATION ON LONG-TERM DISTRIBUTIONS OF WAVE HEIGHT AND WAVE LOADING

The long-term distributions of wave height and wave load have been derived in the manner outlined in Section 4.3 from the extrapolated probability distributions of $H_{1/3}$ obtained in the previous Section, using programs OS25 and OS26 (see Appendix Six).

In Fig. 4.10 the cdf. of individual wave height, H, derived from Eq. (2.3.31) is plotted for various data sets. The most significant observation to be made is that the distribution obtained from the basic 'one-year' scatter diagram data exhibits a 'negative skewness' in the upper range resulting in a considerable under-estimation of wave heights in this region compared with the predictions based on an estimate of the climate extrapolated to include up to the '100-year' $H_{1/3}$, taken here to represent the complete long-term wave climate. It should be appreciated that the use of one-year data does not necessarily result in under-estimation of wave heights. If, for example, the one-year wave climate included a severe storm with a return period much greater than one-year, then the one-year data would assign too high a probability of occurrence to the sea states present in the storm. The resulting long-term distributions would then exhibit a 'positive skewness' with wave height predictions in excess of those obtained from the extrapolated wave climate as will be illustrated later.

The cdf.s of H derived from both the 100-year graphical and 'theoretical' Gumbel extrapolations of $H_{1/3}$, given in Table 4.3, are plotted as curves (B) and (C), respectively in Fig. 4.10. From the plot it can be seen that in this example the graphical extrapolation predicts slightly more severe conditions, as expected from the comparison of the long-term cdf.s of $H_{1/3}$ in Fig. 4.7. As mentioned earlier, the theoretical extrapolation of wave climate using method of moments is preferred and has been used in the remaining applications. The significance of the choice of short-term zero-crossing rates, $E\{N_0^+|H_{1/3}\}$, to be assigned to each class of $H_{1/3}$ in the data is also reflected in Fig. 4.10. Curves (B) and (C) were based on values from the Pierson-Moskowitz relationship of Eq. (4.7), given in

Table 4.3, over the entire range of classes. However, there is a considerable departure in the lower range of $H_{1/3}$ between these estimates of the zero-crossing rates and those obtained from the scatter diagram (given by Eq. (4.5) and computed in Table 4.1), as illustrated in Fig. 4.11. The differences reflect the departure of some of the actual short-term surface elevation spectra from the Pierson-Moskowitz form as discussed in Chapter Three. The effect on the distribution of H is a slight departure of the cdf.s in the lower range as indicated by the departure between curves (B) and (D).

Curve (D) represents the '100-year' theoretical Gumbel distribution for $H_{1/3}$ with zero-crossing rates obtained from the data for classes within the range of the one-year data and the Pierson-Moskowitz relationship for the remaining classes. In this case in the lower range the cdf. follows that obtained from the one-year data set, curve (A), and slightly higher values of wave height than curves (B) and (C), are predicted at given probability levels over the entire range.

Curve (D) does not, however, represent a more severe condition for extreme value estimates than curves (B) and (C) since probability levels are not directly comparable. Plots (B) and (C), using the Pierson-Moskowitz relationship, correspond to a long-term mean zero-upcrossing rate, $\overline{T_z^{-1}}$, of approximately 0.22 cycles per second whilst curves (A) and (B) which use the actual scatter diagram values correspond to a value of 0.151 cycles per second which results in the differences between the 'return-period' scales indicated on Fig. 4.10. Consequently, wave height of a certain return period for curve (B) exceed those of curve (D).

In view of the departure in $\overline{T_z^{-1}}$ the short-term zero-upcrossings from the scatter diagram, obtained using Eq. (4.5), should be included in the description of the extrapolated wave climate. To preserve the trend where $E\{N_0^+|H_{1/3}\}$ decreases with increase in $H_{1/3}$, as seen from Fig. 4.11 for this particular application, data values from Eq. (4.5) have only been used up to $H_{1/3}$ = 5.7m, with Eq. (4.7) used for all other class values, in the remaining computations. This procedure is favoured since it has negligible effect on the long-term cdf. of H which still follows curve (D) and $\overline{T_z^{-1}}$ is unaffected, the long-term zero-crossing rate being relatively insensitive to changes in the zero-crossing rates of short-term conditions with only low probabilities of occurrence.

Another advantage of this approach is that it excludes the data estimates which correspond to only a small number of occurrences in the scatter diagram and which are, therefore, likely to be subject to sampling errors, as may be implied by the oscillation of $E\{N_0^+|H_{1/3}\}$ in Fig. 4.11 over the range $H_{1/3}$ = 6.3m. - 9.3m. An alternative procedure would be to fit a smooth curve between the points from the scatter diagram up to $H_{1/3}$ = 5.7m. with a smooth transition onto the Pierson-Moskowitz curve as shown dotted on Fig. 4.11. Such a procedure may well represent a better description of the short-term zero-crossing rates but, by analogy to the comments made above, the resulting minor modifications will have a negligible effect on the long-term distributions or zero-upcrossing rate and it has not, therefore, been considered here.

The long-term cdf.s of basic and peak loading for the data sets of Fig. 4.10 have been investigated for a 'drag-dominated' 0.5m. diameter vertical member of unit length immersed 7.5m. below still-water-level. The results are not included here as they showed similar characteristics to those observed for individual wave height, although exhibiting less significant deviations in the lower range. Furthermore, the distributions of basic force are independent of, and hence unaffected by changes to, short-term zero-upcrossing rates. Inertia dominated loading cases have not been considered because short-term loading of this form is Gaussian distributed with its peak variate following the Rayleigh distribution. Hence, the peak loading and individual wave height have the same probability structure in the short-term and, therefore, possess similar characteristics in the long-term.

Figs. 4.12 and 4.13 illustrate how the tails of the cdf.s $P_p(F)$ and $P(H)$ are critically dependent on the extreme values of $H_{1/3}$, with associated weightings, $W(H_{1/3})$, present in the data sets. Curve 1 represents the original scatter diagram representation of the wave climate. From Fig. 4.7 it is apparent that this one-year sample contains no extreme sea states ($H_{1/3}$) with return periods greater than one year. Accounting for these extreme states by extrapolating the wave climate ($H_{1/3}$) to simulate conditions of up to 100-year return period using the Gumbel fit by method of moments from Fig. 4.7, produces curves 2 to 6 (where curve 2 uses $H_{1/3}$ classes up to 15.6m. which has return period of 100.7 years, similarly curves 3, 4 and 5 incorporate classes up to 13.8, 12.0 and 10.2m. with return periods of 20.2, 4.0 and 0.8 years, respectively). The effect produced by increasing the length of the extrapolated data set

clearly demonstrates the sensitivity of the tail of long-term distributions to the short-term distributions associated with the sea states of high return period which are likely to be absent from short climate samples.

The trend of these curves with respect to the duration covered by the wave-climate extrapolation suggests that the '100-year' extrapolation may well represent an effective saturation condition adequate for design purposes when typical design lifetimes are only of the order of 20 to 30 years. Using Fig. 4.13 it is seen that the use of the raw wave climate data set would underestimate the 'one-year' wave load (predicted from the 'complete' wave climate description assumed to be represented by the 100-year extrapolation) by 9% and the underestimate would increase to 22% for the '100-year prediction. It was demonstrated earlier that the presence of a range of extreme sea states ($H_{1/3}$), of return period greater than the data collection period, is unlikely in any single wave climate sample and even if present the associated weightings will be incorrect. In the absence of these extreme conditions in the data set underestimates of wave load magnitudes are seen to result from use of the raw wave data. However, if rare storm events were contained in this short record then, due to the incorrect weightings applied to them, wave loads could be overestimated from a raw data set.

This is illustrated by curves 7 and 8 in Figs. 4.12 and 4.13 where the one-year wave climate (associated with curve 5) is enhanced by the presence of a single three-hour observation of the '100-year' sea state for curve 7, and a hypothetical '100-year' storm sketched in Fig.4.14 for curve 8. Since each observation is associated with a probability of occurrence of 1/2920 the weighting, $W(H_{1/3})$, applied to the extreme value of $H_{1/3}$ will be 0.00034 in the 'one-year' sample whilst in the complete population ('100-year Gumbel distribution) its weighting is approximately 0.000003, see Table 4.3. In other words, the weighting applied to the conditional distribution, $P(F|H_{1/3} = 15.3m.)$ would be almost two orders of magnitude greater than it should be. Consequently, wave height and loads far in excess of the correct values are predicted. Uncertainties in load prediction possibly in excess of the differences between values from curves 1 and 7 must, therefore, be expected when using short (single year) samples of wave climate, without extrapolation, in extreme value analysis.

Although it is inevitable that the higher intensity sea state occurrences will vary considerably from year to year, the extrapolation based on 'moments-fitting' of the $H_{1/3}$ data histogram to a theoretical probability distribution may not depart markedly from the correct long-term distribution as illustrated in Fig. 4.14. In the Figure a range of hypothetical short (one-year) samples of the distribution of $H_{1/3}$ are considered: the 'one-year' Gumbel climate; plus its enhancement associated with the presence of the '100-year' $H_{1/3}$ and the '100-year' storm, considered in Fig. 4.13, and a Gumbel wave climate which includes only values of $H_{1/3}$ up to 6.6m. These may thus be considered to represent 'average', 'high intensity sea state biased' and 'low intensity sea state biased' climates respectively. For all these conditions, the fitted distributions of $H_{1/3}$ are very close to the '100-year' parent distribution, sufficiently close that the effect on the long-term wave load (or wave height) distributions will be of secondary importance in comparison with the other uncertainties in the procedures. However, it must be appreciated that if the wave climate variability from sample to sample is not restricted to the extreme sea states (if the distribution, $P(H_{1/3})$, is not consistent from sample to sample for the lower and middle range of $H_{1/3}$ values), then the length of the wave climate record is too short and high degrees of uncertainty in predictions are inevitable, as discussed earlier.

It is interesting to compare wave height estimates obtained by wave climate extrapolation along the lines described here, with other techniques of extreme value prediction. From Fig. 4.12 the '50-year' wave height from the extrapolated wave climate is 28.5m. compared with 23.1m. from use of the one-year data. The most common method of wave height prediction appears to be to plot the distribution of H for the one-year data on Weibull paper, as plotted for the Famita data on Fig. 2.3.3. The plot is usually truncated at the 'one-year' return period and the remaining tail only is either fitted by eye to a straight line for extrapolation or, alternatively, the entire curve is fitted by eye with adjustment of parameter A in the Weibull distribution to straighten the plot. Consequently, as a result of the logarithmic compression of the wave height scale, the abstracted values are highly subjective. For example, from Fig. 2.3.3, the '50-year' wave could lie anywhere within the range 26m. to 28m. Using this technique for the winter data set only Draper and Driver[71] predict a value of 27.4m.

It is also interesting to note that the '100-year' wave, which forms the basis for design recommended by Det Norske Veritas[39] is 30m. from Fig. 4.12. If this wave is assumed to occur during the stationary three-hour sea state of '100-year' severity characterised by $H_{1/3}$ = 15.6m. then the most probable maximum wave, which then corresponds to the '100-year' wave, may be predicted using the relationship derived by Longuet-Higgins[39], which follows from Eq. (2.3.17):

$$H_{max} = H_{1/3} \left[\frac{\ell_n N}{2}\right]^{1/2} \tag{4.8}$$

where N is the number of waves.

Using the zero-uperossing rate from Eq. (4.7) to determine N, the wave height for the Famita location is predicted as 28.4m.

The difference between these two estimates results from the fact that the latter method is unable to account for the possibility that the '100-year' wave may be experienced in a less intense condition than the '100-year' sea state, which might occur for periods well in excess of three hours.

4.6 LIMITATIONS OF THE WAVE CLIMATE EXTRAPOLATION TECHNIQUES

The main objective of this Chapter has béen to reduce the sampling variability associated with wave climate measurements covering typically a one-year period in approximating the characteristics of the long-term wave climate.

The procedures proposed here are based on the scatter diagram representation of wave climate description since this is the form most often available to the designer. As a consequence of this form of wave climate presentation, the sequential variations in sea state intensity are not preserved which prevents extreme wave height or wave load prediction based on storm models[74,75].

In the interpretation of the long-term cdf.s of Figs. 4.10, 4.12 and 4.13 no account has been made for the grouping of large waves, a phenomenon which is often observed in reality. It has been assumed here that if n waves, or load cycles, occur per year then the T-year return period corresponds to a probability of non-exceedence of $(1 - \frac{1}{Tn})$. Although

this is correct over a long-term average, Nolte[74] has pointed out that the average interval between occurrences of amplitude associated with the T-year return period will be greater than T-years because large waves tend to group together in time. For example, if a 'T-year' wave height is exceeded twice in a single storm then the time interval between occurrences must be 2T, thus representing the corrected 'true' return period for this wave height.

The effect of this modification has been shown to be significant when considering wave heights at low return periods, its effect diminishing at the higher return periods most often of interest in structural design. For example, a reduction of 10% on wave heights considered herein might be inferred from Nolte's results at the one-year level reducing to approximately 2% at a 50-year return period. Similar reductions would also be applicable for the peak load distribution but in view of their magnitude in the region of interest in extreme value analyses, the effects of grouping may be considered to be of second order of importance.

The techniques applied herein are strictly applicable to locations which suffer from no directional bias in wave generation where the most extreme wave conditions may result from winds in any direction. For coastal locations where wave generation may be severely restricted by fetch limitations it is essential that the wave climate description includes wind direction in addition to recordings of significant wave height and mean zero-upcrossing period. The above techniques could then be applied to discrete classes of wind direction, the fitted distributions of $H_{1/3}$ being truncated according to the constraints imposed by the fetch available in each direction. The resulting long-term directional distributions of wave height or wave load could be convoluted according to the probability of occurrence of each wind direction band to yield the complete long-term descriptions.

T A B L E 4. . 1

PROBABILITY DISTRIBUTIONS OF $H_{1/3}$ FROM FAMITA SCATTER DIAGRAMS

$H_{1/3}$		'One Year' Data					Winter Data	
Upper Limit (u)	Mid-Class (m)	$E\{N_o^+ \mid H_{1/3}\}$	$W(H_{1/3}{}^m)$	$p(H_{1/3}{}^m)\Delta H_{1/3}$	$P(H_{1/3}{}^u)$		$W(H_{1/3}{}^m)$	$P(H_{1/3}{}^u)$
0.6	0.3	0.1738	96	0.04990	0.0499		5	0.0052
1.2	0.9	0.1734	402	0.20894	0.2587		104	0.1132
1.8	1.5	0.1578	389	0.20218	0.4608		172	0.2918
2.4	2.1	0.1487	321	0.16684	0.6275		152	0.4496
3.0	2.7	0.1419	245	0.12734	0.7548		133	0.5877
3.6	3.3	0.1381	161	0.08368	0.8384		117	0.7092
4.2	3.9	0.1312	132	0.06861	0.9070		111	0.8245
4.8	4.5	0.1224	70	0.03638	0.9434		63	0.8899
5.4	5.1	0.1223	46	0.02391	0.9673		43	0.9346
6.0	5.7	0.1192	23	0.01195	0.9792		23	0.9585
6.6	6.3	0.1051	12	0.00624	0.9855		12	0.9709
7.2	6.9	0.1000	11	0.00572	0.9912		11	0.9823
7.8	7.5	0.09899	8	0.00416	0.9953		8	0.9907
8.4	8.1	0.1177	2	0.00104	0.9964		2	0.9927
9.0	8.7	0.1003	4	0.00208	0.9984		4	0.9969
9.6	9.3	0.07407	2	0.00104	0.9995		2	0.9990
			Σ=1924	*$E\{H_{1/3}\}$=2.2441m; $\sigma_{H_{1/3}}$=1.4240m			Σ962	
$\Delta H_{1/3}$ = 0.6m.	Mean-zero crossing rate Eq. (4.5)	Number of occurrences in class Eq. (4.6)	Probability density histogram values $\frac{W(H_{1/3}{}^m)}{\Sigma}$	Cumulative probability histogram values (Eq. 2.3.29)			Number of occurrences in class Eq. (4.6)	Cumulative probability histogram values

$$*E\{H_{1/3}\} = \sum_{\text{all classes}} H_{1/3}{}^m \, p(H_{1/3}{}^m) \, \Delta H_{1/3}$$

$$E\{H_{1/3}^2\} = \sum_{\text{all classes}} H_{1/3}^2{}^m \, p(H_{1/3}{}^m) \, \Delta H_{1/3}$$

$$\sigma_{H_{1/3}} = E\{H_{1/3}{}^2\} - (E\{H_{1/3}\})^2$$

T A B L E 4 . 2

PROBABILITIES OF EXTREME CONDITIONS, OF RETURN PERIOD GREATER OR EQUAL TO T_r YEARS, OCCURRING DURING AN L_D YEAR PERIOD

Return Period T_r (Years)	Period L_D (Years)		
	1	20	50
1	1.0	1.0	1.0
2	0.5	0.999999	1.0
5	0.2	0.9885	0.999986
10	0.1	0.878	0.9948
20	0.05	0.6415	0.923
50	0.02	0.3324	0.636
100	0.01	0.1821	0.395

TABLE 4.3 LONG-TERM PROBABILITY DISTRIBUTION OF $H_{1/3}$ OBTAINED BY EXTRAPOLATION OF ONE-YEAR DATA

$H_{1/3}$			'100-Year' Extrapolation†				20 Yr. Extrap.†	4 Yr. Extrap.†	1 Yr. Extrap.†	Data Range
Upper Limit (u)	Mid Class (m)	$E\{N_o^+ \mid H_{1/3}\}$	Gumbel (Graphical Fit)		Gumbel (Theoretical Fit)		Gumbel (Theoretical Fit)			
			$P(H_{1/3}u)$	$p(H_{1/3}m)\Delta H$	$P(H_{1/3}u)$	$p(H_{1/3}m)\Delta H$	$p(H_{1/3}m)\Delta H_{1/3}$			
0.6	0.3	0.514	0.07	0.07	0.085	0.085	0.085	0.085	0.085	0.085
1.2	0.9	0.297	0.22	0.15	0.237	0.152	0.152	0.152	0.152	0.1521*
1.8	1.5	0.230	0.40	0.18	0.433	0.196	0.196	0.196	0.1962*	0.1963*
2.4	2.1	0.194	0.59	0.19	0.614	0.181	0.181	0.181	0.1812*	0.1813*
3.0	2.7	0.171	0.72	0.13	0.753	0.139	0.139	0.139	0.139	0.139
3.6	3.3	0.155	0.83	0.11	0.847	0.094	0.09401*	0.09404*	0.09403*	0.09404*
4.2	3.9	0.143	0.895	0.065	0.908	0.061	0.061	0.06103*	0.061	0.061
4.8	4.5	0.133	0.936	0.041	0.945	0.037	0.037	0.03701*	0.037	0.037
5.4	5.1	0.125	0.962	0.026	0.968	0.023	0.023	0.023	0.023	0.023
6.0	5.7	0.118	0.978	0.016	0.981	0.013	0.013	0.013	0.013	0.013
6.6	6.3	0.112	0.987	0.009003*	0.990	0.009003*	0.009005*	0.009004*	0.0090	0.0090
7.2	6.9	0.107	0.9920	0.005002*	0.9936	0.0036	0.003601*	0.003601*	0.0036	0.0036
7.8	7.5	0.103	0.9953	0.0033	0.9962	0.0026	0.002601*	0.002601*	0.0026	0.0026
8.4	8.1	0.0990	0.9973	0.0020	0.9978	0.0016	0.0016	0.0016	0.0016	0.0016
9.0	8.7	0.0955	0.9984	0.0011	0.9987	0.0009004*	0.0009	0.0009	0.0009	0.0009
9.6	9.3	0.0923	0.99908	0.00068	0.99926	0.00056	0.00056	0.00056	0.00056	0.00056
10.2	9.9	0.0895	0.99945	0.00037	0.99957	0.00031	0.00031	0.00031	0.00031	
10.8	10.5	0.0870	0.99968	0.00023	0.99975	0.00018	0.00018	0.00018		
11.4	11.1	0.0845	0.999805	0.000125	0.99985	0.00010	0.00010	0.00010		
12.0	11.7	0.0824	0.99988	0.000075	0.999914	0.000064	0.000064	0.000064		
12.6	12.3	0.0803	0.999933	0.000053	0.999950	0.000036	0.000036			
13.2	12.9	0.0784	0.999960	0.000027	0.999971	0.000021	0.000021			
13.8	13.5	0.0767	0.999976	0.000016	0.999983	0.000012	0.000012			
14.4	14.1	0.0750	0.999986	0.000010	0.9999901	0.0000071				
15.0	14.7	0.0735	0.999992	0.000006	0.9999942	0.0000041				
15.6	15.3	0.0720	0.999995	0.000003	0.9999966	0.0000024				
$\Delta H_{1/3}$=0.6m.		(A)	(B)	Σ = 1.0	(C)	Σ = 1.0	Σ = 1.0	Σ = 1.0	Σ = 1.0	Σ = 1.0

Continued .....

T A B L E 4 . 3

(Continued)

Notes

(A) Estimate of mean-zero crossing rate using Eq. (4.7)

(B) Cumulative probability values read off Fig. (4.7)

(C) Cumulative probability values calculated using $E\{H_{1/3}\}$ and $\sigma_{H_{1/3}}$ from Table (4.1) in Eq. (II.4), Appendix II.

* Figures underlined are slight adjustments to probability values to ensure summation to unity when numbers are written to four significant figures, as required in numerical routines, with negligible effect on the probability distributions.

† Approximate return periods associated with upper limit of largest class of $H_{1/3}$ in extrapolation using theoretical Gumbel distribution [15.6m ≡ 100.73 yrs; 13.8m ≡ 20.15 yrs; 12.0m ≡ 3.98 yrs; 10.2m ≡ 0.80 yrs]

FIG. 4.1. DISTRIBUTIONS OF SIGNIFICANT & INDIVIDUAL WAVE HEIGHTS FROM FAMITA DATA ON RAYLEIGH PAPER.

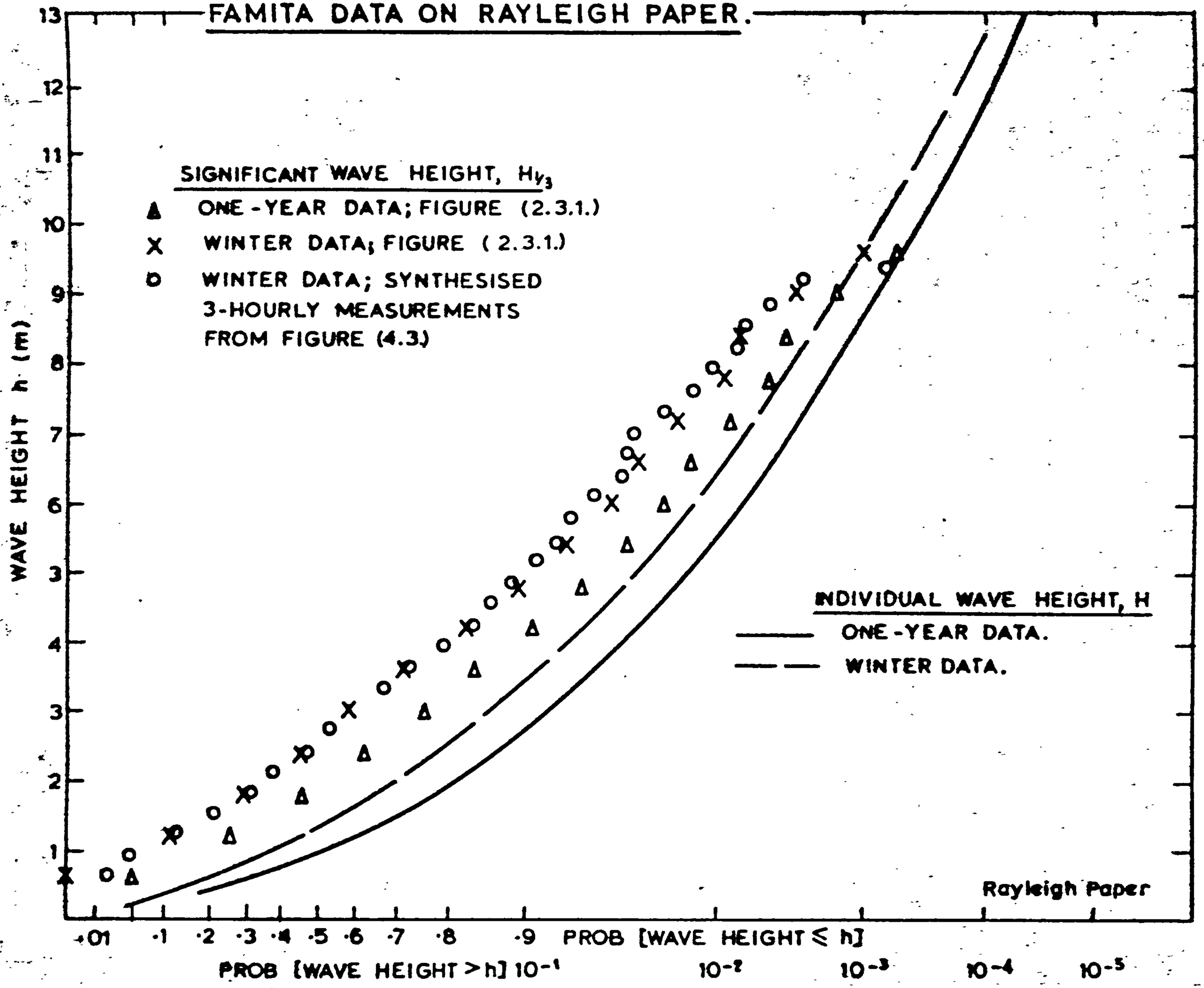

FIG. 4.2. COMPARISON OF LONG-TERM DISTRIBUTIONS OF WAVE LOAD, FOR THE CONDITIONS INDICATED, DEVELOPED FROM THE 'SIX-MONTH WINTER' AND 'ONE-YEAR' FAMITA SCATTER DIAGRAMS.

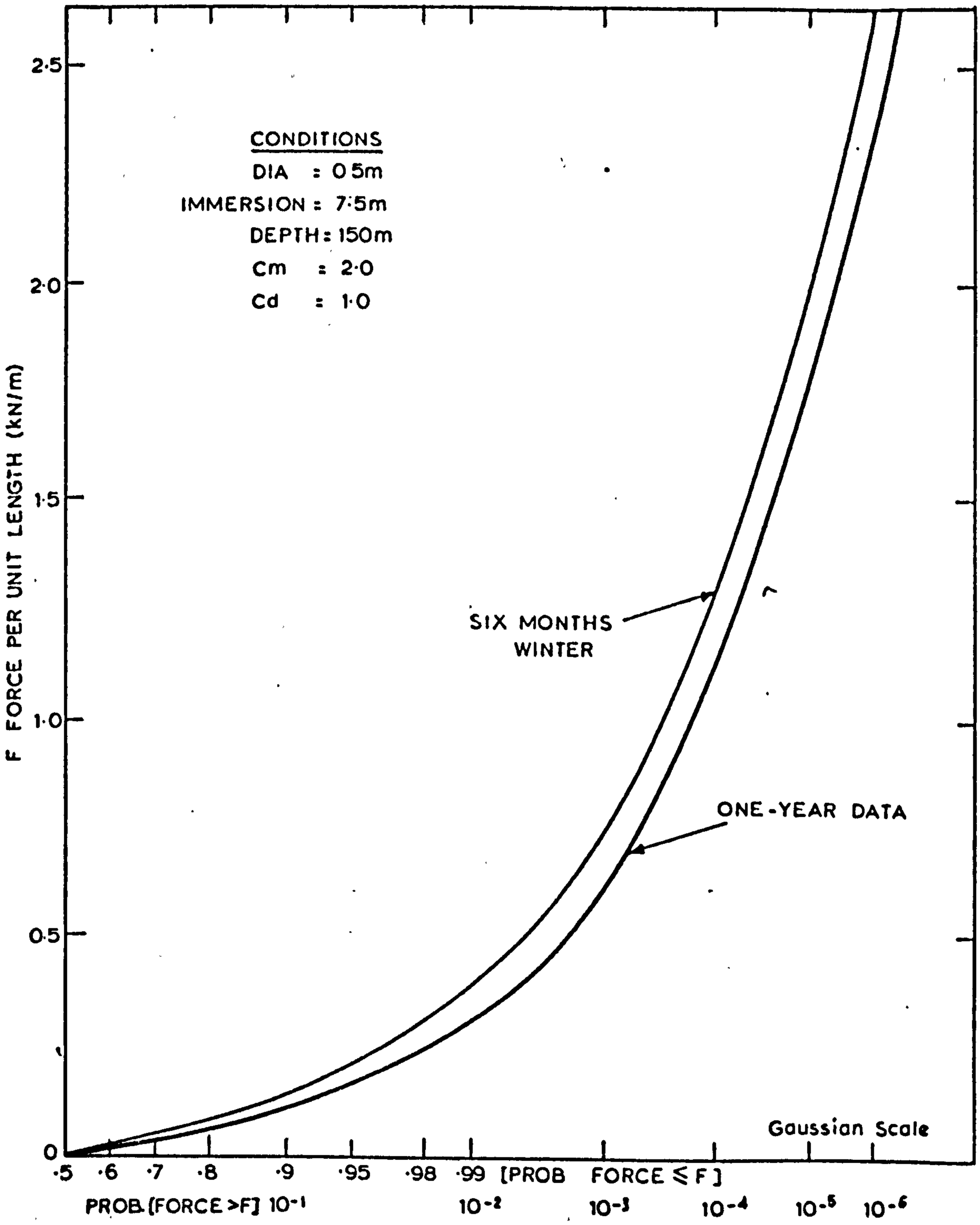

FIG. 4.3. FAMITA WINTER SCATTER DIAGRAM FROM DRAPER AND DRIVER.[71]

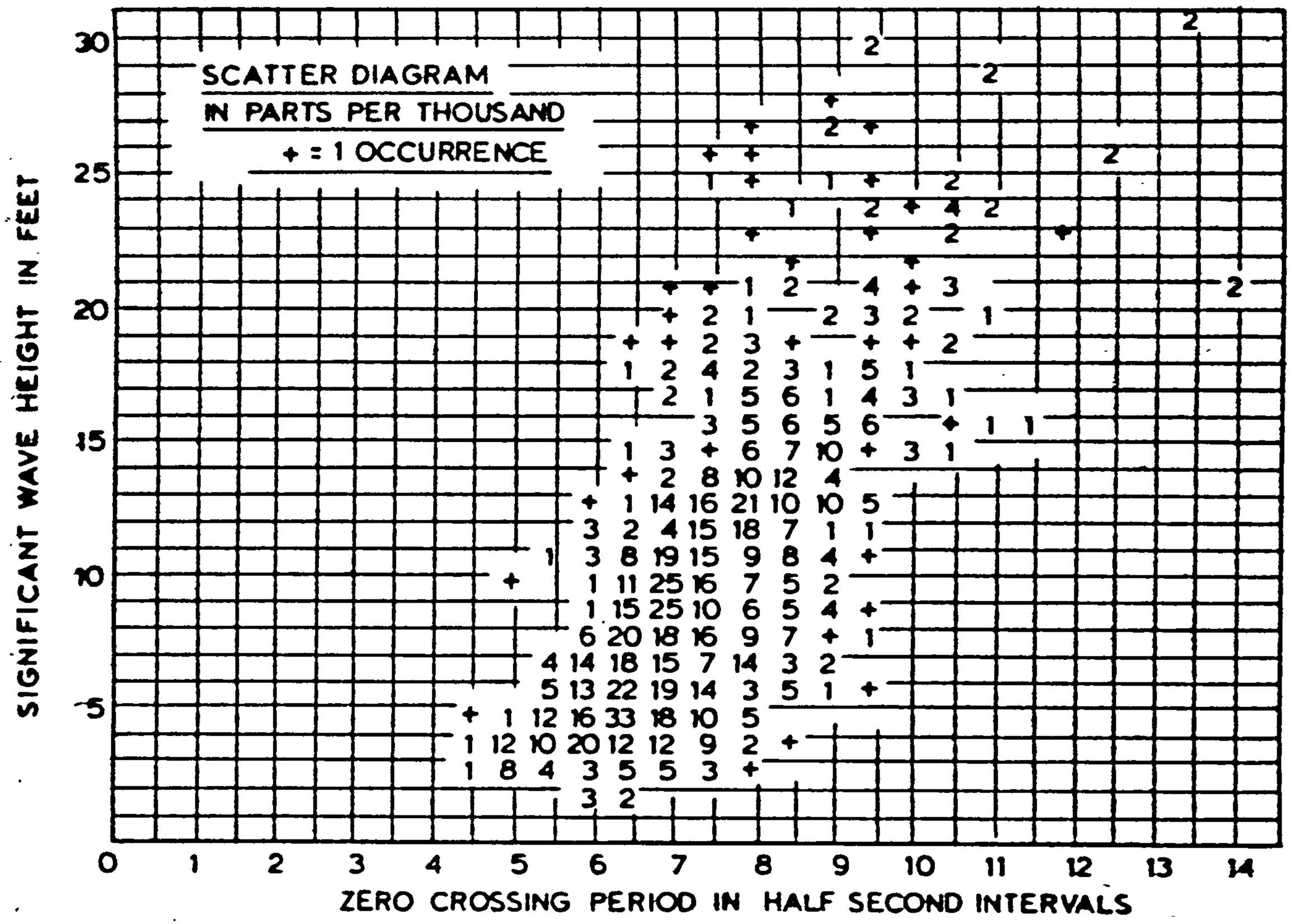

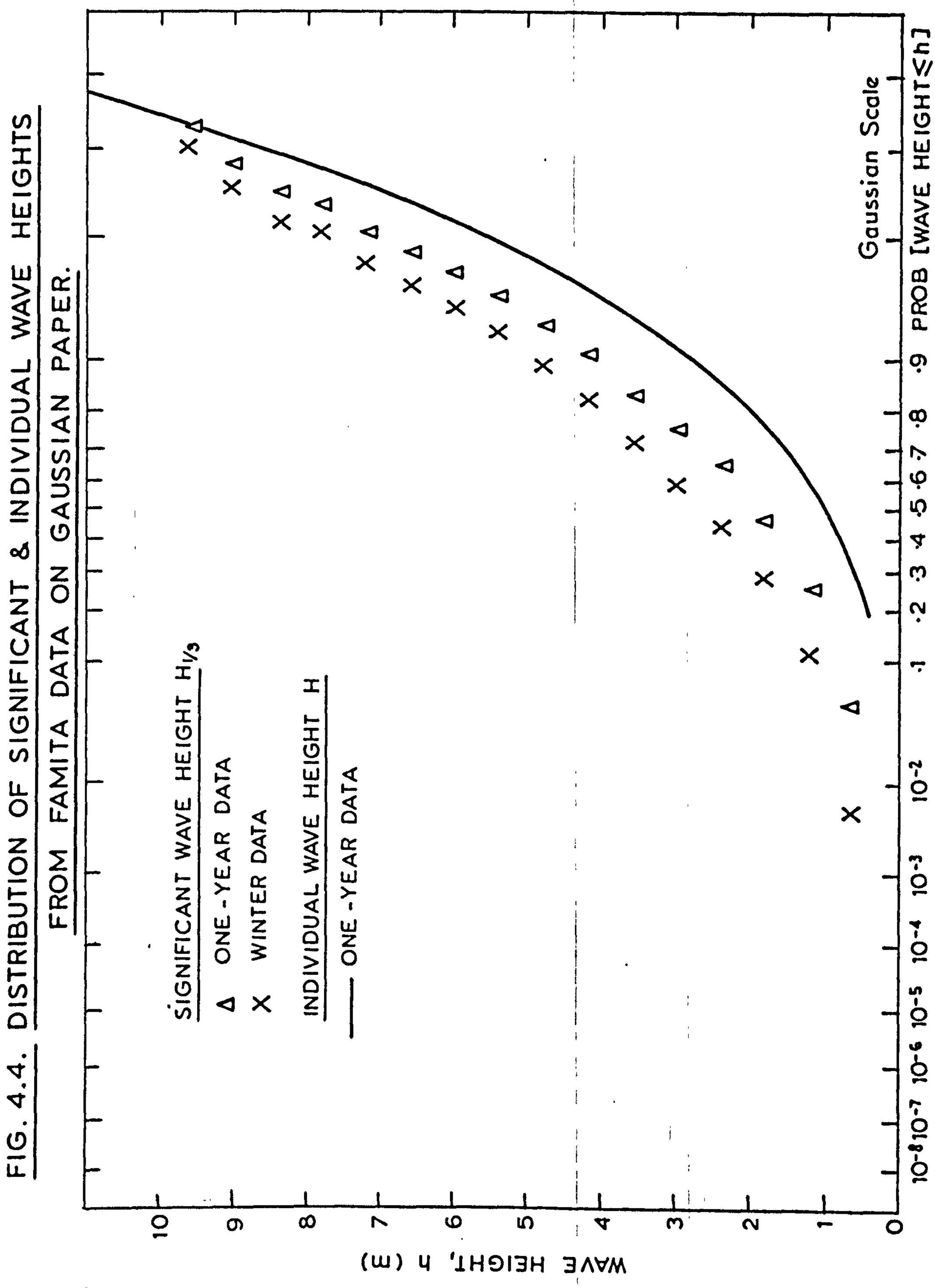

FIG. 4.4. DISTRIBUTION OF SIGNIFICANT & INDIVIDUAL WAVE HEIGHTS FROM FAMITA DATA ON GAUSSIAN PAPER.

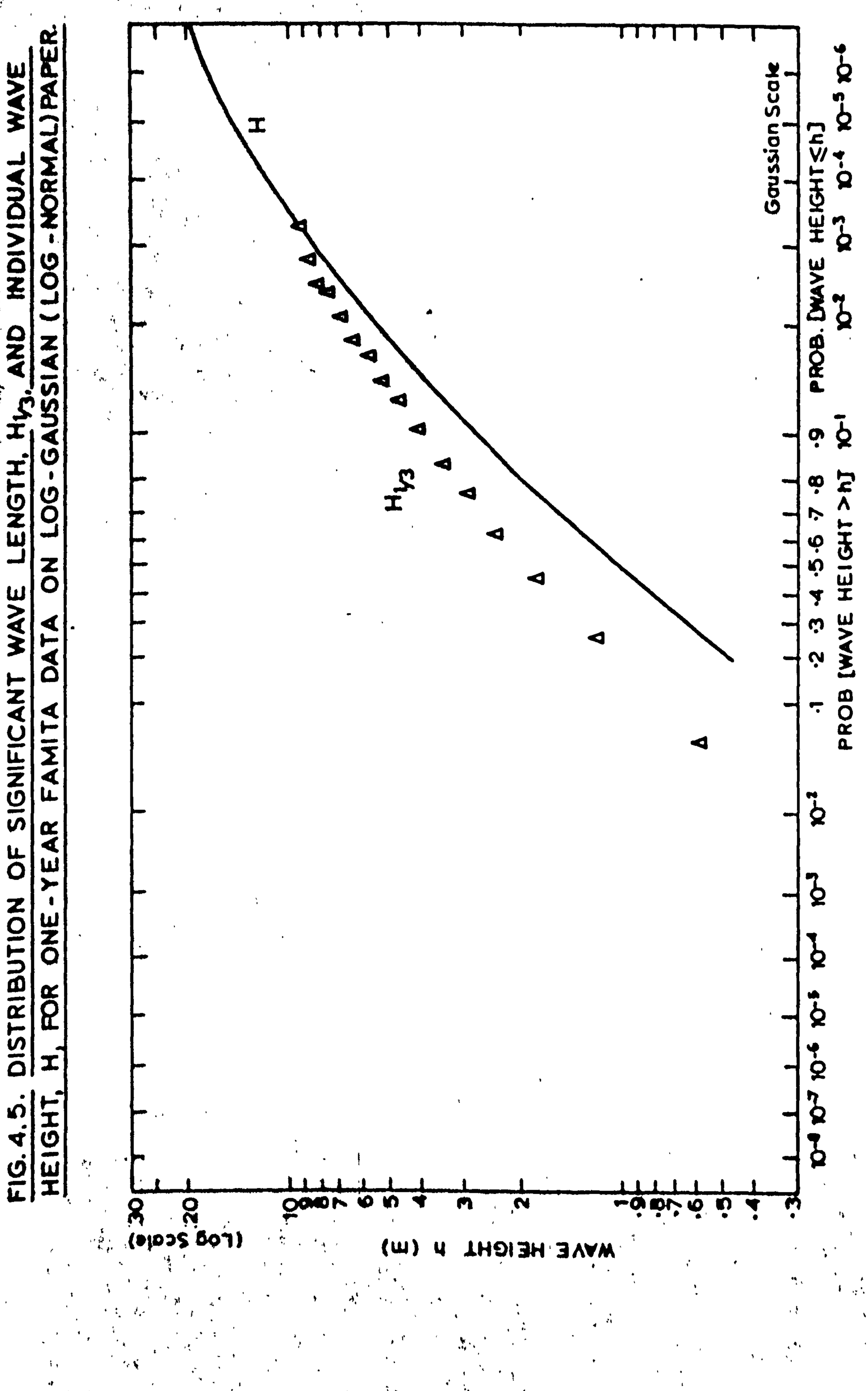

FIG. 4.5. DISTRIBUTION OF SIGNIFICANT WAVE LENGTH, $H_{1/3}$, AND INDIVIDUAL WAVE HEIGHT, H, FOR ONE-YEAR FAMITA DATA ON LOG-GAUSSIAN (LOG-NORMAL) PAPER.

FIG. 4.6. DISTRIBUTION OF INDIVIDUAL WAVE HEIGHT, H, AND SIGNIFICANT WAVE HEIGHT $H_{1/3}$ FOR ONE-YEAR FAMITA DATA ON WEIBULL PAPER.

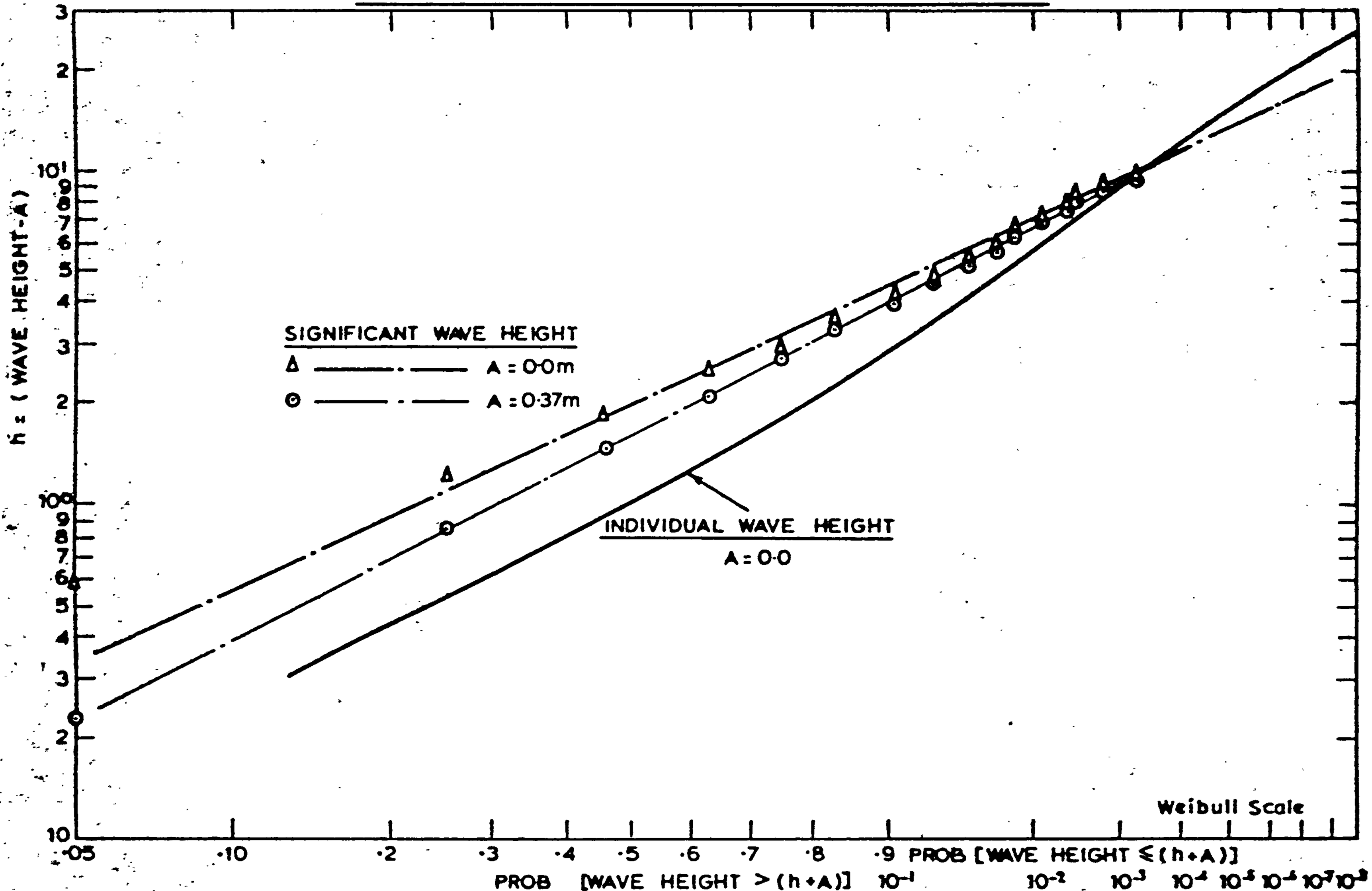

FIG. 4.7. DISTRIBUTIONS OF SIGNIFICANT WAVE HEIGHT, $H_{1/3}$ AND INDIVIDUAL WAVE HEIGHT, H, FOR ONE-YEAR FAMITA DATA ON GUMBEL PAPER.

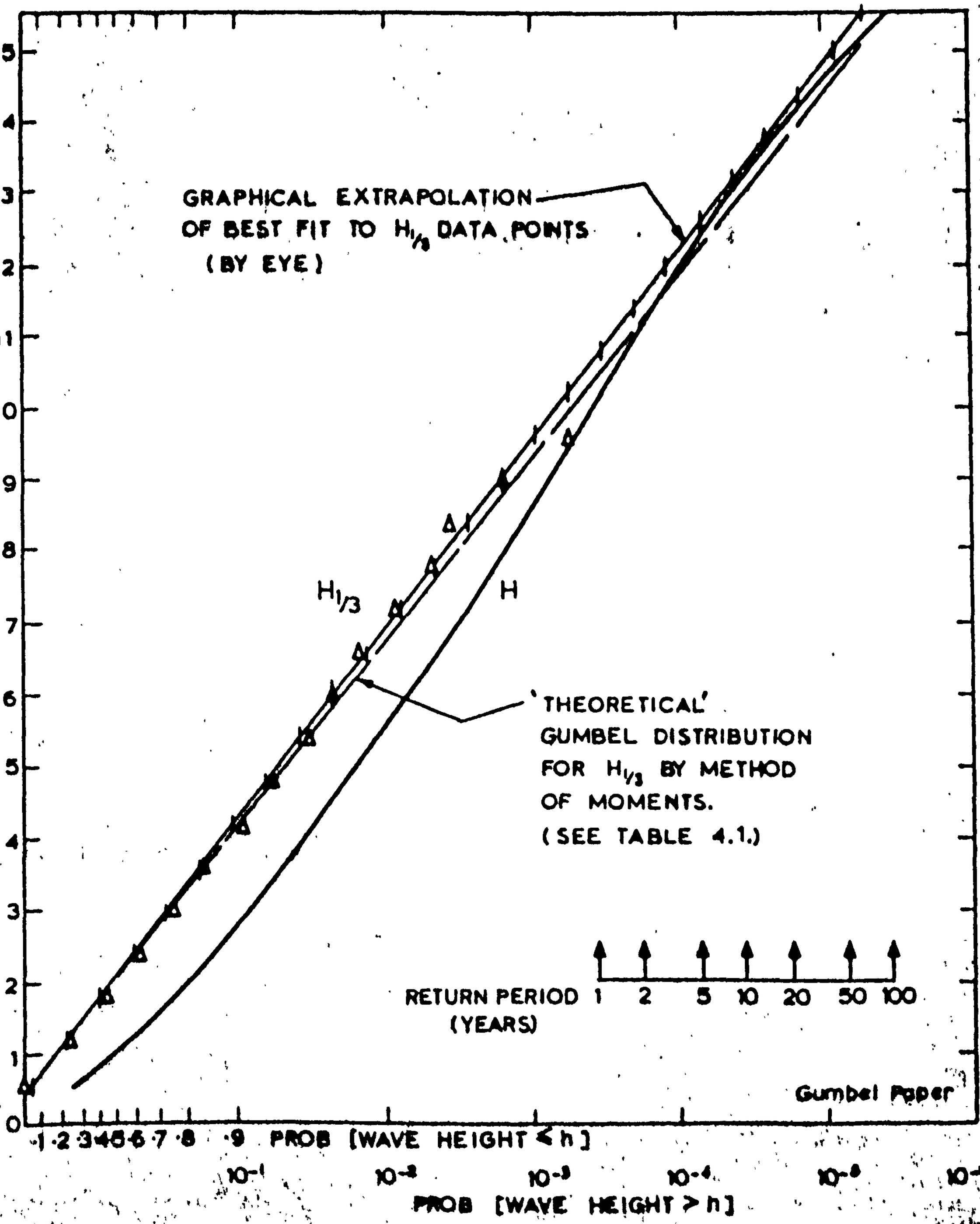

FIG. 4.8. PROBABILITY DENSITY HISTOGRAMS OF SIGNIFICANT WAVE HEIGHT (LOGARITHMIC SCALE)

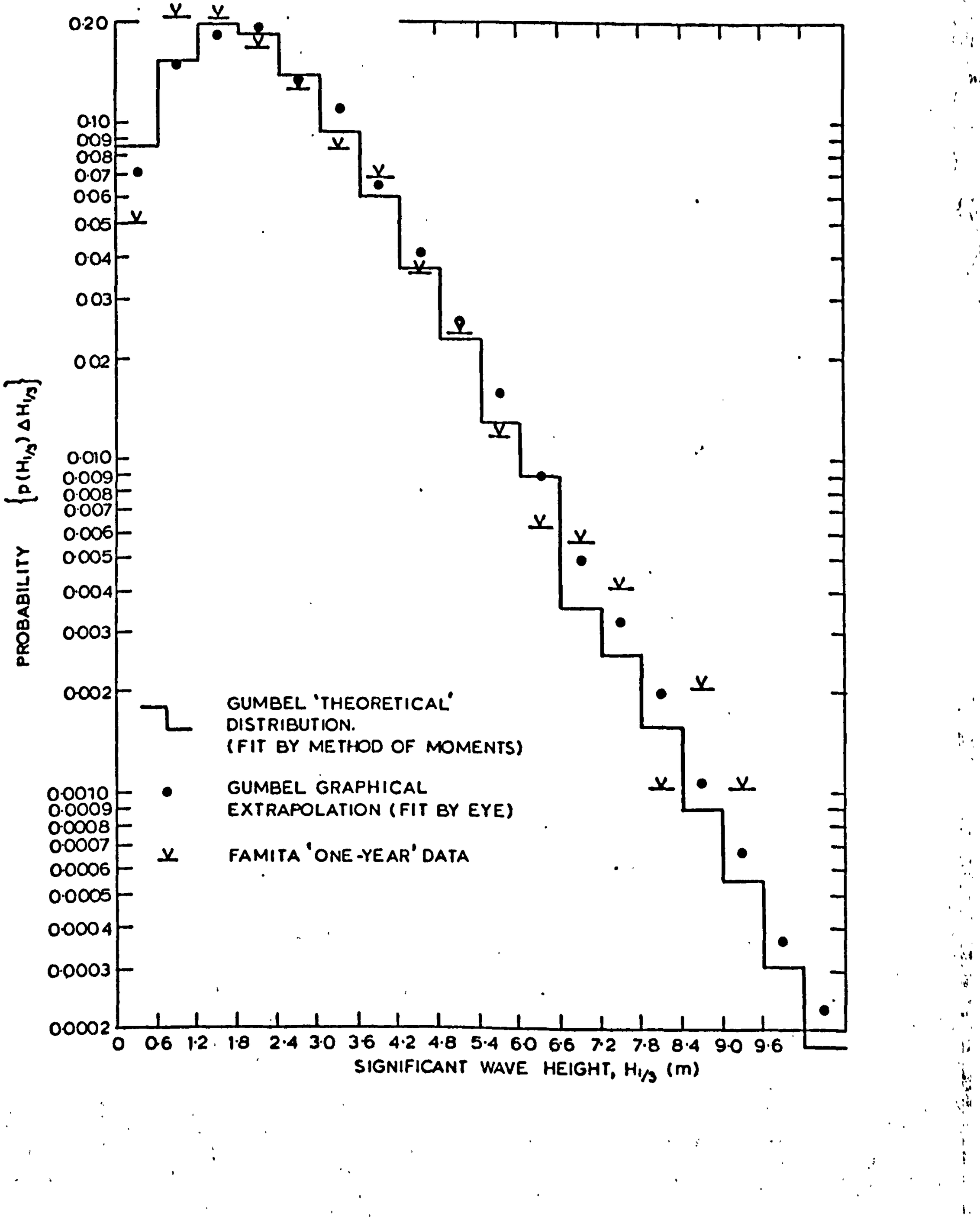

FIG. 4.9. YEARLY VARIATION IN THE PROBABILITY DISTRIBUTION OF SIGNIFICANT WAVE HEIGHT FROM SAETRE [75]

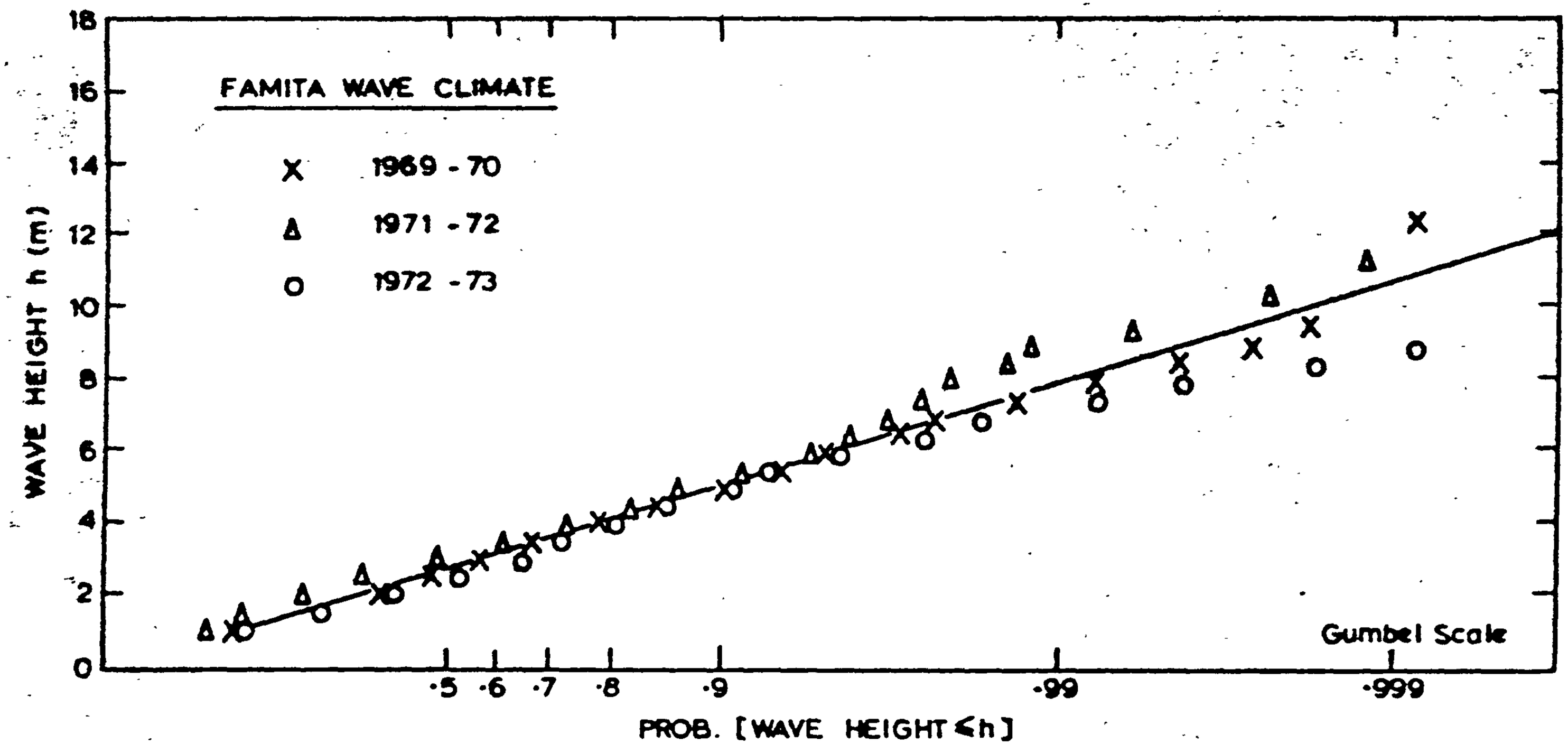

FIG. 4.10. LONG-TERM DISTRIBUTIONS OF INDIVIDUAL WAVE HEIGHT, H, DERIVED FROM VARIOUS ESTIMATES OF LONG-TERM FAMITA WAVE CLIMATE.

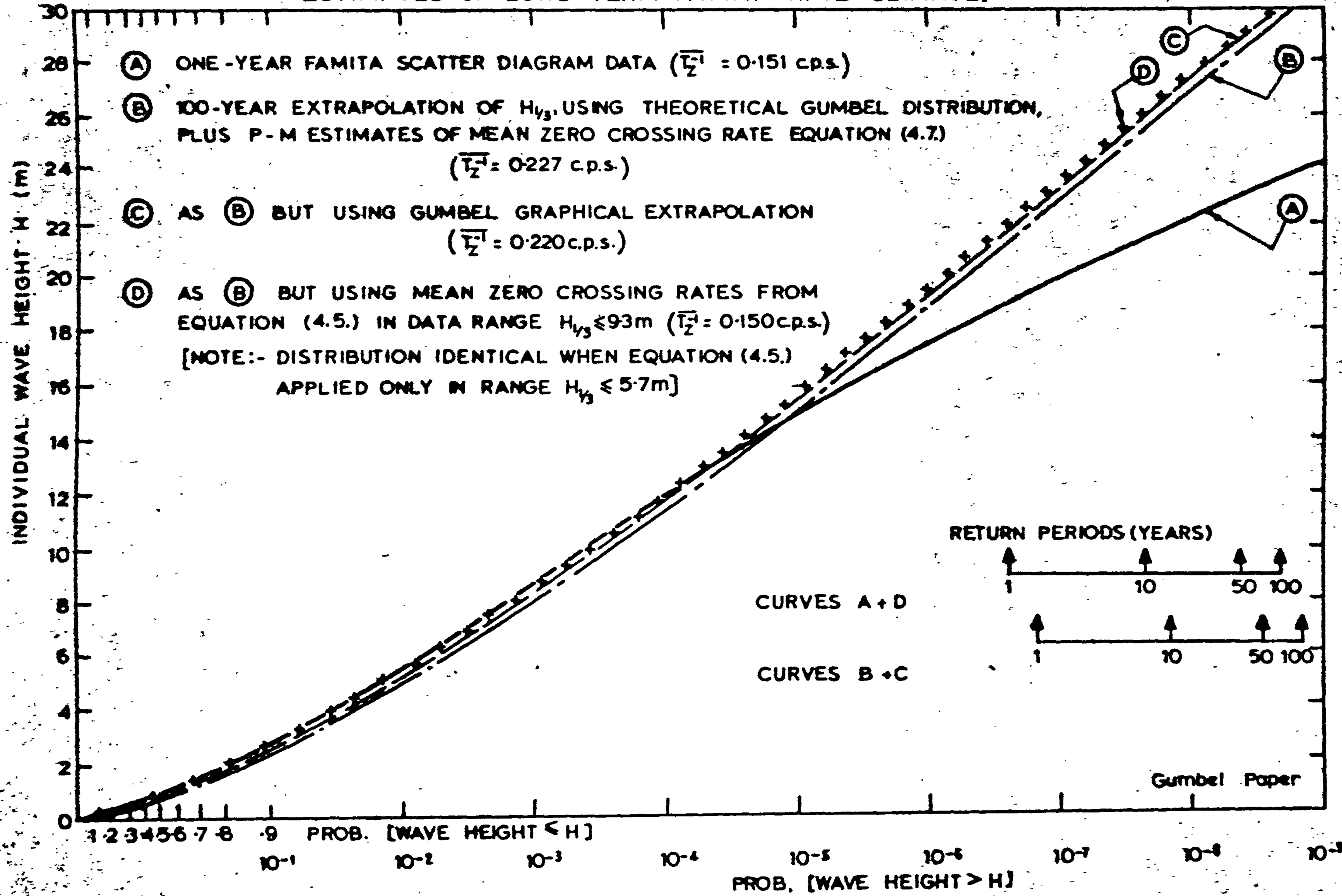

FIG. 4.11. COMPARISON OF SHORT-TERM ZERO-CROSSING RATES OF SURFACE ELEVATION DERIVED FROM FAMITA SCATTER DIAGRAM DATA (EQUATION 4.5.) AND PIERSON-MOSKOWITZ RELATIONSHIPS (EQUATION 4.7.)

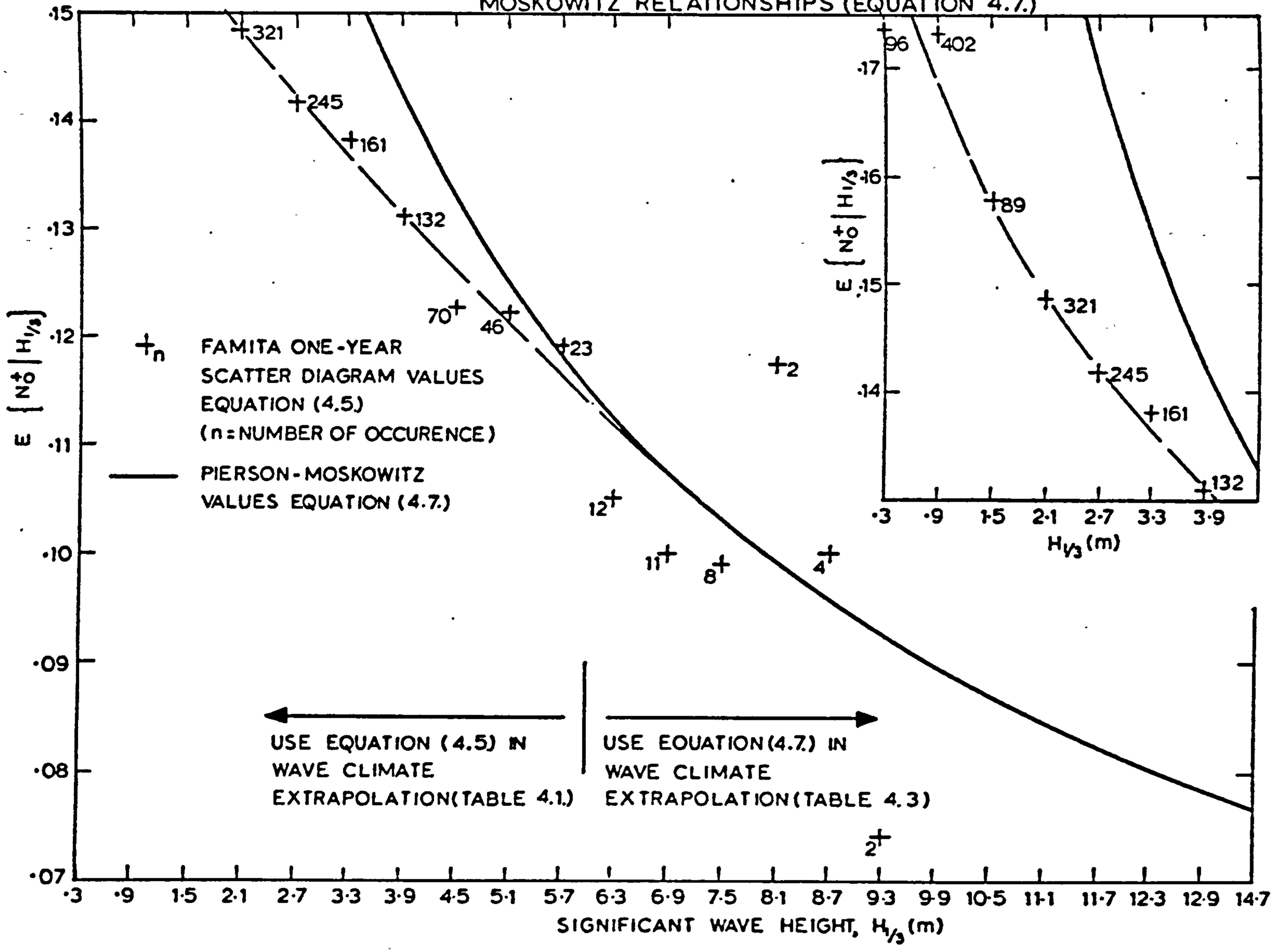

FIG. 4.12. EFFECT OF PERIOD COVERED BY WAVE CLIMATE EXTRAPOLATION ON THE DISTRIBUTION OF INDIVIDUAL WAVE HEIGHT (SHORT-TERM ZERO-CROSSING RATES OBTAINED FROM EQUATION (4.5.) FOR $H_{1/3} \leq 5{\cdot}7m$ OTHERWISE FROM EQUATION (4.7.).

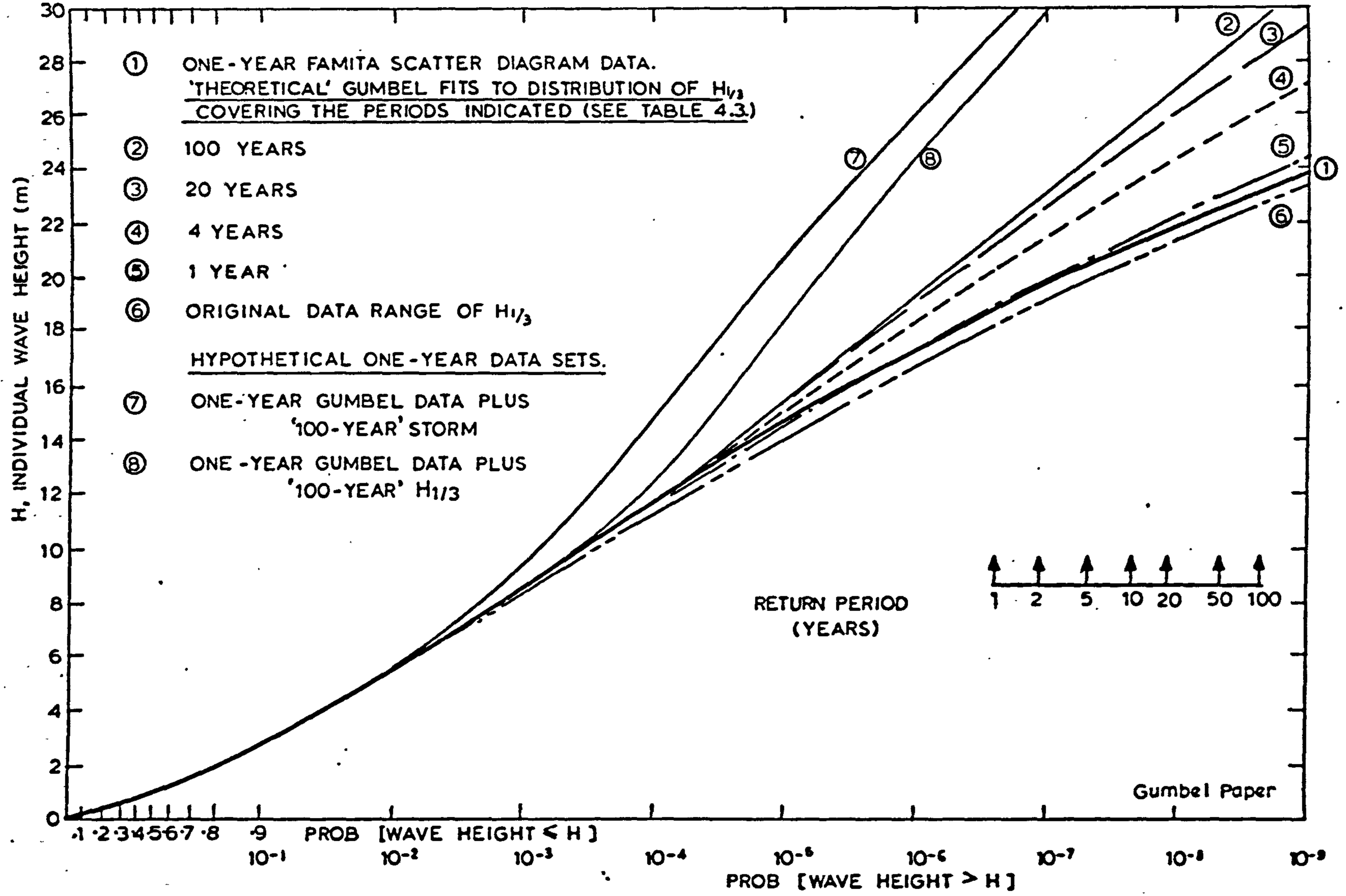

FIG. 4.13. EFFECT OF PERIOD COVERED BY WAVE CLIMATE EXTRAPOLATION ON THE DISTRIBUTION OF PEAK WAVE LOAD PER UNIT LENGTH. (SHORT-TERM ZERO-CROSSING RATES OBTAINED FROM EQUATION (4.5) FOR $H_{1/3} \leq 5{\cdot}7m$ OTHERWISE FROM EQUATION (4.7)

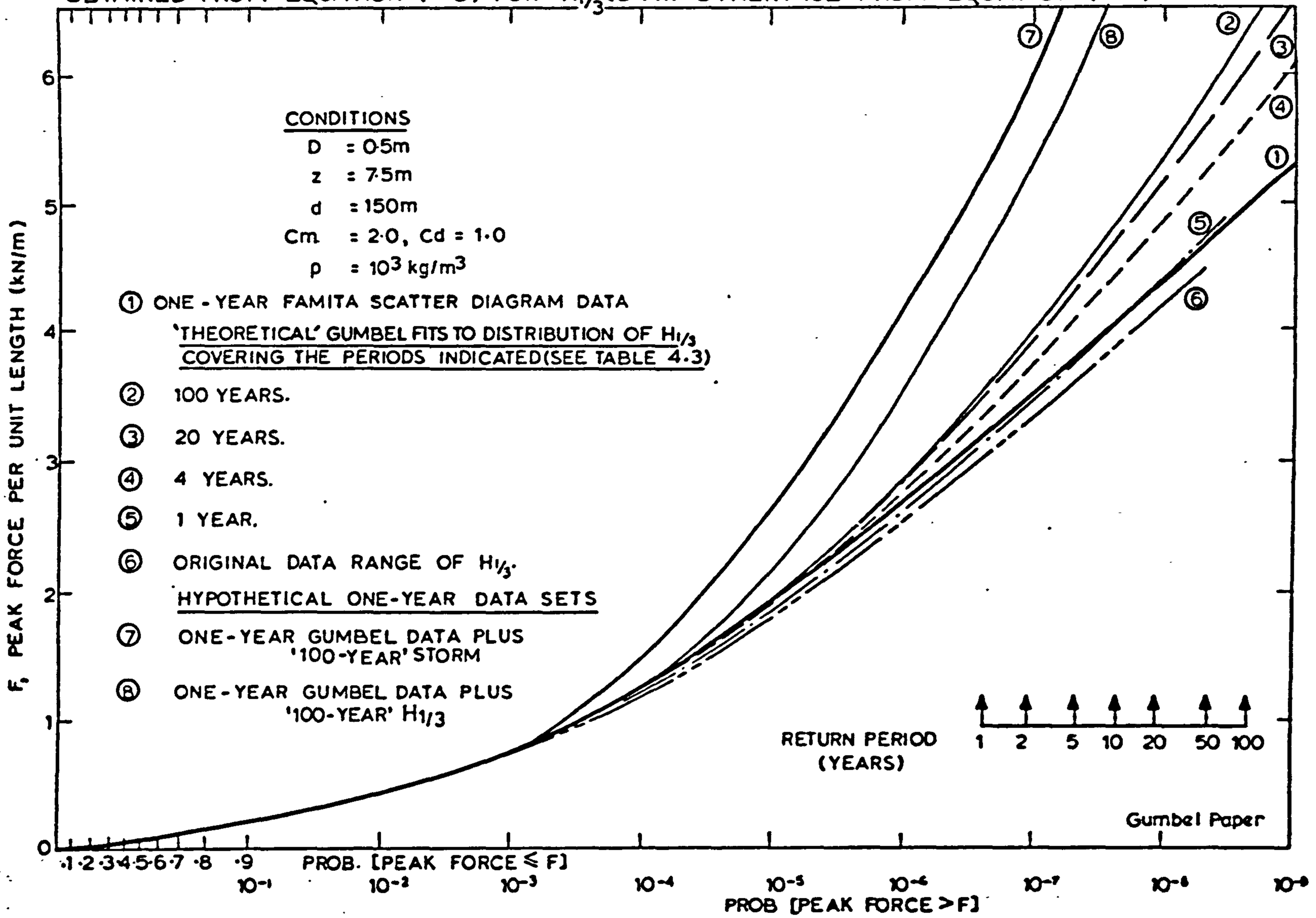

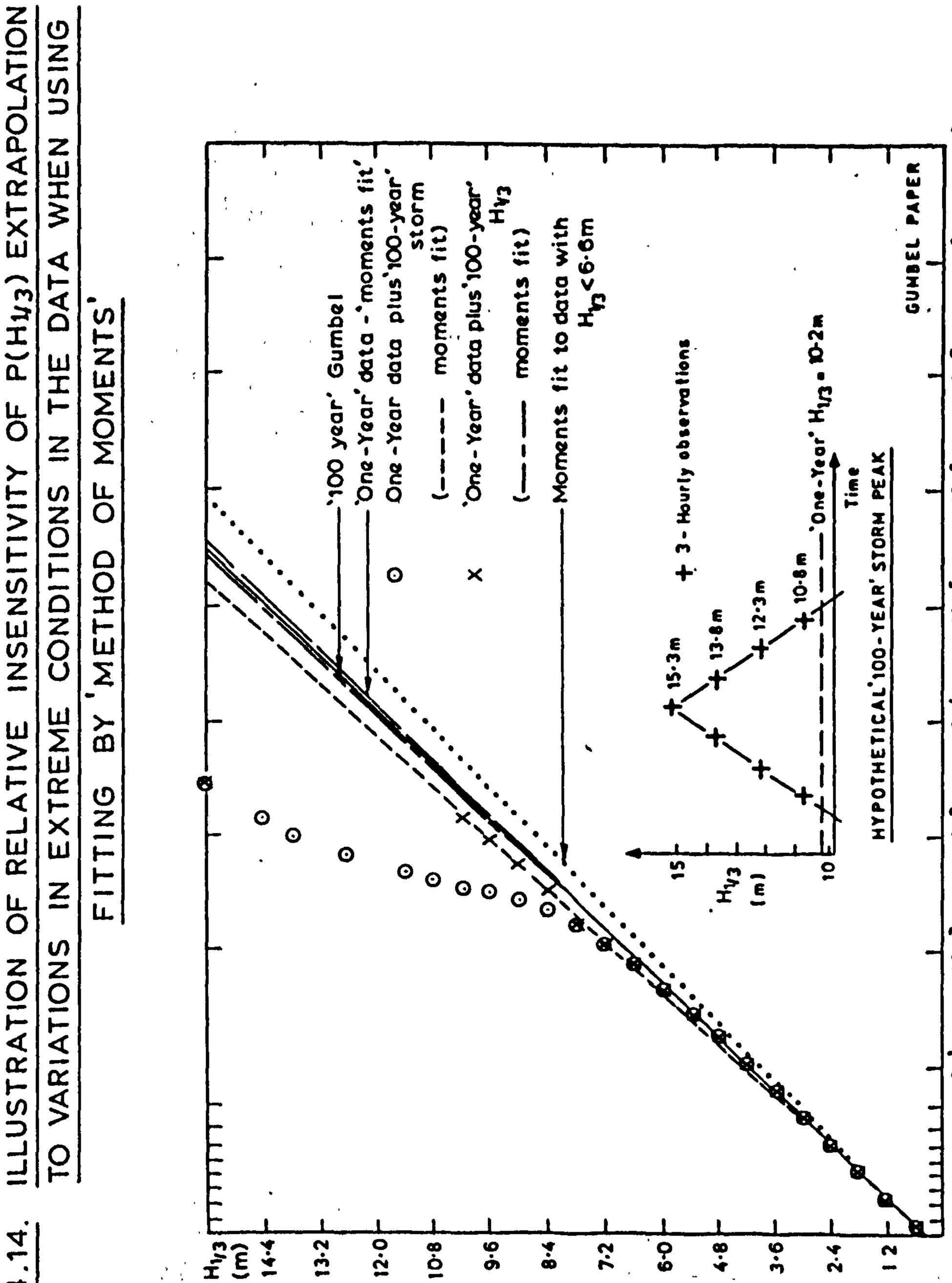

FIG. 4.14. ILLUSTRATION OF RELATIVE INSENSITIVITY OF $P(H_{1/3})$ EXTRAPOLATION TO VARIATIONS IN EXTREME CONDITIONS IN THE DATA WHEN FITTING BY 'METHOD OF MOMENTS'

C H A P T E R F I V E

PROBABILISTIC ANALYSIS OF STRUCTURAL RESPONSE

5.1 INTRODUCTION

The probabilistic description of random wave loading on short sections of structural members has been formulated in Chapter Two and illustrated, with emphasis on long-term conditions, in Chapter Three. Unfortunately, a single component of loading is inadequate to effectively model all but the simplest of structural members. Extension of the probabilistic methods is, therefore, required to describe structural response, such as stress or deformation, for systems comprising of a large number of individual load components.

An extension along these lines is developed in this Chapter for analysis of structures which behave in an essentially static manner, where the frequency content of the excitation is not close to any natural frequencies of the structure and consequently the response of the structure is not subject to dynamic magnification. This assumption is acceptable for many of the current generation of fixed structures as discussed earlier. The procedure is restricted to structures for which all member load components may be expressed in the 'Morison' form subject to wave activity in the absence of uni-directional currents and excluding the intermittency effects of loading in the splash zone.

The structure is idealised into a lumped system with member areas and volumes, and hence 'Morison' load components, concentrated into a discrete set of nodes chosen so as to retain as accurate a model of the real structure as possible. Linear behaviour is assumed where response variables are expressible as a linear combination of the nodal loads.

Theoretical pdf.s of short-term response may be obtained from a multi-variate pdf. of the nodal loads which can be expressed in terms of the multi-variate Gaussian process describing the water particle motions at the locations of these nodes. In this way the properties of response fully account for both the correlations which exist between the particle motions, and hence nodal loads, and the non-linearity of the loading itself.

The above procedure is formulated in Section 5.2 and investigated for a bivariate system, comprising two nodes, in Section 5.3. Extension to more complex systems is prevented by computational limitations. However, the probabilistic properties of response are found to follow quite closely the P-H pdf, which describes the single member loading, as shown previously from both full-scale and laboratory data by Tickell[55]. Since this pdf. is a function of its second and fourth moments (see Section 2.3.6), the short-term probabilistic properties of response may be obtained from the values of these moments, expressions for which are derived in Section 5.4.

Long-term descriptions of response follow by analogy to the procedures developed for the description of long-term wave loading and are outlined briefly in Section 5.5.

Finally, some results of application of the probabilistic methods to typical structural idealisations are presented in Section 5.6 and are compared with results from other methods of load or response prediction, including mathematical time-series simulation.

5.2 MULTI-VARIATE PDF. OF RESPONSE

5.2.1 Multi-variate pdf. of Wave Load

By analogy with the comments made in relation to the univariate force distribution in Section 2.3.6 it is evident that the n-dimensional wave force distribution is a non-linear transformation of the 2n-dimensional Gaussian process involving the particle velocity and acceleration at the locations of each force component.

From Eq. (2.3.45):

$$F_i = X_{2i-1}|X_{2i-1}| + X_{2i} \qquad i = 1, n \qquad (5.2.1)$$

$$\text{where } X_{2i-1} = u_i K_{Di} \quad \text{and} \quad X_{2i} = \dot{u}_i K_{Ii} \qquad (5.2.2)$$

and the random variables, X, are mean-zero Gaussian processes.

The n-dimensional force pdf. may be obtained from the 2n-dimensional Gaussian density given by (Eq. (I.53), Appendix One):

$$p(X_1, \ldots, X_{2n}) = \frac{1}{(2\pi)^n \sqrt{\text{Det } [M]}} \exp\{-\frac{1}{2} \{X\}^T [M]^{-1} \{X\}\} \quad (5.2.3)$$

where $\{X\}^T = (X_1, \ldots, X_{2n})$

$[M]$ = matrix of cross-covariances of $\{X\}$ which are equal to the cross-correlations for mean zero variables.

$$= \begin{vmatrix} R_{11} & R_{12} & \cdot & \cdot & \cdot & R_{1,2n} \\ R_{21} & \cdot & \cdot & \cdot & \cdot & \cdot \\ \cdot & \cdot & \cdot & \cdot & \cdot & , \\ R_{2n,1} & \cdot & \cdot & \cdot & \cdot & R_{2n,2n} \end{vmatrix}$$

with $R_{ij} = E\{X_i X_j\}$ (5.2.4)

where $E\{X_i X_j\}$ is obtained from the second moment of the corresponding particle motions which follows from Section 2.3.5, for example:

$$R_{14} = E\{X_1 X_4\} = \sqrt{K_{D1}}.K_{I2} E\{u_1 \dot{u}_2\}$$

and

$$E\{u_1\dot{u}_2\} = [R_{u_1\dot{u}_2}(\tau)]\big|_{\tau=0}$$

The 2n-dimensional force pdf. may be obtained from Eq. (5.2.3) using the transformation (see Section I.3.2.9, Appendix One):

$$p(F_1, \ldots, F_{2n}) = \frac{p(X_1, \ldots, X_{2n})}{|\text{Det } [J]|} \quad (5.2.5)$$

where force components F_{n+1} to F_{2n} are auxiliary variables of the form $F_{n+j} = X_{2j-1}$; (j = 1, ..., n), which are necessary in the mapping between the two probability spaces and Det[J] is the determinant of the Jacobian, which for the above system is unity.

The required n-dimensional pdf. of force is thus determined from Eq. (5.2.3) by integrating out the auxiliary variables:

$$p(F_1, F_2, \ldots, F_n) = \underbrace{\int_{-\infty}^{\infty} \cdots \int_{-\infty}^{\infty}}_{\text{n-fold}} p(F_1, F_2, \ldots, F_{2n})\, dF_{n+1}, \ldots, dF_{2n} \quad (5.2.6)$$

5.2.2 Quasi-static Response of Linear Structures

For an offshore structure of the steel lattice type, the vector of nodal forces, $\{F_e\}$, may be linearly related to the values of the distributed force at particular stations along each member, $\{F\}$:

$$\{F_e\} = [A]\ \{F\} \tag{5.2.7}$$

where [A] is a transformation matrix.

Nodal response variables $\{Y\}$ are obtained from the stiffness equation when the behaviour of the structure is assumed to be quasi-static and linear:

$$F_e = [K]\ \{Y\} \tag{5.2.8}$$

where [K] is the structural stiffness matrix, hence:

$$\begin{aligned}\{Y\} &= [K]^{-1}\ [A]\ \{F\} \\ &= [S]\ \{F\}\end{aligned} \tag{5.2.9}$$

The multi-variate pdf. of nodal response, Y, may thus be obtained from the multi-variate pdf. of force:

$$p(\{Y\}) = \left|\frac{p(\{F\})}{\text{Det } [S]}\right| \tag{5.2.10}$$

In order to map between the response domain and the force domain it is necessary for each of the probability spaces to be of the same dimension, thus [S] must be a square matrix. This may be achieved by introducing auxiliary variables into Eq. (5.2.9) and integrating them out of the multi-variate pdf. Eq. (5.2.10) in the same way as the auxiliary forces were removed in the previous Section.

A direct approach of the form indicated above is extremely lengthy since to derive the n-dimensional pdf. of force or response requires an n-fold integration. Furthermore to obtain the more practically applicable marginal response distributions (see Section I.3.2.3, Appendix One) an additional (n-1) fold integration must be carried out to remove the unwanted (n-1) response variables. For example, for the marginal pdf. of variable Y_1:

$$p(Y_1) = \underbrace{\int_{-\infty}^{-\infty} \ldots \int_{-\infty}^{-\infty}}_{(n-1)\text{fold}} p(\{Y\})\, dY_2 \ldots dY_n \qquad (5.2.11)$$

5.3 RESPONSE OF SYSTEMS OF TWO LOAD COMPONENTS

5.3.1 Bi-variate and Marginal pdf.s of Response

Consider the system sketched in Fig. 5.3.1 of two load components F_1 and F_2 and assume response variables Y_1 and Y_2 to be linearly related to these loads according to Eq. (5.2.9), i.e:

$$\begin{Bmatrix} Y_1 \\ \\ Y_2 \end{Bmatrix} = \begin{bmatrix} S_{11} & S_{12} \\ \\ S_{21} & S_{22} \end{bmatrix} \begin{Bmatrix} F_1 \\ \\ F_2 \end{Bmatrix} \text{ or } \{Y\} = [S]\ \{F\} \qquad (5.3.1)$$

where S_{ij} are constant influence coefficients.

Applying the procedure of the previous section it can easily be shown that the bi-variate pdf. of response is:

$$p(Y_1Y_2) = \frac{1}{|\text{Det}[S]|\,(2\pi)^2 K_{I_1} K_{I_2} \sqrt{\text{Det}[M]}} \int_{-\infty}^{\infty}\int \exp\{-\frac{1}{2}\frac{(ARG)}{\text{Det}[M]}\}\, du_1\, du_2 \qquad (5.3.2)$$

where [M] = symmetric matrix of the cross-covariances of particle kinematics

$$= \begin{bmatrix} \sigma^2_{u_1} & 0 & R_{u_1u_2} & R_{u_1\dot{u}_2} \\ 0 & \sigma^2_{\dot{u}_1} & -R_{u_1\dot{u}_2} & R_{\dot{u}_1\dot{u}_2} \\ R_{u_1u_2} & -R_{u_1\dot{u}_2} & \sigma^2_{u_2} & 0 \\ R_{u_1\dot{u}_2} & R_{\dot{u}_1\dot{u}_2} & 0 & \sigma^2_{\dot{u}_2} \end{bmatrix}$$

$$\begin{aligned}(ARG) = {} & \{C_{11}\, u_1^2 + C_{22}\, \dot{u}_1^2 + C_{33}\, u_2^2 + C_{44}\, \dot{u}_2^2\} \\ & + 2\{C_{12}\, u_1\, \dot{u}_1 + C_{13}\, u_1\, u_2 + C_{14}\, u_1\, \dot{u}_2 + C_{23}\, \dot{u}_1\, u_2 \\ & + C_{24}\, \dot{u}_1\, \dot{u}_2 + C_{34}\, u_2\, \dot{u}_2\}\end{aligned}$$

C_{ij} are co-factors of [M]

$\dot{u}_1 = (F_1 - K_{D1}\, u_1|u_1|)/K_{I1}$

$\dot{u}_2 = (F_2 - K_{D2}\, u_2|u_2|)/K_{I2}$

$F_1 = (S_{22}\, Y_1 - S_{12}\, Y_2)/\text{Det}\ [S]$

and $F_2 = (S_{11}\, Y_2 - S_{21}\, Y_1)/\text{Det}\ [S]$

The marginal pdf.s follow by integration, for example:

$$p(Y_1) = \int_{-\infty}^{\infty} p(Y_1\, Y_2)\, dY_2 \qquad (5.3.3)$$

As a linear combination of mean-zero processes, the response variables must also be mean-zero and the second moment may be expressed as follows, for Y_1:

$$E\{Y_1^2\} = S_{11}^2\, E\{F_1^2\} + 2S_{11}\, S_{12}\, E\{F_1\, F_2\} + S_{12}^2\, E\{F_2^2\} \qquad (5.3.4)$$

where $E\{F_1^2\}$ and $E\{F_2^2\}$ are given by Eq. (2.3.49) and:

$$E\{F_1\, F_2\} = E\{X_1|X_1|X_3|X_3|\} + E\{X_1|X_1|X_4\} + E\{X_2X_3|X_3|\} + E\{X_2\, X_4\}$$

The expectations involving X_i are solved later in Section 5.4, a solution having been developed previously by Borgman[60]. The particle kinematics inducing loads F_1 and F_2 are all mean-zero symmetrical processes and since the transformations described by Morison's equation, retain the direction, or sign, of these kinematics it follows that the bi-variate pdf. of load has a degree of symmetry, in that:

$$p(F_{1i},\, F_{2j}) = p(-F_{1i},\, -F_{2j})$$

and

$$p(F_{1i},\, -F_{2j}) = p(-F_{1i},\, F_{2j})$$

In other words, that part of the bi-variate pdf. contained within any two adjoining quadrants of the domain of F_1 and F_2 define the complete pdf. since the densities associated with the remaining quadrants are obtained by rotating this probability surface through 180° about the origin.

Furthermore, as the transformation between load and response is linear, the same degree of symmetry is present in the bi-variate response domain, as illustrated by:

$$p(Y_{1i},\, Y_{2j}) = \frac{p(F_{1k},\, F_{2\ell})}{C}\;;\quad C = \text{const., from Eq. (5.2.10)}$$

$$= \frac{p(-F_{1k},\, -F_{2\ell})}{C} = p(-Y_{1i},\, -Y_{2j})$$

It follows, therefore, that the marginal distributions of response are symmetrical and their derivation requires computation of only half of the bi-variate domain of Y_1 and Y_2. For positive values of response the marginal pdf.s may be obtained as:

$$p(Y_1) = \int_{-\infty}^{\infty} p(Y_1\ Y_2)\ dY_2; \quad p(Y_2) = \int_{0}^{\infty} [p(Y_1, Y_2) + p(Y_1, -Y_2)]\ dY_1 \qquad (5.3.5)$$

where only the domain ($Y_1 \geqslant 0$; $-\infty < Y_2 < \infty$) is considered.

5.3.2 Method of Computation and Program Validation Using Bi-variate pdf. of Load

From Eqs. (5.3.3) and (5.3.2) it follows that a 3-fold integration is required for computation of marginal probability densities of response, with a further integration required for its cdf. 'Closed-form' solutions do not exist for these integrations and solution must, therefore, be obtained numerically in a similar manner to that applied in the univariate domain and described briefly in Chapter Three.

The computer programs developed for this procedure are indicated by name only here (and are summarised in Appendix Six) but they follow the same general format and notation as the programs referred to earlier and characterised by program OSF2, documented in Reference 10. Although the programs include algorithms for prediction of long-term conditions, run-time restrictions have prevented utilisation of this facility.

Program OS17 - Constant Step Fixed Range Numerical Integrations

The bi-variate density of Eq. (5.3.2) is computed at a grid of points covering fixed ranges of the response domains. Values of ($0 \leqslant Y_1 \leqslant 8\sigma_{Y_1}$) and ($-8\sigma_{Y_2} \leqslant Y_2 \leqslant 8\sigma_{Y_2}$) are generally found to be acceptable with step widths of 0.2σ in both domains (where σ represents the relevant standard deviation) when 'Simpson's Rule' is applied to yield the marginal densities from Eq. (5.3.5).

Velocity components u_1 and u_2 in Eq. (5.3.2) are removed by constant step numerical integration. Sufficient stability of solution is normally achieved using step widths of 0.2σ over a range of $\pm 5\sigma$ in association with Simpson's Rule summations.

Under certain circumstances the accuracies of the above numerical integrations is inadequate, as will be illustrated later, and hence attempts must be made to increase the accuracy by considering shorter class widths over expanded ranges of the variables to reduce error accumulation.

To minimise computational effort the bi-variate densities are taken as zero and the computations curtailed where the corresponding absolute values of forces F_1 and F_2, from Eq. (5.3.1) exceed 10σ of their marginal values. For the above conditions computer run-times are approximately 65 seconds on the ICL CDC 7600 computer when using the optimised mode of operation (OPT = 2).

Program Validation

To check the procedures the identity matrix was applied for [S] in Eq. (5.3.1) such that the bi-variate and marginal distributions of loading result, the latter of which may be compared with the equivalent uni-variate solution.

A sketch of a bi-variate pdf. of loading is made in Figs. 5.3.2 and 5.3.3, in terms of the conditional distributions $p(F_1\ F_2|F_1)$ and $p(F_1\ F_2|F_2)$, resulting from application of program OS17. For the conditions indicated in these figures the marginal cdf. of force F_1 is plotted as curve 1 on Fig. 5.3.4 and is found to fit exactly the cdf. of uni-variate load F_1, curve 2, obtained using programme OSF2. The corresponding plot for F_2 is made on Fig. 5.3.5 and the marginal cdf, curve 1, is seen to deviate from the uni-variate, curve 2, in the extreme range, this departure being caused by inaccuracies in the numerical integrations as will be explained later.

The fit between the curves in Figs. 5.3.4 and 5.3.5 is typical of the results obtained from computations in the bi-variate domain where, for either load or response, the marginal cdf. with the lowest kurtosis (the most 'linear' or 'inertial-dependent' condition) deviates in the extreme range due to error accumulation. To further illustrate this effect curve 3 on Fig. 5.3.5 results from the previous system, see Fig. 5.3.2 but with a 2.0m. diameter for member 1, a more inertial condition than for the 1.0m. member, and shows only slight departure from the uni-variate distribution. However, the marginal distribution of load on the 2.0m. diameter member, curve 1 on Fig. 5.3.6, shows a deviation from the uni-variate cdf, curve 2, whilst marginal distributions obtained when the other member is of 5.0m. diameter follow this curve exactly.

This behaviour may be explained as follows, noting that the cdf. of the variable with lowest kurtosis assymtotes to the extreme probability of the other variable, as might be expected. Consider, for example, the

conditions in Fig. 5.3.2 where Force F_1 is truncated at $8\sigma_{F_1}$ in Fig. 5.3.4 at a probability of approximately 0.999965, (which may be obtained directly from Fig. 2.3.5 given the value of kurtosis). From curve 2 on Fig. 5.3.5, (or from Fig. 2.3.5) this probability represents approximately $6\sigma_{F_2}$. Consequently, in computing the cdf. of F_2 beyond $6\sigma_{F_2}$ the conditional distributions $p(F_1\ F_2|F_2)$, integrated to yield the marginal densities, are truncated at $F_1 = 8\sigma_{F_1}$ whilst they are likely to contain significant probability mass beyond this limit.

In contrast, in the determination of the cdf. of F_1 close to its limit of $8\sigma_{F_1}$ it is unlikely that any significant probability mass of $p(F_1\ F_2|F_1)$ will be omitted by truncation at even $6\sigma_{F_2}$. This follows because the marginal distribution of F_1, with larger kurtosis, is more 'peaky' showing a greater spread in the tails of the force domain than its counterpart F_2 and it might be expected that the conditional distributions will also exhibit similar characteristics. The limit of $6\sigma_{F_2}$ is indicated on Fig. 5.3.5 from which it is seen that the departure between the marginal cdf, curve 1, and the univariate, curve 2, occurs below this limit, at about $5\sigma_{F_2}$, suggesting that the above characteristics may possibly be enhanced in the conditional distributions.

From the above comments it can be concluded that to avoid deviations in the extremes the limits of the ranges of F_1 and F_2, (or Y_1 and Y_2) should correspond to equivalent cumulative probabilities, which may be deduced from Fig. 2.3.5. However, to carry out such a procedure, with the objective of extending the valid range of the variable with lowest kurtosis, will require increased run-times. This follows because the extensions in ranges of force or response must be provided without increase in step widths if the accuracy of the numerical integrations is not to be adversely affected. It must be appreciated that with the imposition of run-time restrictions there will be a limit to the valid range of the marginal distributions which may be computed due to the error accumulation present in even the most refined numerical integration procedures. From the results obtained herein, this limit was found to correspond to a probability of approximately 0.99999 due to accumulated error of approximately $6 \times 10^{-5}\%$.

Notwithstanding the above remarks, the foregoing results have confirmed the validity of the computational procedures. It now remains to describe some modifications to program OS17 which were introduced to optimise the computations.

Program OS14 - Approximate Integrations Over Velocity Domains Using Quadrature Techniques

Program OS14 was developed to reduce computer run-times by application of Gaussian-Hermite quadrature (see Section 3.5) in the integration of velocity variables u_1 and u_2 in Eq. (5.3.2). Using this technique the bi-variate pdf. may be expressed as:

$$p(Y_1\ Y_2) = \frac{2\sqrt{\text{Det}\ [M]}}{|\text{Det}[S]|(2\pi)^2 K_{I_1} K_{I_2}\sqrt{C_{11}\ C_{33}}} \sum_{j=1}^{m} A_j^{(m)} \sum_{k=1}^{n} A_k^{(n)}\ f(x_{1j}, x_{2k}) \qquad (5.3.6)$$

where $f(x_{1j}, x_{2k}) = \exp\{-\frac{1}{2}\ \frac{(ARG^*)}{\text{Det}[M]}\}$

$$(ARG^*) = (ARG) - C_{11}\ u_{1j}^2 - C_{33}\ u_{2k}^2$$

$$u_{1j}^2 = \frac{2\ \text{Det}[M]\ x_{1j}^2}{C_{11}}$$

$$u_{2k}^2 = \frac{2\ \text{Det}[M]\ x_{2k}^2}{C_{33}}$$

and $A_j^{(m)}$, $A_k^{(n)}$ are the weighting coefficients with x_{1j}, x_{2k} the function values of Gaussian Hermite quadrature of order m, n, respectively.

Some instability of solution is experienced in using the method, as illustrated in curve 3 of Fig. 5.3.4 for the situation when m = n = 20, where oscillation about the true marginal distribution results. However, this effect is much less marked than that present in the uni-variate application of the quadrature (see Section 3.5) and decays as the kurtosis of the loading components decrease. Use of this method is, therefore, acceptable for conditions of low drag dependence in the loading input and with m = n = 20 typical run-time requirements for Program OS14 are reduced to about 20 seconds, only 30% of the equivalent values for Program OS17.

Programs OS15, OS18 - Floating Range Integration for Response Variable Y_2

The applications described so far all correspond to conditions with relatively low correlation between the load components. This is typified by the correlation coefficient, $r_F = 0.292$ for the conditions in Fig. 5.3.2, where:

$$r_F = E\{F_1 F_2\}/\sqrt{E\{F_1^2\} E\{F_2^2\}} \qquad (5.3.7)$$

and $E\{F_1 F_2\}$ is given with Eq. (5.3.4).

Considerable reduction in accuracy of solution is experienced with Programs OS14 and OS17 when the correlation is high. Fig. 5.3.7 illustrates such a condition, with loading close to the Gaussian form, and it is seen that the conditional distributions from the bi-variate pdf. have probability mass over only a limited range of the domains covered in the integrations.

It is evident from Fig. 5.3.7 that integrations over the fixed ranges considered previously, and indicated on the figure, will be inaccurate. Curves 4 in Figs. 5.3.4 and 5.3.5 demonstrate this effect and correspond to the conditions of Fig. 5.3.2 but with $x_1 = x_2 = 100$m. yielding a correlation coefficient $r_F = 0.90$. The behaviour of these marginal distributions is a result of accumulative errors in the numerical integrations yielding cumulative probabilities in the high force region in excess of unity. Normalising these cdf.s, by dividing the cumulative probabilities by the erroneous assymptotic probability at the extreme of the force range considered (in these cases in excess of 1.0) produces curves 4A showing a better fit to the uni-variate cdf. than the original distribution but still deviating significantly in the extreme range, as might be expected. This procedure accounts for the error by assuming it to be evenly spread over the entire force range.

A more logical procedure is to assume that the percentage errors in the numerical integration of the conditional distributions of force are of the same order of magnitude. It, therefore, follows that the bulk of the error will be contained in the resulting marginal densities in the low range of force where the conditional probability masses are the largest. This hypothesis may thus be investigated by fitting the marginal cdf. at the upper extreme to the probability obtained from the uni-variate condition and plotting the remainder of the cdf. in reverse from this

point using the originally computed probability steps associated with successive class levels of loading. This procedure constrains all the error to the initial class level adjoining the origin, F = 0. Applying such an approach yields a modified marginal cdf. which follows exactly the uni-variate distribution in Fig. 5.3.4. In view of the error in the extreme range of the marginal cdf.s in Fig. 5.3.5, resulting from the force range truncation adopted, as discussed earlier, the fit in this case should be made at a force level in the region of 5-6σ_F for which an exact agreement with the uni-variate cdf. again results.

In summary, the goodness of fit of these 'corrected' marginal distributions demonstrates that the most significant errors in the numerical integrations are concentrated in the region close to zero of the marginal variable under investigation. Although this error is not evident in the lower region of the marginal cdf. it causes considerable distortion in the extreme range by virtue of the nature of the probability scales.

Programs OS15 and OS18 were developed, to replace respectively OS14 and OS17, as an attempt to minimise error accumulation in the integration from the bi-variate to the marginal response domains when correlation between response variables is high. In these programs response Y_2 is integrated over a floating range centred over the peak of the conditional pdf. $p(Y_1\ Y_2|Y_1)$ and covering only the range of the significant probability mass, thereby optimising the constant step numerical integration for the marginal densities of Y_1.

Since in general neither Y_1 nor Y_2 will be Gaussian distributed, the values of the mean and variance of $p(Y_1\ Y_2|Y_1)$, required to define the range of Y_2 at any level of Y_1, are unknown. They may, however, be approximated by the equivalent Gaussian values, see Section I.3.3.2, Appendix One:

$$E\{Y_2|Y_1\} = r_Y\ Y_1\sqrt{E\{Y_2^3\}/E\{Y_1^2\}} \qquad (5.3.8)$$

and

$$\sigma^2_{Y_2|Y_1} = \sigma^2_{Y_2}(1 - r_Y^2) \qquad (5.3.9)$$

where r_Y is the form of Eq. (5.3.7).

These estimates are used in Programs OS15 and OS18 and from inspection of the resulting bi-variate response distributions this technique appears to locate the significant region of the probability mass of $p(Y_1\ Y_2|Y_1)$ if the range of Y_2 considered covers about $\pm 16\sigma_{Y_2|Y_1}$ centred at the mean $E\{Y_2|Y_1\}$.

Although producing an improvement on the fixed range integration the approach is not sufficiently refined to suppress the problem of error accumulation when correlations are high, given restrictions on the sensitivity of the numerical integrations imposed by computational limitations. Consequently, significant inaccuracy must be expected in investigations of response from bi-variate systems under these conditions.

5.3.3 Illustration of the Impracticability of Investigation of Tri-variate Systems of Loads

It is instructive here to demonstrate the limitations of application of the multi-variate analysis for structural response.

Using the optimised mode of operation on the ICL CDC 7600, computer programs OS17/OS18 demand run-times of at least 65 seconds whilst Programs OS14/OS15 require at least 20 seconds. With reference to Section 5.2, extension into the tri-variate loading domain would imply additional integrations over a response and velocity domain. Assuming numerical integrations of a similar sensitivity to those applied in the bi-variate case, the number of computations of the argument in Eq. (5.2.11) would be increased by a factor of at least (20 x 81) ≃ 1600 for OS14/OS15 over those required for the bi-variate system. Furthermore, a large part of the run-time consumption is within the algorithm describing the integrations of this argument. Consequently, run-times for tri-variate systems are likely to be of the order of (20 x 1600) ≃ 32000 seconds, far in excess of the limitation imposed.

Even if such run-times were available, in view of the increased problems of error accumulation experienced in extension from uni-variate to bi-variate loading, these problems might be expected to be excessive in the tri-variate loading applications.

5.3.4 Marginal Distributions of Response from Bi-variate Systems Using Program OS18

Some marginal cdf.s of response, computed using Program OS18, are plotted in Figs. 5.3.8 to 5.3.10. Also included in the figures are estimates of the second and fourth statistical moments obtained from the marginal pdf.s, the kurtosis and the equivalent Gaussian cdf.s of response. In addition, the theoretical values of the moments of response, computed from the expressions developed in Section 5.4, are included and are seen to show close agreement with the numerically computed 'marginal' estimates.

From the results presented in the Figures it is immediately apparent that the distribution of response deviates from the Gaussian form when the loading is drag dependent and hence non-linear. The linear nature of the transformation from force to response for the general multi-variate system suggests that the distribution of response may be of a similar form to that of the loading, namely the Pierson-Holmes pdf. for short-term conditions.

This is evidently the case when inertial effects dominate the loading, since multi-variate Gaussian input through linear systems produce Gaussian output. Tickell[55] has supported the proposition for general drag/inertia loading from analysis of strain records from members of a prototype structure in the Southern North Sea and also from laboratory tests.

The hypothesis is tested in Figs. 5.3.8 to 5.3.10 by plotting the Pierson-Holmes cdf. from the second and fourth moments of response, there being found negligible deviation between the results obtained from the two sets of moments included in the Figures. Program OS16 (see Appendix Six) was written to compute the P-H distribution $P_H(\gamma)$ from Eq. (2.3.54), using constant step integration with 81 steps for variable γ over a range from zero to $8\sigma_\gamma$ and 201 steps for dummy variable ψ_1 over a range of $\pm 5\sigma_{\psi_1}$:

In Fig. 5.3.8 a good fit is achieved between the marginal distributions and the equivalent P-H cdfs, the deviations which exist probably resulting from error accumulation in the numerical integrations as discussed previously in Section 5.3.2. The marginal cdf. in Fig. 5.3.9 shows considerable departure from the P-H form. However, for this highly correlated condition, following the procedure applied to curve 4 in Fig. 5.3.4 and discussed in Section 5.3.2,

normalisation improves the fit and exact agreement is obtained if the distribution is fitted at the extreme. It, therefore, follows that the deviation is a result of numerical inaccuracies in the integrations concentrated in the marginal densities at low response levels.

Finally, Fig. 5.3.10 illustrates the instability of solutions from the bi-variate load system involving 4-fold numerical integration for a predominantly inertial condition. The plot of the corresponding P-H distribution shows a similar degree of inaccuracy from only a 2-fold integration.

In summary, the deviations which exist between the marginal cdf.s of response and the equivalent P-H cdf.s may be explained by numerical inaccuracies in the computations. The errors are concentrated in the low response region of the cdf.s and thus have little effect on the statistical moments resulting from the marginal pdf.s. Further results of the above analysis supporting these statements are presented in References 11 and 14.

It may, therefore, be concluded that the probability distribution of response for bi-variate systems is accurately described by the Pierson-Holmes distribution. Moreover, it follows directly that this statement may be generalised to cover systems of any number of load components. It should be explained at this stage that it has not been found possible to prove mathematically that the probability structure of a linear combination of random variables following the P-H distribution also follows that distribution. However, as mentioned earlier, the proposition is supported by the results from experimental measurements[55].

Further evidence of the goodness of fit of response to the P-H distribution is presented later from the results of mathematical time-series simulation. In view of the problems associated with error accumulation in numerically derived cdf.s, it is considered to be more appropriate to make comparisons of the probability structure of response in terms of the values of the statistical moments, which are relatively insensitive to such errors as discussed earlier. Close agreement between statistical moments of up to fourth order implies for practical purposes equivalence between the probability distributions producing the moments.

Accepting the above hypothesis, response from multi-variate systems may be described probabilistically from knowledge of its second and fourth order statistical moments. These may be developed from the known statistics of the particle kinematics at the nodal 'load-points'. This procedure, developed in the following sections, avoids many of the computational problems associated with the multi-variate probability domains, thereby relaxing the restriction on system complexity.

5.4 SECOND AND FOURTH MOMENTS OF RESPONSE

A particular nodal response variable taken from Eq. (5.2.9) may be expressed in the form:

$$Y = S_1 F_1 + S_2 F_2 \quad \ldots \quad + S_n F_n \tag{5.4.1}$$

where S_1, S_n are flexibility coefficients.

Clearly, since all forces are mean zero in this study and have symmetrical distributions then all odd moments of Y will be zero, i.e:

$$E\{Y^k\} = 0 \qquad k = \text{odd integer} \tag{5.4.2}$$

The second moment of Y is given by:

$$E\{Y^2\} = \sum_{i=1}^{n} S_i^2 E\{F_i^2\} + 2 \sum_{i=1}^{n-1} \sum_{j=i+1}^{n} S_i S_j E\{F_i F_j\} \tag{5.4.3}$$

Similarly, the fourth moment of Y is:

$$E\{Y^4\} = \sum_{i=1}^{n} S_i^4 E\{F_i^4\} + 4 \sum_{i=1}^{n} \sum_{\substack{j=1 \\ j\neq i}}^{n} S_i^3 S_j E\{F_i^3 F_j\}$$

$$+ 6 \sum_{i=1}^{n-1} \sum_{j=i+1}^{n} S_i^2 S_j^2 E\{F_i^2 F_j^2\} + 12 \sum_{i=1}^{n} \sum_{j=1 \atop j\neq i}^{n-1} \sum_{k=j+1 \atop k\neq i}^{n} S_i^2 S_j S_k E\{F_i^2 F_j F_k\}$$

$$+ 24 \sum_{i=1}^{n-3} \sum_{j=i+1}^{n-2} \sum_{k=j+1}^{n-1} \sum_{\ell=k+1}^{n} S_i S_j S_k S_\ell E\{F_i F_j F_k F_\ell\} \tag{5.4.4}$$

Evaluation of the joint moments of force given on the right hand side of Eqs. (5.4.3) and (5.4.4) may be achieved by expansion of the arguments in terms of the X variables using Eq. (5.2.2). The resulting expectations of X must then be determined in terms of the cross-covariances of X, R_{ij}, which are known, as illustrated in Section 5.2.1.

Following this procedure it can be easily shown that expressions for a total of 23 expectations are required as follows:

$$E1 = E\{X_i^4\}$$
$$E2 = E\{X_i^8\}$$
$$E3 = E\{X_i\ X_j\}$$
$$E4 = E\{X_i^2\ X_j^2\}$$
$$E5 = E\{X_i^3\ X_j\}$$
$$E6 = E\{X_i^4\ X_j^2\}$$
$$E7 = E\{X_i^4\ X_j^4\}$$
$$E8 = E\{X_i|X_i|X_j\}$$
$$E9 = E\{X_i^5|X_i|X_j\}$$
$$E10 = E\{X_i|X_i|X_j^3\}$$
$$E11 = E\{X_i|X_i|X_j|X_j|\}$$
$$E12 = E\{X_i^5|X_i|X_j|X_j|\}$$
$$E13 = E\{X_i^2\ X_j\ X_k\}$$
$$E14 = E\{X_i^4\ X_j\ X_k\}$$
$$E15 = E\{X_i|X_i|X_j^2\ X_k\}$$
$$E16 = E\{X_i|X_i|X_j^4\ X_k\}$$
$$E17 = E\{X_i|X_i|X_j|X_j|X_k^2\}$$
$$E18 = E\{X_i|X_i|X_j|X_j|X_k^4\}$$
$$E19 = E\{X_i\ X_j\ X_k\ X_\ell\}$$
$$E20 = E\{X_i|X_i|X_j\ X_k\ X_\ell\}$$
$$E21 = E\{X_i|X_i|X_j|X_j|X_k\ X_\ell\}$$
$$E22 = E\{X_i|X_i|X_j|X_j|X_k|X_k|X_\ell\}$$
$$E23 = E\{X_i|X_i|X_j|X_j|X_k|X_k|X_\ell|X_\ell|\}$$

5.4.1 Solution of Expectations E1 to E23

From Eq. (I.33), Appendix One:

$$\underline{E1} = \underline{E\{X_i^4\}} = 3R_{ii}^2 \tag{5.4.5}$$

$$\underline{E2} = \underline{E\{X_i^8\}} = 105R_{ii}^4 \tag{5.4.6}$$

The first bi-variate moment is the basic result:

$$\underline{E3} = \underline{E\{X_i\ X_j\}} = R_{ij} \tag{5.4.7}$$

Other bi-variate moments require application of Price's theorem (Eq. (I.60), Appendix One) for solution:

$$\underline{E4} = \underline{E\{X_i^2\ X_j^2\}} = 4\int_0^{R_{ij}} E\{X_i\ X_j\}\, dR_{ij} + E\{X_i^2\}\ E\{X_j^2\}$$
$$= 2R_{ij}^2 + R_{ii}\ R_{jj} \tag{5.4.8}$$

and similarly:

$$\underline{E5} = \underline{E\{X_i^3\ X_j\}} = 3R_{ii}\ R_{ij} \tag{5.4.9}$$

$$\underline{E6} = \underline{E\{X_i^4\ X_j^2\}} = 3R_{ii}(4R_{ij}^2 + R_{ii}\ R_{jj}) \tag{5.4.10}$$

$$\underline{E7} = \underline{E\{X_i^4 X_j^4\}} = 24R_{ij}^4 + 9R_{ii} R_{jj}(8R_{ij}^2 + R_{ii} R_{jj}) \qquad (5.4.11)$$

Moments E8 to E10 are solved using the following property[78]:

$$E\{g_1 g_2, \ldots, g_n\} = E\{g_1 g_2, \ldots, g_{n-1} E\{g_n | X_1 X_2, \ldots, x_{n-1}\}\} \qquad (5.4.12)$$

where g_i is an arbitrary function of X_i and $E\{g_n|X_1 X_2, \ldots, X_{n-1}\}$ is the expected value of g_n given the values of X_1 to X_{n-1}.

Hence:

$$\underline{E8} = \underline{E\{X_i|X_i|X_j\}} = E\{X_i|X_i|E\{X_j|X_i\}\}$$

and the conditional mean value, $E\{X_j|X_i\}$ is obtained from Eq. (I.55), Appendix One, yielding:

$$E8 = \frac{R_{ij}}{R_{ii}} E\{|X_i^3|\}$$

and using Eq. (I.34), Appendix One:

$$\underline{E8} = \frac{4}{\sqrt{2\pi}} R_{ii}^{1/2} R_{ij} \qquad (5.4.13)$$

Similarly:

$$\underline{E9} = \underline{E\{X_i^5|X_i|X_j\}} = \frac{96}{\sqrt{2\pi}} R_{ii}^{5/2} R_{ij} \qquad (5.4.14)$$

Applying Price's theorem, using Eq. (5.4.12) and Eqs. (I.58) and (I.34), Appendix One:

$$\underline{E10} = \underline{E\{X_i|X_i|X_j^3\}} = \frac{4}{\sqrt{2\pi}} \frac{R_{ij}}{R_{ii}^{1/2}}(3R_{ii} R_{jj} + R_{ij}^2) \qquad (5.4.15)$$

Solution of the remaining bi-variate moments is more complex than for the above and it is, therefore, instructive to develop the solution for E11 in detail here.

Applying Price's theorem:

$$\underline{E11} = \underline{E\{X_i|X_i|X_j|X_j|\}} = 4 \int_0^{R_{ij}} E\{|X_i X_j|\}\, dR_{ij} + E\{X_i|X_i|\}\, E\{X_j|X_j|\} \qquad (5.4.16)$$

and from the mean-zero symmetrical nature of X_i and X_j:

$$E\{X_i|X_i|\} = E\{X_j|X_j|\} = 0$$

Applying Price's theorem to the argument of the integral in Eq. (5.4.16):

$$E\{|X_i\ X_j|\} = \int_0^{R_{ij}} E\{\text{sign}(X_i)\ \text{sign}(X_j)\}\ dR_{ij} + E\{|X_i|\}\ E\{|X_j|\} \qquad (5.4.17)$$

and $E\{|X_i|\}$, $E\{|X_j|\}$ are obtained from Eq. (I.34), Appendix One,

also $\frac{\partial}{\partial X_i}\{\text{sign}(X_i)\} = 2\delta(X_i)$ where $\delta(.)$ is the dirac delta function.

Thus applying Price's theorem to the argument in the integral of Eq. (5.4.17):

$$E\{\text{sign}(X_i)\ \text{sign}(X_j)\} = 4\int_0^{R_{ij}} E\{\delta(X_i)\ \delta(X_j)\}\ dR_{ij} + E\{\text{sign}(X_i)\}\ E\{\text{sign}(X_j)\} \qquad (5.4.18)$$

and $E\{\text{sign}(X_i)\} = 0$

also $E\{\delta(X_i)\ \delta(X_j)\} = \int_{-\infty}^{\infty}\int_{-\infty}^{\infty} \delta(X_i)\ \delta(X_j)\ p(X_i\ X_j)\ dX_i\ dX_j$

$$= p(X_i = 0,\ X_j = 0)$$

From Eq. (I.53), Appendix One:

$$p(X_i = 0,\ X_j = 0) = 1/[2\pi(R_{ii}\ R_{jj})^{1/2}\ (1 - r^2)^{1/2}] \qquad (5.4.19)$$

where $r = R_{ij}/(R_{ii}\ R_{jj})^{1/2}$ (5.4.20)

Hence, substituting successively from Eq. (5.4.19) to (5.4.16) yields:

$$\underline{E11} = \frac{R_{ii}\ R_{ij}}{\pi}\ [(4r^2 + 2)\ \text{arc sin}\ r + 6r(1 - r^2)^{1/2}] \qquad (5.4.21)$$

a result previously obtained by Borgman[60].

Following the same procedure:

$$\underline{E12} = \underline{E\{X_i^5 |X_i| X_j |X_j|\}} = \frac{2R_{ii}^3 R_{jj}}{\pi}\{15 \arcsin r(1 + 6r^2)$$

$$+ r(1 - r^2)^{1/2} (81 + 28r^2 - 2r^4)\} \quad (5.4.22)$$

The remaining expectations involve more than two variables and must, therefore, be reduced, if possible, to expressions involving only two variables, by substitution using Eq. (5.4.12), to enable the application of Price's theorem as applied above. With reference to Section I.3.3.3, Appendix One, it is apparent that in its general form Price's theorem covers multi-variate expectations of any order. However, attempts to apply this directly to expectations in three and four variables result in third and fourth order differential equations, the solutions of which proved to be more difficult to obtain than the solutions to the bi-variate problem which results from the above substitution.

$$\underline{E13} = \underline{E\{X_i^2 X_j X_k\}} = E\{X_i^2 X_j E\{X_k|X_i X_j\}\}$$

and using Eq. (I.55), Appendix One:

$$E\{X_k|X_i X_j\} = a_i X_i + a_j X_j \quad (5.4.23)$$

where $a_i = (R_{jj} R_{ik} - R_{ij} R_{jk})/(R_{ii} R_{jj} - R_{ij}^2)$

$$a_j = (R_{ii} R_{jk} - R_{ij} R_{ik})/(R_{ii} R_{jj} - R_{ij}^2)$$

Hence:

$$\underline{E13} = \underline{E\{X_i^2 X_j X_k\}} = a_i(E5) + a_j(E4) \quad (5.4.24)$$

Similarly:

$$\underline{E14} = \underline{E\{X_i^4 X_j X_k\}} = 15a_i R_{ii}^2 R_{ij} + a_j(E6) \quad (5.4.25)$$

$$\underline{E15} = \underline{E\{X_i |X_i| X_j^2 X_k\}} = \frac{4a_i}{\sqrt{2\pi}} R_{ii}^{1/2}(3R_{ij}^2 + R_{ii} R_{jj}) + a_j(E10) \quad (5.4.26)$$

$$\underline{E16} = \underline{E\{X_i |X_i| X_j^4 X_k\}} = \frac{4R_{ii} R_{jj}^2}{\sqrt{2\pi}} [3a_i R_{ii}^{1/2}(r^4 + 6r^2 + 1)$$

$$+ a_j R_{jj}^{1/2} r(15 + 10r^2 - r^4)] \quad (5.4.27)$$

Solution of E17 requires the expression for the conditional second moment given in Eq. (I.58), Appendix One:

$$\underline{E17} = \underline{E\{X_i|X_i|X_j|X_j|X_k^2\}} = E\{X_i|X_i|X_j|X_j|\ E\{X_k^2|X_i\ X_j\}\}$$

$$= [R_{kk} - (a_i\ R_{ik} + a_j\ R_{jk})]\ E\{X_i|X_i|X_j|X_j|\}$$

$$+ a_i^2\ E\{X_i^3|X_i|X_j|X_j|\} + 2a_i\ a_j\ E\{|X_i^3\ X_j^3|\}$$

$$+ a_j^2\ E\{X_i|X_i|X_j^3|X_j|\} \qquad (5.4.28)$$

where $E\{X_i|X_i|X_j|X_j|\}$ is E11

and applying Price's theorem:

$$E\{X_i^3|X_i|X_j|X_j|\} = \frac{2R_{ii}^2\ R_{jj}}{\pi}\ [(12r^2 + 3)\ \text{arc sin}\ r + r(1 - r^2)^{1/2}.\ (2r^2 + 13)] \qquad (5.4.29)$$

$$E\{|X_i^3\ X_j^3|\} = \frac{R_{ii}^{3/2}\ R_{jj}^{3/2}}{\pi}\ [6r\ \text{arc sin}\ r(2r^2 + 3) + (1 - r^2)^{1/2}.\ (22r^2 + 8)] \qquad (5.4.30)$$

$E\{X_i|X_i|X_j^3|X_j|\}$ is obtained by comparison with Eq. (5.4.29).

Expectation E18 requires an expression for the conditional fourth moment which follows from extension of the procedure in Section I.3.3.2, Appendix One, by considering the third and fourth central moments.

Retaining the notation of Appendix One for Gaussian variables x_o to x_n the conditional mean of x_o is $\bar{x}_{oc} = E\{x_o|x_1, \ldots, x_n\}$ and the conditional variance, or second central moment, is $\sigma_{oc}^2 = E\{(x_o - \bar{x}_{oc})^2|x_1, \ldots, x_n\}$, expressions for these moments, and the resulting conditional second moment:

$$E\{x_o^2|x_1, \ldots, x_n\} = \sigma_{oc}^2 + \bar{x}_{oc}^2$$

are given in Section I.3.3.2, Appendix One, the conditional mean and second moment having been used in the preceding derivations.

Since the conditional distribution $p(x_o|x_1, \ldots, x_n)$ is Gaussian in form the third central moment must be zero, hence:

$$E\{(x_o - \bar{x}_{oc})^3 | x_1, \ldots, x_n\} = E\{(x_o^3 - 3x_o^2\,\bar{x}_{oc} + 3x_o\,\bar{x}_{oc}^2 - \bar{x}_{oc}^3) | x_1, \ldots, x_n\}$$

$$= E\{x_o^3 | x_1, \ldots, x_n\} - 3\bar{x}_{oc}\,E\{x_o^2 | x_1, \ldots, x_n\}$$

$$+ 3\bar{x}_{oc}^2\,E\{x_o | x_1, \ldots, x_n\} - \bar{x}_{oc}^3$$

$$= 0$$

and substituting from above:

$$E\{x_o^3 | x_1, \ldots, x_n\} = \bar{x}_{oc}[3\sigma_{oc}^2 + \bar{x}_{oc}^2] \qquad (5.4.31)$$

From Eq. (I.33), Appendix One, the fourth central moment will be:

$$E\{(x_o - \bar{x}_{oc})^4 | x_1, \ldots, x_n\} = 3\sigma_{oc}^4$$

and expanding the expectation in the above manner:

$$E\{x_o^4 | x_1, \ldots, x_n\} = 3\sigma_{oc}^4 + 6\sigma_{oc}^2\,\bar{x}_{oc}^2 + \bar{x}_{oc}^4 \qquad (5.4.32)$$

Returning to expectation E18:

$$\underline{E18} = \underline{E\{X_i | X_i | X_j | X_j | X_k^4\}} = E\{X_i | X_i | X_j | X_j |\ E\{X_k^4 | X_i\ X_j\}\}$$

and using Eq. (5.4.32) in conjunction with Eqs. (I.55) and (I.57), Appendix One:

$$\underline{E18} = \{3[R_{kk} - (a_i\,R_{ik} + a_j\,R_{jk})]^2\,E\{X_i | X_i | X_j | X_j |\}$$

$$+ 6[R_{kk} - (a_i\,R_{ik} + a_j\,R_{jk})]\ [a_i^2\,E\{X_i^3 | X_i | X_j | X_j |\}$$

$$+ 2a_i\,a_j\,E\{|X_i^3\,X_j^3|\} + a_j^2\,E\{X_i | X_i | X_j^3 | X_j |\}]$$

$$+ a_i^4\,E\{X_i^5 | X_i | X_j | X_j |\} + 4a_i^3\,a_j\,E\{|X_i^5 | X_j^3|\}$$

$$+ 6a_i^2\,a_j^2\,E\{X_i^3 | X_i | X_j^3 | X_j |\} + 4a_i\,a_j^3\,E\{|X_i^3\,X_j^5|\}$$

$$+ a_j^4\,E\{X_i | X_i | X_j^5 | X_j |\}\} \qquad (5.4.33)$$

where $E\{X_i|X_i|X_j|X_j|\}$ is E11

$E\{X_i^3|X_i|X_j|X_j|\}$ is given by Eq. (5.4.29)

$E\{|X_i^3\ X_j^3|\}$ is given by Eq. (5.4.30)

$E\{X_i^5|X_i|X_j|X_j|\}$ is E12

and applying Price's theorem:

$$E\{X_i^3|X_i|X_j^3|X_j|\} = \frac{2R_{ii}^2\ R_{jj}^2}{\pi}\ [3 \text{ arc sin } r(8r^4 + 24r^2 + 3)$$

$$+ r(1 - r^2)^{1/2}\ (50r^2 + 55)] \qquad (5.4.34)$$

and

$$E\{|X_i^5\ X_j^3|\} = \frac{2R_{ii}^{5/2}\ R_{jj}^{3/2}}{\pi}\ [15r \text{ arc sin } r(4r^2 + 3) + 5(1 - r^2)^{1/2}.$$

$$(4r^2 + 17) - 3(1 - r^2)^{3/2}\ (2r^2 + 23)] \qquad (5.4.35)$$

The remaining expectations, E19 to E23, involve four variables and, therefore, require a double application of Eq. (5.4.12).

So far, for conditional statistics, coefficients a_i and a_j have been used for the description of moments of X_k conditional on X_i and X_j. In the following coefficients b_i, b_j and b_k are required for description of the moments of X_ℓ conditional on X_i, X_j, X_k and with reference to Section I.3.3.2, Appendix One, are obtained as solution to:

$$[R]\ \{b\} = \{R_{(\ell)}\} \qquad (5.4.36)$$

where $[R]$ is the matrix of cross-covariances of variables X_i, X_j, X_k;
$\{b\} = (b_i\ b_j\ b_k)^T$; and
$\{R_{(\ell)}\} = (R_{i\ell}\ R_{j\ell}\ R_{k\ell})^T$.

Hence, using Eq. (I.55), Appendix One:

$$\underline{E19} = \underline{E\{X_i\ X_j\ X_k\ X_\ell\}} = E\{X_i\ X_j\ X_k\ E\{X_\ell|\ X_i\ X_j\ X_k\}\}$$

$$= b_i\ E\{X_i^2\ X_j\ X_k\} + b_j\ E\{X_i\ X_j^2\ X_k\} + b_k\ E\{X_i\ X_j\ X_k^2\} \qquad (5.4.37)$$

where expectations are of the form E13.

$$\underline{E20} = \underline{E\{X_i|X_i|X_j\,\underline{X_k}\,\underline{X_\ell}\}} = b_i\,E\{|X_i^3|X_j\,X_k\} + b_j\,E\{X_i|X_i|X_j^2\,X_k\}$$

$$+ b_k\,E\{X_i|X_i|X_j\,X_k^2\} \tag{5.4.38}$$

where $$E\{|X_i^3|X_j\,X_k\} = a_i\,E\{X_i^3|X_i|X_j\} + a_j\,E\{|X_i^3|X_j^2\} \tag{5.4.39}$$

$$E\{X_i|X_i|X_j^2\,X_k\} = a_i\,E\{|X_i^3|X_j^2\} + a_j\,E\{X_i|X_i|X_j^3\} \tag{5.4.40}$$

$$E\{X_i|X_i|X_j\,X_k^2\} = E\{X_i|X_i|X_k^2\,E\{X_j|X_i\,X_k\}\}$$

$$= c_i\,E\{|X_i^3|X_k^2\} + c_k\,E\{X_i|X_i|X_k^3\} \tag{5.5.41}$$

with c_i and c_k the solutions to:

$$[R]\,\{c\} = \{R_{(j)}\} \tag{5.4.42}$$

where [R] is the matrix of covariances of variables X_i, X_k

$\{c\} = (c_i,\ c_k)^T$

$\{R_{(j)}\} = (R_{ij}\ R_{jk})^T$

The expectations on the right hand side of Eqs. (5.4.39) to (5.4.41) are of the form:

$$E\{X_i|X_i|X_j^3\} = E10$$

$$E\{|X_i^3|X_j^2\} = \frac{4R_{ii}^{1/2}}{\sqrt{2\pi}}\,(3R_{ij}^2 + R_{ii}\,R_{jj}) \tag{5.4.43}$$

which is obtained in the derivation of E15, and applying Price's theorem:

$$E\{X_i^3|X_i|X_j\} = \frac{16R_{ii}^{3/2}\,R_{ij}}{\sqrt{2\pi}} \tag{5.4.44}$$

$$\underline{E21} = \underline{E\{X_i|X_i|X_j|X_j|X_k\,\underline{X_\ell}\}}$$

$$= b_i\,E\{|X_i^3|X_j|X_j|X_k\} + b_j\,E\{X_i|X_i||X_j^3|X_k\}$$

$$+ b_k\,E\{X_i|X_i|X_j|X_j|X_k^2\} \tag{5.4.45}$$

The first two expectations on the right hand side are of the same form and may be expanded as follows:

$$E\{|X_i^3|X_j|X_j|X_k\} = a_i\ E\{X_i^3|X_i|X_j|X_j|\} + a_j\ E\{|X_i^3\ X_j^3|\}$$

the expectations on the right hand side being given by Eqs. (5.4.29) and (5.4.30).

The final expectation in Eq. (5.4.45), $E\{X_i|X_i|X_j|X_j|X_k^2\}$, is E17.

$$\underline{E22} = \underline{E\{X_i|X_i|X_j|X_j|X_k|X_k|X_\ell\}}$$

$$= b_i\ E\{|X_i^3|X_j|X_j|X_k|X_k|\} + b_j\ E\{X_i|X_i||X_j^3|X_k|X_k|\}$$

$$+ b_k\ E\{X_i|X_i|X_j|X_j||X_k^3|\} \qquad (5.4.46)$$

In order to expand the expectations on the right hand side it is necessary to determine the conditional expectations of the form $E\{X_k|X_k|\,\big|\,X_i\ X_j\}$ or alternatively $E\{|X_k^3|\,\big|\,X_i\ X_j\}$.

It can be shown that the former expectation may be expressed as:

$$E\{X_k|X_k|\,\big|\,X_i\ X_j\} = [R_{kk} - (a_i\ R_{ik} + a_j\ R_{jk})].[(1 + \Omega^2)\ (1 - 2Q(\Omega))$$

$$+ 2\Omega Z(\Omega)] \qquad (5.4.47)$$

where $\Omega = (a_i\ X_i + a_j\ X_j)/[R_{kk} - (a_i\ R_{ik} + a_j\ R_{jk})]^{1/2}$

$$Z(\alpha) = \frac{1}{\sqrt{2\pi}} \exp\{-\frac{1}{2}\alpha^2\}$$

$$Q(\alpha) = \int_\alpha^\infty Z(\lambda)\ d\lambda$$

Clearly, the presence of functions of the form of $Z(\Omega)$ and $Q(\Omega)$ prevent any further expansion of Eq. (5.4.46), following substitution by Eq. (5.4.47) along the lines of the method adopted so far. Similar difficulties are also likely to be experienced in an expansion of $E\{|X_k^3|X_i\ X_j\}$.

$$\underline{E23} = \underline{E\{X_i|X_i|X_j|X_j|X_k|X_k|X_\ell|X_\ell|\}}$$

Expansion of this requires the conditional expectation, $E\{X_\ell|X_\ell|\,\big|\,X_i\ X_j\ X_k\}$ which will have a similar form to Eq. (5.4.47) and direct solution is, therefore, also prevented.

Attempts were made to solve E22 and E23 by direct application of the general multi-variate form of Price's theorem. However, the shear complexity of the problem results in practically unsurmountable difficulties, as might be appreciated from the formulation of the problem for E23 given below:

Repeated application of Price's theorem, Eq. (I.59) Appendix one yields

$$\frac{\partial^6(E23)}{\Pi\partial R} = (\text{const})\ E\{\delta(X_i)\ \delta(X_j)\ \delta(X_k)\ \delta(X_\ell)\} \qquad (5.4.48)$$

where $\partial^6(.)/\Pi\partial R$ represents a product of derivatives of cross-covariances of variables X_i, X_j, X_k and X_ℓ.

From Eq. (5.2.3):

$$E\{\delta(X_i)\ \delta(X_j)\ \delta(X_k)\ \delta(X_\ell)\} = \frac{1}{2\pi^2\ \sqrt{\text{Det }[M]}} \qquad (5.4.49)$$

where [M] = matrix of covariances of variables X_i, X_j, X_k and X_ℓ.

At least 13 possible combinations of partial derivatives may yield the right hand side of Eq. (5.4.48) from (E23) as follows:

$$\Pi\partial R = \partial R^3_{ij}\ \partial R^3_{k\ell};\ \ \partial R^3_{ik}\ \partial R^3_{j\ell};\ \partial R^3_{i\ell}\ \partial R^3_{jk};\ \partial R^2_{ij}\ \partial R^2_{k\ell}\ \partial R_{ik}\ \partial R_{j\ell};$$

$$\partial R^2_{ij}\ \partial R^2_{k\ell}\ \partial R_{i\ell}\ \partial R_{jk};\ \partial R^2_{ik}\ \partial R^2_{j\ell}\ \partial R_{ij}\ \partial R_{k\ell};\ \partial R^2_{ik}\ \partial R^2_{j\ell}\ \partial R_{i\ell}\ \partial R_{jk};$$

$$\partial R^2_{i\ell}\ \partial R^2_{jk}\ \partial R_{ij}\ \partial R_{k\ell};\ \partial R^2_{i\ell}\ \partial R^2_{jk}\ \partial R_{ik}\ \partial R_{j\ell};$$

$$\partial R_{ij}\ \partial R_{ik}\ \partial R_{i\ell}\ \partial R_{jk}\ \partial R_{j\ell}\ \partial R_{k\ell};\ \partial R_{ii}\ \partial R_{jj}\ \partial R_{kk}\ \partial R_{\ell\ell}\ \partial R_{ij}\ \partial R_{k\ell};$$

$$\partial R_{ii}\ \partial R_{jj}\ \partial R_{kk}\ \partial R_{\ell\ell}\ \partial R_{ik}\ \partial R_{j\ell};\ \partial R_{ii}\ \partial R_{jj}\ \partial R_{kk}\ \partial R_{\ell\ell}\ \partial R_{i\ell}\ \partial R_{jk}$$

The value of E23 must, therefore, satisfy each of the 13 solutions from six-fold integration of the right hand side of Eq. (5.4.49) with respect to the covariances in the above groups.

Solution of E22 and E23 by Numerical Integration

In the absence of closed-form solutions for expectations E22 and E23, their values have been obtained by numerical integration over the relevant probability spaces.

The unsolved expectations on the right hand side of Eq. (5.4.46), describing E22, may be obtained from the tri-variate space of X_i, X_j and X_k, for example:

$$E\{|X_i^3|X_j|X_j|X_k|X_k|\} = \int_{-\infty}^{\infty}\int\int \{|X_i^3|X_j|X_j|X_k|X_k|\}\, p(X_i\, X_j\, X_k)\, dX_i\, dX_j\, dX_k \tag{5.4.50}$$

Similarly, the other expectations following in an identical manner:

$$E23 = \int_{-\infty}^{\infty}\int\int\int\int \{X_i|X_i|X_j|X_j|X_k|X_k|X_\ell|X_\ell|\}\, p(X_i\, X_j\, X_k\, X_\ell)\, dX_i\, dX_j\, dX_k\, dX_\ell \tag{5.4.51}$$

the multi-variate pdf. of the mean-zero Gaussian random variables in the above equations is obtained from Eq. (I.53), Appendix One.

5.4.2 Method of Computation and Limitations on Structure Complexity

Program OS19 was developed for the computation of the moments of response from input covering structure and short-term sea state conditions. The notation used for the expectations of variables X in the program differs from the E1-E23 notation used herein but use of multiple comment statements, with the arguments of expectations printed, prevents serious confusion.

Numerical integration over the 3 and 4-dimensional probability spaces for E22 and E23, respectively, according to Eqs. (5.4.50) and (5.4.51), is performed by constant step integration using Rectangular Rule summations. For each cycle of integration the relevant conditional probability distribution is Gaussian in form. Therefore, to centre the computations over the significant range of this probability mass the integration is performed over a range of ±5 standard deviations of this conditional distribution about its conditional mean value, these moments being obtained from Eqs. (I.55) and (I.57), Appendix One.

Table 5.4.1 illustrates the sensitivity of the numerical integrations to the number of steps chosen. In the Table, E18 is included in place of E22 to illustrate the numerically derived tri-variate expectation since in the initial investigation the closed-form solution of E18 had not been

obtained and numerical integration was, therefore, required. Although the results presented in the Table correspond to a particular set of member conditions, they may be considered to be generally representative of any application. This follows because the probability spaces considered will be Gaussian for any member conditions and the standardisation of the grid of integration points, resulting from the use of conditional mean and variance for definition of the integration limits, will account for differing correlations between the variables present in each application.

From Table 5.4.1 it is seen that constant step integration using only 11 steps yields results for the numerically derived expectations which depart by less than 0.13% from the values obtained by 35 steps, which represents the most sensitive integration possible in the run-times available and may be considered to be the 'exact' solution. Values of E18 derived numerically using 11 steps were subsequently found to be within at worst 1% of the values obtained analytically. The inaccuracy associated with the 11 step integration is, therefore, considered to be sufficiently small for practical purposes to justify its usage and thereby minimise computer run-times.

Computer Run-time Requirements

As mentioned above when numerical integration with 35 steps in each cycle of integration is applied only systems of up to four nodes can be analysed in the 30 minute run-times available on the ICL 1906S computer at the University of Liverpool. Reduction in the number of steps to 11 enables the analysis of systems comprising of up to 12 nodes.

From the above statements it may be inferred that much of the time consumption in the computer program is used in the numerical integration associated with solution of expectations of the form of E22 and E23. This may be illustrated from Table 5.4.2 which shows the number of combinations of the second and fourth order expectations of force resulting from the moments of response through Eqs. (5.4.3) and (5.4.4). It can be easily shown that expectations of the form E22 are present in the expansion of force expectations $E\{F_p^2 F_q F_r\}$ and $E\{F_p F_q F_r F_s\}$ while E23 results only from the latter. For example, expanding the three and four-variate expectations in Eq. (5.4.4) in terms of variables X using Eq. (5.2.1) for the set p = 1, q = 2, r = 3, s = 4:

$$E\{F_1^2\ F_2\ F_3\} = E\{X_1^4\ X_3|X_3|X_5|X_5| + X_1^4\ X_4\ X_5|X_5| + \underline{2X_1|X_1|X_2|X_3|X_3|X_5|X_5|}$$
$$+ 2X_1|X_1|X_2\ X_4\ X_5|X_5| + X_2^2\ X_3|X_3|X_5|X_5| + X_2^2\ X_4\ X_5|X_5|$$
$$+ X_1^4\ X_3|X_3|X_6 + X_1^4\ X_4\ X_6 + 2X_1|X_1|X_2\ X_3|X_3|X_6$$
$$+ 2X_1|X_1|X_2\ X_4\ X_6 + X_2^2\ X_3|X_3|X_6 + X_2^2\ X_4\ X_6\} \quad (5.4.52)$$

$$E\{F_1\ F_2\ F_3\ F_4\} = E\{\underline{X_1|X_1|X_3|X_3|X_5|X_5|X_7|X_7|} + \underline{X_1|X_1|X_3|X_3|X_5|X_5|X_8}$$
$$+ \underline{X_1|X_1|X_3|X_3|X_6|X_7|X_7|} + X_1|X_1|X_3|X_3|X_6\ X_8$$
$$+ X_1|X_1|X_4\ X_5|X_5|X_7|X_7| + X_1|X_1|X_4\ X_5|X_5|X_8$$
$$+ X_1|X_1|X_4\ X_6\ X_7|X_7| + X_1|X_1|X_4\ X_6\ X_8$$
$$+ \underline{X_2\ X_3|X_3|X_5|X_5|X_7|X_7|} + X_2\ X_3|X_3|X_5|X_5|X_8$$
$$+ X_2\ X_3|X_3|X_6\ X_7|X_7| + X_2\ X_3|X_3|X_6\ X_8 + X_2\ X_4\ X_5|X_5|X_7|X_7|$$
$$+ X_2\ X_4\ X_5|X_5|X_8 + X_2\ X_4\ X_6\ X_7|X_7| + X_2\ X_4\ X_6\ X_8\} \quad (5.4.53)$$

Arguments forming expectations of the form of E22 and E23 are underlined. Variables with odd numbered subscripts are related to the water particle velocities through Eq. (5.2.2) and it can be deduced from the above expressions that, following the expansion of expectations E22 in the manner of Eq. (5.4.46), the numerical integrations are required for combinations of these variables only. Furthermore, all expectations associated with E22 from Eq. (5.4.53) may be solved within the cycles of numerical integration for expectation E23.

In Section 5.4.4 approximations for expectations E22 and E23 are considered which may be solved in closed-form obviating the need for numerical integration. However, due to the considerable rate of growth of the number of terms to be computed as n increases, illustrated in Table 5.4.2, the upper ceiling on system complexity appears to be approximately 35 nodes within the existing run-times available.

5.4.3 Validation of the Theoretical Moments and Some Properties of Response for Simple Systems

Comparison of the theoretical moments (derived through the procedure of Section 5.4.1 using Program OS19) for systems of 2-nodes with the moments obtained from the marginal pdf.s (resulting from the numerically derived bi-variate response domain, using the techniques of Section 5.3.4), provides a check on the expressions for all but the three and four-variate expectations of force, as may be deduced from Table 5.4.2. Such a procedure, as illustrated by both sets of moments in Figs. 5.3.8 to 5.3.10, confirms the validity of the theoretical moments since differences are in all cases within about 2%.

Further confirmation is presented in Fig. 5.4.1 which illustrates the variations in the statistics of total force on two unit length cylinders at the same depth of immersion with change in horizontal spacing. Standard deviation and kurtosis are used in place of the second and fourth moments in the figure and the corresponding values from the marginal pdf.s are indicated by circles and crosses, respectively.

Also included in the figure is the correlation coefficient between the component forces and Fig. 5.4.2 shows the corresponding coefficients between the water particle kinematics at the load points. It may be deduced from these relationships that the statistical properties of response for these conditions are governed largely by the correlation between the velocity pair and the acceleration pair with little weight attached to the correlation between velocity at one member and acceleration at the other.

Fig. 5.4.3 shows a similar plot to Fig. 5.4.1 for different member conditions. In both these figures the values of theoretical standard deviation ($\sigma_Y = \sqrt{E\{Y^2\}}$) and the estimate from the marginal pdf. are in close agreement whilst the corresponding values of kurtosis ($\beta_Y = E\{Y^4\}/[E\{Y^2\}]^2$) are lower from the marginal pdf.s. The major part of the deviation in the estimates of β_Y can be shown to be a result of the finite truncation on the range of response applied in the bi-variate approach, a value of $8\sigma_Y$ being used herein as discussed in Section 5.3. Clearly the effect of omission of high response levels above the truncation point, with corresponding small probability densities, is greater for the fourth statistical moment than for the second by virtue of the increased weightings. In fact, the effect of the truncation is negligible for the latter moment as reflected in the agreement between the value of σ_Y in Figs. 5.4.1, 5.4.3 and Figs. 5.3.8 to 5.3.10. However, the truncation is seen to be the major cause of the under-estimation of β_Y by consideration of Fig. 5.4.4, where the deviation between the statistical moments obtained from histograms of the Pierson/Holmes distribution and the true moments defining the pdf. are compared. The histograms cover the same range of the variable, 8σ, as applied in the bi-variate approach of Section 5.3 and it can be seen that the under-estimations observed in β_Y are of the same order of magnitude as those inferred from Fig. 5.4.4.

Fig. 5.4.5 indicates the variation of σ and β for the force per unit length of a 0.5m. diameter member with change in the depth of immersion below still water level. Fig. 5.4.6 indicates the variation in statistics of response for bi-variate loading with variation in the elevations of the members and, as with Figs. 5.4.1 and 5.4.3, values obtained from the marginal distributions are included. Again, the deviations in β are caused largely by the upper truncation of the range of response considered.

The above investigation has confirmed the validity of those theoretical expressions derived in Section 5.4.1 and programmed in OS19, for the second and fourth moments of response, which are utilised for two component systems. The remaining expressions, in the fourth moment, resulting from the three and four force variate expectations in Eq. (5.4.4) have been verified by ensuring that:

i) a kurtosis of 3.0 results for inertia dominated systems of three or four components;

ii) the kurtosis of total load from a system of four unit length members of identical diameter all grouped at practically the same location in space, is equivalent to that which would result from load on a single such member located at the centroid of the four member group.

To illustrate how this latter requirement is satisfied, consider 0.5m. diameter members in 150m. of water with x/z space co-ordinates according to Fig. 5.3.1 of (99m/142.5m), (101m/142.5m), (100m/143.5m) and (100m/141.5m). Defining the loads on each of these members, when subject to a sea state with $H_{1/3}$ = 9.3m, as F_1 - F_4 then $Y = 0.25(F_1 + F_2 + F_3 + F_4)$ is equivalent to the load, F_5, on an identical member at location (100m/142.5m) for which, $E\{F_5^2\} = 1.941 \times 10^5$ N^2 and $\beta_{F_5} = 7.963$.

Using Program OS19 with 11 step numerical integration the corresponding properties of Y are, $E\{Y^2\} = 1.944 \times 10^5$ N^2 and $\beta_Y = 7.973$, within 0.15% of the above values, the slight differences resulting from the minor deviations from 100% correlation between the particle motions at the nodes.

Further verification of the procedures results from their application to typical structures in Section 5.6 by comparison with moments obtained by mathematical time-series simulation.

Finally, to illustrate the application of the method to systems of up to 12 nodes, Fig. 5.4.7 is included which shows the variation in σ and β for total force on a varying length section of vertical piling idealised as a number of equally spaced load components.

5.4.4 Approximations for E22 and E23

An alternative approach to the use of numerical integration for the solution of expectations E22 and E23 is to employ a polynomial approximation for some of the $X|X|$ terms enabling evaluation in the manner applied for the other expectations.

Polynomial approximations for $X|X|$, resulting from minimisation of the 'mean-square' error in the statistical sense, are given by Borgman[79] as follows:

i) Linear approximation

$$X|X| \simeq \sqrt{\frac{8}{\pi}}\, R_{xx}^{1/2}\, X \qquad (5.4.54)$$

a result previously applied, in Section 3.2, for linearisation of the 'Morison' loading mechanism.

ii) Cubic approximation

$$X|X| \simeq \sqrt{\frac{2}{\pi}}\, (R_{xx}^{1/2}\, X + \frac{X^3}{3R_{xx}^{1/2}}) \qquad (5.4.55)$$

iii) Quintic approximation

$$X|X| \simeq \sqrt{\frac{2}{\pi}}\, (\frac{3}{4}\, R_{xx}^{1/2}\, X + \frac{X^3}{2R_{xx}^{1/2}} - \frac{X^5}{60R_{xx}^{3/2}}) \qquad (5.4.56)$$

These are plotted in Fig. 5.4.8 and it is evident that the linear approximation offers a reasonable solution only to about two standard deviations whilst the cubic is very accurate to more than three and the quintic is good to about four standard deviations.

Re-stating the unsolved expectations:

$$E22 = E\{X_i|X_i|X_j|X_j|X_k|X_k|X_\ell\} \tag{5.4.57}$$

$$E23 = E\{X_i|X_i|X_j|X_j|X_k|X_k|X_\ell|X_\ell|\} \tag{5.4.58}$$

Using substitution from Eqs. (5.4.55) to (5.4.56), approximations to these expectations may be obtained as follows:

'Linear' approximations for E22 and E23

Substituting for $X_k|X_k|$ from Eq. (5.4.55):

$$E22 \simeq \sqrt{\frac{8}{\pi}}\, R_{kk}^{1/2}\, E\{X_i|X_i|X_j|X_j|X_k\, X_\ell\}$$

$$\simeq \sqrt{\frac{8}{\pi}}\, R_{kk}^{1/2}(E21) \tag{5.4.59}$$

Substituting for $X_k|X_k|$ and $X_\ell|X_\ell|$ from Eq. (5.4.55):

$$E23 \simeq \frac{8}{\pi}\, R_{kk}^{1/2}\, R_{\ell\ell}^{1/2}(E21) \tag{5.4.60}$$

'Cubic' approximation for E22

Substituting for $X_k\, X_k$ from Eq. (5.4.55):

$$E22 \simeq \sqrt{\frac{2}{\pi}} \left[R_{kk}^{1/2}(E21) + \frac{1}{3R_{kk}^{1/2}}\, E\{X_i|X_i|X_j|X_j|X_k^3\, X_\ell\} \right] \tag{5.4.61}$$

and, using Eq. (5.4.12):

$$\begin{aligned} E\{X_i|X_i|X_j|X_j|X_k^3\, X_\ell\} &= E\{X_i|X_i|X_j|X_j|X_k^3\, E\{X_\ell|X_i\, X_j\, X_k\}\} \\ &= b_i\, E\{|X_i^3|X_j|X_j|X_k^3\} + b_j\, E\{X_i|X_i||X_j^3|X_k^3\} \\ &\quad + b_k\, E\{X_i|X_i|X_j|X_j|X_k^4\} \end{aligned} \tag{5.4.62}$$

where the b's are defined in Eq. (5.4.36):

$E\{X_i|X_i|X_j|X_j|X_k^4\}$ is E18

and the remaining expectations are of the same form, which may be expanded using Eqs. (5.4.12) and (5.4.31) as follows:

$$E\{|X_i^3|X_j|X_j|X_k^3\} = 3\sigma_{kc}^2\, a_i\, E\{X_i^3|X_i|X_j|X_j|\} + 3\sigma_{kc}^2\, a_j\, E\{|X_i^3\, X_j^3|\} + a_i^3\, E|X_i^5|X_i|X_j|X_j|\} + 3a_i^2\, a_j\, E\{|X_i^5\, X_j^3|\} + 3a_i\, a_j^2\, E\{X_i^3|X_i|X_j^3|X_j|\} + a_j^3\, E\{|X_i^3\, X_j^5|\} \quad (5.4.63)$$

where $\sigma_{kc}^2 = R_{kk} - (a_i R_{ik} + a_j R_{jk})$ from Eq. (I.57), Appendix One
a_i, a_j are defined with Eq. (5.4.23)
and the expectations of the r.h.s. of Eq. (5.4.63) have been derived previously for E18.

'Cubic/Linear' approximation for E23

Substituting from $X_k|X_k|$ from Eq. (5.4.54) and for $X_\ell|X_\ell|$ from Eq. (5.4.55):

$$E23 \simeq \frac{4}{\pi}\left[R_{kk}^{1/2}\, R_{\ell\ell}^{1/2}(E21) + \frac{R_{kk}^{1/2}}{3R_{\ell\ell}^{1/2}} E\{X_i|X_i|X_j|X_j|X_k\, X_\ell^3\} \right] \quad (5.4.64)$$

where the first expectation on the r.h.s. is E21 and the second expectation is of the form of Eq. (5.4.62).

(c) 'Cubic' Approximation for E23

Substituting for both $X_k|X_k|$ and $X_\ell|X_\ell|$ from Eq. (5.4.55):

$$E23 \simeq \frac{2}{\pi}\left[R_{kk}^{1/2}\, R_{\ell\ell}^{1/2}(E21) + \frac{R_{kk}^{1/2}}{3R_{\ell\ell}^{1/2}} E\{X_i|X_i|X_j|X_j|X_k\, X_\ell^3\} + \frac{R_{\ell\ell}^{1/2}}{3R_{kk}^{1/2}} E\{X_i|X_i|X_j|X_j|X_k^3\, X_\ell\} + \frac{1}{9R_{kk}^{1/2}\, R_{\ell\ell}^{1/2}} E\{X_i|X_i|X_j|X_j|X_k^3\, X_\ell^3\} \right] \quad (5.4.65)$$

where the middle two expectations are of the form of Eq. (5.4.62) and $E\{X_i|X_i|X_j|X_j|X_k^3\, X_\ell^3\}$ can be expanded using expressions for the conditional moments, as summarised in Appendix Five. However, this expansion yields some expectations the solution of which have not been ascertained to date.

Two additional versions of Program OS19 have been developed, one including the linear approximations for E22 and E23 and the other including the cubic approximation for E22 and the cubic/linear approximation for E23. Some typical results from these approaches are given in Table 5.4.3. It is seen that the cubic approximation for E22 offers a considerable improvement in accuracy over the linear approximator and for many terms is in very close agreement with the numerically computed values. However, for certain terms, notably (c), (i) and (j) in the table, the error is substantial. The reason for this behaviour is not clear but, fortunately, it appears to apply to the expectations with lower numerical values and hence their effect on the final moment is small. The approximators for E23 are evidently deficient, demonstrating the need for a higher order approximator.

The polynomial expressions considered so far represent the estimators which minimise the 'mean-square' error in a statistical sense. The linear estimator A, is the solution to:

$$\frac{\partial}{\partial A}\left[E\{(X|X| - A_1X)^2\}\right] = \frac{\partial}{\partial A}\left[\int_{-\infty}^{\infty} (X|X| - A_1X)^2\, p(X)\, dX\right] = 0$$

yielding:

$$A_1 = E\{|X^3|\}/E\{X^2\}$$

which, using Eqs. (I.33) and (I.34), Appendix One, gives the result in Eq. (5,4.54).

There is no reason to suppose that this value of A_1 should minimise the errors in the application of a linear approximation of E22 and E23. For example, in E22 the optimum linear approximator A_{22} might be considered as that which again minimises the 'mean-square' error:

$$\frac{\partial}{\partial A}\left[E\{X_i^4\, X_j^4\, X_\ell^2 (X_k|X_k| - A_{22}\, X_k)^2\}\right] = 0$$

hence

$$A_{22} = \frac{E\{X_i^4\, X_j^4\, X_\ell^2 |X_k^3|\}}{E\{X_i^4\, X_j^4\, X_\ell^2\, X_k^2\}} \qquad (5.4.66)$$

Following a similar procedure the best approximator for E23 may be defined as, A_{23}, the value minimising:

$$E\{X_i^4\, X_j^4 (X_k|X_k|X_\ell|X_\ell| - A_{23}\, X_k\, X_\ell)^2\}$$

No attempt has yet been made to obtain these optimised linear estimates, or indeed their higher order counterparts. This will be the subject of on-going research and it is anticipated that the solutions for the expectations defining A_{22} and A_{23}, and the corresponding higher order coefficients, will be achieved using the techniques applied previously in this Chapter. However, from analogy with the expansion of most complex expectation considered so far, namely $E\{X_i|X_i|X_j|X_j|X_k^3\, X_\ell^3\}$ summarised in Appendix Five, it may be deduced that the solutions to the expectations in Eq. (5.4.66) will require considerable effort both in algebraically expanding the expectations and in performing the multi-stage integrations resulting from application of Price's theorem.

Although the presently applied approximations are inadequate, the resulting moments of response do not appear to deviate too significantly from the true values. This behaviour, with deviations less than 0.1%, was found to be typical of four-node systems, the errors increasing as the system complexity increases. Errors of at worst 1% were obtained for a 12-node system analysed in Section 5.6. The error growth results from the increased weighting attached to terms of the form of E22 and E23, as might be expected, with reference to Eqs. (5.4.52) and (5.4.53) and Table 5.4.2, due to the increase in the number of such terms.

As mentioned in Section 5.4.2, the inclusion of the polynomial approximations enables systems of up to about 35 nodes to be analysed against the limit of 12 nodes if numerical integration is applied for solution of E22 and E23. However, the full potential of the method cannot be realised until optimised polynomial approximations for $X|X|$ have been developed since there is no means of judging the level of inaccuracy present in the moments derived using the existing approximations for systems in excess of 12 components.

5.5 LONG-TERM PROBABILITY DISTRIBUTIONS OF PEAK AND EXTREME RESPONSE

It has so far been demonstrated, in Section 5.3 and 5.4, that the short-term distribution of response may be described by the Pierson-Holmes pdf, Eq. (2.3.54). Tickell[55] has shown that the narrow-band 'type-2' cdf, formulated in Section 2.3.6, for the distribution of peak values shows a reasonable fit to prototype strain response data from a platform in the Southern North Sea.

Long-term distributions of peak and extreme response may, therefore, be obtained in the manner described in Section 2.3.6.2 making the assumption that the short-term zero-crossing rates of response are the same as those for surface elevation, according to Eq. (2.3.67). This is again a supposition previously made for single member loading (see Section 3.3). However, the wave climate data forming input to the long-term analysis should be processed in the manner discussed in Chapter Four. In many fatigue analyses the distribution of response, or force, range is required rather than the distribution of the peak variate. One possible description of response (stress) range results if each positive peak of response is assumed to be followed by a negative peak of equal magnitude, yielding:

Response range, $Y_R = 2Y$

and

$$P(Y_R) = P_p(Y = Y_R/2) \qquad (5.5.1)$$

where $P_p(Y)$ is the cdf. of positive peak response.

Although this assumption be likely to be found unrealistic from observations of actual behaviour it might be expected to yield reasonable results since the procedure is analogous to that accepted for the prediction of wave height from the distribution of wave amplitude as developed by Longuet-Higgins[39].

More rigorous definitions of response range could be developed but it is unlikely that they would be of significant practical value in view of the inevitable increase in the level of computational complexity which would be required for their evaluation.

5.6 APPLICATION OF THE METHODS TO TYPICAL STRUCTURES

In this Section the procedures developed in this Chapter are applied to some typical structural idealisations under short-term conditions and the results are compared with those derived by other methods.

The major source of comparison has been obtained from the results of time-series simulation, where the random sea surface is simulated at a discrete set of time points. At each point in time the particle kinematics, and the induced member forces and structural responses are computed, yielding data sets which can be formulated into probability histograms and statistical moments of these variables. The technique developed for this procedure in Program OS23 (see Appendix Six) follows that described by Borgman[79].

The structures considered here are:

i) a fixed vertical pile;
ii) a conductor tube; and
iii) a tower idealisation.

The first of these has previously been described in Reference 14 and the other two structures are the subject of Reference 15. In respect of (ii)

and (iii) above, the author must acknowledge the contribution made by his colleague, Mr. Tickell, who performed both the structural analysis and deterministic response computations presented here.

5.6.1 Test Structure I: Fixed Vertical Pile

Consider the determination of total shear or moment at the base of a vertical cantilever fixed to the sea bed.

The relative strength of the drag and inertia terms in Morison's Equation, is a function of depth of immersion below still-water-level, as illustrated in Section 3.2, and hence the Pierson-Holmes pdf. of load per unit length also changes with depth. Consequently, to obtain a realistic estimate of total loading a number of 'Morison' components must be considered to yield a reasonable approximation to the actual loading variation along the member.

Such a system, as shown in Fig. 5.6.1, was recently investigated using simulation techniques by Chen[80]. In this study the shear, Q(t), and moment M(t), at the fixed end of the pile were simulated using Gaussian quadrature techniques with only five points to limit computer time, as follows:

The Gaussian Quadrature Formula[81] is:

$$\int_{-1}^{1} F(\psi)\, d\psi = \sum_{j=1}^{n} H_j\, F(a_j) \qquad (5.6.1)$$

where a_j = abcissa coefficients
H_j = weighting coefficients
n = number of Gauss points considered
$F(\psi)$ = the polynomial function of ψ
$F(a_j)$ = the value of the function at specified point a_j

Transforming Eq. (5.6.1) to yield the shear and moment at the fixed end:

$$Q(t) = \int_{o}^{d} F(t, z)\, dz = \sum_{j=1}^{n} H_j\, F(t, z_j)\, \frac{d}{2} \qquad (5.6.2)$$

$$M(t) = \int_{o}^{d} F(t, z)\, z.dz = \sum_{j=1}^{n} H_j\, F(t, z_j)\, \frac{d}{2}.z_j \qquad (5.6.3)$$

where $F(t, z_j)$ is the force per unit length at z_j.

Thus the force distribution along the pile as shown in Fig. 5.6.1 is idealised to n force components at locations z_j. Eqs. (5.6.2) and (5.6.3) are of the same form as Eq. (5.4.1), where coefficients S_j are now replaced by weightings $(\frac{d}{2} \times H_j)$ and $(\frac{d}{2} \times H_j \times z_j)$, respectively, for shear and moment which take the values given in Table 5.6.1.

Applying the method of Section 5.4, using Program OS19, the second and fourth moments of shear and response result, which upon substitution into Eq. (2.3.54), using Program OS16, produce the Pierson-Holmes cdf.s plotted as the solid lines in Figs. 5.6.2 and 5.6.3. Points marked with a triangle on the figures represent the cumulative histograms obtained from simulation by Chen. The dotted lines represent the Pierson-Holmes cdf. derived from the statistical moments produced by the simulation.

Both sets of results show the departure from the Gaussian form which signifies the importance of the drag component of the wave loading. The deviations between the theoretical distributions and those obtained by simulation in the extreme ranges is probably the result of inaccuracies in the latter method caused in part by the finite size of the data sets (2,000 points).

5.6.2 Test Structures II and III

The following description of the tests has been abstracted from Reference 15.

5.6.2.1 Conductor tube

Fig. 5.6.4a shows a conductor tube which is assumed to be completely fixed at the mudline and it is restrained from horizontal movement at points 2, 3, 5, 7, 9 and 10 but it remains free to rotate or move vertically at these positions.

The structural properties are assumed to be as follows:

Young's Modulus	-	1.95×10^{11} N/m^2
External Diameter	-	0.5m.
Structural Cross-section	-	0.05m^2
Moment of Inertia	-	0.001m^4

The response variables considered were bending moment and shear at the support node 7. The distributed wave loading was considered to be replaced by equivalent concentrated loads at the positions shown in Fig. 5.6.4b. Table 5.6.2 gives the flexibility coefficients (S_{ij}) between the response variables and loads at the nine positions, where these loads have been modified in each case to represent the effect of a distributed force of 1KN/m over the length of member associated with that particular load position.

The conductor tube was analysed subject to a sea-state equivalent to a Pierson-Moskowitz spectrum with a significant wave height ($H_{1/3}$) of 9.3m. The Morison coefficients used were C_M = 2.0 and C_D = 1.0 and the density of water taken to be 1000kg/m^3.

For the purposes of comparison, the problem was also analysed subject to a deterministic wave with height H = 18.9m. and period T = 10.9 seconds, corresponding to the expected maximum wave height in a 12-hour storm with $H_{1/3}$ of 9.3m. obtained from Eq. (2.3.17). The wave period was arbitrarily taken to be T_z, the zero crossing period, for the spectrum and as such, the wave represents a realistic design steepness of approximately one-tenth.

5.6.2.2 Tower

The tower, shown in Fig. 5.6.5, was treated as a frame structure in two-dimensions only and no out-of-plane actions were included in the analysis. Encastré support conditions were assumed at the mudline for the two main legs of the tower, which stood in 62.5m. of water.

Young's modulus was taken to be 1.95 x 10^{11} N/m^2 and Fig. 5.6.5 shows the properties of individual members. The equivalent hydrodynamic volumes (V_H) and areas (A_H) were computed at 12 points and these values are quoted in Table 5.6.3, together with the flexibility coefficients derived from unit horizontal forces applied at the 12 positions.

Three response variables were considered, horizontal deflection of the deck, axial force at the bottom of a main leg and moment at load position three in the member running between positions three and six (see Fig. 5.6.5). Morison's coefficients were taken to be C_M = 2.0 and C_D = 1.0 at all load positions and the density of water was 1000kg/m^3.

The tower was analysed subject to a random sea represented by a Pierson-Moskowitz spectrum for significant wave height ($H_{1/3}$) of 6.9m. Again, for the purposes of comparison, the problem was analysed subject to a deterministic 'design' wave with height H = 14.2m. and period T = 9.3 secs, corresponding to the expected maximum wave height in a storm of 12 hours duration.

5.6.2.3 Results

In Tables 5.6.4 and 5.6.5 the second and fourth moments of load and response are presented for the test structures. The theoretical moments of load are derived from the variances of the particle kinematics according to Eqs. (2.3.49) and (2.3.50). In addition to the theoretical moments of response derived using the method of Sections 5.4.1 and 5.4.2 with numerical integration for expectations E22 and E23, the results of application of the polynomial approximations in these expectations (using cubic approx in E22 and cubic/linear in E23) are also included in brackets. The approximation yields results within 1% of the true values.

The moments derived by simulation result from 10,000 data points with 0.75 second time steps. They show reasonable agreement with the theoretical values, all being with 15%, although even with such a large number of data points the values are not completely stable, as may be deduced from the moments of force pairs (F_8, F_{10}) and (F_{11}, F_{12}) of the tower structure. As expected, the estimates of the fourth moment show considerably greater departure from the theoretical values than the second moment, this being typical of results obtained from finite data sets.

The deviation of the moments of load estimated by simulation from the theoretical values gives a measure of the likely inaccuracy of the simulation procedure, which implies probable over-estimation of kurtosis by up to 15% from the results obtained here. The general level of agreement between the properties of response resulting from the two methods is within the bounds of inaccuracy present in the properties of loading, thereby providing further verification of the probabilistic procedures developed in this Chapter.

In the examples considered here the simulation technique is quicker to perform than the 'full' probabilistic method, as indicated in Tables 5.6.4b and 5.6.5b, and can be extended to systems of more than 12 components, but it is slower than the 'approximate' probabilistic method. Furthermore, extrapolating the trend in run-times shown for the simulation techniques indicates that a limit of the order of 35 component systems is likely to be imposed by 30-minute run-time restrictions for simulation with the sensitivity applied here. This figure corresponds to the upper limit on the approximate method as discussed in Section 5.4.4. It may, therefore, be concluded that until optimisation of the 'approximate' probabilistic method is achieved, simulation techniques provide the most reliable and economic means of estimation of the statistics of response for systems with in excess of 12 nodes.

Although, for the applications considered here, the approximate probabilistic method predicts moments with greater accuracy than does simulation, this result should not be interpreted as being generally true. This follows because the inaccuracy of the simulation results from the discretisation of the time histories and the finite nature of the data sets and is, therefore, likely to be independent of the number of load load components considered, as might be inferred from the similar levels of inaccuracy in the moments of response to those of load. In contrast the accuracy of the approximate probabilistic method is likely to decrease with increase in system complexity, as mentioned in Section 5.4.4.

Estimates of extreme values of response are required in design against first excursion failure. The most probable value of the extreme peak, (MPPV), of a random variable during a given period of exposure represents the mode of the pdf. of extreme peak values. For the P-H probability distribution this can be shown (see Section 3.4) to correspond to the value taken off the cdf. of peak values, Fig. 2.3.5, at the probability level corresponding to that period of exposure. Considering here a 12-hour period for the short-term sea conditions, and assuming the number of peaks of force and response to equal the number of waves, the relevant probabilities of non-exceedence associated with the largest peak are approximately 0.99975 and 0.99978 for the conductor tube and tower, respectively. MPPV estimates of the extremes of the response variables are thus obtained using Fig. 2.3.5 as summarised in Tables 5.6.6 and 5.6.7.

Estimates of the extreme peak load based on a deterministic wave, representing the expected extreme height during the period of exposure associated with a steepness of approximately one-tenth are also included in Tables 5.6.6 and 5.6.7. Expected extreme values are slightly greater than MPPV estimates due to the positive skewness of extreme pdf.s.

The predictions for the conductor tube response deviate by as much as 33% between the probabilistic (from theoretical moments) and deterministic methods whilst for the tower the departures are within 10%. However, too detailed a comparison should not be made between individual response estimates derived from the different approaches due to the lack of rational basis for the deterministic method, resulting largely from the arbitrary selection of a 'realistic' wave period or steepness to be associated with the predicted wave height. The comparison does, nevertheless, illustrate a measure of agreement in the magnitude of load predictions resulting from the two quite distinct approaches.

Finally, it is instructive to assess the consequences of linearising the loading mechanism as discussed in Section 3.2, before application of the probabilistic analysis since this yield results equivalent to those from linear spectral analysis, loading and response then being Gaussian distributed. The standard deviation of load, or response, would be slightly underestimated with linearisation and the kurtosis would be constant at 3.0. From Fig. 2.3.5 the MPPV response would then correspond to approximately $4.1\sigma_Y$. for the 12-hour period of exposure. Omitting the underestimation in the standard deviation, the linearisation would, therefore, predict extreme values of response between 26 and 40% below those from the non-linear probabilistic method, given in Tables 5.6.6 and 5.6.7. Underestimates of this order may thus be expected from a linear spectral analysis of the test structures.

TABLE 5.4.1

SUMMARY OF SENSITIVITY INVESTIGATION INTO MOMENTS OF NUMERICALLY OBTAINED MULTI-DIMENSIONAL (3 & 4D) PROBABILITY SPACES FOR DIFFERENT NUMBERS OF DATA POINTS USING REGTANGULAR RULE

Number of Steps = N*	5	7	9	11	15	21	25	31	35
Total Probability for 4-D Space = $\int\int\int\int p(X_i X_j X_k X_\ell)\, dX_i dX_j dX_k dX_\ell$	1.38588	1.00658	1.00003	1.00000	1.00000	1.00000	0.999999	0.999999	0.999999
$\frac{(E23)_N}{(E23)_{31}}$ %	145.19	95.63	100.35	100.10	100.07	100.04	100.02	100.00	99.99
$\frac{(E18)_N}{(E18)_{31}}$ %									
Mean of all combinations in a 4 member system	149.00	95.57	100.57	100.13	100.09	100.05	100.03	100.00	99.99
Range of variation of values (%)	9.35	0.487	0.195	0.022	0.015	0.008	0.004	-	0.004
Standard deviation of values	-	0.158	0.064	0.007	0.005	0.002	0.001	-	0.001

*Quoted number of steps in a range of ±5 'conditional' standard deviations about the conditional mean in each cycle of integration.

TABLE 5.4.2

NUMBER OF COMBINATIONS OF 2ND AND 4TH ORDER EXPECTATIONS OF FORCE DERIVED THROUGH EQS. (5.4.3) AND (5.4.4) FOR STRUCTURAL IDEALISATIONS OF 'n' NODES

Expectation	$E\{F_p^2\}$ $E\{F_p^4\}$	$E\{F_p F_q\}$ $E\{F_p^2 F_q^2\}$	$E\{F_p^3 F_q\}$	$E\{F_p^2 F_q F_r\}$	$E\{F_p F_q F_r F_s\}$
Number of Combinations of p, q, r, s in n Component Systems	n	$\frac{n(n-1)}{2}$	$n(n-1)$	$\frac{n(n-1)(n-2)}{2}$	$\frac{n(n-1)(n-2)(n-3)}{4!}$
n					
1	1	0	0	0	0
2	2	1	2	0	0
3	3	3	6	3	0
4	4	6	12	12	1
5	5	10	20	30	5
10	10	45	90	360	210
12	12	66	132	660	495
15	15	105	210	1,365	1,365
20	20	190	380	3,420	4,845
30	30	435	870	12,180	27,405
40	40	780	1,560	29,640	91,390
50	50	1,225	2,450	58,800	230,300
100	100	4,950	9,900	485,100	3,921,225

T A B L E 5 . 4 . 3

TYPICAL RESULTS FROM APPROXIMATIONS OF E22 AND E23

Response $Y = F_1 + F_2 + F_3 + F_4$

where F_i = force on unit length member i

Conditions:

Member Number	X(m)	Z(m)	D(m)
1	100.0	142.5	0.5
2	125.0	135.0	0.5
3	150.0	135.0	1.0
4	175.0	135.0	1.0

d = 150m; $\rho = 10^3$ kg/m^3; $C_M = 2.0$; $C_D = 1.0$; P-M ($H_{1/3} = 9.3$m)

	Method of Computation	Numerical Integration (15 steps)	Linear Approxi-mations	Cubic/Linear Approxi-mations	
	EXPECTATION				
E23	$X_1\|X_1\|X_3\|X_3\|X_5\|X_5\|X_7\|X_7\|$	10.71	7.453	7.197	x10^9
E22	a $X_1\|X_1\|X_2\ X_3\|X_3\|X_5\|X_5\|$	- 7.181	- 5.788	- 7.173	x10^9
	b $X_1\|X_1\|X_2\ X_3\|X_3\|X_7\|X_7\|$	- 1.760	- 1.818	- 1.745	x10^9
	c $X_1\|X_1\|X_2\ X_5\|X_5\|X_7\|X_7\|$	1.780	- 6.139	2.420	x10^8
	d $X_3\|X_3\|X_4\ X_1\|X_1\|X_5\|X_5\|$	3.297	10.36	3.183	x10^8
	e $X_3\|X_3\|X_4\ X_1\|X_1\|X_7\|X_7\|$	- 1.875	- 1.937	- 1.856	x10^9
	f $X_3\|X_3\|X_4\ X_5\|X_5\|X_7\|X_7\|$	- 8.353	- 6.527	- 8.372	x10^9
	g $X_5\|X_5\|X_6\ X_1\|X_1\|X_3\|X_3\|$	2.297	1.358	2.393	x10^{10}
	h $X_5\|X_5\|X_6\ X_1\|X_1\|X_7\|X_7\|$	1.812	1.467	1.823	x10^{10}
	i $X_5\|X_5\|X_6\ X_3\|X_3\|X_7\|X_7\|$	3.034	4.449	- 1.758	x10^6
	j $X_7\|X_7\|X_8\ X_1\|X_1\|X_3\|X_3\|$	7.784	-11.97	9.198	x10^8
	k $X_7\|X_7\|X_8\ X_1\|X_1\|X_5\|X_5\|$	11.88	8.787	11.99	x10^9
	ℓ $X_7\|X_7\|X_8\ X_1\|X_1\|X_5\|X_5\|$	3.341	1.977	3.485	x10^{10}
	m $X_1\|X_1\|X_3\|X_3\|X_5\|X_5\|X_8\|$	3.238	2.743	3.237	x10^{10}
	n $X_1\|X_1\|X_3\|X_3\|X_6\|X_7\|X_7\|$	- 7.235	- 7.468	- 7.210	x10^9
	o $X_1\|X_1\|X_4\|X_5\|X_5\|X_7\|X_7\|$	5.009	3.790	5.052	x10^9
	p $X_2\|X_3\|X_3\|X_5\|X_5\|X_7\|X_7\|$	-14.63	- 9.319	-14.67	x10^9
	$E(Y^4)$	4.1913	4.1097	4.1881	x10^{13}

TABLE 5.6.1

GAUSSIAN QUADRATURE APPROXIMATION TO WAVE LOADING

USING FIVE ABSCISSA FOR 50.0m WATER DEPTH

j	Gaussian Abscissa	Elevation z_j m.	Gaussian Weighting H_j	Weighting Coefficients for Shear $(\frac{d}{2} H_j)$	Weighting Coefficients for Moment $(\frac{d}{2} H_j \cdot z_j)$
5	+1	50.0	0.236927	5.92	282.2
4	.90618	47.65	0.478629	11.97	460.2
3	.53847	38.46	0.56887	14.22	355.6
2	0.0	25.0	0.478629	11.97	138.1
1	- .53817	11.54	0.236927	5.92	13.9
	- .90618	2.346			
	-1	0			

T A B L E 5 . 6 . 2

FLEXIBILITY COEFFICIENTS - CONDUCTOR TUBE

Load Position	Elevation Above Seabed (m)	Element Length (m)	Moment S_{ij} (Nm/(kN/m))	Shear S_{ij} (N/(kN/m))
1	153.0	5.67	$1.494_{10}{}^{4}$	$-5.573_{10}{}^{2}$
2	141.7	11.33	$2.326_{10}{}^{4}$	$-8.678_{10}{}^{2}$
3	127.5	17.0	$4.452_{10}{}^{4}$	$-1.334_{10}{}^{4}$
4	110.5	17.0	$2.457_{10}{}^{4}$	$-3.670_{10}{}^{3}$
5	93.5	17.0	$-1.192_{10}{}^{4}$	$1.652_{10}{}^{3}$
6	76.5	17.0	$-6.569_{10}{}^{3}$	$9.104_{10}{}^{2}$
7	59.5	17.0	$3.162_{10}{}^{3}$	$-4.383_{10}{}^{2}$
8	42.5	17.0	$1.702_{10}{}^{3}$	$-2.360_{10}{}^{2}$
9	17.0	17.0	$-1.297_{10}{}^{3}$	$1.798_{10}{}^{2}$

TABLE 5.6.3

FLEXIBILITY COEFFICIENTS - TOWER

Load Position	V_H (m^2)	A_H (m^2)	Deflection S_{ij} m/kN	Axial Force S_{ij} N/kN	Moment S_{ij} Nm/kN
1	22.1	18.8	$1.743_{10}{}^{-6}$	$4.219_{10}{}^{1}$	$1.176_{10}{}^{3}$
2	22.1	18.8	$1.743_{10}{}^{-6}$	$7.537_{10}{}^{0}$	$-5.726_{10}{}^{1}$
3	56.6	77.3	$5.155_{10}{}^{-6}$	$2.550_{10}{}^{1}$	$-3.298_{10}{}^{2}$
4	52.7	93.7	$3.808_{10}{}^{-6}$	$-8.080_{10}{}^{0}$	$-1.739_{10}{}^{2}$
5	56.6	77.3	$5.155_{10}{}^{-6}$	$-4.715_{10}{}^{1}$	$-1.415_{10}{}^{2}$
6	22.1	18.8	$8.233_{10}{}^{-6}$	$-1.808_{10}{}^{2}$	$2.282_{10}{}^{3}$
7	22.1	18.8	$8.233_{10}{}^{-6}$	$-2.455_{10}{}^{2}$	$-1.350_{10}{}^{2}$
8	50.4	74.2	$1.096_{10}{}^{-5}$	$-4.838_{10}{}^{2}$	$1.110_{10}{}^{1}$
9	52.7	93.7	$9.571_{10}{}^{-6}$	$-5.049_{10}{}^{2}$	$-8.568_{10}{}^{1}$
10	50.4	74.2	$1.096_{10}{}^{-5}$	$-5.223_{10}{}^{2}$	$-7.972_{10}{}^{1}$
11	4.9	6.3	$1.383_{10}{}^{-5}$	$-7.460_{10}{}^{2}$	$-6.877_{10}{}^{2}$
12	4.9	6.3	$1.383_{10}{}^{-5}$	$-7.838_{10}{}^{2}$	$-5.455_{10}{}^{1}$

TABLE 5.6.4a

STATISTICAL MOMENTS OF WAVE LOADING AND STRUCTURAL RESPONSE

ON CONDUCTOR TUBE IDEALISATION

(a) Wave Loading per Unit Length, F_i, at Locations Indicated in Fig. 5.6.4

i	Theoretical Moments			Simulation		
	$E\{F_i^2\}_{N^2}$	$E\{F_i^4\}_{N^4}$	β	$E\{F_i^2\}_{N^2}$	$E\{F_i^4\}_{N^4}$	β
1	5.948×10^5	3.065×10^{12}	8.663	5.833×10^5	2.792×10^{12}	8.205
2	1.207×10^5	1.118×10^{11}	7.673	1.199×10^5	1.128×10^{11}	7.846
3	3.104×10^4	6.156×10^9	6.388	3.135×10^4	6.845×10^9	6.963
4	9.204×10^3	4.287×10^8	5.061	9.364×10^3	4.952×10^8	5.646
5	3.553×10^3	5.246×10^7	4.156	3.616×10^3	6.003×10^7	4.591
6	1.657×10^3	9.961×10^6	3.632	1.685×10^3	1.118×10^7	3.935
7	9.024×10^2	2.735×10^6	3.359	9.191×10^2	3.016×10^6	3.570
8	5.675×10^2	1.038×10^6	3.223	5.802×10^2	1.133×10^6	3.367
9	3.718×10^2	4.341×10^5	3.141	3.827×10^2	4.706×10^5	3.213

T A B L E 5 . 6 . 4 b

STATISTICAL MOMENTS OF WAVE LOADING AND STRUCTURAL RESPONSE

ON CONDUCTOR TUBE IDEALISATION

(b) Moment at Node 7, Y_1, and Shear at Node 7, Y_2 (on Member 6-7) in Fig. 5.6.4

j	Theoretical Moments			Simulation			
	$E\{Y_j^2\}$	$E\{Y_j^4\}$	β	$E\{Y_j^2\}$	$E\{Y_j^4\}$	β	
1	7.754×10^8	4.466×10^{18}	7.429	7.697×10^8	4.460×10^{18}	7.527	Nm Units
	(7.754×10^8)	(4.434×10^{18})	(7.376)				
2	1.046×10^7	7.236×10^{14}	6.608	1.052×10^7	7.828×10^{14}	7.076	N Units
	(1.046×10^7)	(7.226×10^{14})	(6.598)				
Computer Run-Times	7.15 (0.18)			6.49			Minutes on ICL 1906S

TABLE 5.6.5a

STATISTICAL MOMENTS OF WAVE LOADING AND STRUCTURAL RESPONSE ON TOWER IDEALISATION

(a) Wave Loading, F_i, at Nodes Indicated in Fig. 5.6.5

i	Theoretical Moments			Simulation		
	$E\{F_i^2\}_{N^2}$	$E\{F_i^4\}_{N^4}$	β	$E\{F_i^2\}_{N^2}$	$E\{F_i^4\}_{N^4}$	β
1	4.146×10^7	5.196×10^{15}	3.023	4.198×10^7	5.599×10^{15}	3.318
2	4.146×10^7	4.196×10^{15}	3.023	4.105×10^7	5.575×10^{15}	3.308
3	4.442×10^8	6.306×10^{17}	3.196	4.440×10^8	7.076×10^{17}	3.589
4	4.254×10^8	6.263×10^{17}	3.461	4.283×10^8	7.326×10^{17}	3.994
5	4.442×10^8	6.306×10^{17}	3.196	4.436×10^8	7.004×10^{17}	3.559
6	1.196×10^8	4.395×10^{16}	3.071	1.188×10^8	4.621×10^{16}	3.273
7	1.196×10^8	4.395×10^{16}	3.071	1.188×10^8	4.571×10^{16}	3.241
8	2.169×10^9	1.851×10^{19}	3.933	2.174×10^9	1.996×10^{19}	4.222
9	2.728×10^9	3.348×10^{19}	4.499	2.738×10^9	3.697×10^{19}	4.897
10	2.169×10^9	1.851×10^{19}	3.933	2.170×10^9	1.935×10^{19}	4.108
11	1.196×10^8	6.212×10^{16}	4.345	1.199×10^8	6.243×10^{16}	4.380
12	1.196×10^8	6.212×10^{16}	4.345	1.187×10^8	5.904×10^{16}	4.189

T A B L E 5 . 6 . 5 b

STATISTICAL MOMENTS OF WAVE LOADING AND STRUCTURAL RESPONSE ON TOWER IDEALISATION

(b) Deflection, Y_1; Axial Force, Y_2; and Moment, Y_3; in Fig. 5.6.5

j	Theoretical Moments			Simulation			
	$E\{Y_j^2\}$	$E\{Y_j^4\}$	β	$E\{Y_j^2\}$	$E\{Y_j^4\}$	β	
1	2.395×10^0	2.461×10^1	4.201	2.407×10^0	2.851×10^1	4.920	mm Units
	(2.395×10^0)	(2.440×10^1)	(4.254)				
2	3.978×10^9	7.061×10^{19}	4.463	3.999×10^9	8.093×10^{19}	5.061	N Units
	(3.978×10^9)	(7.040×10^{19})	(4.450)				
3	6.941×10^8	1.829×10^{18}	3.796	6.912×10^8	1.953×10^{18}	4.088	Nm Units
	(6.941×10^8)	(1.822×10^{18})	(3.781)				
Computer Run-Times	27.06 (0.44)			9.26			Mins. on ICL 1906S

5.6.6

TABLE 5.6.6 EXTREME RESPONSE IN CONDUCTOR TUBE

j	Probabilistic MPPV† Response Using Fig. 2.3.5			Deterministic Extreme Peak Response*
	β	$\left(\frac{Y_j}{\sigma_{Y_j}}\right)$ **	$(Y_j)_{MPPV}$	
1	7.429	6.80	189 kNm 21.2kN	234 kNm 28.1kN
2	6.608	6.55		

† Most probable peak value - represents mode of pdf. of extreme values

* Peak response from passage of regular wave with H = 18.9m. and T = 10.9 seconds, using linear wave theory

** $\sigma_{Y_j} = \sqrt{E\{Y_j^2\}}$

T A B L E 5 . 6 . 7

EXTREME RESPONSE IN TOWER

j	Probabilistic MPPV† Response Using Fig. 2.3.5			Deterministic Extreme Peak Response*
	β	$\left(\frac{Y_j}{\sigma_{Y_j}}\right)$ **	$(Y_j)_{MPPV}$	
1	4.500	5.80	8.98mm	8.17mm
2	4.580	5.85	369 kN	370 kN
3	4.081	5.55	146 kNm	151 kNm

† See note below Table 5.6.6

* Peak response from passage of regular wave with H = 14.2m. and T = 9.3 seconds using linear wave theory

** $\sigma_{Y_j} = \sqrt{E\{Y_j^2\}}$

FIG. 5.3.1. IDEALISED SYSTEM OF TWO FORCE COMPONENTS ON VERTICAL CYLINDRICAL MEMBERS SEPARATED IN SPACE UNDER THE ACTION OF RANDOM WAVES.

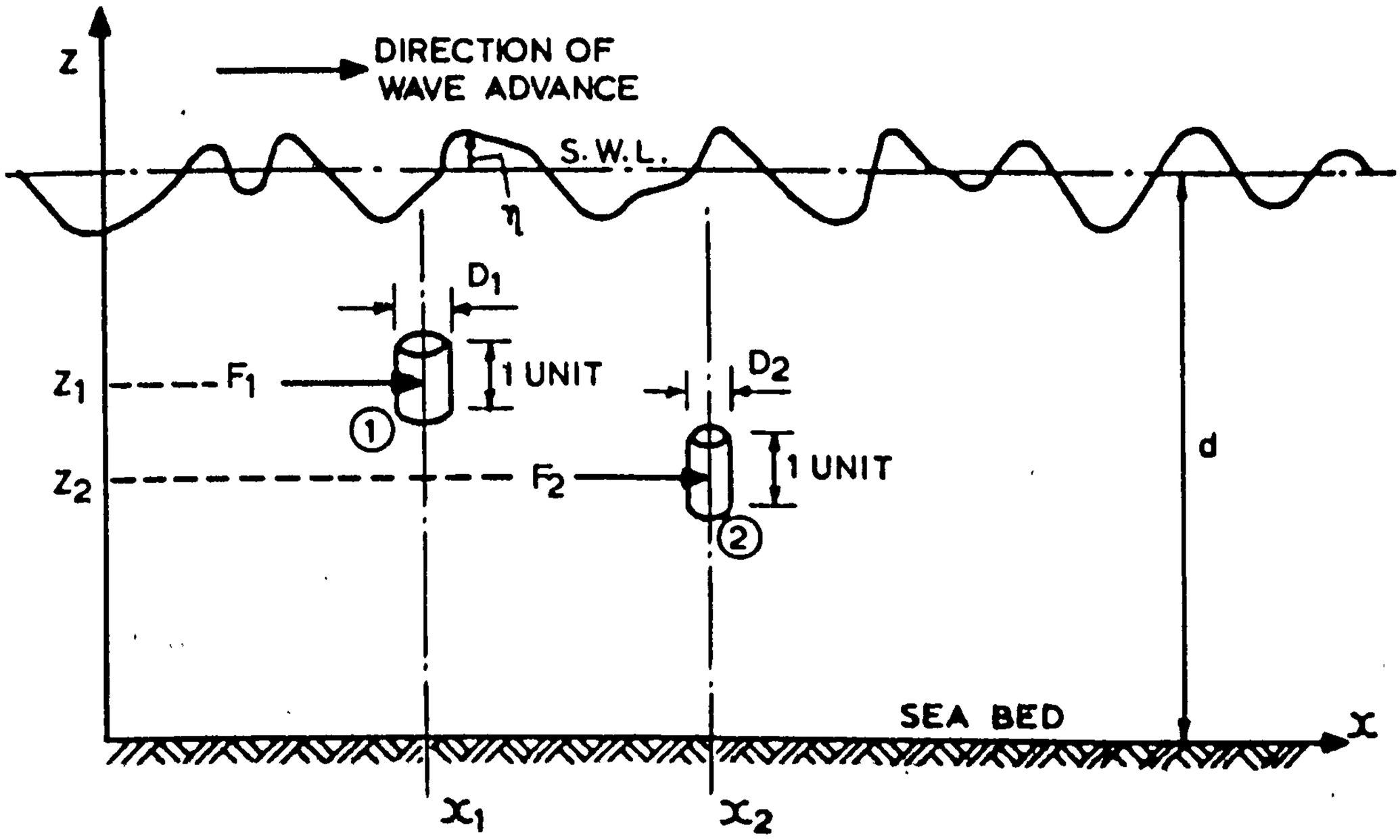

FIG. 5.3.2. SKETCH OF BIVARIATE PDF OF LOADING ON A TWO MEMBER SYSTEM, AS INDICATED IN FIG. 5.3.1. (See also Fig. 5.3.3.) WITH CORRELATION OF 0·29 BETWEEN LOADS.

CONDITIONS

$D_1 = 0{\cdot}5m$ $Z_1 = 142{\cdot}5m.$ $X_1 = 100m$

$D_2 = 1{\cdot}0m$ $Z_2 = 135{\cdot}0m$ $X_2 = 150m$

$d = 150m$

$C_M = 2{\cdot}0$ $C_D = 1{\cdot}0$

$\rho = 10^3 kg/m^3$

P-M spectrum ($H_{1/3} = 9{\cdot}3m$)

$$r_F = \frac{E\{F_1 F_2\}}{\sqrt{E\{F_1^2\} F\{F_2^2\}}} = 0{\cdot}292$$

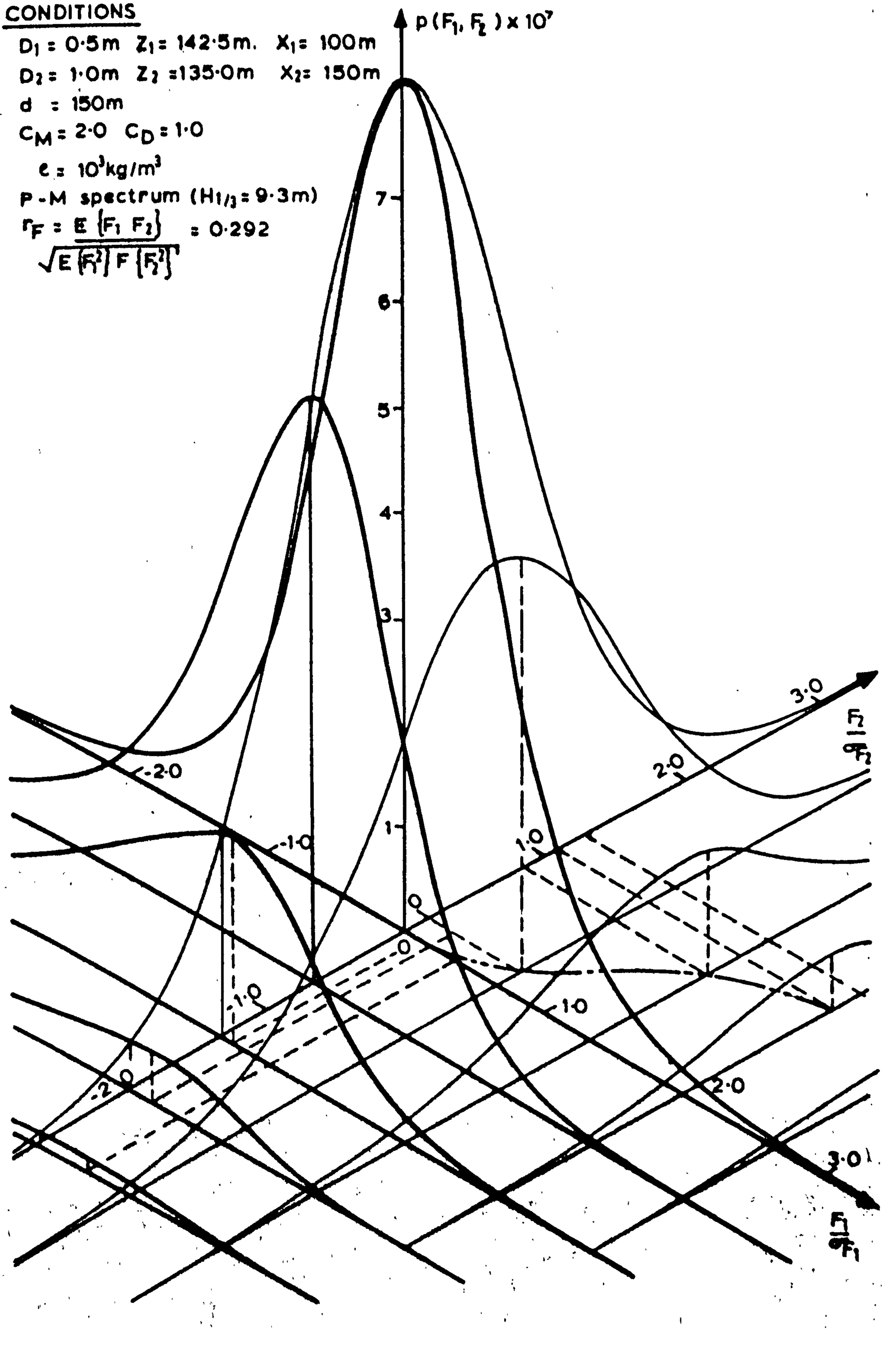

FIG. 5.3.3. CONDITIONAL DISTRIBUTIONS FROM THE BIVARIATE PDF. OF LOADING ON A TWO MEMBER SYSTEM, AS INDICATED IN FIG 5.3.1.) (See also Fig.5.3.2.)

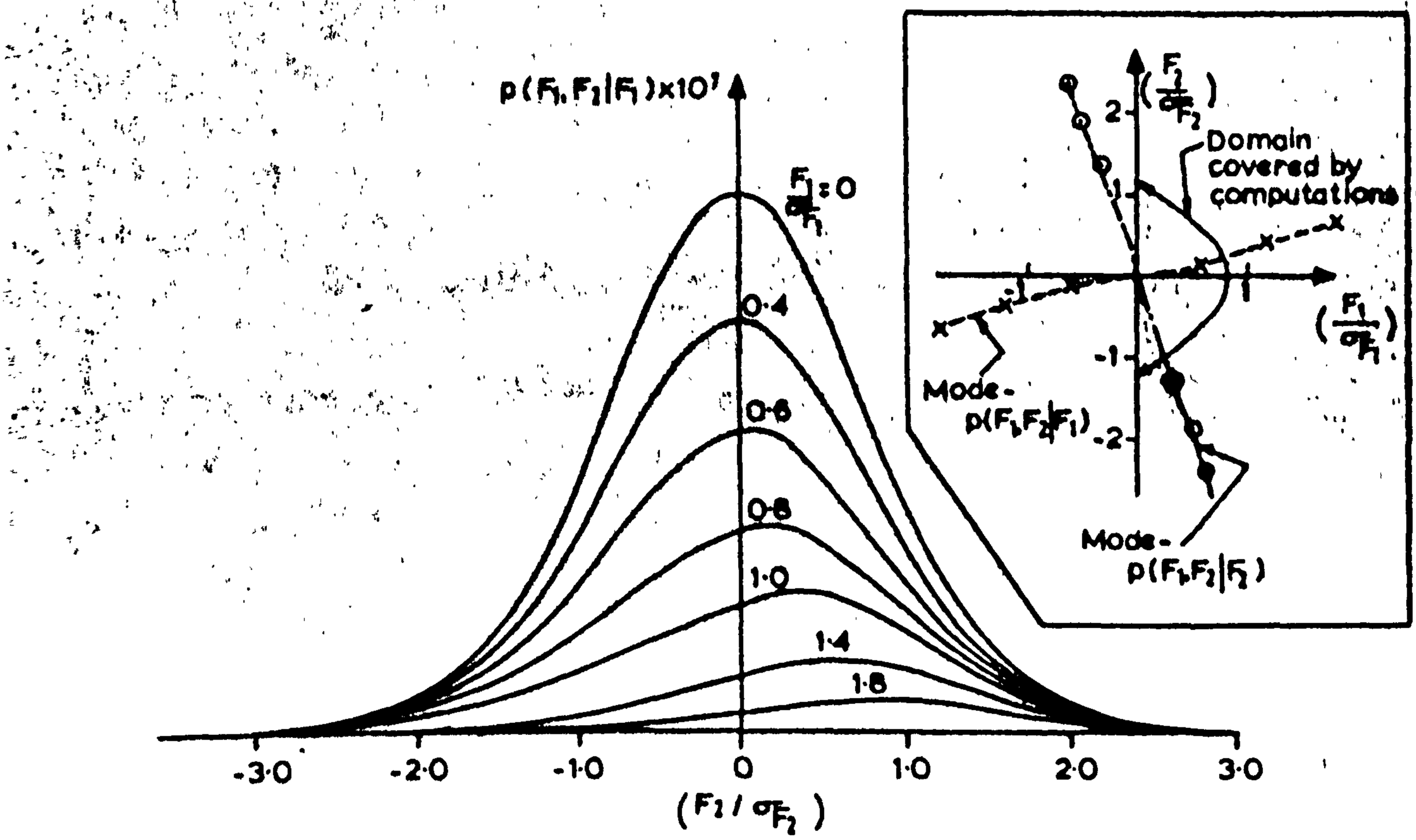

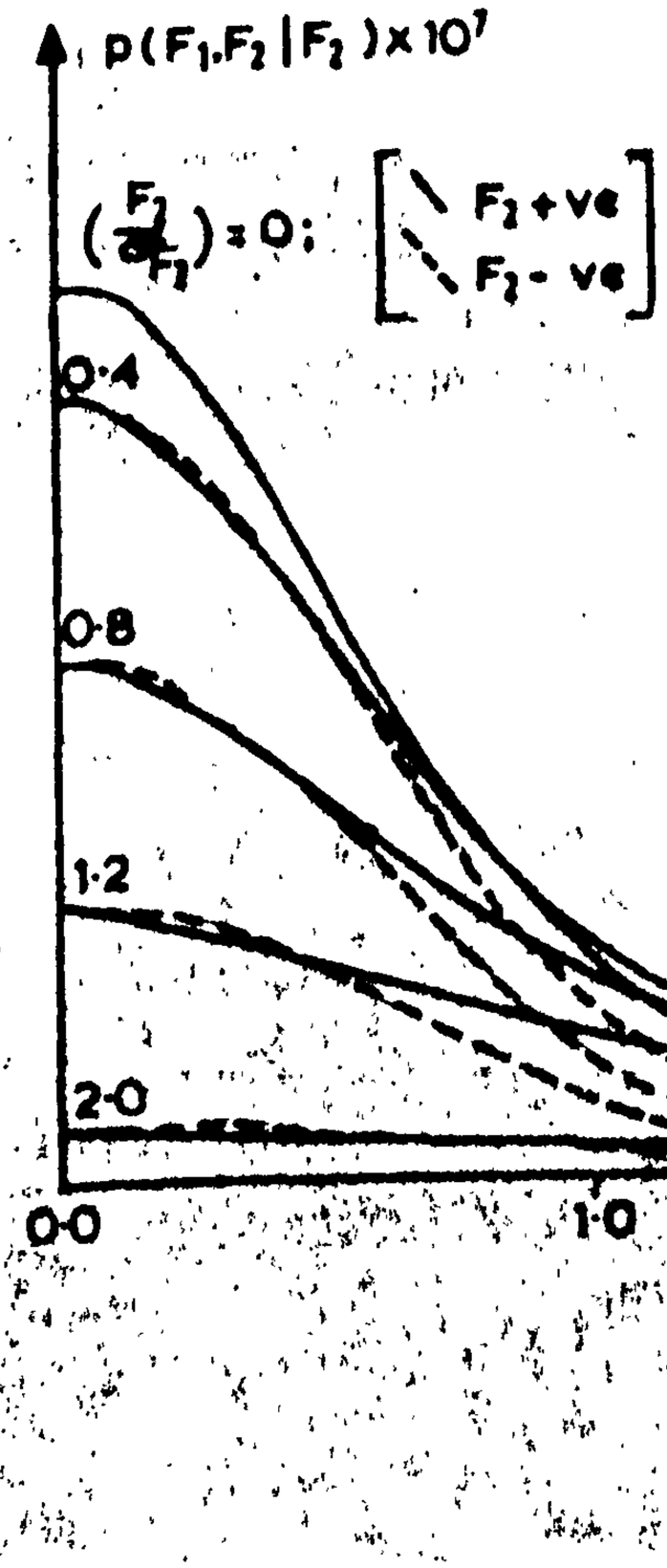

CONDITIONS

$D_1 = 0.5m$ $Z_1 = 142.5m$ $X_1 = 100m$

$D_2 = 1.0m$ $Z_2 = 135.0m$ $X_2 = 150m$

$d = 150m$

$C_M = 2.0$ $C_D = 1.0$

$\rho = 10^3 kg/m^3$

P-M spectrum ($H_{1/3} = 9.3m$)

$$\eta = \frac{E[F_1 F_2]}{\sqrt{E[F_1^2]\,E[F_2^2]}} \times 0.292$$

FIG.5.3.4. MARGINAL CDFs OF FORCE OBTAINED FROM JOINT FORCE DISTRIBUTIONS FOR A TWO MEMBER SYSTEM COMPARED WITH THE UNIVARIATE, PIERSON-HOLMES CDF.

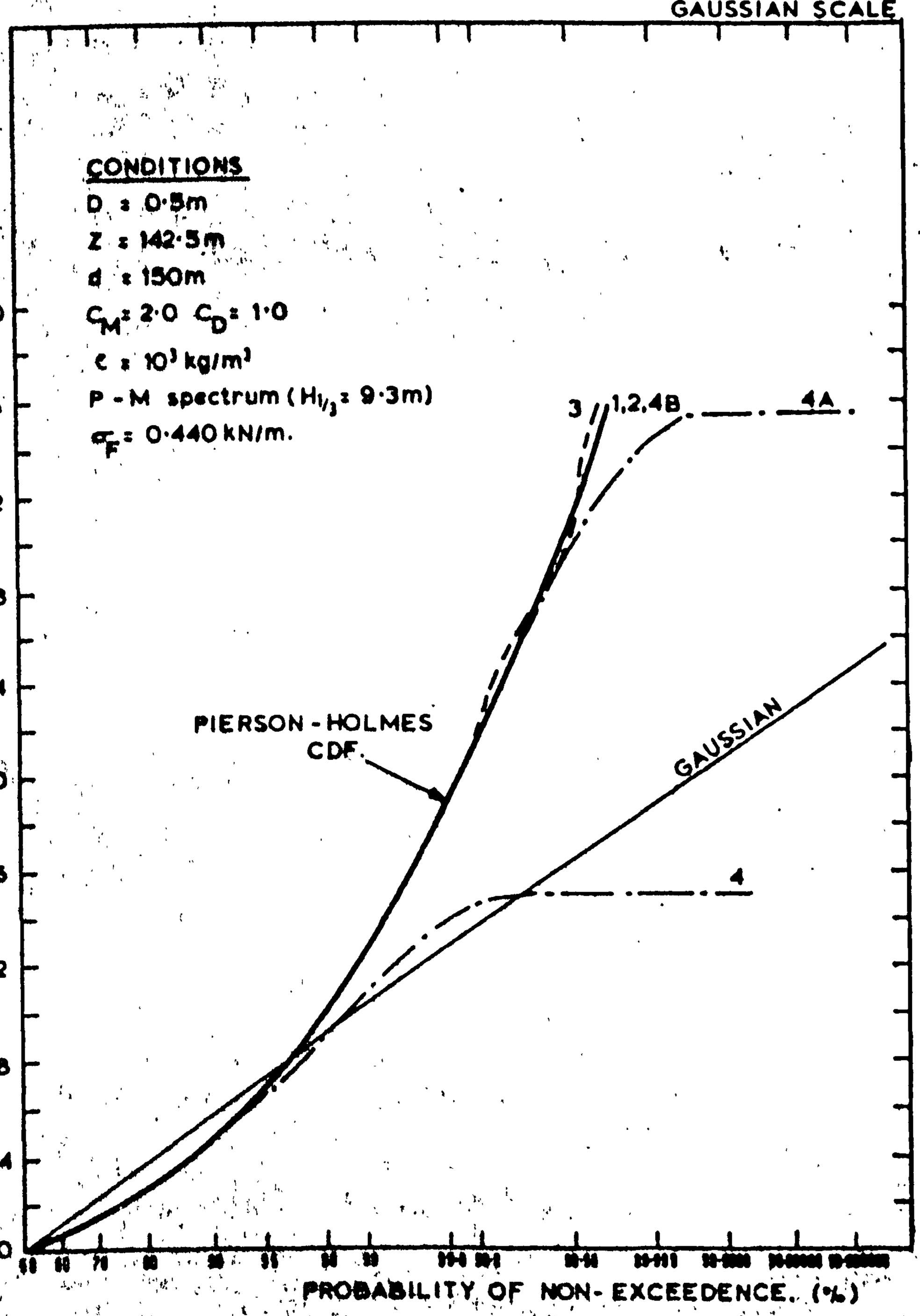

FIG. 5.3.5. MARGINAL CDFs OF FORCE OBTAINED FROM JOINT DISTRIBUTION FOR A TWO MEMBER SYSTEM COMPARED WITH THE UNIVARIATE, PIERSON-HOLMES CDF.

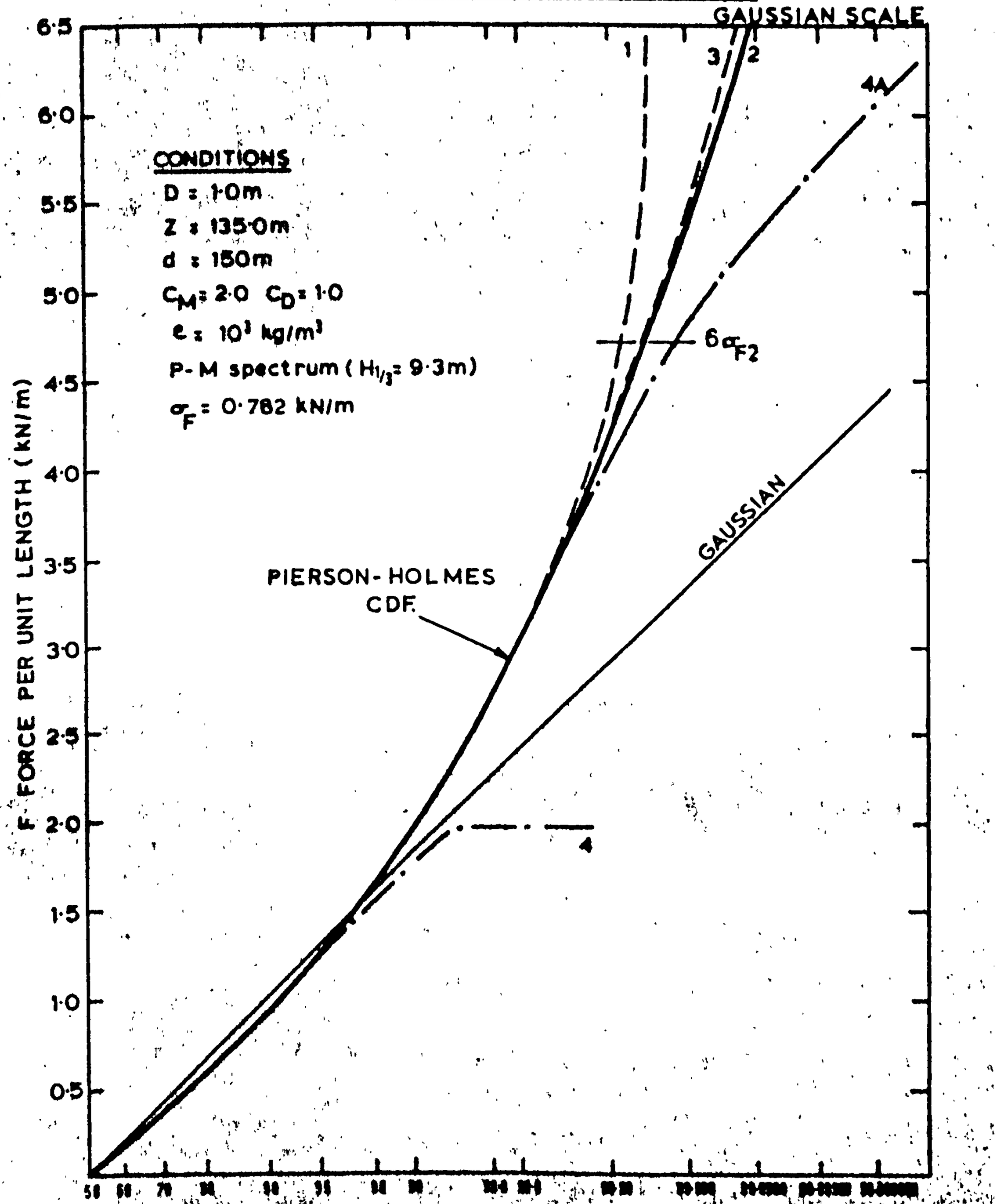

FIG. 5.3.6. MARGINAL CDFs OF FORCE OBTAINED FROM JOINT DISTRIBUTION FOR A TWO MEMBER SYSTEM COMPARED WITH THE UNIVARIATE PIERSON-HOLMES CDF.

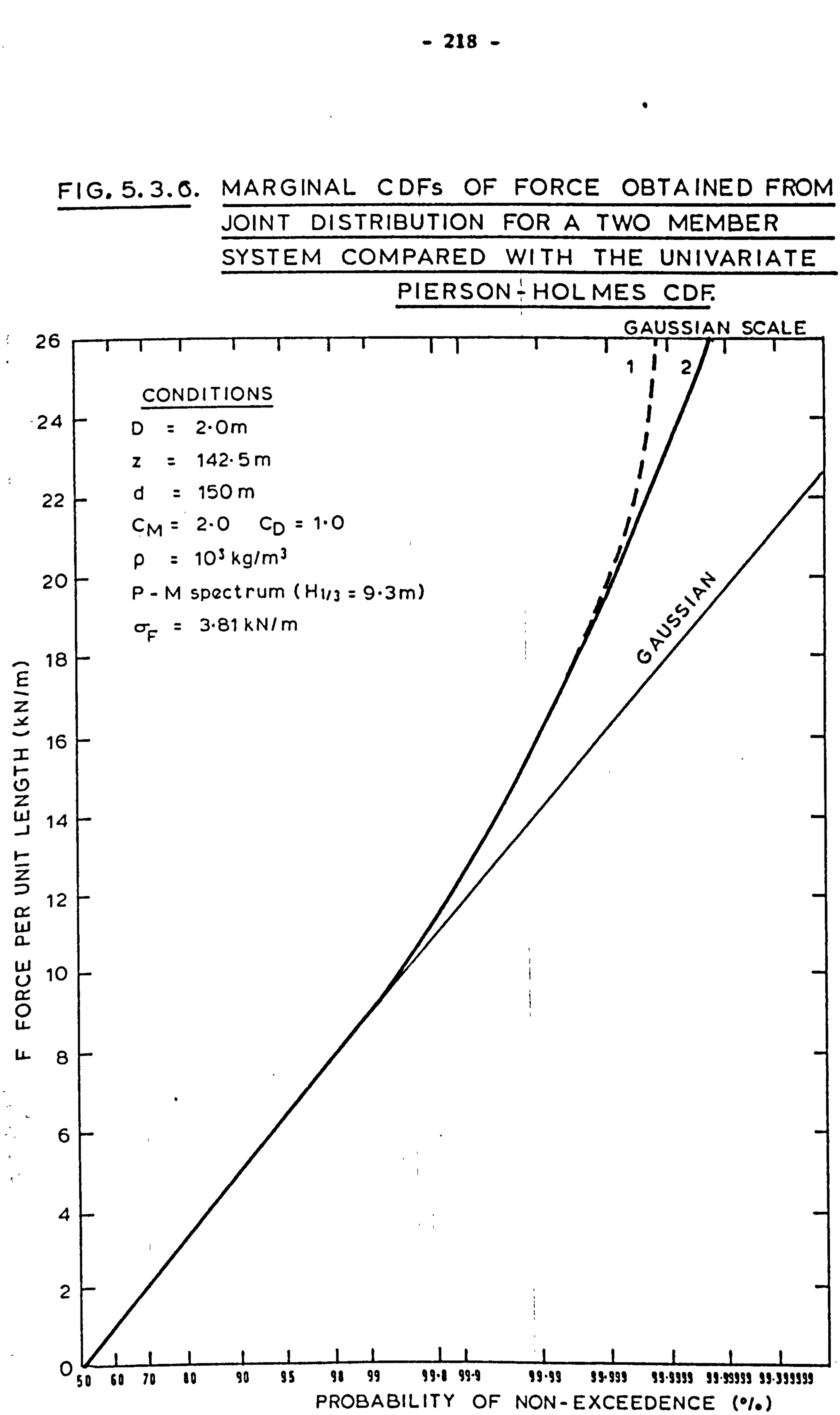

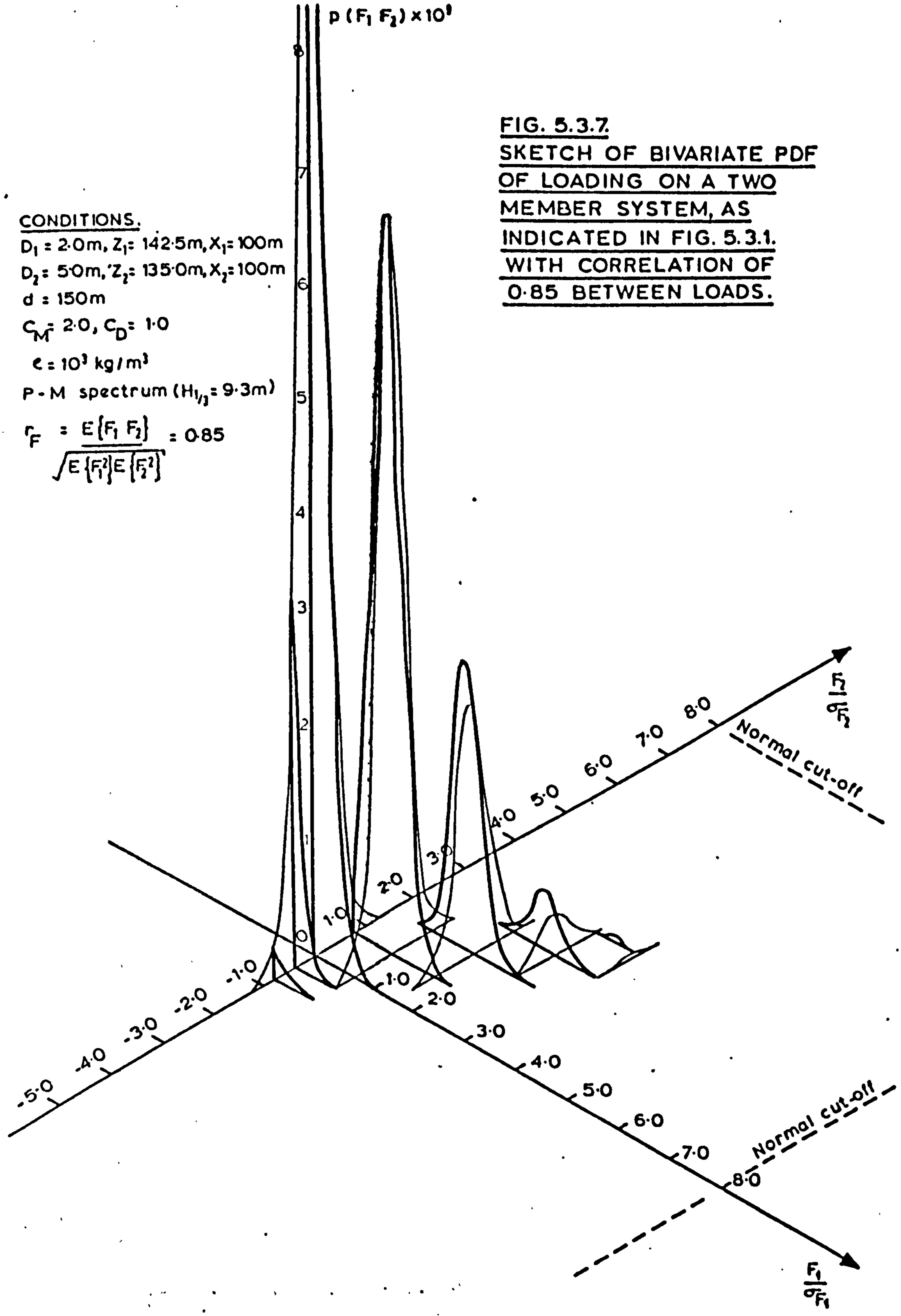

CONDITIONS.

D_1 = 2·0m, Z_1= 142·5m, X_1= 100m

D_2 = 5·0m, Z_2= 135·0m, X_2= 100m

d = 150m

C_M= 2·0, C_D= 1·0

ρ = 10^3 kg/m^3

P - M spectrum ($H_{1/3}$= 9·3m)

$$r_F = \frac{E\{F_1 F_2\}}{\sqrt{E\{F_1^2\}E\{F_2^2\}}} = 0.85$$

FIG. 5.3.7.
SKETCH OF BIVARIATE PDF OF LOADING ON A TWO MEMBER SYSTEM, AS INDICATED IN FIG. 5.3.1. WITH CORRELATION OF 0·85 BETWEEN LOADS.

FIG. 5.3.8. CUMULATIVE DISTRIBUTION OF RESPONSE $Y = F_1 + F_2$ FOR THE SYSTEM SKETCHED BELOW.

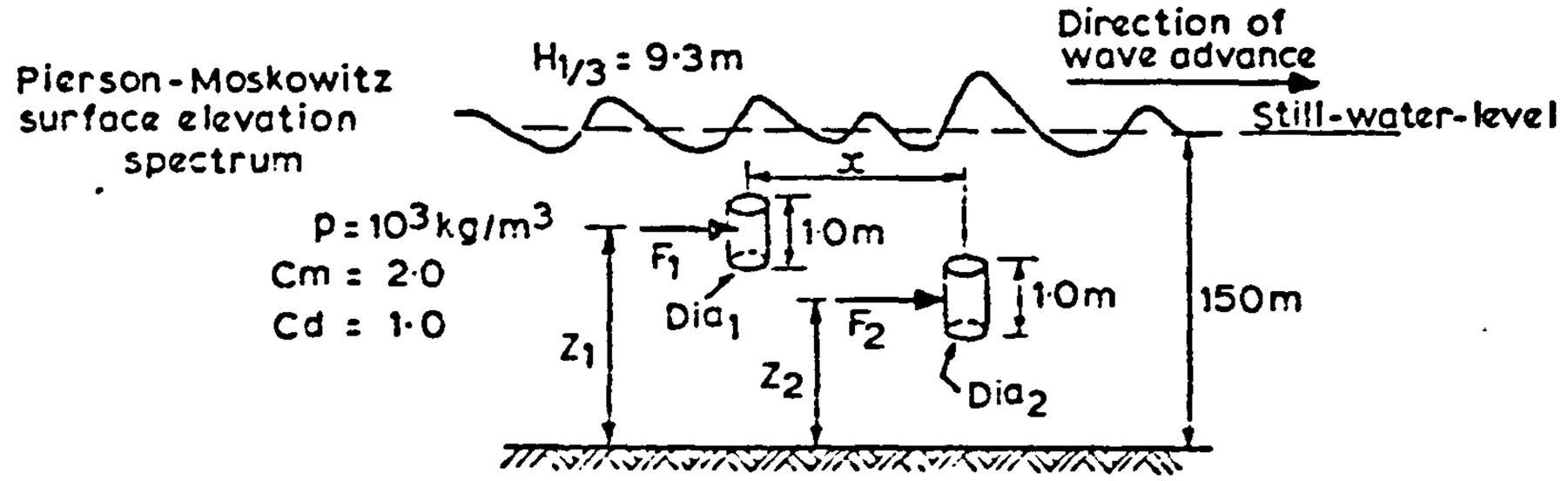

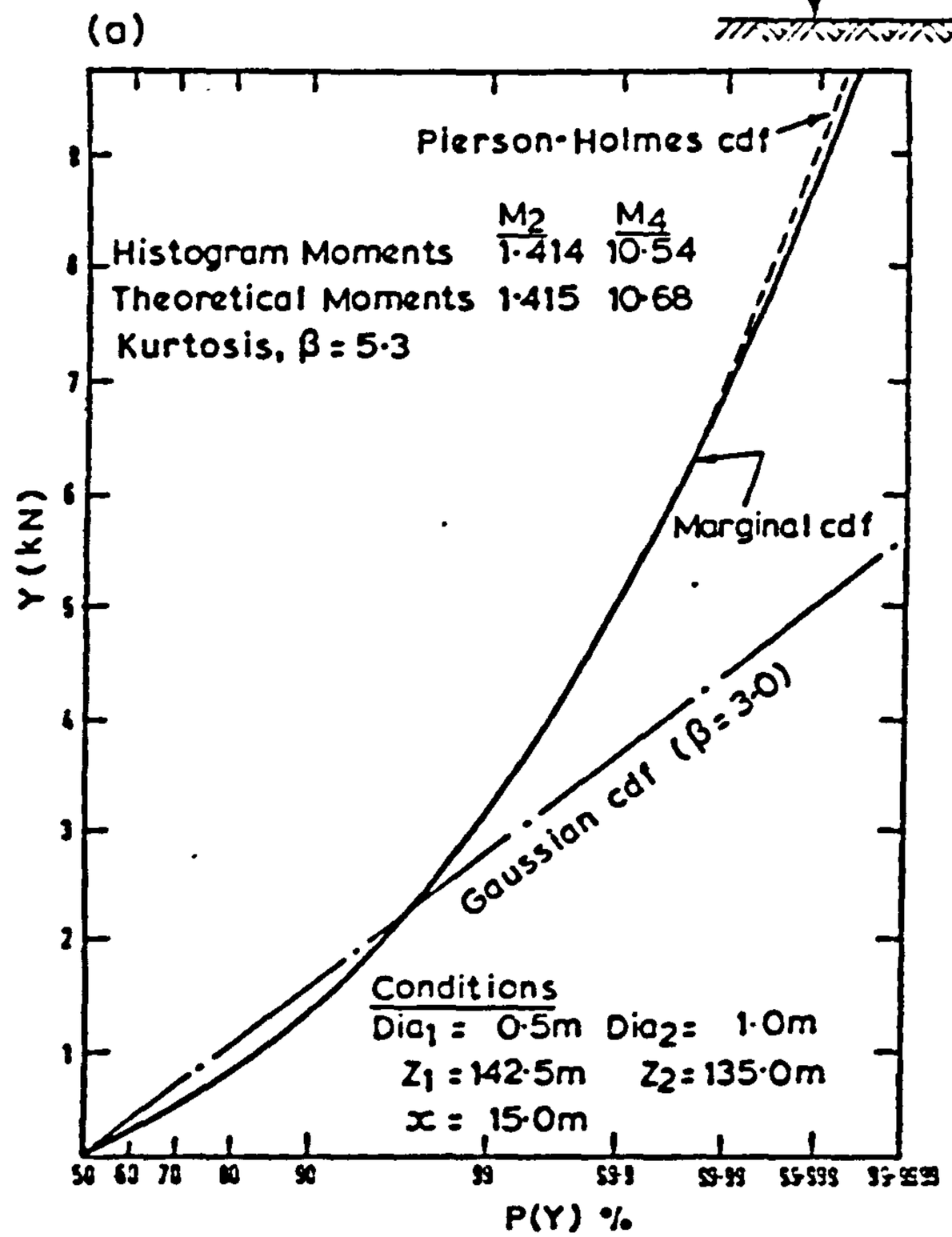

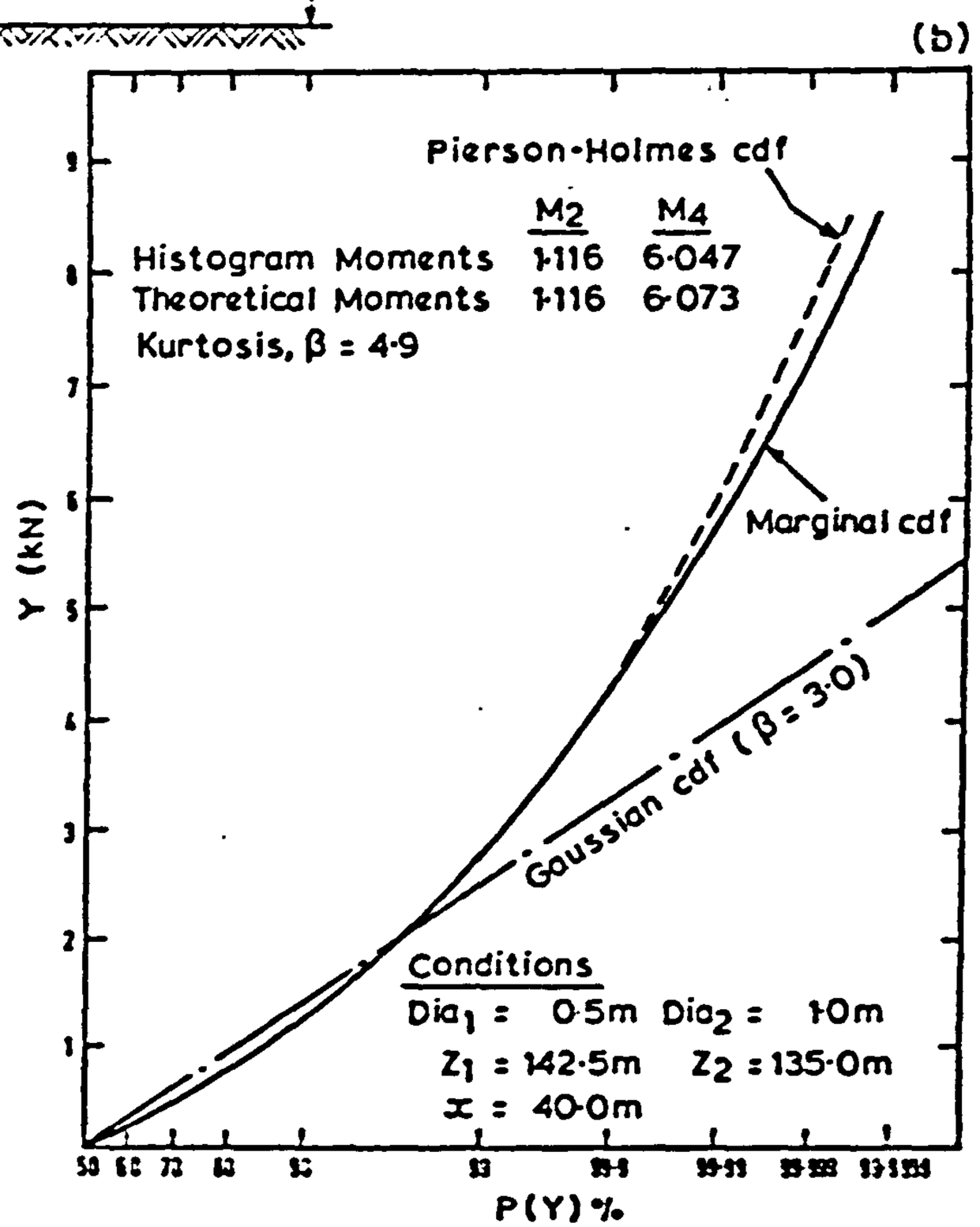

FIG. 5.3.9. CUMULATIVE DISTRIBUTION OF RESPONSE $Y = F_1 + F_2$ FOR THE SYSTEM SKETCHED IN FIG. 5.3.8.

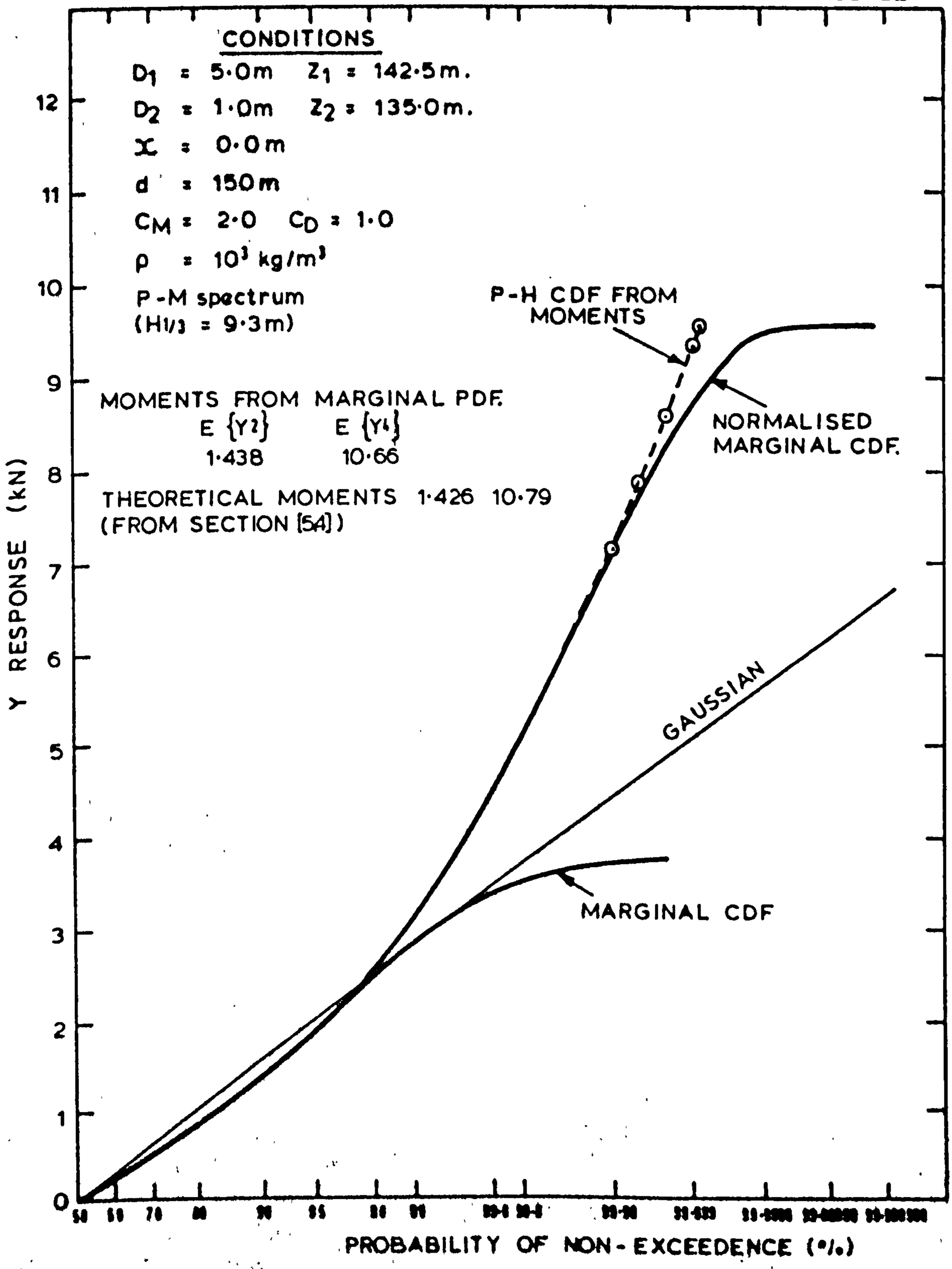

FIG. 5.3.10. CUMULATIVE DISTRIBUTION OF RESPONSE $Y = F_1 + 0{\cdot}5F_2$ FOR THE SYSTEM SKETCHED IN FIG. 5.3.8.

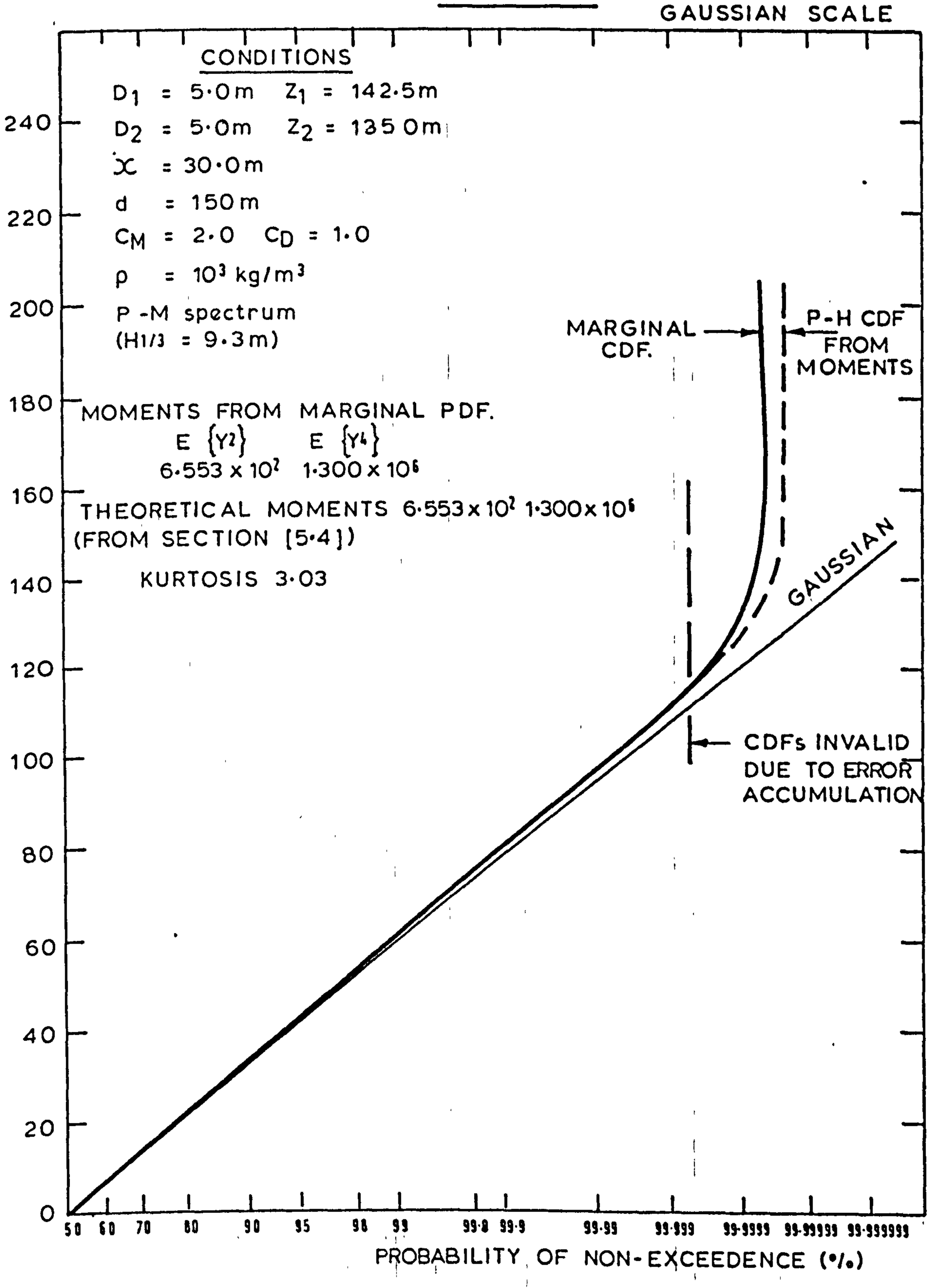

FIG. 5.4.1. VARIATION IN THE STATISTICS OF TOTAL FORCE, $Y = F_1 + F_2$, (STANDARD DEVIATION σ_y, AND KURTOSIS, β_y,) ON TWO UNIT LENGTH VERTICAL MEMBERS OF CYLINDRICAL SECTION WITH CHANGE IN THE HORIZONTAL SPACING FOR THE CONDITIONS BELOW.

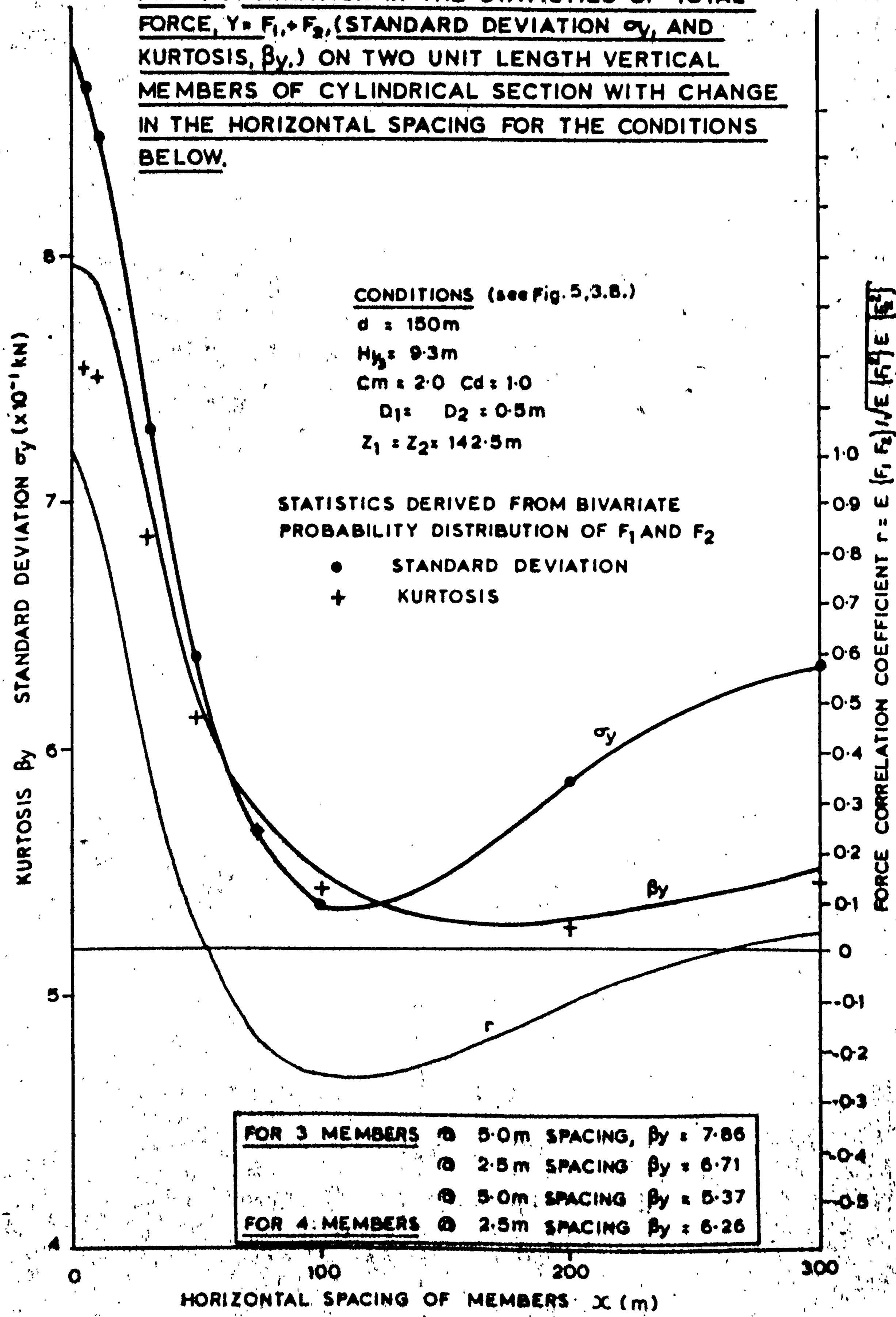

FIG. 5.4.2. VARIATION OF PARTICLE KINEMATIC CORRELATION COEFFICIENTS, WITH CHANGE IN HORIZONTAL SPACING.

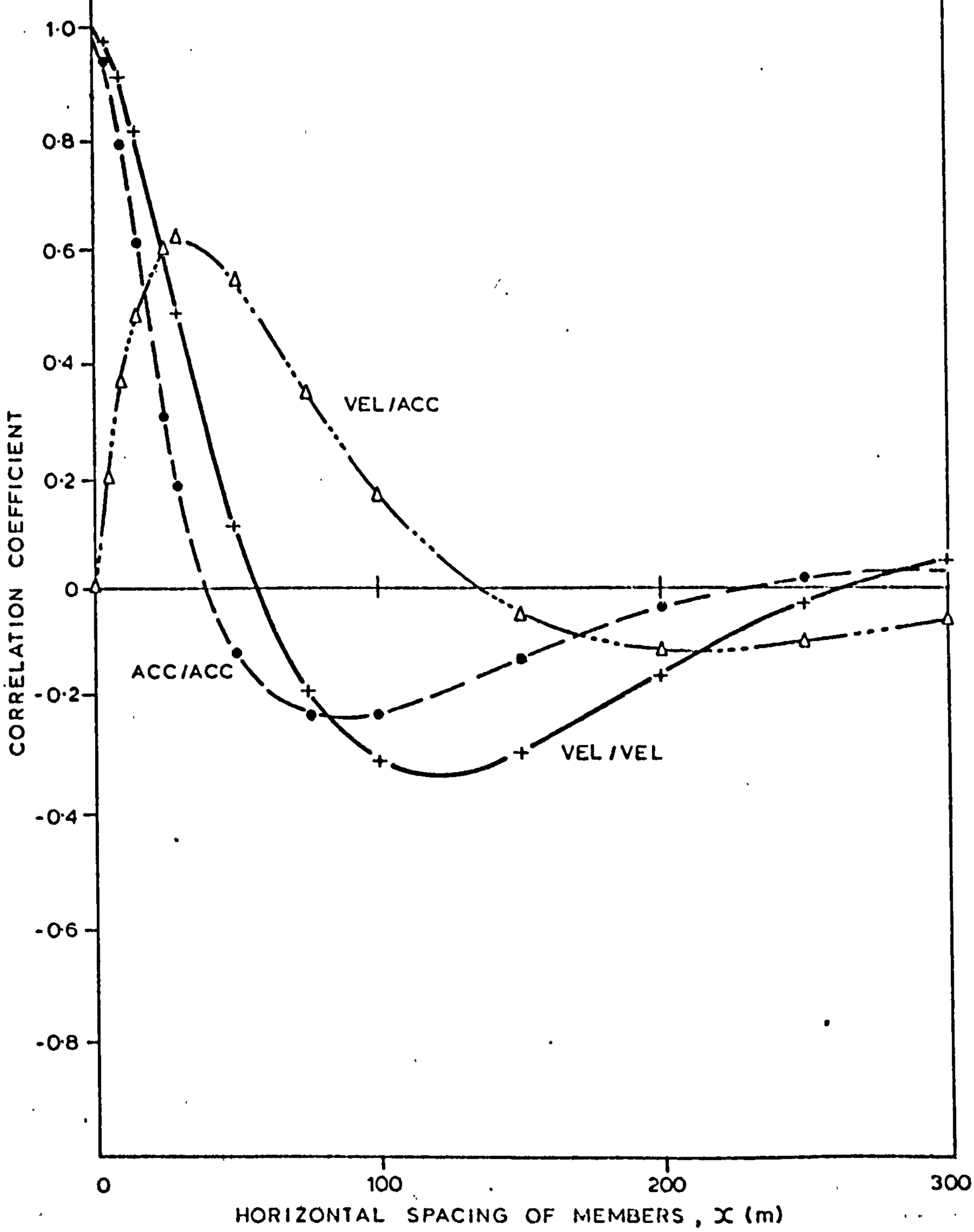

FIG. 5.4.3. VARIATION IN THE STATISTICS OF TOTAL FORCE, $Y = F_1 + F_2$, (STANDARD DEVIATION, σ_y, AND KURTOSIS, β_y) ON TWO UNIT LENGTH VERTICAL MEMBERS OF CYLINDRICAL SECTION WITH CHANGE IN THE HORIZONTAL SPACING FOR THE CONDITIONS BELOW.

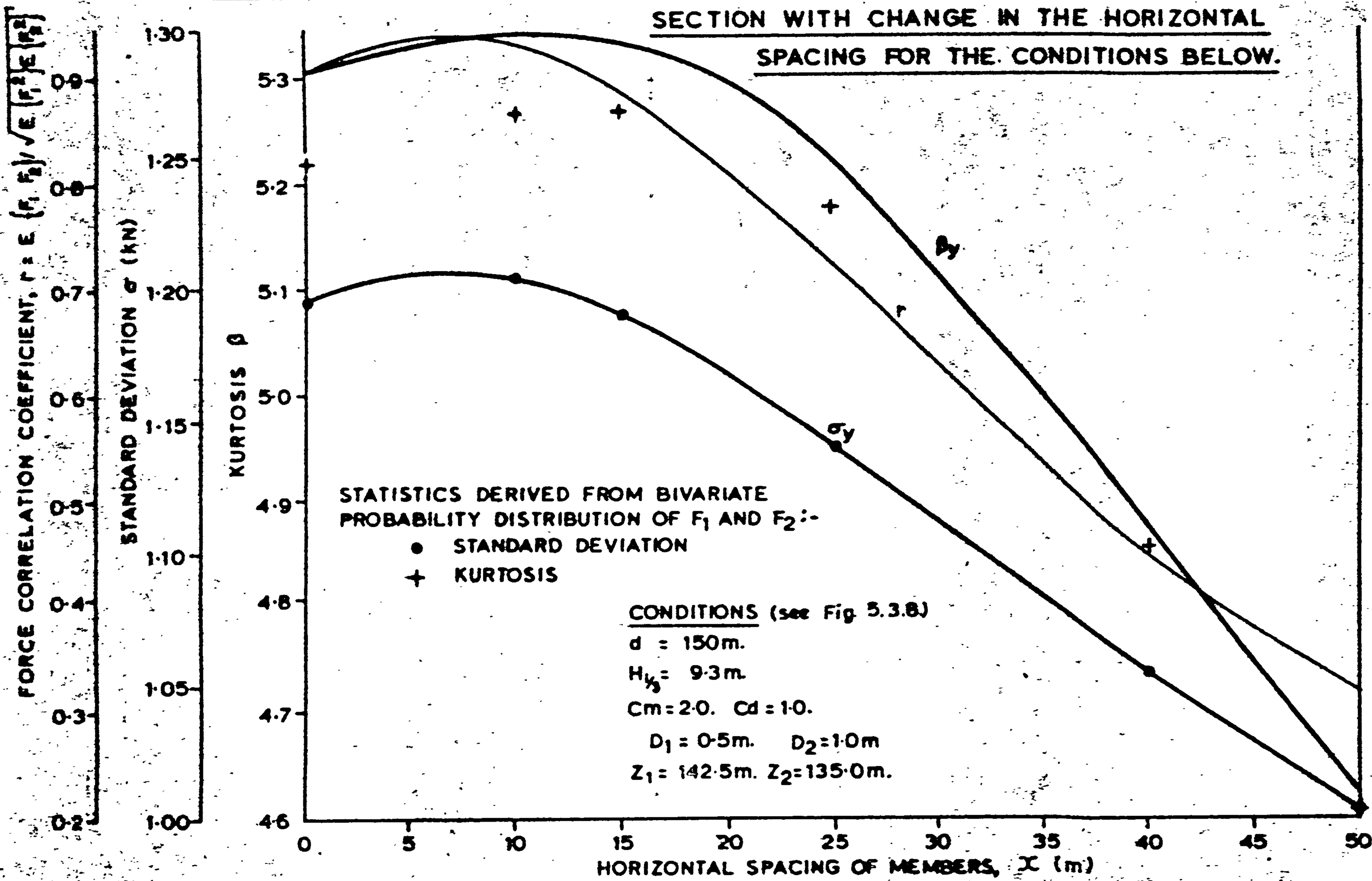

FIG. 5.4.4. UNDERESTIMATION OF STATISTICAL MOMENTS OF THE PIERSON/HOLMES DISTRIBUTION OBTAINED FROM PROBABILITY HISTOGRAMS AS DESCRIBED BELOW.

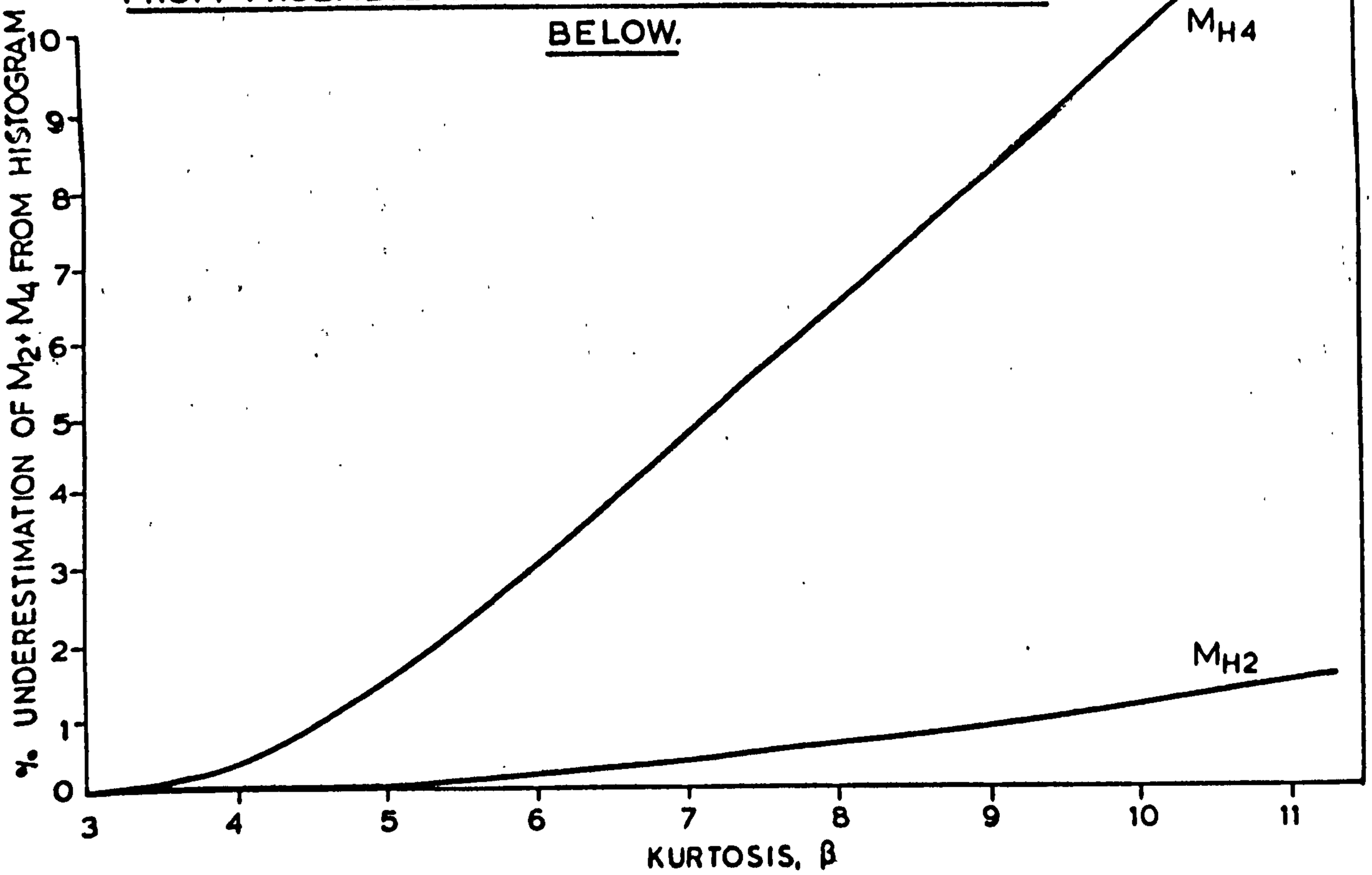

Theoretical statistical moments defining a Pierson/Holmes distributed random variable, γ, are:-

$$M_2 = E\{\gamma^2\} \; ; \; M_4 = E\{\gamma^4\} \text{ and KURTOSIS of } \gamma \text{ is } \beta = M_4/M_2^2$$

In discrete form Pierson/Holmes probability densities, for positive values of γ, may be expressed as:-

$$p(\gamma_i) = \frac{1}{2\pi\sigma_{\psi_1}\sigma_{\psi_2}} \sum_{j=1}^{N\psi_1} \left[\exp\{-\frac{1}{2}(\frac{\psi_{1_j}^2}{\sigma_{\psi_1}} + \frac{\psi_2^2}{\sigma_{\psi_2}^2})\}\right] \Delta\psi_1$$

where $\psi_2 = \gamma_i - \psi_{1_j}|\psi_{1_j}|$, $\psi_{1_j} = \psi_{1_{MIN}} + (j-1)\,\Delta\psi_1$; $\gamma_i = (i-1)\Delta_\gamma$, $i=1, N_\gamma$

$$\sigma_{\psi_1}^2 = [(M_4 - 3M_2^2)/78]^{\frac{1}{2}} \quad \text{and} \quad \sigma_{\psi_2}^2 = M_2 - 3\sigma_{\psi_1}^4$$

$$\Delta_\gamma = \gamma_{MAX}/(N_\gamma - 1)$$

The second and fourth statistical moments are obtained from the resulting histogram as follows:-

$$M_{H2} = 2 \sum_{i=1}^{N_\gamma} \gamma_i^2 \, p(\gamma_i)\Delta\gamma \; ; \; M_{H4} = 2 \sum_{i=1}^{N_\gamma} \gamma_i^4 \, p(\gamma_i)\Delta\gamma$$

The results presented graphically above were determined using the following discretisation:-

$\Delta_\gamma = \sqrt{M_2/10}$ $\quad N_\gamma = 81$

$\Delta_{\psi_1} = \sigma_{\psi_1}/20$ $\quad N_{\psi_1} = 201$ $\quad \psi_{1\,MIN} = -5\sigma_{\psi_1}$

FIG. 5.4.5. VARIATION IN KURTOSIS, β_F AND STANDARD DEVIATION σ_F, OF FORCE PER UNIT LENGTH ON VERTICAL MEMBER OF 0·5m DIAMETER IN SEA STATE WITH INTENSITY GIVEN BY $H_{1/3}$ = 9·3m (MORISION COEFFICIENTS Cm = 2·0 AND Cd = 1·0), WITH CHANGE IN DEPTH OF IMMERSION.

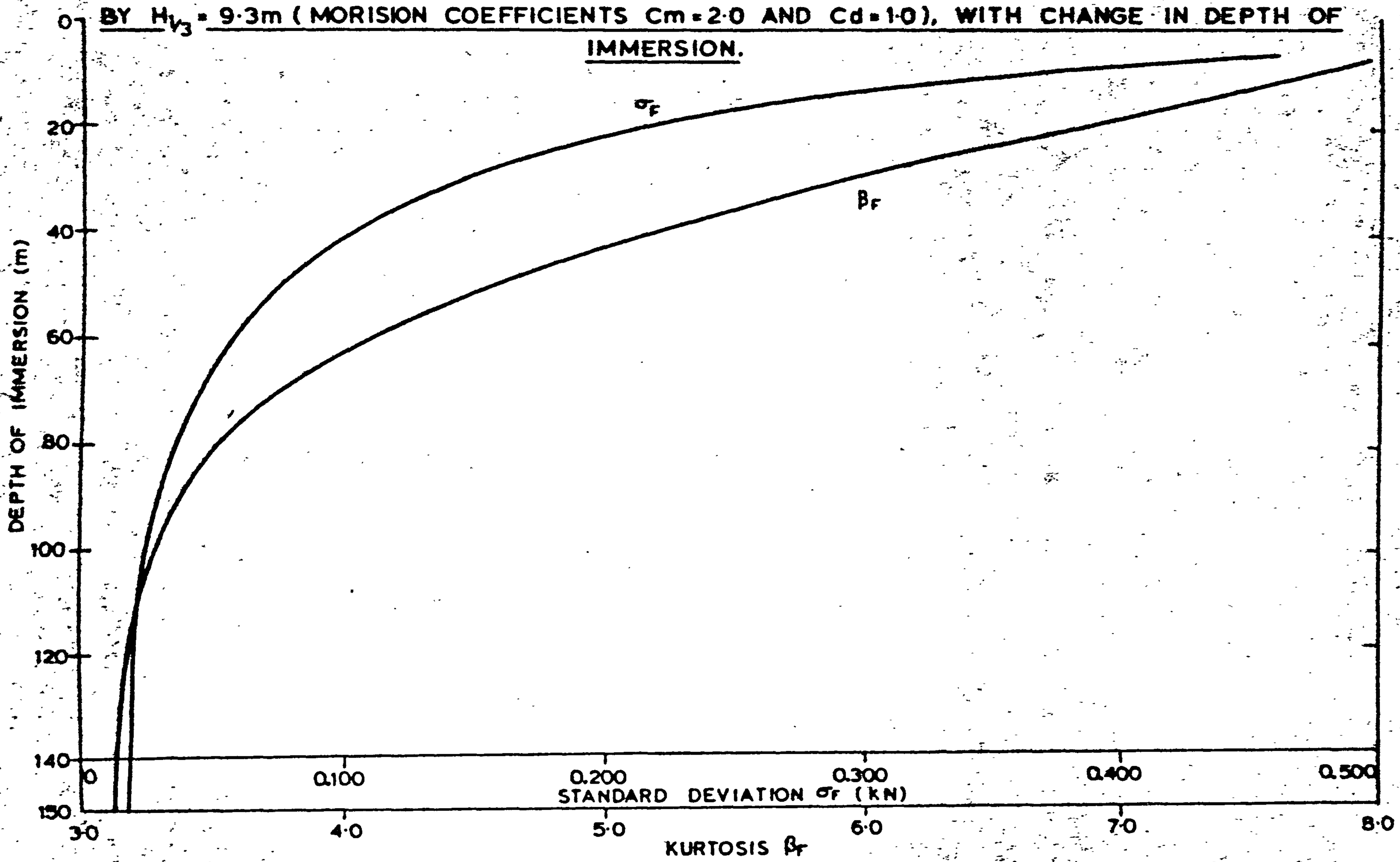

FIG.5.4.6. VARIATION IN THE STATISTICS OF TOTAL FORCE, $Y = F_1 + F_2$, (STANDARD DEVIATION σ_y, AND KURTOSIS, β_y) ON TWO UNIT LENGTH SECTIONS OF A VERTICAL CYLINDRICAL MEMBER WITH CHANGE IN THE VERTICAL SPACING FOR THE CONDITIONS BELOW.

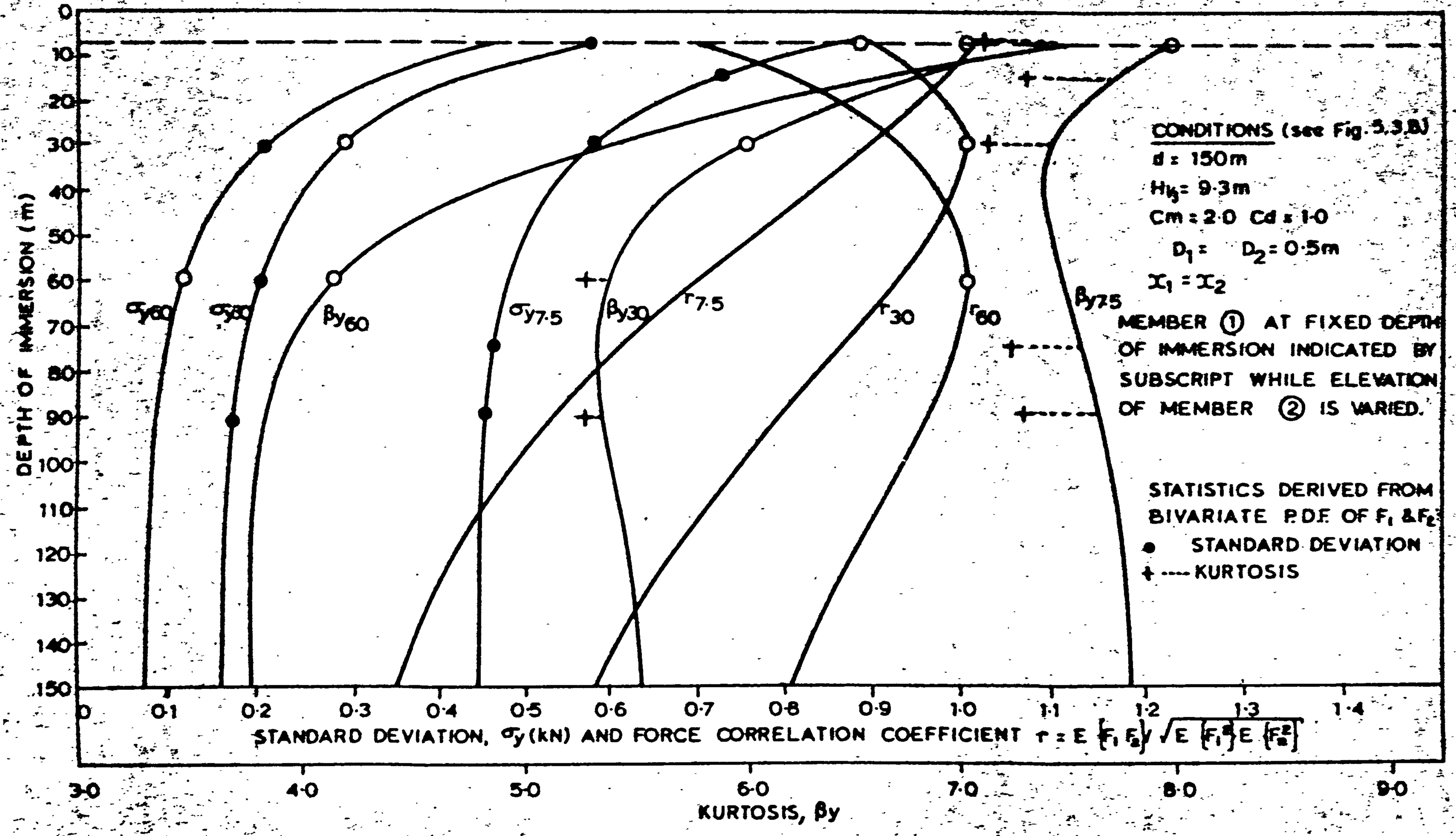

FIG.5.4.7. KURTOSIS AND STANDARD DEVIATION OF TOTAL FORCE, $Y = \sum_{i=1}^{N} F_i$, FROM N UNIT LENGTH COMPONENTS OF A VERTICAL CYLINDRICAL MEMBER FOR THE CONDITIONS INDICATED. (Note: Total force on equivalent continuous member can be considered as (15Y) if member areas and volumes are considered to be lumped at the nodes indicated)

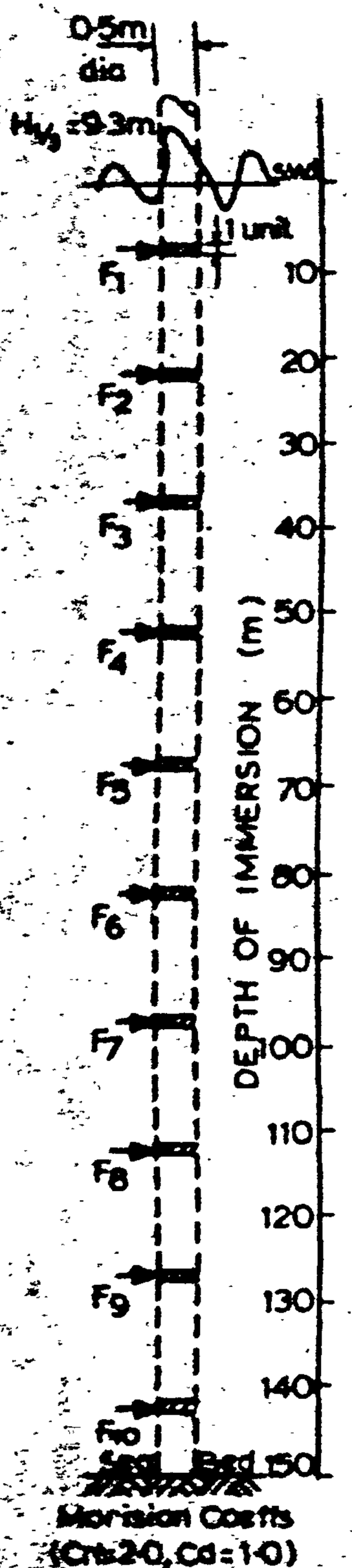

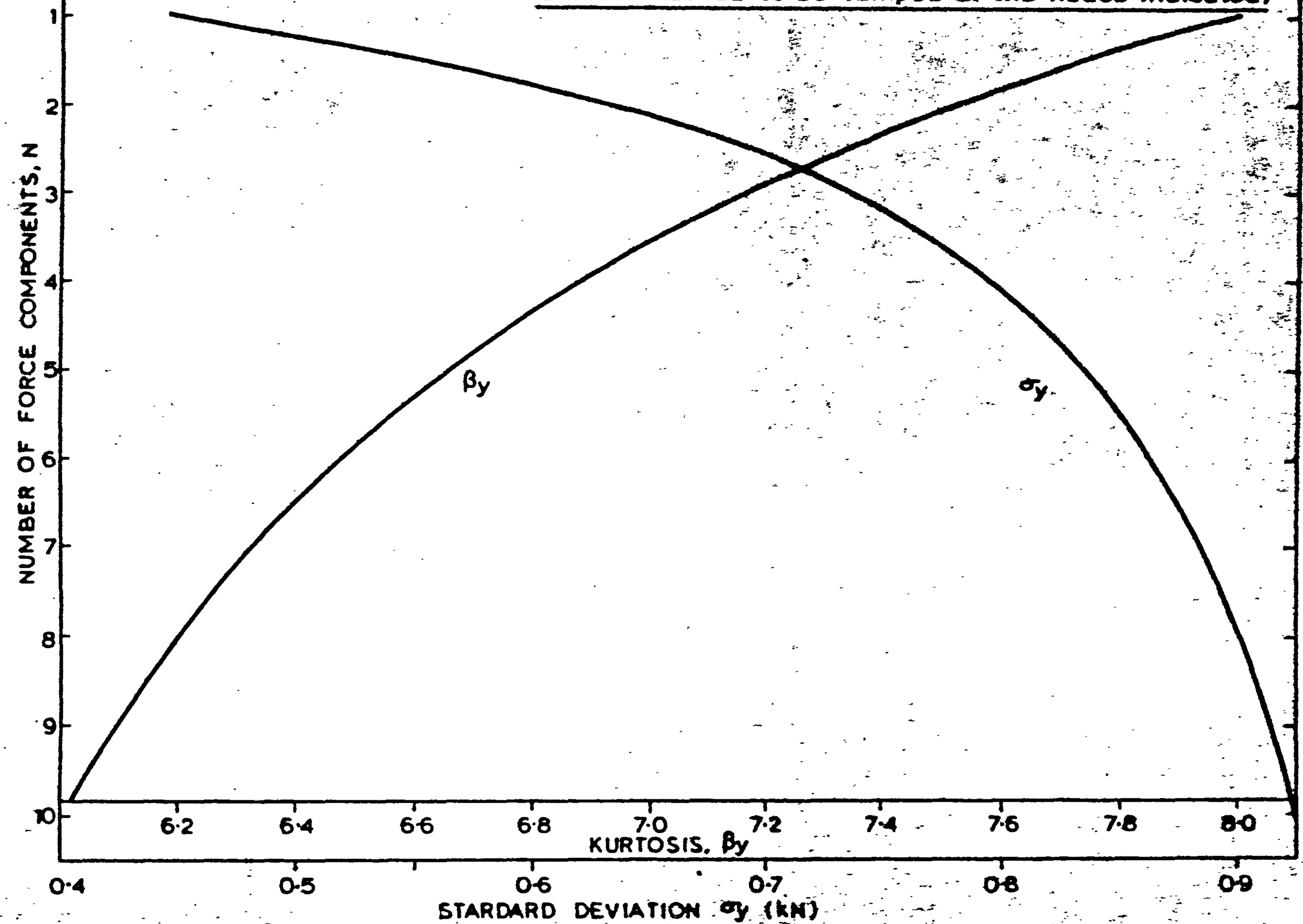

FIG. 5.4.8. POLYNOMIAL APPROXIMATION TO X|X|

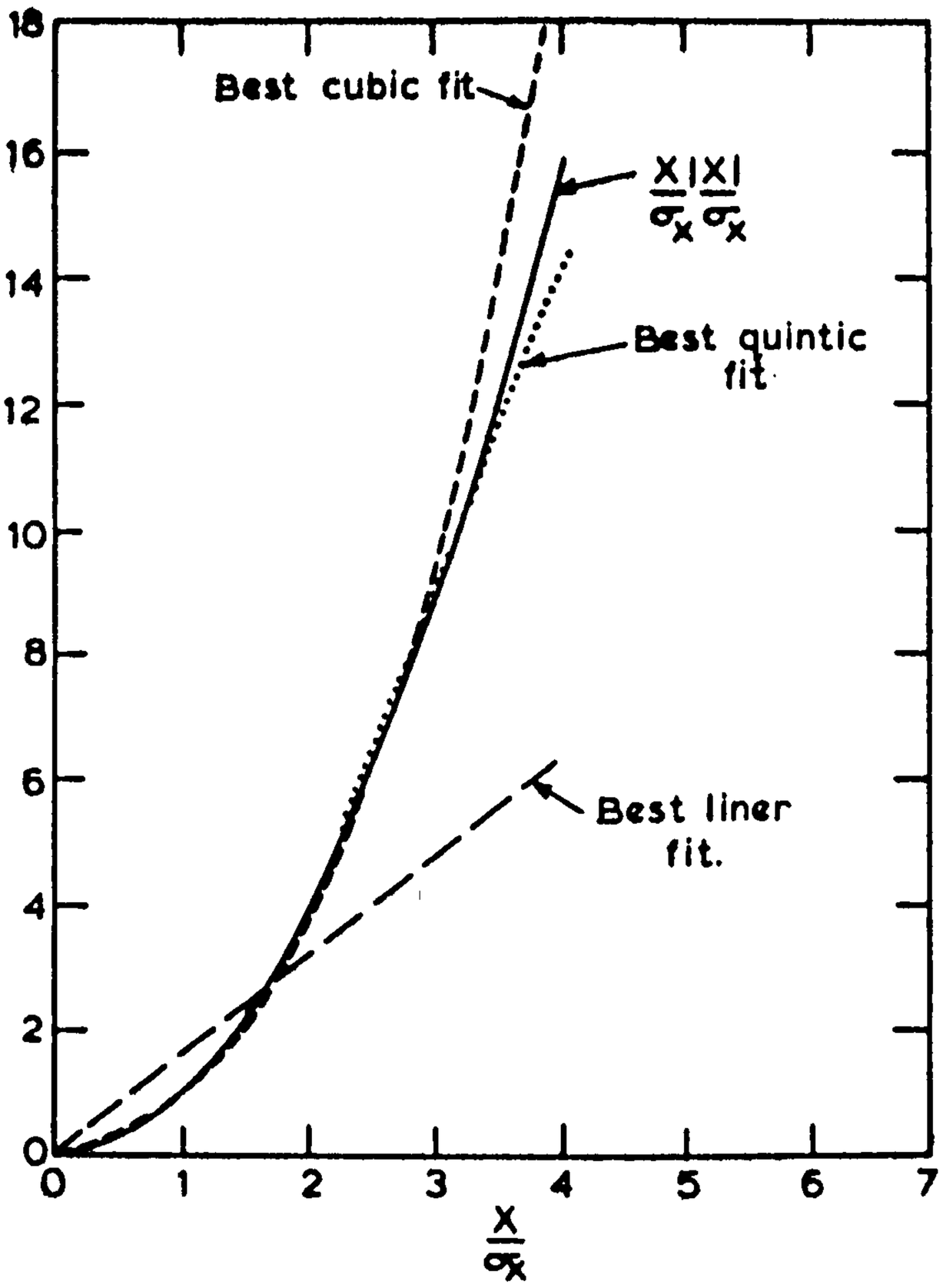

FIG. 5.6.1. WAVE LOADING ON SINGLE PILE.

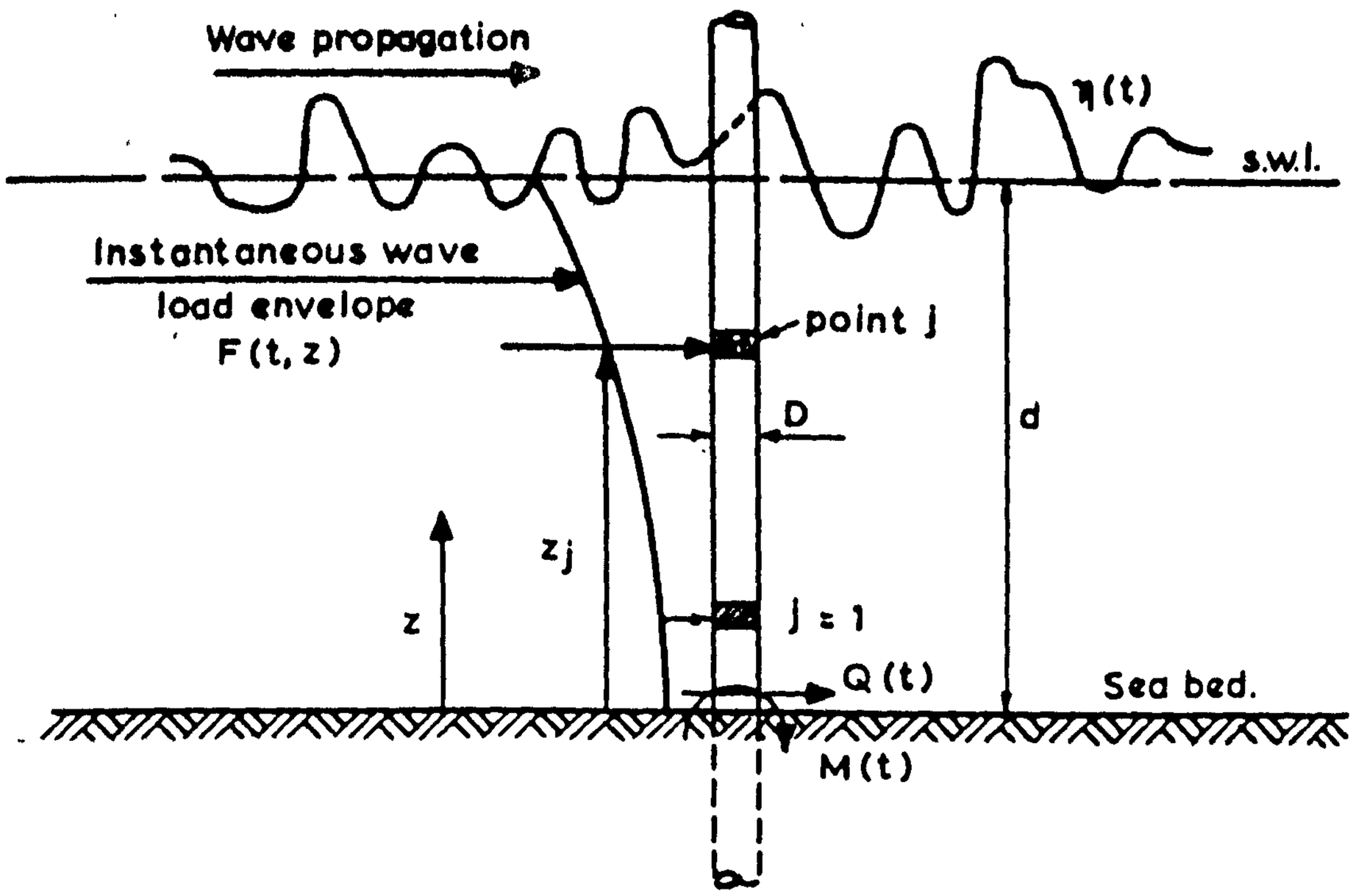

CONDITIONS.

$H_{1/3}$ = 4·8m

d = 50·0m

g = 9·807m/s²

ρ = 1·05 x 10^3 kg/m³

D = 0·5m

C_M = 2·0

C_D = 1·2

FIG. 5.6.2. CUMULATIVE DISTRIBUTION FUNCTION (c.d.f.) OF SHEAR AT THE BASE OF A VERTICAL CYLINDRICAL PILE.

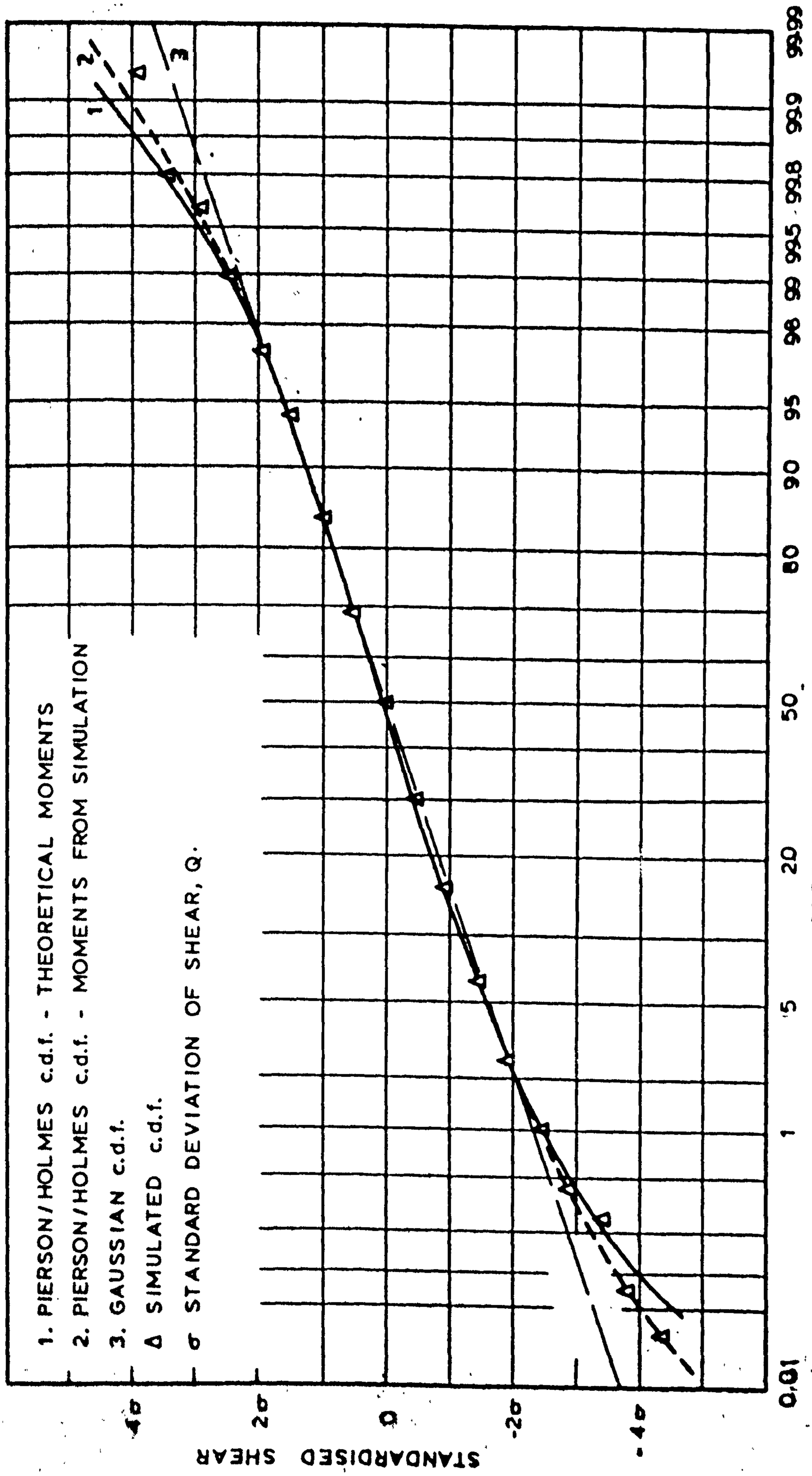

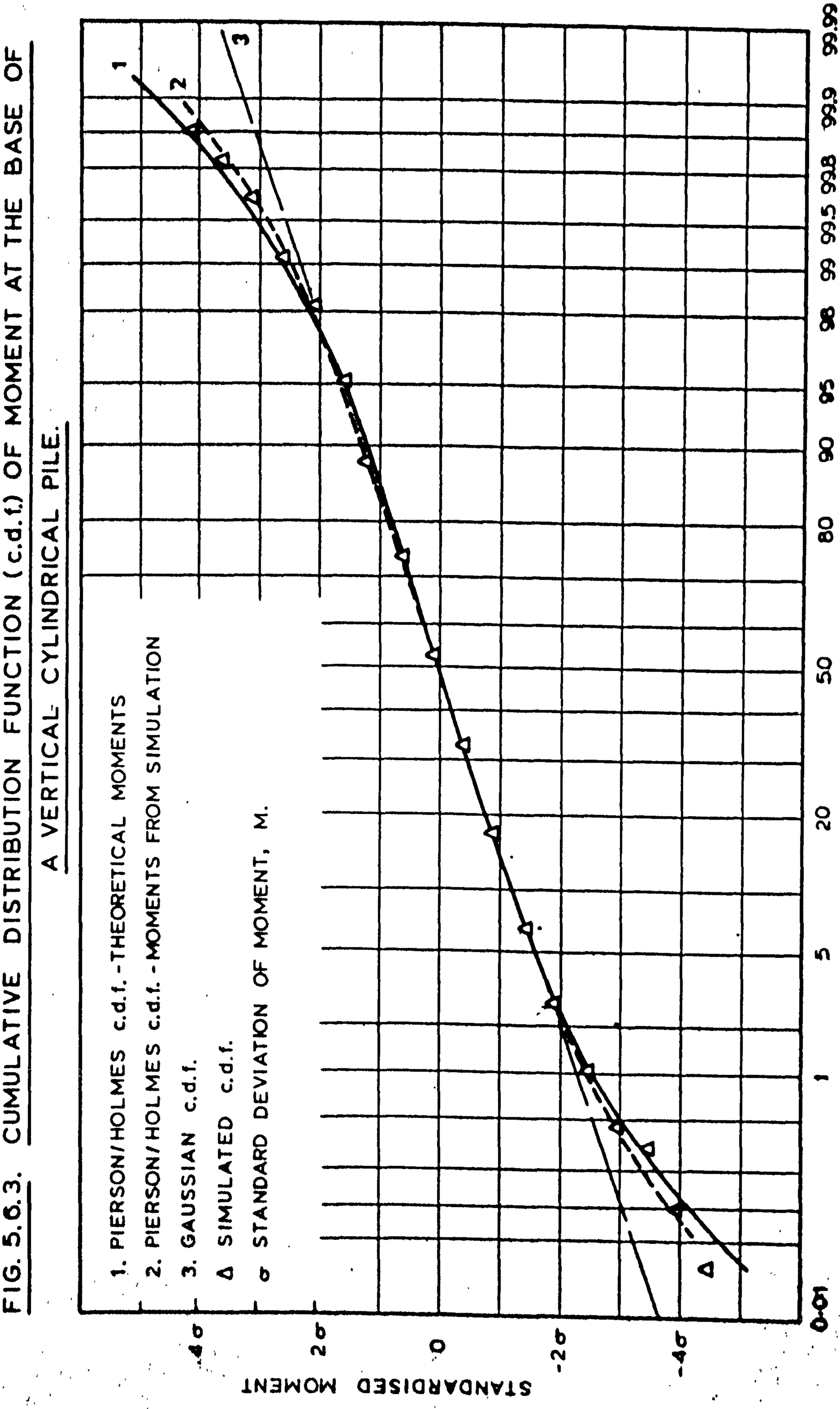

FIG. 5.6.3. CUMULATIVE DISTRIBUTION FUNCTION (c.d.f.) OF MOMENTS AT THE BASE OF A VERTICAL CYLINDRICAL PILE.

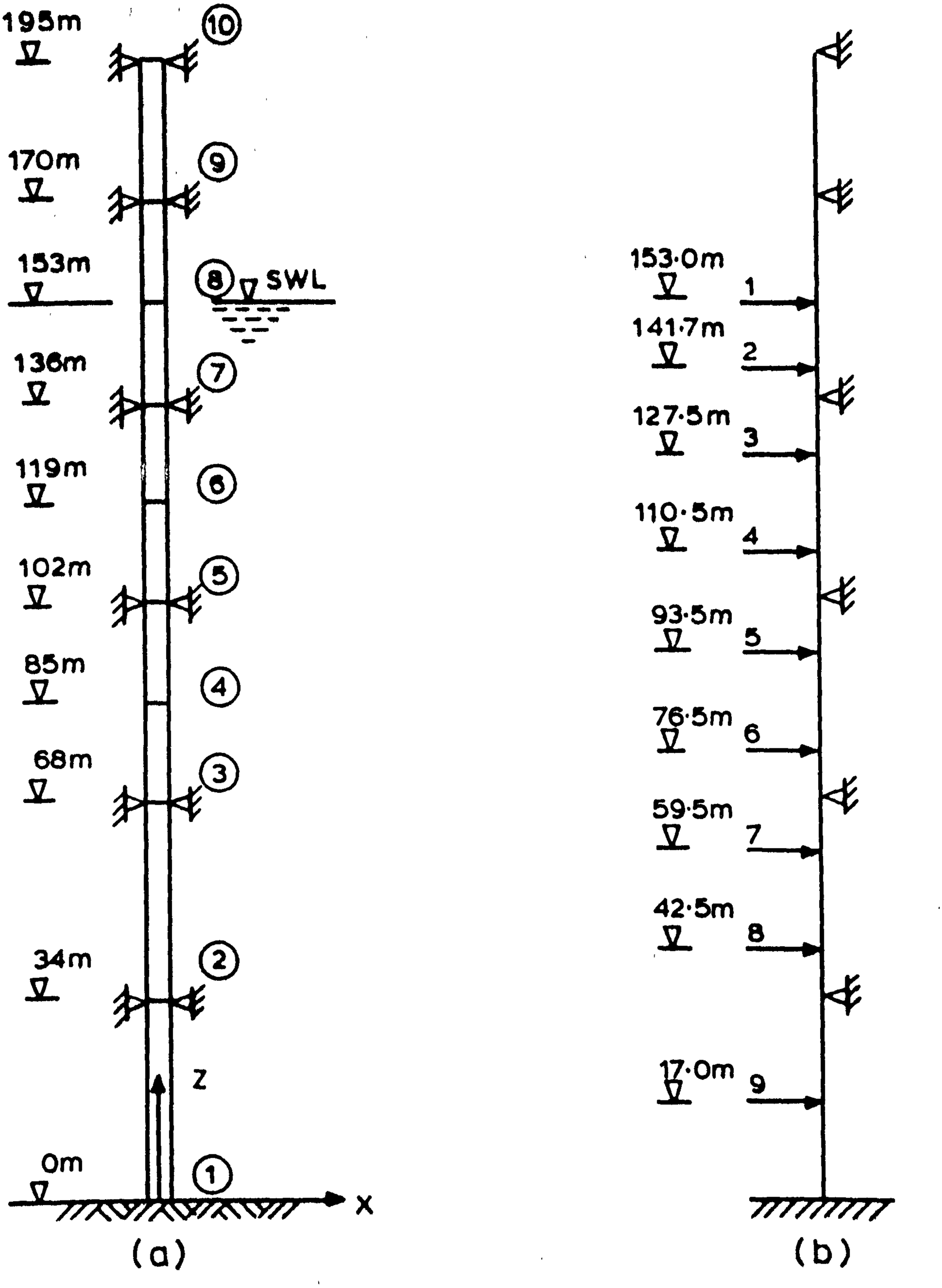

NODE POSITIONS

LOAD POSITIONS

FIG. 5.6.4. CONDUCTOR TUBE - IDEALISATION.

FIG.5.6.5. IDEALISATION OF SIMPLE SYMMETRICAL FRAME STRUCTURE IN TWO DIMENSIONS.

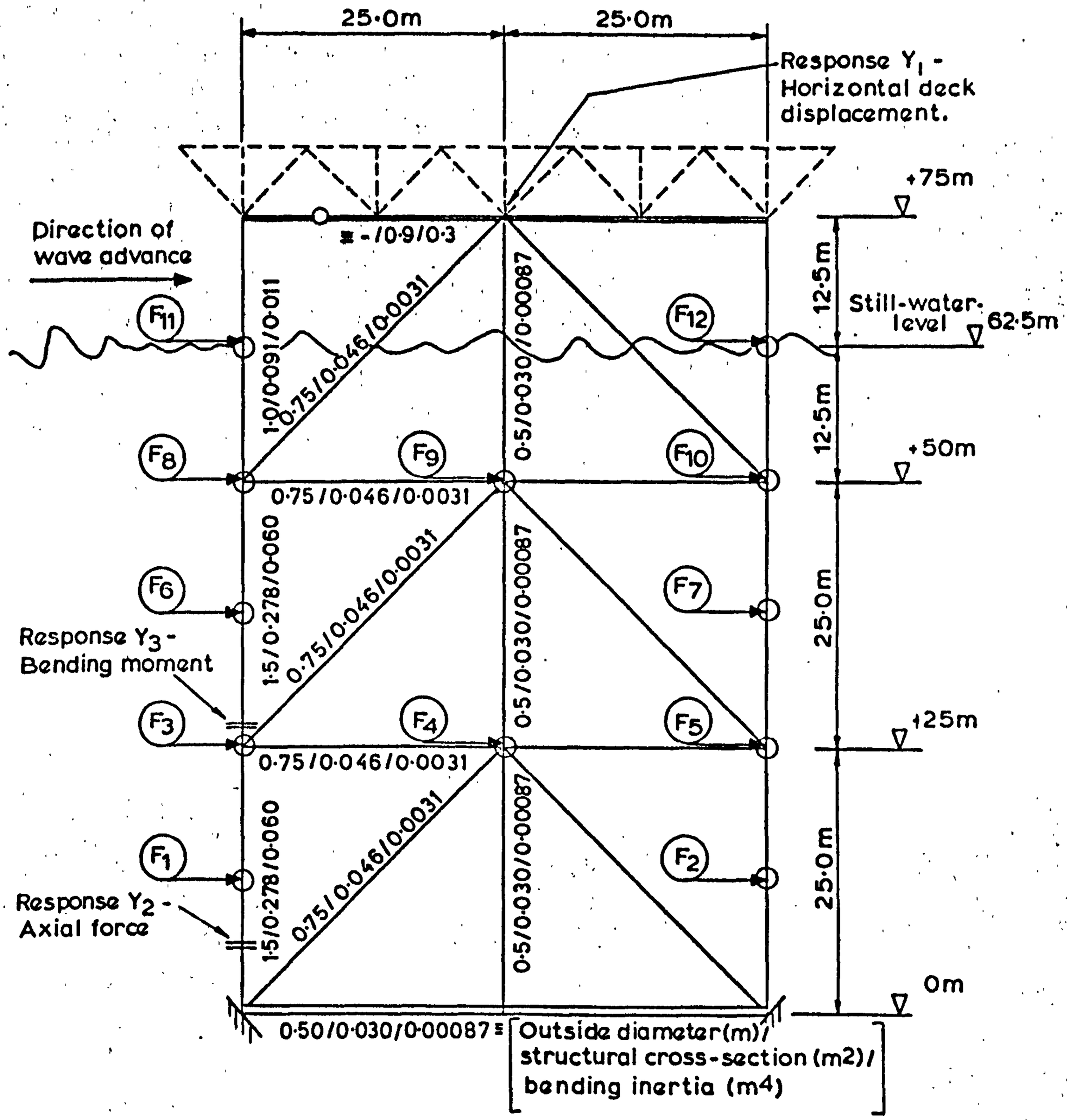

C H A P T E R S I X

CONCLUSIONS

1. A rational approach to the risk analysis problem in the design of offshore structures against fatigue and first excursion failure calls for an understanding of the probabilistic properties of the random loading induced by the waves and the resulting structural response.

2. A proper treatment of the non-linear drag component in Morison's wave load equation is essential for the probabilistic analysis of structures of the steel lattice type where member diameters are generally small in relation to significant wave lengths. Linearisation of this term permits simplified analysis but has been shown to lead to considerable under-estimation of extreme loads for small diameter members.

3. In the short-term, over a period of several hours, assuming long-crested sea conditions and applying linear wave theory, the wave induced loading on short members follows the Pierson-Holmes pdf, a function which degenerates to the Gaussian pdf. as the drag effects diminish.

4. Making narrow-band assumptions for the behaviour of loading, a proposition justified previously by others, the further assumption that loading is statistically independent of its first time derivative is found to produce reasonable results for the distribution of peak values. Furthermore, this approach, which yields the cdf. of peak load as a function of only the Pierson-Holmes pdf. is shown to represent the most refined practicable model for the prediction of peak load, or response, in realistic applications which involve systems of multiple load components.

5. Using, as a basic wave climate description, the bivariate histogram, or scatter diagram of $H_{1/3}$ and T_z the properties of loading are found to be dependent on the spectral model used to generate the description of the sea surface. The values of $H_{1/3}$ and T_z are

related to the moments of the surface spectrum and, therefore, for most classes of the scatter diagram different spectra result from derivation based on $H_{1/3}$ alone, T_z alone or both $H_{1/3}$ and T_z as a result of the departures between the actual surface spectrum and the assumed spectral model. From the results presented it has been proposed that derivation based on $H_{1/3}$ only probably represents the most acceptable technique in association with either the Pierson-Moskowitz or Jonswap spectral forms. Adopting this procedure the number of short-term sea states describing the wave climate is reduced to the number of class values of $H_{1/3}$ thereby reducing considerably the computational effort necessary in the convolution into long-term descriptions. The only information which needs to be preserved from the T_z domain is the mean value of zero-upcrossing rate ($1/T_z$) associated with each class of $H_{1/3}$.

6. The probability distributions of the extreme values of wave loading, derived from the assumption of independence between individual peaks, results from the product of the cumulative probabilities abstracted from the short-term cdf.s of extreme values which are found to follow the Gumbel distribution.

7. The long-term probabilistic analysis of wave loading relies extensively on numerical integration and as such makes considerable demand on computational resources. Gaussian quadrature techniques have been considered for computer run-time minimisation with only limited success for the most drag dependent conditions due to inherent instability yielding cdf.s which oscillate about the correct values.

8. A technique for computation of long-term cdf.s of basic peak and extreme loading by hand has been developed, based on standardised plots of the Pierson-Holmes cdf.s which describe the short-term conditions. This places at the disposal of the design engineer the means for accurate wave load prediction for the solution of isolated problems which do not justify the expenditure on computing resources necessary for the complete analysis.

9. The importance of the wave climate description, forming input to the long-term analysis, has been demonstrated. It has been shown that this data should cover a complete number of years to ensure

suppression of seasonal fluctuations which may have significant effect on the cdf.s of load in the lower range, of particular importance in fatigue analysis. A method of wave climate extension from a scatter diagram covering six winter months to a synthetic 'one-year' equivalent has been developed.

10. For the prediction of extreme loading over long-periods of exposure it has been shown that the wave climate data should be extrapolated to account for the presence of the entire range of physically feasible sea states prior to application of the probabilistic wave load analysis. A method of extrapolation has been proposed, based on the marginal distribution of $H_{1/3}$ where 'method of moments' fitting of the data to either the Gumbel or Weibull theoretical pdf.s is employed. This method of fitting minimises the weighting attached to the extreme conditions which are subject to most uncertainty in respect to their 'true' frequency of recurrence and are, therefore, liable to erroneously 'skew' the tails of the cdf.s of $H_{1/3}$ on probability paper.

11. The probabilistic properties of individual member loading are of limited value for the design of complete structures where probabilistic descriptions of critical response variables are a pre-requisite, which depend on the simultaneous loading on many interconnected members. The non-Gaussian multi-variate pdf. of such variables has been formulated for an idealisation of a complex structure, where member volumes and areas, and hence 'Morison' wave load components, are lumped at a discrete set of nodes. The pdf. of individual, 'marginal', response variables required for risk analysis may be abstracted from this multi-variate pdf. The procedure applies for wave loading in the absence of currents and intermittency effects near the free surface and where behaviour of the structure is assumed to be quasi-static and linear.

12. Results presented, for application to simple systems comprising of two nodes, have illustrated the similarity between the form of probability distribution describing response and that of the wave loading, namely the Pierson-Holmes pdf. for short-term conditions.

13. It has been shown that excessive computer run-time requirements prevent extension of the multi-variate procedures to systems more complex than two load points. However, assuming the short-term pdf. of response to be of the Pierson-Holmes form, a proposition further supported by prototype and laboratory data analysis performed by Tickell[55], it is fully described by its second and fourth order statistical moments. Expressions for these moments have been developed in terms of the known statistics of the water particle motions at the nodes. The pdf.s of response derived in this way make considerably less demand on computational resources than the multi-variate approach, permitting systems of up to 12 nodes to be analysed.

14. This latter restriction on system complexity results in part from numerical integrations required for the solution of certain four-variate expectations in the fourth order moment of response. Various approximations for these terms have been considered which obviate the need for numerical integration and thus enable systems of up to about 35 nodes to be investigated. However, the presently applied approximations have been found to be insufficiently accurate for use in complex systems and a procedure for the development of more precise approximations has been outlined.

15. Some applications of the probabilistic procedures to typical structures have been illustrated and compared with those from time series simulation. The agreement shown between the results of these different approaches has provided an indication of the validity of the mathematical models developed herein. For systems of up to 12 nodes the probabilistic method would appear to have both 'accuracy' and 'run-time' advantages over simulation. However, in the absence of an improved 'approximate' probabilistic method, discussed in 14 above, the use of time simulation for the estimation of the moments of response provides the most reliable and economic approach for analysis of systems of greater than 12 nodes.

C H A P T E R S E V E N

RECOMMENDATIONS

1. The outlined procedure for improvement of the approximations incorporated in the expression for the fourth moment of response should be investigated. This will permit extension of the probabilistic techniques from systems at present limited to 12 load components to structural idealisations comprising up to about 35 components.

2. Application of the probabilistic procedures developed herein to real structures should be performed with the aid of advice of a structural nature on the optimal means of structural idealisation into the limited number of load components which can be handled by the method. The aim of such idealisations is to retain as realistic a description as possible of the response variables of interest.

3. The importance of an accurate description of the long-term wave climate on the prediction of extreme values of wave load or structural response has been illustrated. It is proposed that further work should be carried out on the problems of suppression of annual variability for purposes of data extrapolation. This will involve the collection of existing wave climate measurements, in the form of scatter diagrams of $H_{1/3}$ and T_z, spanning as many years as available. Analysis of this data should then be performed, in conjunction with an analysis of wind records to ascertain the typicality of the climate recorded, with the aim of producing a method of fitting of the data (in terms of $H_{1/3}$ only) to theoretical

probability distributions such that the effects of annual variability are minimised.

In this way more reliable extrapolation will be possible from limited data bases.

Items 1 to 3 above all follow directly from the results of the work described herein. Each of these areas of further research were included in the proposals of the University of Liverpool, in the Science & Engineering Research Council funded Marine Technology Programme of the North West Consortium of Universities. Items 1 and 2 were subsequently approved, as part of Project 1.1 which commenced in October 1978 with the author a joint investigator in association with his colleagues Professor P. Holmes and Mr. R. G. Tickell. The wave climate programme was deferred in view of the existence of wave climate analysis programmes currently being undertaken at other establishments.

4. The probabilistic analysis described herein is limited to conditions where waves are assumed to be long-crested and uni-directional. In the absence of information on wave direction in addition to the short-term sea state parameters of $H_{1/3}$ and T_z it may be considered appropriate and conservative to perform the probabilistic analysis, using the complete wave climate, for wave advance from a number of predominant wave directions.

However, as more extensive wave climate measurements become available, it will be necessary to account for wave directionality in the probabilistic analyses. Two levels of directionality exist, the first represents the variation in direction from wave to wave. Theoretical models for this situation are available where wave energy is dispersed about the predominant wave direction. Inclusion of this behaviour in the probabilistic analysis is unlikely to be possible as a straightforward extension of the existing techniques discussed herein. The second level of directionality describes the variation in predominant wave direction from one short-term sea state to the next. If this information is made available then scatter diagrams could be formulated for a number of discrete bands of wave direction. In this situation the probabilistic analysis for response developed herein could be performed for each direction, with a final convolution to yield the complete long-term characteristics.

5. As offshore installations move into deeper water and as the new generation of tethered or 'guyed' structures are introduced, the effects of dynamic response of the structures will become more significant. In these circumstances the motion of the structure will no longer be negligible and wave loading will be related to the relative motion of the fluid past the structural members. Furthermore, descriptions of response will also be dependent on the interaction between the structure and its foundations.

Probabilistic models for response will not, therefore, result from procedures along the lines investigated herein. They are more likely to follow indirectly from advanced techniques involving high order spectral analysis, including bi- and tri-spectra, as discussed briefly in Section 2.3.4. This will yield statistical moments of response, in excess of the second moment obtained from the basic 'linear' spectral analysis, thereby accounting for the inherent non-linearities resulting from the loading.

REFERENCES

1. DRAPER, L.
'Environmental conditions'
Proc. Symp. on Offshore Drilling Rigs, The Royal Inst. Naval Architects, 1970.

2. PIERSON, W. J. Jr. and HOLMES, P.
'Irregular wave forces on a pile'
Waterways & Harbors Div., ASCE, 1965, 91, WW4, 1.

3. BORGMAN, L. E.
'Wave forces on piling for narrow-band spectra'
Waterways & Harbors Div., ASCE, 1965, 91, WW3, 65-90.

4. BRETSCHNEIDER, C. L.
'Probability distribution of wave force'
Waterways & Harbors Div., ASCE, 1967, 93, WW2, 5.

5. TUNG, C. C. and HUANG, N. E.
'Interactions between waves and currents and their influence on fluid forces'
BOSS '76, Behaviour of Offshore Structures Conf., Norwegian Inst. Technology, 1976.

6. TUNG, C. C.
'Statistical properties of wave force'
Eng. Mechanics Div., ASCE, 1975, EM1, 1-11.

7. BATTJES, J. A.
'Long-term wave height distribution at seven stations around the British Isles'
National Institute of Oceanography, Godalming, 1970, Report A44.

8. SÖDING, H.
'Calculation of long-term extreme loads and fatigue loads of marine structures'
Int. Symp. on 'The Dynamics of Marine Vehicles and Structures in Waves', Inst. Mechanical Engineers, April 1974.

9. PENZIEN, J., KAUL, M. K. and BERGE, B.
'Stochastic response of offshore towers to random sea waves and strong motion earthquakes'
Computers and Structures, 1972, 2, 733-756.

10. HOLMES, P., TICKELL, R. G. and BURROWS, R.
'Prediction of long-term wave loading on offshore structures'
OSFLAG 5 Report A, Univ. Liverpool, Dept. Civ. Eng., 1975, June.

11. HOLMES, P., TICKELL, R. G. and BURROWS, R.
'Prediction of long-term wave loading on offshore structures'
OSFLAG 5 Report B, Univ. Liverpool, Dept. Civ. Eng., 1978.

12. TICKELL, R. G., BURROWS, R. and HOLMES, P.
'Long-term wave loading on offshore structures'
Proc. Pt. 2, Research & Theory, ICE, 1976, 61, March, 145-162.

13. BURROWS, R.
'Probabilistic model for the quasi-static response of offshore structures'
MCE/2/76, Univ. Liverpool, Dept. Civ. Eng., 1976, June.

14. BURROWS, R.
'Quasi-static response of offshore structures using probabilistic methods'
Applied Mathematical Modelling, 1977, 1, September.

15. BURROWS, R., TICKELL, R. G. and HOLMES, P.
'A note on the non-Gaussian probabilistic analysis of wave loading on offshore structures'
MCE/1/78, Univ. Liverpool, Dept. Civ. Eng., 1978, January.

16. BURROWS, R.
'Probabilistic description of the response of offshore structures to random wave loading'
Proc. IAHR Symp. on 'Mechanics of Wave Induced Forces on Cylinders', Univ. Bristol, 1978, September.

17. BURROWS, R.
'A simple technique for the prediction of non-linear random wave loading'
Proc. Pt. 2, Research & Theory, ICE, 1978, 65, December, 731-748.

18. BURROWS, R., CHAPLIN, J. R., HEDGES, T. S., HOLMES, P. and TICKELL, R. G.
Discussion 'Estimation of fluid loading on offshore structures'
Proc. Pt. 2, Research & Theory, ICE, 1978, 65, December, 954-958.

19. BURROWS, R.
'A comparative study of simulation and probabilistic techniques for wave loading on offshore structures'
MCE/1/79, Univ. Liverpool, Dept. Civ. Eng., 1979.

20. BURROWS, R.
'The choice of period when estimating loading on cylinders from regular waves'
Proc. Pt. 2, Research & Theory, ICE, 1979, 67, June.

21. MORISON, J. R., O'BRIEN, M. P., JOHNSON, J. W. and SHAAF, S. A.
'The forces exerted by surface waves on piles'
Petroleum Trans., Am. Inst. Mech. Engrs., 1950, 189, May, 149-154.

22. BURROWS, R.
'Probabilistic description of wave load and structural response - Computer Programs'
Univ. Liverpool, Dept. Civ. Eng., 1978, February.

23. HOGBEN, N.
'Wave loads on structures',
BOSS '76, Behaviour of Offshore Structures Conf., Norwegian Inst. Technology, 1976, 187-219.

24. WIEGEL, R. L.
'Oceanographical Engineering'
Prentice-Hall, 1964.

25. MALHOTRA, A. K. and PENZIEN, J.
'Non-deterministic analysis of offshore structures'
Eng. Mechanics Div., ASCE, 1970, 96, EM6, 985-1003.

26. MILGRAM, J. H.
'Waves and wave forces'
BOSS '76, Behaviour of Offshore Structures Conf., Norwegian Inst. Tech., 1976.

27. HOGBEN, N. et al
'Estimation of fluid loading on offshore structures'
Proc. Pt. 2, Research & Theory, ICE, 1977, 63, September, 515-562.

28. BORGMAN, L. E.
'Computation of the ocean-wave forces on inclined cylinders'
Trans. Am. Geophysical Union, 1958, 39, No. 5, October.

29. DET NORSKE VERITAS
'Rules for design, construction and inspection of fixed offshore structures'
Det Norske Veritas, Oslo, 1974.

30. SHORE PROTECTION MANUAL
U.S. Army Coastal Eng. Research Center, 1973.

31. THE BRITISH SHIP RESEARCH ASSOCIATION
Contract Report NOW 278, 'A critical evaluation of the data on wave force coefficients', 1976, August.

32. DEAN, R. G.
'Relative validities of water wave theories'
Waterways & Harbors Div., ASCE, 1970, WW1, 105-119.

33. LAMB, H.
'Hydrodynamics'
Dover Publications, New York, 1945.

34. STOKES, G. G.
'On the theory of oscillatory waves'
Mathematical and physical papers, 1, Cambridge: Cambridge Univ. Press, 1880.

35. SKJELBREIA, L.
'Gravity waves, Stokes' third order approximation'
Berkeley, Calif., The Eng. Foundation Council on Wave Research, 1959.

36. SKJELBREIA, L. and HENDRICKSON, J.
'Fifth order gravity wave theory'
Proc. 7th Conf. on Coastal Eng., Netherlands, 1960, Pub. Council on Wave Research, The Eng. Foundation, Berkeley, Univ. California.

37. BORGMAN, L. E.
'Directional spectra models for design use'
Offshore Technology Conf. Proc. 1969, Paper 1069.

38. PIERSON, W. J. Jr.
'Wind-generated gravity waves'
Advances in Geophysics, 1955, 2, 93-178.

39. LONGUET-HIGGINS, M. S.
'The heights of sea waves'
Jnl. of Marine Research, 1952, 11, No. 3, 245-

40. OCHI, M. K.
'On prediction of extreme values'
Jnl. of Ship Research, 1973, March, 29-37.

41. DRAPER, L. and DRIVER, J. S.
'Winter waves in the Northern North Sea at 57°30'N 3°00'E recorded by m.v. Famita'
National Inst. of Oceanography, Godalming, NIO Report A48, 1971, August.

42. SAETRE, H. J.
'On high wave conditions in the Northern North Sea'
Inst. Oceanographic Sciences (formerly Nat. Inst. of Oceanography), Godalming, Report No. 3, 1974.

43. PIERSON, W. J. Jr. and MOSKOWITZ, L. J.
'A proposed spectral form for fully-developed wind seas based on the similarity theory of S. A. Kitaigorodskii'
Jnl. Geophysical Research, 1964, 69, No. 24, 5181.

44. HOWARD, D.
Ph.D. Thesis, Univ. Liverpool, Dept. Civ. Eng., 1974.

45. LIN, Y. K.
'Probability theory of structural dynamics'
McGraw-Hill, New York, 1967.

46. WILLIAMS, A. K. and RINNE, J. E.
'Fatigue analysis of steel offshore structures'
Proc. Pt. 1, ICE, 1976, 60, November, 635-654.

47. BENDAT, J. S. and PIERSOL, A. G.
'Random data: analysis and measurement procedures'
Wiley-Interscience, 1971.

48. CIRIA
'Dynamics of marine structures: methods of calculating the dynamic response of fixed structures subject to wave and current action'
Report UR8, 1977.

49. AKAIKE, H.
'Note on higher order spectra'
Ann. Inst. Statistical Mathematics, 1966, 18, No. 1, 123-126.

50. NAGATA, Y.
'Lag joint probability, higher order co-variance function and higher order spectrum'
La Mer, 1970, 8, No. 2, 78-94.

51. YAMANOUCHI, Y.
'Ship's behaviour on ocean waves as a stochastic process'
Int. Symp. on 'The Dynamics of Marine Vehicles and Structures in Waves', Inst. Mech. Engrs., 1974, April.

52. VASSILOPOULOS, L. A.
'The application of statistical theory of non-linear systems to ship motion performance in random seas'
ISP, 1967, 14, No. 150, 54-65.

53. FOSTER, E. T.
'Statistical prediction of wave-induced responses in deep-ocean tower structures'
Hydraulics Eng. Lab., Report HEL 9-14, Univ. California, Berkeley, 1967, October.

54. HOLMES, P. and TICKELL, R. G.
'The long-term probability distribution of peak wave induced loads on structural sections'
Report MCE/Nov.74, Univ. Liverpool, Dept. Civ. Eng., 1974.

55. TICKELL, R. G.
'Continuous random wave loading on structural members'
The Structural Engineer, 1977, 55, No. 5, May, 209-221.

56. BENDAT, J. S.
'Probability functions for random responses: prediction of peaks, fatigue damage and catastrophic failures'
Measurement Analysis Corporation, Los Angeles, California, 1964.

57. MINER, M. A.
'Cumulative damage in fatigue'
Jnl. Applied Mechanics, 1945, 12, 159-164.

58. GUMBEL, E. J.
'Statistics of extremes'
Columbia Univ. Press, 1958.

59. BURROWS, R., HEDGES, T. S. and MASON, W. G.
'The influence of wave-current interaction on induced fluid loading'
Proc. Symp. on 'Hydrodynamics in Ocean Engineering', Trondheim, Norway, August 1981.

60. BORGMAN, L. E.
'Statistical models for ocean waves and wave forces'
In 'Advances in Hydroscience', Academic Press, London, 1972, 8, 139-181.

61. NEUMANN, G.
'Zur charakteristik des seeganges'
Arch. für Meteorol, Geophys. und Bioclamatologie, 1954, Serie A7, 352-377.

62. DARBYSHIRE, J.
'An investigation of storm waves in the North Atlantic Ocean'
Proc. Royal Society, London, 1955, Ser. A, Vol.230, 560-569.

63. BRETSCHNEIDER, C. L. et al
'Data for high wave conditions observed by the OWS "Weather Reporter" in December 1959'
Deutsche Hydrographische Zeitschrift, Band 15, Heft 6, 1962.

64. ABRAHAMSEN, E.
'Recent developments in the practical philosophy of ship structural design'
Det Norske Veritas, 1967, Pub. 60.

65. HASSELMANN, K. et al
'Measurements of wind-wave growth and swell decay during the Joint North Sea Wave Project (JONSWAP)'
Deutsche Hydrographische Zeitschrift, Reihe A (8°), No. 12, 1973.

66. EWING, J. A.
'Some results from the Joint North Sea Wave Project of interest to engineers'
Int. Symp. on Dynamics of Marine Vehicles and Structures in Waves', Inst. Mech. Eng., April 1974.

67. PHILLIPS, O. M.
'The dynamics of the upper ocean'
Cambridge Univ. Press, 1966.

68. HOUMB, O. G. and OVERVIK, T.
'Parameterisation of wave spectra and long-term joint distribution of wave height and period'
BOSS '76, Behaviour of Offshore Structures Conf., Norwegian Inst. Tech., 1976, 144-168.

69. KRYLOV, V. I.
'Approximate calculation of integrals'
Macmillan, 1962.

70. PEDERSEN, B.
'Predictions of long-term wave conditions with special emphasis on the North Sea'
Proc. Int. Conf. on 'Port & Ocean Engineering under Arctic Conditions', Trondheim, 1971, Vol. II.

71. DRAPER, L. and DRIVER, J. S.
'Winter waves in the Northern North Sea at 57°30'N 3°00'E recorded by m.v. Famita'
National Institute of Oceanography, Godalming, 1971, August, NIO Int. Report A.48.

72. JASPER, N. H.
'Statistical distribution patterns of ocean waves and of wave-induced ship stresses and motions, with engineering applications'
Trans. Soc. Naval Arch. and Marine Engrs., 1956, Vol. 64, 415-432.

73. WEIBULL, W.
'A statistical distribution of wide applicability'
Jnl. of Applied Mech., 1951, Vol. 18, 293-297.

74. NOLTE, K. G.
'Statistical methods for determining extreme sea state'
Second Int. Conf. on 'Port and Ocean Eng. under Arctic Conditions', Univ. Iceland, Reykjavik, 1973.

75. SAETRE, H. J.
'On high wave conditions in the Northern North Sea'
Inst. Oceanographic Sciences, Godalming, 1974, Report No. 3.

76. CHOW, V. T.
'Handbook of applied hydrology'
McGraw-Hill, 1964.

77. METEOROLOGICAL OBSERVERS HANDBOOK
HMWO, 3rd Ed., 1969.

78. PAPOULIS, A.
'Probability, random variables and stochastic processes'
McGraw-Hill, 1965.

79. BORGMAN, L. E.
'Ocean wave simulation for engineering design'
J. Waterways & Harbors Div., ASCE, 1969, 95, WW4, 557-583.

80. CHEN, J. J.
'Simulated random wave loading on horizontal and vertical members of an offshore structure'
Dissertation for Diploma of Maritime Civil Engineering, Univ. Liverpool, Dept. Civ. Eng., 1975, September.

81. ZIENKIEWICZ, O. C. and CHEUNG, Y. K.
'The finite element method in structural and continuum mechanics'
McGraw-Hill, 1967.

82. PRICE, R.
'A useful theorem for non-linear devices having Gaussian inputs'
IRE, PGIT, Vol. IT-4, 1958.

A P P E N D I X O N E

ANALYSIS OF RANDOM VARIABLES

INTRODUCTION

The purpose of this Appendix is to outline the essential concepts and statistical parameters used to describe continuous random phenomena. No attempt has been made to produce a comprehensive or rigorous account of all such concepts or parameters.

I.1 DETERMINISTIC AND RANDOM PHENOMENA

Any physical phenomenon can be broadly classified as being either deterministic or random.

Deterministic phenomena are those which can be predicted exactly in terms of known parameters of the problem.

Random phenomena must be described in terms of probability statements or statistical averages. In these cases, for time varying quantities, the value of the quantity at any point in time is unknown but it is possible to say that there is a certain probability that it will exceed a particular value.

I.2 DESCRIPTIVE PROPERTIES OF RANDOM VARIABLES

The properties of time varying random variables may be described in either the time, frequency or amplitude domains. The time and frequency domains are outlined below, a more detailed account being given by Bendat and Piersol[47]. Description in the amplitude domain concerns probability theory which is covered in the following Section I.3.

I.2.1 Time Domain

I.2.1.1 Basic statistical parameters

Given the time history of a random variable x(t) as demonstrated in Fig. I.1, the following parameters are basic:

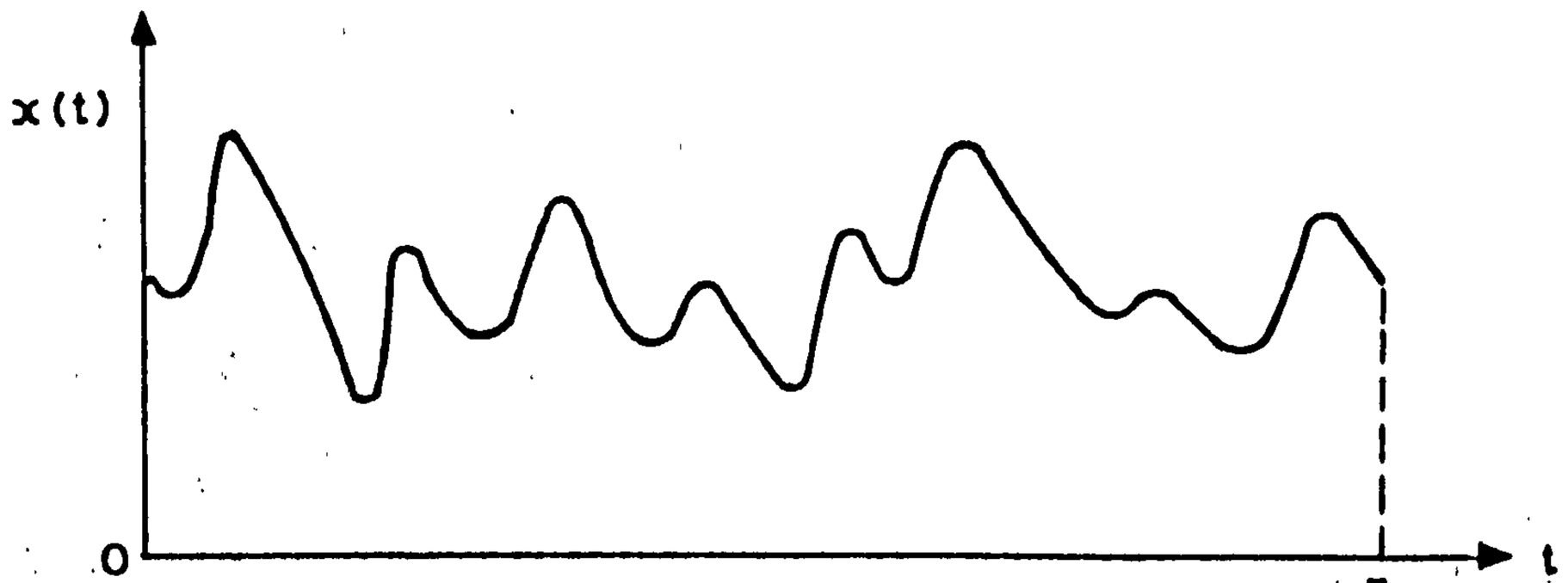

Fig. I.1 - Sample Time History of Random Variable x

the MEAN value:

$$\bar{x} = \lim_{T\to\infty} \frac{1}{T} \int_{t=0}^{T} x(t)\, dt \qquad (I.1)$$

the MEAN SQUARE value:

$$\psi_x^2 = \lim_{T\to\infty} \frac{1}{T} \int_{t=0}^{T} x^2(t)\, dt \qquad (I.2)$$

and the VARIANCE:

$$\sigma_x^2 = \lim_{T\to\infty} \frac{1}{T} \int_{t=0}^{T} (x(t) - \bar{x})^2\, dt \qquad (I.3)$$

where σ_x is the STANDARD DEVIATION:

$$= \sqrt{\psi_x^2 - \bar{x}^2}$$

These parameters are considered to be basic because they are sufficient to fully define most theoretical probability distributions used to describe continuous random variables, for example, the Gaussian distribution. However, this is not the case for all probability distributions and so it may be necessary to consider higher order parameters, as follows:

The n-th order (statistical) moment is defined as:

$$M_n = \lim_{T\to\infty} \frac{1}{T} \int_{t=0}^{T} x^n(t)\, dt \qquad (I.4)$$

with $M_1 = \bar{x}$ and $M_2 = \psi_x^2$.

The n-th order central moment, or n-th order moment about the mean, is defined as:

$$M_{cn} = \lim_{T\to\infty} \frac{1}{T} \int_{t=0}^{T} (x - \bar{x})^n \, dt \qquad (I.5)$$

with $M_{c2} = \sigma_x^2$.

I.2.1.2 Auto-correlation function

The general dependence of values of x(t) at one time to those at another time, τ units later, is described by the auto-correlation function:

$$R_x(\tau) = \lim_{T\to\infty} \int_{t=0}^{T} x(t)\, x(t+\tau)\, dt . \frac{1}{T} \qquad (I.6)$$

which has the properties:

$$R_x(-\tau) = R_x(\tau) \qquad (I.7)$$

$$R_x(0) = \psi_x^2 \geq |R_x(\tau)| \qquad (I.8)$$

I.2.1.3 Cross-correlation function

The inter-relationship between two sets of random variables $x_1(t)$ and $x_2(t)$ can be described by the cross-correlation function:

$$R_{x_1x_2}(\tau) = \lim_{T\to\infty} \frac{1}{T} \int_{t=0}^{T} x_1(t)\, x_2(t+\tau)\, dt \qquad (I.9)$$

which has the properties:

$$R_{x_1x_2}(-\tau) \neq R_{x_1x_2}(\tau) \qquad (I.10)$$

$$= R_{x_2x_1}(\tau)$$

and if $R_{x_1x_2}(0) = 0$, then $x_1(t)$ and $x_2(t)$ are uncorrelated.

I.2.1.4 Auto-covariance function, cross-covariance function and correlation coefficient

Auto-covariance and cross-covariance functions are similar to the corresponding correlation functions but include an adjustment for the mean as follows:

$$C_x(\tau) = \lim_{T\to\infty} \int_{t=0}^{T} [x(t) - \bar{x}]\,[x(t+\tau) - \bar{x}]\,dt.\frac{1}{T} \qquad (I.11)$$

and

$$C_{x_1x_2}(\tau) = \lim_{T\to\infty} \int_{t=0}^{T} [x_1(t) - \bar{x}_1]\,[x_2(t+\tau) - \bar{x}_2]\,dt.\frac{1}{T} \qquad (I.12)$$

These expressions revert to $R_x(\tau)$ and $R_{x_1x_2}(\tau)$, respectively, when the random variables are mean zero ($\bar{x}_1 = \bar{x}_2 = 0$).

The correlation coefficient is defined as:

$$r_{x_1x_2} = \frac{C_{x_1x_2}(0)}{\sigma_{x_1}\,\sigma_{x_2}} \qquad (I.13)$$

I.2.1.5 Stationarity and ergodicy

A random variable, x(t), is stationary if its statistical properties, described above, are independent of the time origin.

A stationary random variable is ergodic if its statistical properties calculated from one sample record, of the form of Fig. I.1, are equal to those calculated from other samples of x(t) taken during the same time interval.

Random data representing stationary physical phenomena are generally ergodic and hence the properties of stationary random phenomena can be estimated correctly from a single observed time history record, if the finite time interval, T, considered is sufficiently long.

I.2.2 Frequency Domain (Spectral Approach)

I.2.2.1 Power spectral density function

The power spectral density function (or autospectral density function) of a random variable, x(t), describes the distribution of the mean square value as a function of frequency.

The mean square value of the portion of x(t) within the frequency band between ω and $\omega + \Delta\omega$ is given by:

$$\psi_x^2(\omega, \Delta\omega) = \lim_{T\to\infty} \int_0^T x^2(t, \omega, \Delta\omega)\, dt.\frac{1}{T} \qquad (I.14)$$

where ω is in radian measure.

As $\Delta\omega \to 0$ the power spectral density function may be defined as:

$$S_x(\omega) = \lim_{\Delta\omega\to 0} \frac{1}{\Delta\omega} \psi_x^2(\omega, \Delta\omega) \qquad (I.15)$$

For a stationary random process, the spectral density function and the correlation function, Eq. (I.6), are related by a Fourier transform:

$$S_x(\omega) = \frac{2}{\pi} \int_0^\infty R_x(\tau)\, e^{-i\omega\tau}\, d\tau$$

$$= \frac{2}{\pi} \int_0^\infty R_x(\tau) \cos \omega\tau\, d\tau \qquad (I.16)$$

The mean square value of x(t) is obtained from the inverse relationship and setting $\tau = 0$:

$$R_x(0) = \psi_x^2 = \int_0^\infty S_x(\omega)\, d\omega \qquad (I.17)$$

and is thus equal to the area under the spectral density function or 'spectrum'.

I.2.2.2 Spectral moments

The n-th order moment of $S_x(\omega)$ with respect to the origin, $\omega = 0$, is defined as:

$$m_n = \int_0^\infty \omega^n S_x(\omega)\, d\omega \qquad (I.18)$$

and hence $m_0 = \psi_x^2 = R_x(0)$.

I.2.2.3 Spectral bandwidth

The spectral bandwidth ε is used in connection with the probabilistic properties of the random variable, x(t), giving a measure of the number of 'extrema' or peaks of the process in relation to the number of crossings of the mean amplitude level, $\bar{x}$, and is defined as (see Section I.3.4.4):

$$\varepsilon = [(m_0 m_4 - m_2^2)/m_0 m_4]^{1/2} \qquad (I.19)$$

I.3 PROBABILITY THEORY

I.3.1 One Random Variable

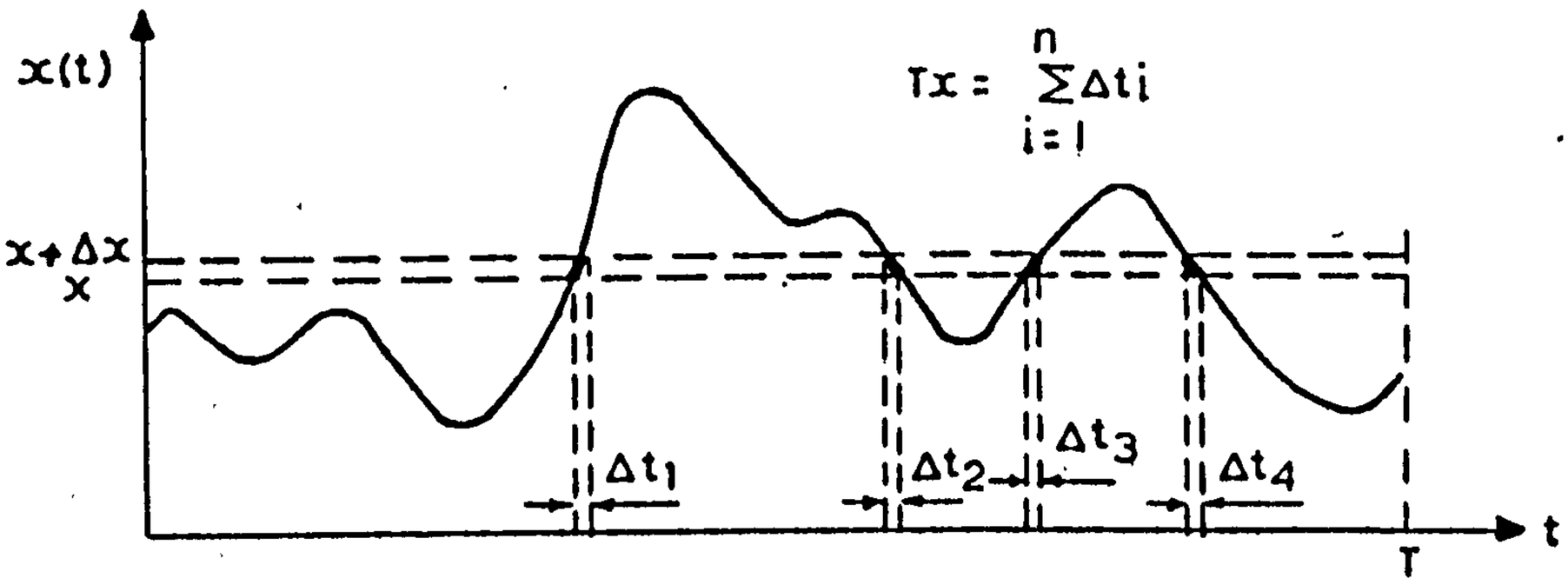

Fig. I.2

Consider a continuous time varying random variable, x(t), as sketched over a time interval from 0 to T in Fig. I.2.

I.3.1.1 Probability density function (pdf.)

The pdf. p(x), describes the probability that x(t) will take a value within some defined range (x, x + Δx) at any instant of time.

$$\text{Prob}[x \leqslant x(t) \leqslant x + \Delta x] = \lim_{T\to\infty} \left(\frac{T_x}{T}\right)$$

and

$$p(x) = \lim_{\Delta x\to 0} \frac{1}{\Delta x} \left[\lim_{T\to\infty} \left(\frac{T_x}{T}\right) \right] \qquad \text{(I.20)}$$

This density function has the properties that:

$$p(x) \geqslant 0$$

and

$$\int_{-\infty}^{\infty} p(x)\, dx = 1$$

I.3.1.2 Cumulative probability distribution function (cdf.)

The cdf. describes the probability of x(t) having a value less than or equal to a given value x:

$$P(x) = \text{Prob}[x(t) \leqslant x] = \int_{-\infty}^{x} p(\alpha)\, d\alpha \qquad \text{(I.21)}$$

This distribution function has the properties that:

$$0 \leq P(x) \leq 1$$

and

$$p(x) = \frac{dP(x)}{dx}$$

I.3.1.3 Statistical moments

The n-th order moment of the pdf. about the origin is defined as:

$$E\{x^n\} = \int_{-\infty}^{\infty} x^n \, p(x) \, dx \qquad (I,22)$$

where E{ } is the expected value operator and represents the expected value, or expectance, of its argument.

With reference to the description of the time domain in Section I.2.1:

$$M_n = E\{x^n\} \qquad (I.23)$$

and in particular, the mean value is:

$$\bar{x} = M_1 = E\{x\} \qquad (I.24)$$

and the mean square value:

$$\psi_x^2 = R_x(0) = M_2 = E\{x^2\} \qquad (I.25)$$

The n-th order moments of the pdf. about the mean are defined as:

$$E\{(x - \bar{x})^n\} = \int_{-\infty}^{\infty} (x - \bar{x})^n \, p(x) \, dx \qquad (I.26)$$

and again with reference to Section I.2.1:

$$M_{cn} = E\{(x - \bar{x})^n\} \qquad (I.27)$$

and in particular:

$$\sigma_x^2 = M_{c2} = E\{(x - \bar{x})^2\}$$

Skewness, $\gamma = M_{c3}/(M_{c2})^{3/2}$

and Kurtosis, $\beta = M_{c4}/(M_{c2})^2$

By the linear nature of E{ } the central moments M_{cn} may be expressed in terms of the moments M_n by expanding the arguments as follows:

$$\begin{aligned} \underline{M_{c2}} &= E\{x^2 - 2x\bar{x} + \bar{x}^2\} \\ &= E\{x^2\} - 2\bar{x}\,E\{x\} + \bar{x}^2 \\ &= E\{x^2\} - \bar{x}^2 \\ M_{c2} &= M_2 - M_1^2 = \sigma_x^2 \end{aligned} \tag{I.28}$$

as given in Eq. (I.3).

Similarly:

$$M_{c3} = M_3 - 3M_2M_1 + 2M_1^3 \tag{I.29}$$

$$M_{c4} = M_4 - 4M_3M_1 + 6M_2M_1^2 - 3M_1^4 \tag{I.30}$$

etc.

I.3.1.4 Expected values of functions of a random variable

Consider the arbitrary functions $g_1(x)$ and $g_2(x)$ and constants k_1 and k_2, then by the linearity of E{ } we may write:

$$E\{k_1g_1(x) + k_2g_2(x)\} = k_1E\{g_1(x)\} + k_2E\{g_2(x)\} \tag{I.31}$$

I.3.1.5 Properties of Gaussian (or normal) random variables

A random variable is Gaussian (or normally) distributed if its density function is of the form:

$$p(x) = \frac{1}{\sqrt{2\pi}\,\sigma_x} \exp\{-\frac{1}{2}\,(\frac{x - \bar{x}}{\sigma_x})^2\} \tag{I.32}$$

as sketched in Fig. I.3a.

It is clear that p(x) is symmetrical with mean, mode and median values coincident (see Fig. I.3) and is fully defined by the first two statistical moments, M_1 and M_2 with reference to Eqs. (I.24) and (I.28), as indicated in Section I.2.1.1.

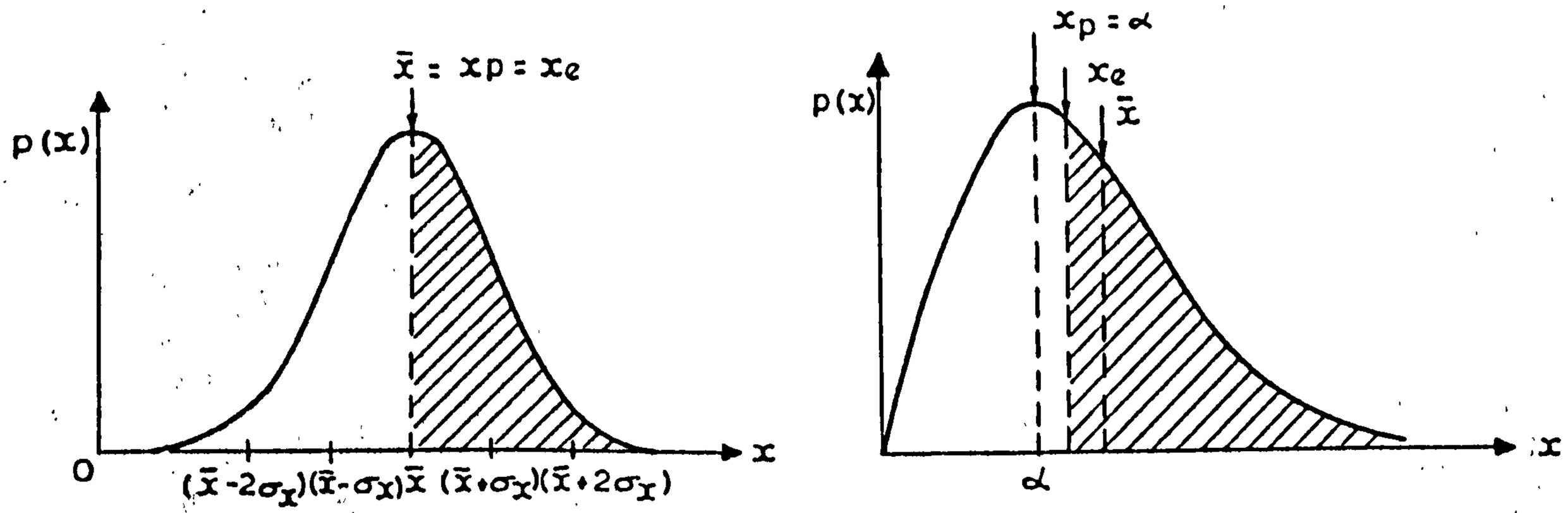

(a) Gaussian pdf. (b) Rayleigh pdf.

Mean: $\bar{x} = E\{x\}$

Mode: x_p represents the peak of the pdf. given by $[dp(x)/dx] = 0$

Median: x_e divides the area under the pdf. into two and is given by:

$$P(x) = 0.5 = \int_{-\infty}^{x_e} p(x)\,dx = \int_{x_e}^{\infty} p(x)\,dx$$

Fig. I.3 - Gaussian and Rayleigh Probability Density Functions

If x(t) is mean zero the moments may be expressed as:

$$M_n = E\{x^n\} = \begin{cases} 1.3 \quad \ldots \quad (n-1)\,\sigma_x^{\,n} & \text{for } n \text{ even} \\ 0 & \text{for } n \text{ odd} \end{cases} \qquad (I.33)$$

and the 'absolute' moments are:

$$E\{|x|^n\} = \begin{cases} 1.3 \quad \ldots \quad (n-1)\,\sigma_x^{\,n} & \text{for } n = 2k \\ \sqrt{\frac{2}{\pi}}\,2^k.k!\,\sigma_x^{\,n} & \text{for } n = 2k+1 \end{cases} \qquad k = \text{integer} \qquad (I.34)$$

I.3.1.6 Properties of a random variable following the Rayleigh distribution

The Rayleigh density function is given by:

$$p(x) = \frac{x}{\alpha^2} \exp\{-\frac{x^2}{2\alpha^2}\} \qquad x \geq 0 \qquad (I.35)$$

and is sketched on Fig. I.3b. Its moments are:

$$M_n = E\{x^n\} = \begin{cases} \sqrt{\frac{\pi}{2}}.1.3 \ldots n\alpha^n & \text{for n odd} \\ 2^k\ k!\alpha^{2k} & \text{for } n = 2k = \text{even} \end{cases} \qquad (I.36)$$

hence:

$$M_1 = \bar{x} = \alpha\sqrt{\frac{\pi}{2}}$$

and

$$\sigma_x^2 = (2 - \frac{\pi}{2})\ \alpha^2$$

Thus the Rayleigh distribution is an unsymmetrical one-parameter distribution, being fully defined by its first moment, M_1, through α.

I.3.2 Multiple Random Variables

The concepts outlined in this Section are covered in more depth by Papoulis[78].

I.3.2.1 Multi-variate cdf.

The cumulative distribution for n random variables $x_1(t)$, ..., $x_n(t)$ is defined as:

$$P(x_1, \ldots, x_n) = \text{Prob}\{x_1(t) \leq x_1, \ldots, x_n(t) \leq x_n\} \qquad (I.37)$$

This distribution is described as the n-th order multi-variate cdf. of random variables x_1 to x_n.

I.3.2.2 Multi-variate pdf.

The corresponding density function has the same interpretation as in the uni-variate case considered in the previous Section and is obtained by differentiation:

$$p(x_1, \ldots, x_n) = \frac{\partial^n P(x_1, \ldots, x_n)}{\partial x_1, \ldots, \partial x_n} \qquad (I.38)$$

and

$$P(x_1, \ldots, x_n) = \int_{-\infty}^{x_1}, \ldots, \int_{-\infty}^{x_n} p(x_1, \ldots, x_n)\ dx_1, \ldots, dx_n \qquad (I.39)$$

with

$$P(\infty, \ldots, \infty) = 1 \qquad (I.40)$$

I.3.2.3 Marginal pdf's

Variables can be integrated out of the multi-variate pdf. as follows:

$$p(x_1, \ldots, x_{n-1}) = \int_{-\infty}^{\infty} p(x_1, \ldots, x_n)\ dx_n \qquad (I.41)$$

Hence the uni-variate or <u>marginal</u> pdf. of a particular random variable can be obtained from the n-th order multi-variate pdf, for example:

$$p(x_1) = \underbrace{\int_{-\infty}^{\infty} \cdots \int_{-\infty}^{\infty}}_{(n-1)\text{fold}} p(x_1, \ldots, x_n)\, dx_2, \ldots, dx_n \qquad (I.42)$$

I.3.2.4 <u>Conditional pdf.s</u>

The conditional density function describes the probability of a sub-set of random variables each having a prescribed value when the values of the remaining set of variables are fixed. Hence:

$$p(x_1, \ldots, x_k | x_{k+1}, \ldots, x_n) = \frac{p(x_1, \ldots, x_n)}{p(x_{k+1}, \ldots, x_n)} \qquad (I.43)$$

is the conditional density of $x_1, \ldots, x_k$ assuming values for $x_{k+1}, \ldots, x_n$.

I.3.2.5 <u>Expected values of a function of n-random variables</u>

By analogy to the definition of the expected value operator in the uni-variate case, the expected value of function $g(x_1, \ldots, x_n)$ is:

$$E\{g(x_1, \ldots, x_n)\} = \underbrace{\int_{-\infty}^{\infty} \cdots \int_{-\infty}^{\infty}}_{n\text{-fold}} g(x_1, \ldots, x_n)\, p(x_1, \ldots, x_n)\, dx_1, \ldots, dx_n \qquad (I.44)$$

I.3.2.6 <u>Conditional expected values</u>

The conditional expected value of function $g(x_1, \ldots, x_k)$ given the values of $x_{k+1}, \ldots, x_n$ is obtained from the conditional pdf. as:

$$E\{g(x_1, \ldots, x_k) | x_{k+1}, \ldots, x_n\} = \underbrace{\int_{-\infty}^{\infty} \cdots \int_{-\infty}^{\infty}}_{k\text{-fold}} g(x_1, \ldots, x_k)\, p(x_1, \ldots, x_k | x_{k+1}, \ldots, x_n).dx_1, \ldots, dx_k \qquad (I.45)$$

I.3.2.7 <u>Independent random variables</u>

Random variables $x_1, \ldots, x_n$ are said to be independent if the events $\{x_1(t) \leq x_1\}, \ldots, \{x_n(t) \leq x_n\}$ are independent for any values of $x_1, \ldots, x_n$. If this condition is satisfied.

$$\begin{aligned} P(x_1, \ldots, x_n) &= P(x_1) \ \ldots \ P(x_n) \\ p(x_1, \ldots, x_n) &= p(x_1) \ \ldots \ p(x_n) \end{aligned} \qquad (I.46)$$

and for arbitrary functions $g_i(x_i)$:

$$E\{g_1(x_1), \ldots, g_n(x_n)\} = E\{g_1(x_1)\} \ \ldots \ E\{g_n(x_n)\} \qquad (I.47)$$

It can be shown that Gaussian random variables are independent if they are uncorrelated (see Section I.2.1.3).

I.3.2.8 Cross-correlation and cross-covariance

The joint moment $E\{x_1x_2\}$ is the expected value of the product of x_1 and x_2 and, with reference to Section I.2.1.3:

$$E\{x_1x_2\} = R_{x_1x_2}(0) = R_{12} \qquad (I.48)$$

where R_{12} will be defined as the cross-correlation between x_1 and x_2. Similarly, the joint moment $E\{(x_1 - \bar{x}_1)\ (x_2 - \bar{x}_2)\}$, with reference to Section I.2.1.4; is

$$E\{(x_1 - \bar{x}_1)\ (x_2 - \bar{x}_2)\} = C_{x_1x_2}(0) = C_{12} \qquad (I.49)$$

where C_{12} will be defined as the cross-covariance between x_1 and x_2 and $C_{12} = R_{12}$ when $\bar{x}_1 = \bar{x}_2 = 0$.

I.3.2.9 Transformations of random variables

Consider the two sets of random variables $y_1(t), \ldots, y_k(t)$ and $x_1(t), \ldots, x_n(t)$ for which the multi-variate density $p(x_1, \ldots, x_n)$ is known, together with the set of functions:

$$y_i = g_i(x_1, \ldots, x_n) \qquad i = 1, k \qquad (I.50)$$

The problem to be solved is to determine the multi-variate density of the set $y_1, \ldots, y_k$.

Following the procedure from Papoulis[78]:

If $k > n$, the unknown density is singular and it is necessary to first compute the density of $y_1 - y_n$.

If $k < n$, auxiliary variables must be defined, for example:

$y_{k+1} = x_{k+1}, \ldots, y_n = x_n$.

The multi-variate density of $y_1(t)$, ..., $y_n(t)$ for a given set of values y_1, ..., y_n is obtained by solving the system of simultaneous equations for the values of x_1, ..., x_n. If this system has a single real solution then:

$$p(y_1, \ldots, y_n) = \frac{p(x_1, \ldots, x_n)}{|J(x_1, \ldots, x_n)|} \tag{I.51}$$

where J(.) is the Jacobian of the transformation matrix given by:

$$J(x_1, \ldots, x_n) = \text{Det} \begin{vmatrix} \frac{\partial g_1}{\partial x_1}, & \ldots, & \frac{\partial g_1}{\partial x_n} \\ \vdots & & \vdots \\ \frac{\partial g_n}{\partial x_1}, & \ldots, & \frac{\partial g_n}{x_n} \end{vmatrix}$$

Det represents the Determinant and the values of x_i on the right hand side of the equation are expressed as functions of y_i, the solutions of Eqs. (I.50).

If auxiliary variables were required, they may be removed by integration:

$$p(y_1, \ldots, y_k) = \underbrace{\int_{-\infty}^{\infty}, \ldots, \int_{-\infty}^{\infty}}_{(n-k)\,\text{fold}} p(y_1, \ldots, y_k)\, dy_{k+1}, \ldots, dy_n \tag{I.52}$$

I.3.3 Multiple Gaussian Random Variables

I.3.3.1 Multi-variate pdf.

$$p(x_1, \ldots, x_n) = \frac{1}{(2\pi)^{n/2}\sqrt{\text{Det}|[c]|}} \exp\{-\tfrac{1}{2}\{x\}\,[c]^{-1}\,\{x\}^T\} \tag{I.53}$$

where $\{x\} = (x_1, \ldots, x_n)$

$[c]$ = square matrix of cross-covariances, see Eq. (I.49)

$$= \begin{vmatrix} c_{11}, & \ldots, & c_{1,n} \\ & & \\ c_{n1}, & \ldots, & c_{nn} \end{vmatrix}$$

I.3.3.2 Conditional pdf.s and moments

The conditional uni-variate pdf.s obtained from the multi-variate Gaussian pdf. are also Gaussian and are, therefore, defined by the corresponding conditional mean and variance. For example, the conditional pdf. of x_0 from the set of random variables x_0, ..., x_n is:

$$p(x_0|x_1, \ldots, x_n) = \frac{1}{\sqrt{2\pi}\,\sigma_c} \exp\{-\frac{1}{2} \frac{(x_0 - \bar{x}_{0c})^2}{\sigma_{0c}^2}\} \qquad (I.54)$$

It can be shown that the conditional mean, $\bar{x}_{0c}$ is given by:

$$\bar{x}_{0c} = E\{x_0|x_1, \ldots, x_n\} = a_1x_1 + \ldots + a_n x_n \qquad (I.55)$$

where a_i are obtained from the solution to:

$$[R]\ \{a\} = \{R_0\} \qquad (I.56)$$

in which [R] is the matrix of cross-correlations R_{ij} of variables, x_1 to x_n (see Eq. (I.48)).

$\{R_0\}$ is the vector $(R_{01}, R_{02}, \ldots, R_{0n})^T$
$\{a\}$ is the vector $(a_1, \ldots, a_n)^T$

The conditional variance or second central moment, σ_{0c}^2, is:

$$\begin{aligned}\sigma_{0c}^2 &= E\{(x_0 - \bar{x}_{0c})^2|x_1, \ldots, x_n\} \\ &= R_{00} - (a_1 R_{01} + \ldots + a_n R_{0n})\end{aligned} \qquad (I.57)$$

and conditional second moment is:

$$E\{x_0^2|x_1, \ldots, x_n\} = \sigma_{0c}^2 + \bar{x}_{0c}^2 \qquad (I.58)$$

I.3.3.3 Price's theorem and joint moments

Price's theorem[82] states that for a set of Gaussian random variables $x_1, \ldots, x_n$ and arbitrary functions $g_1(x_1), \ldots, g_n(x_n)$:

$$\left[\frac{\partial^k E\{\prod_{i=1}^{n} g_i(x_i)\}}{\prod_{m=1}^{N} (\partial C_{r_m s_m})^{k_m}}\right] = \left[\left(\frac{1}{2}\right)^{\sum_{m=1}^{n} \gamma k_m}\right] \left[E\{\prod_{i=1}^{n} g_i{}^{\delta}(x_i)\}\right] \qquad (I.59)$$

where r_m, s_m; m = 1, ..., N, are integers lying between 1 and n inclusive and are not necessarily distinct;

$C_{r_m s_m}$ is the co-variance of x_{r_m} and x_{s_m} (see Eq. (I.49));

k_m are positive integers with $k = \sum_{m=1}^{N} k_m$;

$\delta = \sum_{i=1}^{N} \epsilon_{im} k_m$ where ϵ_{im} is the number of times i appears in (r_m, s_m);

$g_i^{\delta}(x_i)$ denotes the δ-th derivative of $g_i(x)$, taken at x_i; and

$$\gamma = \begin{cases} 1 \text{ when } r_m = s_m \\ 0 \text{ when } r_m \neq s_m \end{cases}$$

This expression has been investigated in the bi-variate domain by Papoulis[78] who states that for an arbitrary function $g(x_1x_2)$ the theorem may be expressed as:

$$\frac{\partial^n E\{g(x_1x_2)\}}{\partial C_{12}^n} = E\{\frac{\partial^{2n} g(x_1x_2)}{\partial x^n \partial y^n}\} \qquad (I.60)$$

Joint or bi-variate moments may be determined by a recursion formula developed from this equation. Consider joint moment $E\{x_1^k x_2^r\}$, from Eq. (I.60):

$$\frac{\partial E\{x_1^k x_2^r\}}{\partial C_{12}} = kr\, E\{x_1^{k-1} x_2^{r-1}\} \qquad (I.61)$$

If $C_{12} = 0$ then x_1 and x_2 are independent, and:

$$E\{x_1^k x_2^r\} = E\{x^k\}\, E\{x^r\} \qquad (I.62)$$

Therefore, integrating Eq. (I.61) and using (I.62) we obtain the required formula:

$$E\{x_1^k x_2^r\} = kr \int_0^{C_{12}} E\{x_1^{k-1} x_2^{r-1}\}\, d\, C_{12} + E\{x^k\}\, E\{x^r\} \qquad (I.63)$$

I.3.4 Probabilistic Characteristics of Threshold Crossings and Peak Values

The probability theory covered in the previous Sections has been concerned with the characteristics of the basic continuous random variable, x(t) of Fig. I.2, enabling solution to questions of the form; what will be the probability that x(t) exceeds a certain threshold level x? or, for what proportion of the time will the magnitude of x(t) exceed x?

In many problems involving continuous random variables additional probabilistic characteristics are required, namely:

(1) Threshold crossings - description of the number of times that x(t) crosses a certain threshold x in a given period of time.

(2) Peak distributions - description of the number of peaks (positive or negative peaks; maxima or minima; crests or troughs) in x(t) which exceed a certain threshold x in a given period of time.

The following sections outlining these concepts have been extracted from a more detailed account given by Lin[45] and Bendat[56].

I.3.4.1 Threshold crossings

For a continuous random variable, x(t), Lin[45] has shown that the expected rate of threshold crossing of the level x, E{N(x)}, is given by:

$$E\{N(x)\} = \int_{-\infty}^{\infty} |\dot{x}|\, p(x, \dot{x})\, d\dot{x} \qquad (I.64)$$

where $p(x, \dot{x})$ is the bi-variate pdf. of x(t) and its first time derivative $\dot{x}(t)$, itself a continuous random variable.

The rate of threshold crossing from below is required in some applications and since, for such crossings, the slope must be positive:

$$E\{N^{+}(x)\} = \int_{0}^{\infty} \dot{x}\, p(x, \dot{x})\, d\dot{x} \qquad (I.65)$$

$$= \frac{1}{2} E\{N(x)\} \text{ for stationary random variables}$$

I.3.4.2 Threshold crossings for a mean-zero Gaussian process

If x(t) is stationary and mean zero following a Gaussian distribution, its derivative $\dot{x}(t)$ will be statistically independent of x(t) and using Eq. (I.53) the bi-variate pdf. may be expressed as:

$$p(x, \dot{x}) = \frac{1}{2\pi\, \sigma_x\, \sigma_{\dot{x}}} \exp\{-\frac{1}{2}\, (\frac{x^2}{\sigma_x^2} + \frac{\dot{x}^2}{\sigma_{\dot{x}}^2}) \qquad (I.66)$$

and

$$E\{N^{+}(x)\} = \frac{1}{2\pi} \frac{\sigma_{\dot{x}}}{\sigma_x} \exp\{-\frac{1}{2} \frac{x^2}{\sigma_x^2}\} \qquad (I.67)$$

The expected rate of zero crossings from below is, therefore, given by:

$$E\{N^{+}(0)\} = \frac{1}{2\pi} \frac{\sigma_{\dot{x}}}{\sigma_x} \qquad (I.68)$$

This may be expressed in terms of the relevant spectral density functions since from Eq. (I.17), when $\bar{x} = 0$:

$$\sigma_x^2 = R_x(0) = \int_0^\infty S(\omega)\, d\omega = m_0 \tag{I.69}$$

and

$$\sigma_{\dot{x}}^2 = \int_0^\infty \omega^2\, S(\omega)\, d\omega = m_2 \tag{I.70}$$

Hence:

$$E\{N^+(0)\} = \frac{1}{2\pi}\cdot\sqrt{\frac{m_2}{m_0}} \tag{I.71}$$

I.3.4.3 Peak distributions

A positive peak on the time history of x(t) corresponds to the condition of zero slope, $\dot{x}(t) = 0$, and a negative value to the second derivative of x, $\ddot{x}(t)$. Using this criterion, it can be shown[45] that the number of positive peaks per unit time of magnitude greater than or equal to x is:

$$E\{M(x)\} = -\int_x^\infty \int_{-\infty}^0 \ddot{x}\, p(x, 0, \ddot{x})\, d\ddot{x}\, dx \tag{I.73}$$

and the total number of positive peaks is, therefore:

$$E\{M_T\} = -\int_0^\infty \int_{-\infty}^0 \ddot{x}\, p(x, 0, \ddot{x})\, d\ddot{x}\, dx \tag{I.74}$$

where $p(x, \dot{x}, \ddot{x})$ is the tri-variate pdf. of x(t) and its first two time derivatives.

The ratio of $E\{M(x)\}$ to $E\{M_T\}$ gives the proportion of the total number of peaks that exceed the threshold level x. Using the heuristic assumption[45] that this ratio may be related to the probability distribution of the peaks, the cdf. of the peaks of x(t) is obtained as:

$$P_p(x) = 1 - \frac{E\{M(x)\}}{E\{M_T\}} \tag{I.75}$$

and the corresponding pdf. is:

$$p_p(x) = \frac{-1}{E\{M_T\}} \int_{-\infty}^0 \ddot{x}\, p(x, 0, \ddot{x})\, d\ddot{x} \tag{I.76}$$

I.3.4.4 Peak distributions for a mean-zero Gaussian process

With the same requirements as those made in Section I.3.4.2 the trivariate Gaussian pdf. can be expressed, using Eq. (I.53), in terms of the variances of x(t) and its first two derivatives, which may be expressed in terms of the spectral density functions using Eqs. (I.69) and (I.70) and[45]:

$$\sigma_{\ddot{x}}^2 = \int_0^\infty \omega^4 \, S(\omega) \, d\omega = m_4 \qquad (I.77)$$

The expected total number of peaks per unit time is;

$$E\{M_T\} = \frac{1}{2\pi} \frac{\sigma_{\ddot{x}}}{\sigma_{\dot{x}}} = \frac{1}{2\pi} \sqrt{\frac{m_4}{m_2}}$$

and the ratio of the number of zero-crossings from below to the number of positive peaks is:

$$\alpha = \frac{E\{N^+(0)\}}{E[M_T]} = \frac{\sigma_{\dot{x}}^2}{\sigma_x \, \sigma_{\ddot{x}}} = \sqrt{\frac{m_2^2}{m_0 \, m_4}} \qquad (I.78)$$

and the spectral bandwidth, defined in Eq. (I.19), is:

$$\varepsilon = (1 - \alpha^2)^{1/2} = [(m_0 \, m_4 - m_2^2)/m_0 \, m_4]^{1/2} \qquad (I.79)$$

Wideband processes

If $\varepsilon = 1$, ($\alpha = 0$) the process is described as being wideband and there are many more positive peaks than zero crossings.

Narrow band processes

If $\varepsilon = 0$, ($\alpha = 1$) the process is described as being narrow banded. Each threshold crossing with positive slope leads to a single positive peak and all positive peaks have positive magnitudes. Under these conditions the peak distribution may be simplified to:

$$P_p(x) = 1 - \frac{E\{N^+(x)\}}{E\{N^+(0)\}} \qquad (I.80)$$

Furthermore, for the narrow band case it can be shown[45] that this peak distribution is Rayleigh, as described in Section I.3.1.6, where:

$$p_p(x) = \frac{x}{\sigma_x^2} \exp\left(-\frac{x^2}{2\sigma_x^2}\right) \qquad (I.81)$$

I.3.4.5 Approximate peak distributions for non-Gaussian narrow band processes

Eq. (I.80) makes no restrictions on the distribution of the underlying narrow band process and can thus be employed when $x(t)$ is non-Gaussian:

$$P_p(x) = 1 - \int_{-\infty}^{\infty} |\dot{x}|\ p(x, \dot{x})\ d\dot{x} \Big/ \int_{-\infty}^{\infty} |\dot{x}| p(0, \dot{x})\ d\dot{x}$$

to give the narrow band 'type 1' cdf.

A further simplification can be made when $x(t)$ is independent of $\dot{x}(t)$ since:

$$p(x, \dot{x}) = p(x)\ p(\dot{x})$$

for which we have:

$$E\{N^+(0)\} = p(0) \int_0^{\infty} |\dot{x}|\ p(\dot{x})\ d\dot{x} \qquad (I.82)$$

and

$$P_p(x) = 1 - \frac{p(x)}{p(0)} \qquad (I.83)$$

termed the 'type 2' narrow band cdf.

where $p(0)$ is the pdf. of $x(t)$ evaluated at $x = 0$.

A P P E N D I X T W O

CONSTRUCTION AND USE OF PROBABILITY PAPERS

Probability papers are much used by engineers for the analysis of randomly varying phenomena especially in the fields of oceanography, meteorology and hydrology and are constructed to produce straight line plots for a particular theoretical probability distribution[76].

Thus, by plotting the cumulative distribution, or cumulative histogram for discrete data, of the phenomenon under investigation on this paper the goodness-of-fit of its probability structure to the theoretical distribution of the paper is measured by the goodness-of-fit of the data plot to a straight line.

Having found a paper which gives a reasonably straight line fit, it may be supposed that the phenomenon is approximately distributed according to the theoretical distribution of that paper. The probability structure of the phenomenon may then be described graphically by inserting the best fit straight line by eye or by using statistical fitting methods to the data points. Alternatively, the theoretical pdf. may be defined in terms of the statistical moments of the data set, typically the estimates of the mean and standard deviation, a technique known as the method of moments.

Derivations of the scales required for the preparation of probability papers for Gaussian, log-Gaussian, Rayleigh, Gumbel and Weibull probability distributions are given below in Sections II.1 to II.5 and the method of plotting discrete data on these papers is outlined in Section II.6.

II.1 GAUSSIAN (OR NORMAL) PROBABILITY PAPERS

The Gaussian cdf. of variable x is given by:

$$P(x) = \int_{-\infty}^{x} \frac{1}{\sqrt{2\pi}} \exp\{ - \frac{x^2}{2}\} \, dx \qquad (II.1)$$

where x is mean zero with unit variance.

In this case the probability paper may be constructed using an implicit method by plotting x on a linear scale for one co-ordinate axis and obtaining the values of x corresponding to the probability levels required for the scale of the other axis by interpolation, from the evaluation of Eq. (II.1) at values of x in the region of interest.

Following this method the probability paper shown in Fig. II.1 may be obtained.

II.2 LOG-GAUSSIAN (OR LOG-NORMAL) PROBABILITY PAPERS

For this probability paper the logarithm of variable x is assumed to follow the Gaussian distribution, above, and hence the replacement of the linear scale by a logarithmic scale on the Gaussian probability paper results in a straight line plot of the cdf. of variable x. This paper is shown in Fig. II.2.

II.3 RAYLEIGH PROBABILITY PAPER

In standardised form the Rayleigh cdf. of variable x may be expressed as:

$$P(x) = 1 - \exp(-\frac{x^2}{2}) \qquad (II.2)$$

Taking logs of both sides:

$$x = \{\log_e(1 - P(x))^{-1}\}^{1/2}\ \sqrt{2} \qquad (II.3)$$

Thus a plot of the Rayleigh distribution is a straight line on paper with x as one co-ordinate and $\{\log_e(1 - P(x))^{-1}\}^{1/2}$ as the other. For the paper used herein probabilities are indicated in preference to values of the logarithmic function as indicated in Fig. II.3.

II.4 GUMBEL PROBABILITY PAPER

The Gumbel distribution of variable x may be expressed as:

$$P(x) = \exp\{-\exp[-\alpha(x - u)]\} \qquad (II.4)$$

where $\alpha = \frac{\pi}{\sqrt{6}\sigma_x}$;

$u = \bar{x} - \frac{0.5772}{\alpha}$ is the mode of the pdf; and

$\bar{x}$ and σ_x are the mean and standard deviation of x.

Taking logarithms of Eq. (II.4):

$$\alpha(x - u) = - \log_e[- \log_e P(x)] \qquad \text{(II.5)}$$

Thus, a plot of x vs. $- \log_e[- \log_e P(x)]$ will result in a straight line. Again, for the paper used herein probabilities rather than values of the function on the right-hand side of Eq. (II.5) are used as shown in Fig. II.4. Note that for graphical representation of a variable on this paper the values of α and u need not be known.

II.5 WEIBULL PROBABILITY PAPER

The three parameter Weibull distribution function of a variable x is given by:

$$\left.\begin{aligned} 1 - P(x) &= \exp\{- (\tfrac{x - A}{B})^{C}\} \quad \text{for } x \geq A \\ &= 1 \quad \text{for } x < A \end{aligned}\right\} \text{ and } \begin{matrix} B > 0 \\ C > 0 \end{matrix} \qquad \text{(II.6)}$$

where A is a lower limiting value of x;

B is a scale parameter; and

C is a shape parameter.

Taking logarithms of Eq. (II.6) twice:

$$\log_e \log_e\{(1 - P(x))^{-1}\} = C \log_e(x - A) - C \log_e B \qquad \text{(II.7)}$$

A plot of the Weibull distribution is a straight line on paper with $\log_e(x - A)$ as one co-ordinate axis and $\log_e \log_e\{(1 - P(x)\}$ as the other axis as shown in Fig. II.5.

Clearly, data should only be plotted on Weibull paper after determination of the value of A although little attention has been paid to this in the past and the actual values of x are often plotted in place of (x - A) on the paper. A semi-graphical method for the determination of A is given in Reference 42.

However, parameter A is often small compared with the values of x of interest in the estimation of extremes and in this region there is negligible difference between the plots using x or (x - A) as far as the

'goodness-of-fit' to a straight line is concerned. In the low range of x omission of parameter A in the plots causes considerable distortion and departure from the straight line form.

Criteria and numerical procedures for evaluation of the 'goodness-of-fit' of a set of data to a proposed density function are given in Reference 76.

II.6 PLOTTING POSITIONS FOR DATA ON PROBABILITY PAPERS

Consider a sample of n measurements of a certain random population of variable x. If these data points are ranked according to magnitude assigning the rank m = 1 to the smallest value x_1 then from this data the cumulative probability histogram may be developed since:

$$\text{Prob}(x \leq x_m) = P(x_m) = \frac{m}{n} \tag{II.8}$$

However, this approximation assigns probability of exceedance of 1.0 to the highest value, x_n, which cannot be plotted on probability paper. Consequently, a number of modified plotting techniques have been proposed, as compared by Gumbel[58], which enable all data points to be plotted. The most commonly applied plotting position is that recommended by Gumbel and sometimes referred to as the 'Weibull plotting position', where:

$$P(x_m) = \frac{m}{n + 1} \tag{II.9}$$

The expression yields probabilities with an insignificant deviation from those derived from Eq. (II.8) when n is large.

FIG.(II. 1.) GAUSSIAN (OR NORMAL) PROBABILITY PAPER.

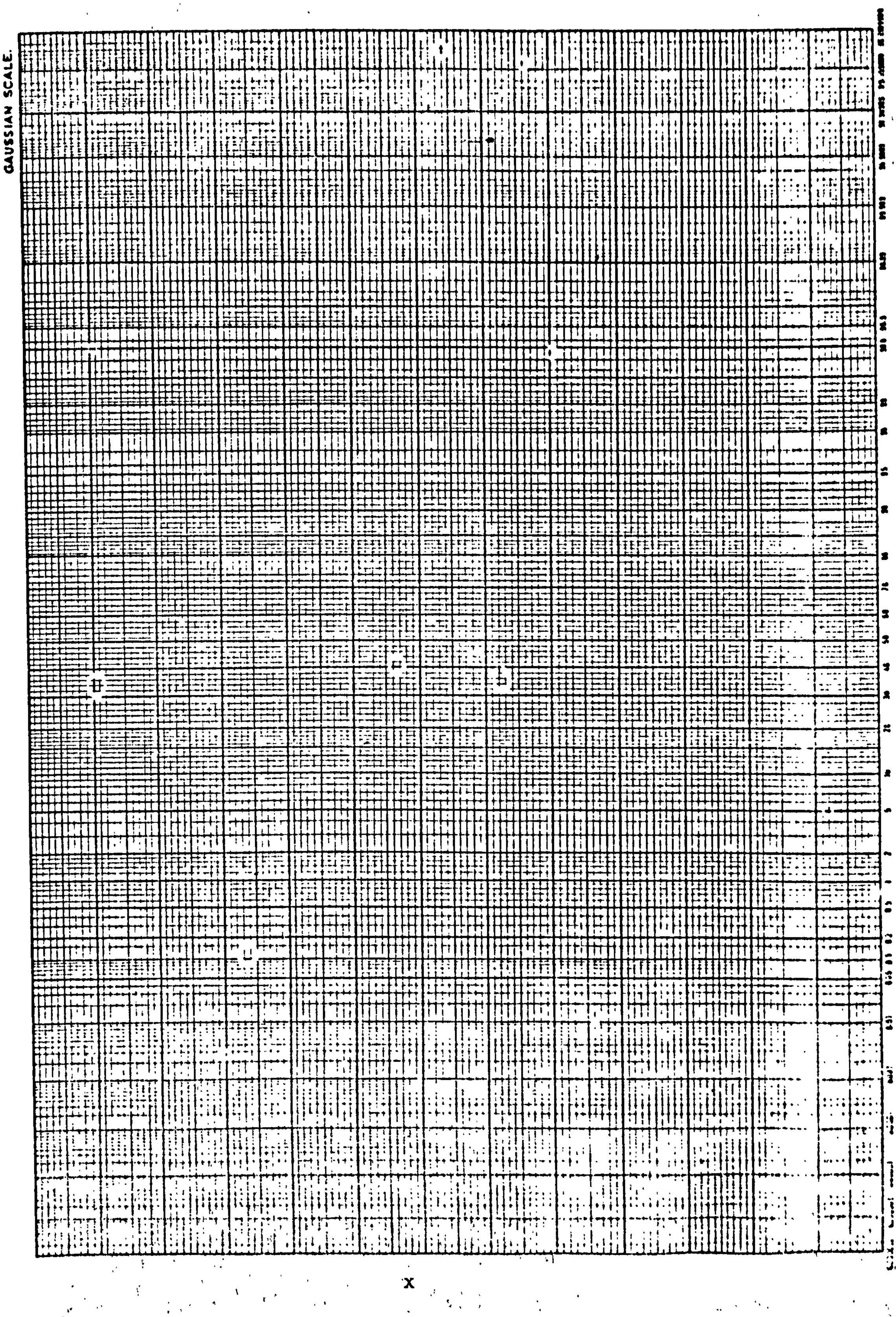

FIG.(II.2.) LOG-GAUSSIAN (OR LOG-NORMAL) PROBABILITY PAPER.

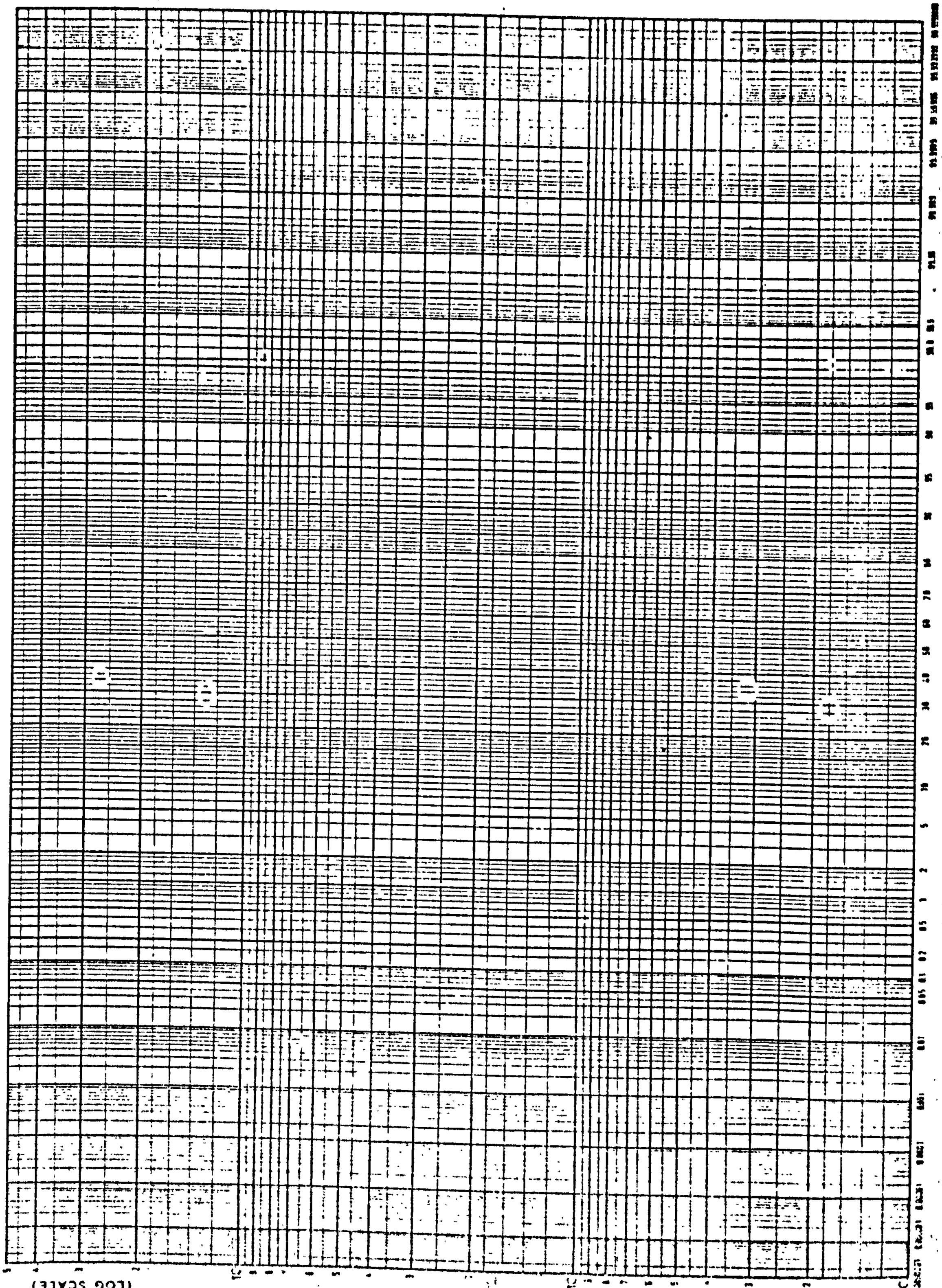

FIG. (II.3.) RAYLEIGH PROBABILITY PAPER.

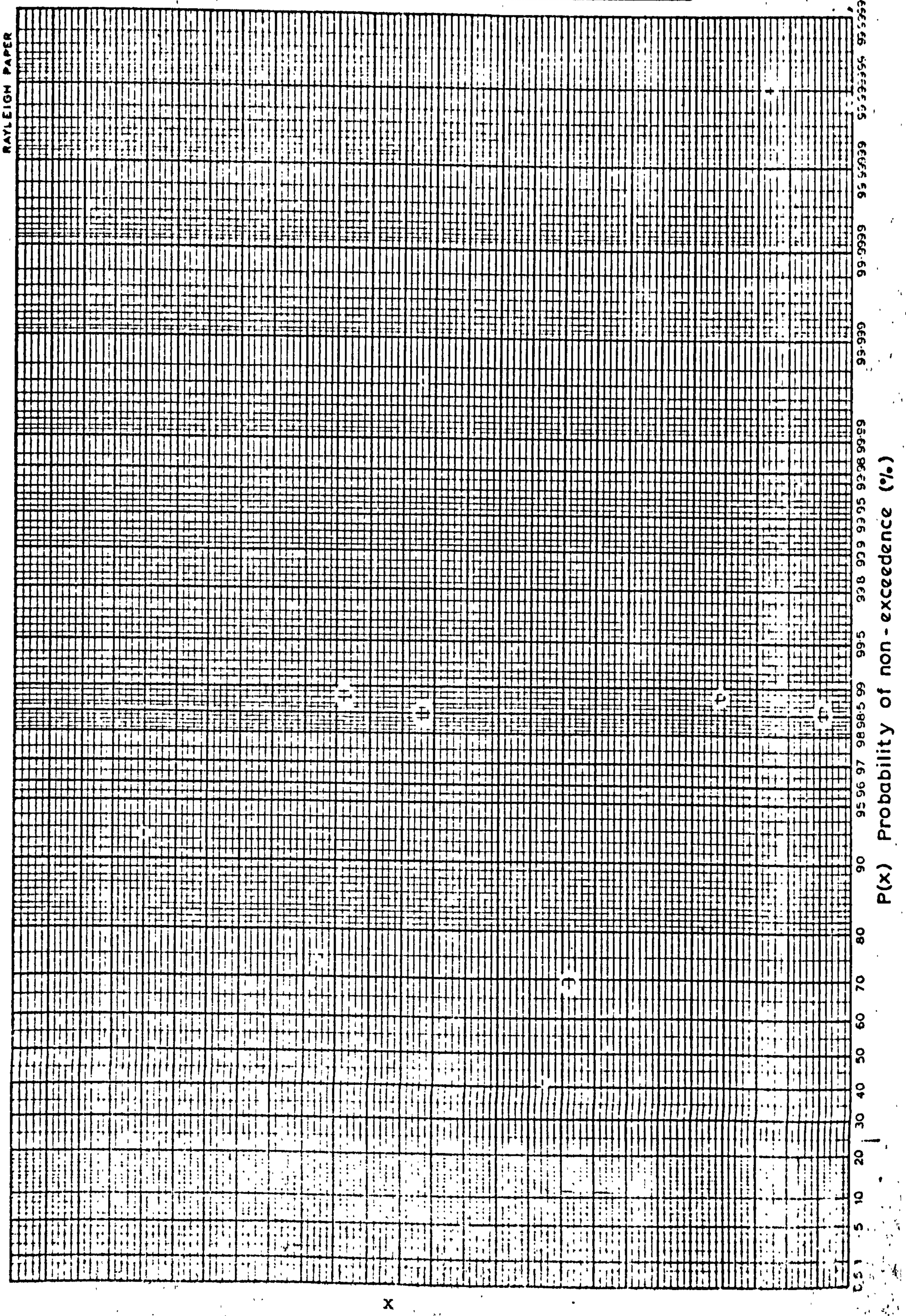

FIG. (II.4). GUMBEL PROBABILITY PAPER.

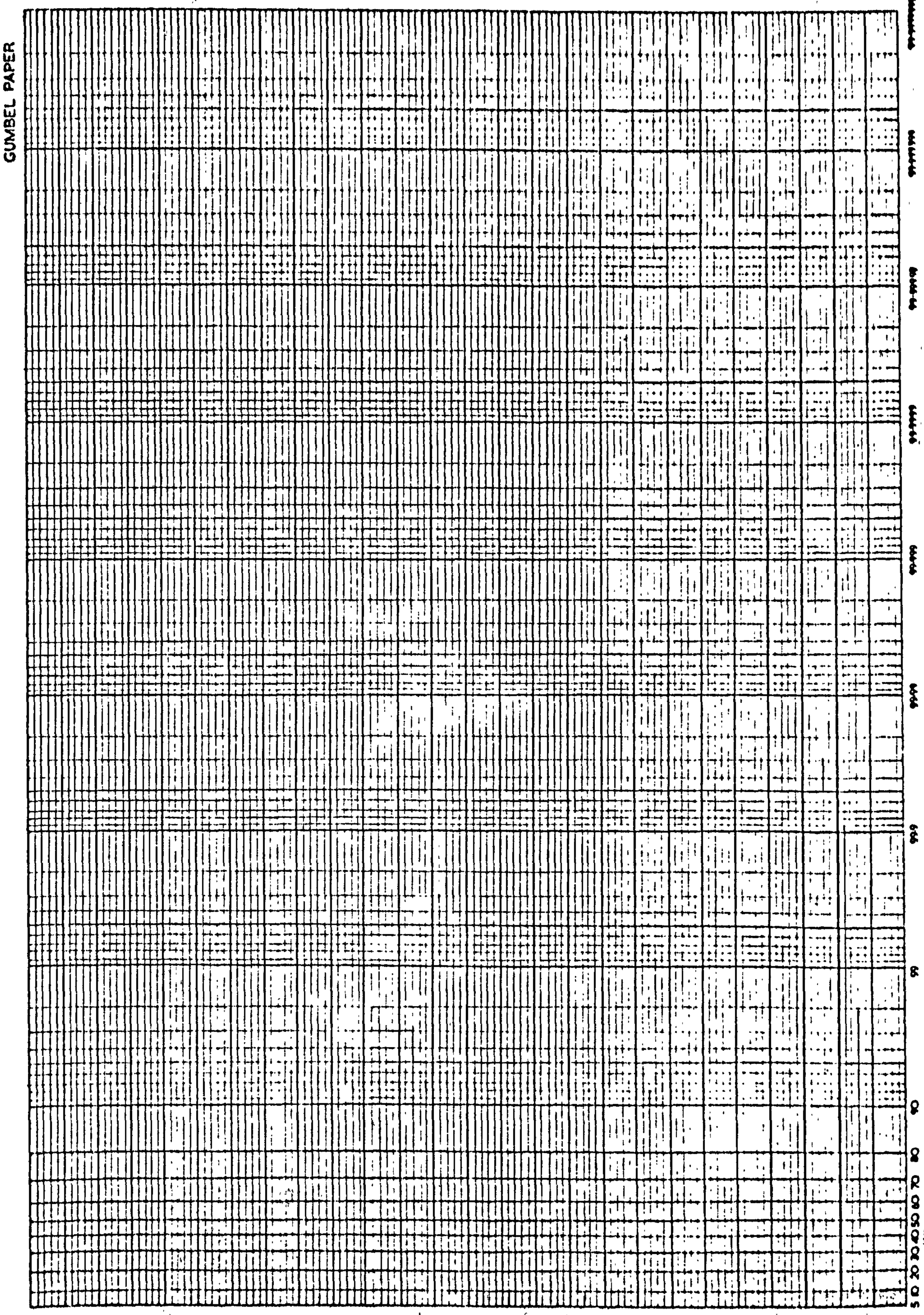

FIG.(II.5.) WEIBULL PROBABILITY PAPER.

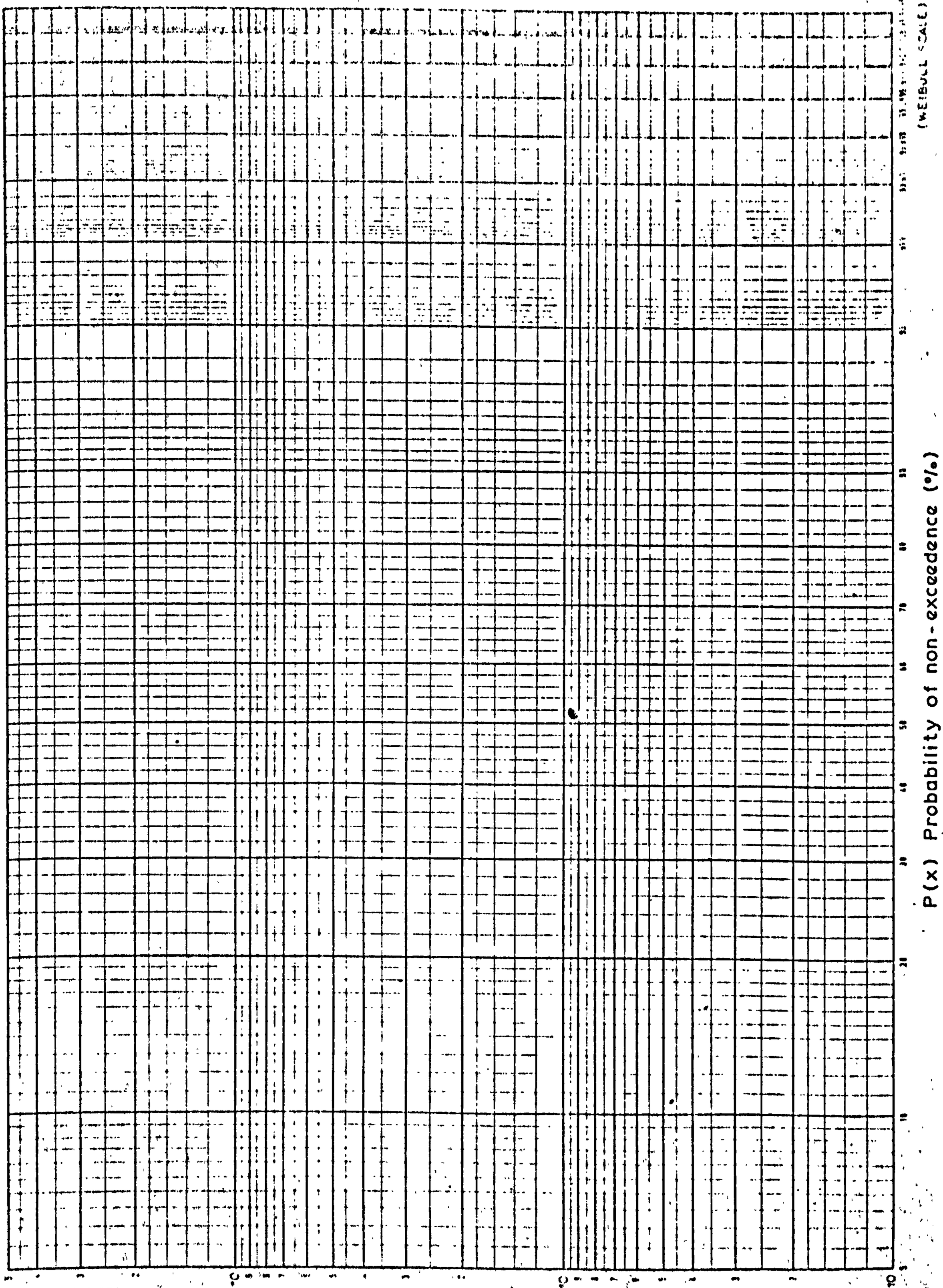

A P P E N D I X T H R E E

EXTENSION OF SCATTER DIAGRAMS COVERING SIX WINTER MONTHS TO REPRESENT ONE YEAR'S WAVE CLIMATE

The purpose of this Appendix is to summarise the procedure employed in this study to extend a six-months winter data set to yield a prediction of the one-year wave climate by the estimation of a corresponding six-months summer scatter diagram for the Famita location. Scatter diagrams covering both summer and winter periods for another North Sea location were available to aid this extension but this data cannot be mentioned explicitly here because of restrictions on publication and will be referred to as (S) and (W) data, respectively.

Simple empirical methods have been suggested for the prediction of a scatter diagram for a summer six-month period from a winter data set. In these methods the distribution of T_z is assumed to be unchanged while the summer values of $H_{1/3}$ are taken as either a half or two-thirds of the winter values. These propositions were tested on the (S) and (W) data and were found to perform badly, as described below, and thus an alternative method of prediction was developed.

III.1 THE PERFORMANCE OF EMPIRICAL METHODS OF SUMMER SCATTER DIAGRAM PREDICTION

The performance of the empirical methods for summer wave climate simulation from winter data was investigated by comparing the predictions based on the winter (W) data set with the actual summer (S) data.

The empirical methods make the assumption that the distribution of T_z remains unchanged from winter to summer. However, a plot of the marginal distribution of T_z from the (W) and (S) data sets demonstrated that although the shapes of the distributions were similar, there was a general shift towards lower values of T_z in the summer. This was also reflected by the mean values of T_z for the (W) and (S) data sets, the latter being approximately 0.67 seconds lower.

The summer distributions of $H_{1/3}$ predicted from the empirical methods, were compared with the actual summer (S) distributions. A plot of marginal pdf.s and cdf.s showed the (S) data to lie between the predictions, whilst investigation of the conditional distributions of $H_{1/3}$ over a wide range of T_z values demonstrated generally poor agreement between the (S) data and empirically predicted values. This behaviour further demonstrated the significant change in the distribution of T_z between summer and winter.

In view of the above comments it was decided to develop a more rigorous method of wave climate prediction as described below.

III.2 A METHOD FOR PREDICTION OF SUMMER WAVE CLIMATE AT FAMITA (FS) FROM MEASURED WINTER DATA (FW) BY COMPARISON WITH (W) AND (S) DATA

The two winter data sets (W) and (FW) were compared and were found to show a similar spread in the T_z domain with only a 10% departure between the mean values, the (W) data having the larger mean. The (W) data covered a larger range of $H_{1/3}$ and possessed a mean value 35% greater than that at Famita, demonstrating the existance of more severe sea conditions at this location. The cumulative conditional distributions of $H_{1/3}$ from the winter data sets were plotted and were found to show reasonable agreement in view of the uncertainties present in histogram plots of finite sized data sets.

As a result of the measure of agreement between the conditional distributions of $H_{1/3}$ for (W) and (FW) and the apparent shift, with little change in shape, of the T_z distributions between summer, (S), and winter, (W), the following procedure was developed and employed[10,12] for the prediction of the summer scatter diagram for Famita (FS).

The basic assumption was made that the ratio between the conditional probability densities of the summer data sets for a value $T_z = t$ would be the same as the corresponding ratio for the winter data sets at $T_z = t + 0.5$, hence:

$$p(H_{1/3}|T_z=t)_{(FS)} = p(H_{1/3}|T_z=t)_{(S)} \cdot \frac{p(H_{1/3}|T_z=t+0.5)_{(FW)}}{p(H_{1/3}|T_z=t+0.5)_{(W)}} \qquad \text{(III.1)}$$

This expression includes an attempt to account for the shift (of about 0.5 seconds) observed between the (W) and (S) data.

Eq. (III.1) may be expanded in terms of the bi-variate distribution of $H_{1/3}$ and T_z using the relationship (Appendix One):

$$p(H_{1/3}|T_z) = \frac{p(H_{1/3}, T_z)}{p(T_z)} \qquad \text{(III.2)}$$

Substituting this expression into Eq. (III.1) and assuming that the shape of marginal distributions of T_z between summer and winter to be the same:

$$[p(T_z = t)]_{(S)} = [p(T_z = t + 0.5)]_{(W)}$$

and likewise for the Famita densities, we obtain:

$$p(H_{1/3}, T_z=t)_{(FS)} = p(H_{1/3}, T_z=t)_{(S)} \frac{p(H_{1/3}, T_z=t+0.5)_{(FW)}}{p(H_{1/3}, T_z=t+0.5)_{(W)}} \qquad \text{(III.3)}$$

Ensuring that the class widths for each pair of data sets, (W) and (S) and (FW) and (FS), are the same and, furthermore, assuming the total number of occurrences in the (FS) and (FW) scatter diagrams to be the same, Eq. (III.3) becomes:

$$[N^0(H_{1/3}, T_z=t)]_{(FS)} = [F(H_{1/3}, T_z=t)]_{(S)} \frac{[N^0(H_{1/3}, T_z=t+0.5)]_{(FW)}}{[F(H_{1/3}, T_z=t+0.5)]_{(W)}} \qquad \text{(II.4)}$$

where $N^0(H_{1/3}, T_z)$ is the number of occurrences in the scatter diagram present in the class centred at $(H_{1/3}, T_z)$ and $F(H_{1/3}, T_z)$ is the fraction of the total number of occurrences in the scatter diagram present in the class centred at $(H_{1/3}, T_z)$.

Eq. (III.4) could now be used to calculate the number of occurrences for the (FS) scatter diagram. However, a modification was applied to account for a variation in the mean values and variance of the conditional histograms of $H_{1/3}$ between the winter data sets, by replacing $H_{1/3}$ in Eq. (III.4) by a non-dimensional normalised variable:

$$H^* = \frac{H_{1/3} - \overline{H}_{1/3}/T_z}{\sigma/T_z} \qquad \text{(III.5)}$$

where $H_{1/3}/T_z$ and σ/T_z are the mean and standard deviation of the particular conditional distribution of $H_{1/3}$.

The functions $F(H_{1/3}, T_z)$ and $N^0(H_{1/3}, T_z)$ on the right-hand-side of Eq. (III.4) thus modified to $F(H^*, T_z)$ and $N^0(H^*, T_z)$ were then plotted to yield histograms conditional on the values of T_z for the (FW), (W) and (S) data sets. These histograms were approximated by continuous curves, obtained as the best fits by eye, which were then used to derive the required function, $N^0(H^*, T_z)_{FS}$ using the modified form of Eq. (III.4). This is demonstrated in the sample computation of Fig. III.1. Numbers of occurrences at the required values of $H_{1/3}$ (class centres) were obtained from the plots of H* for this summer condition using the assumptions that:

$$(\bar{H}_{\frac{1}{3}/T_z=t})_{(FS)} = (\bar{H}_{\frac{1}{3}/T_z=t})_{(S)} \cdot \frac{(H_{\frac{1}{3}/T_z=t+0.5})_{(FW)}}{(H_{\frac{1}{3}/T_z=t+0.5})_{(W)}} \qquad \text{(III.6)}$$

with an identical expression for $(\sigma_{/T_z=t})_{(FS)}$ as indicated in the figure.

The use of standardised variable, H*, as described above was preferred to the application of Eq. (III.4) in terms of $H_{1/3}$ since it ensures that the computations are carried out over the central range of the histograms, as indicated in Fig. III.1.

It should be appreciated at this stage that in the performance of the above procedure no assumptions have been made regarding the form of the conditional distributions of $H_{1/3}$ for the winter data sets and no attempt has been made to adjust them to similar forms. The proposition made was that these distributions were found to show reasonable agreement and hence it would appear reasonable to suppose that the same is true for the summer data sets and the procedure outlined above is one method of achieving this measure of agreement.

The computations outlined in Fig. III.1 were carried out for all classes of T_z for which there were a sufficient number of occurrences in the scatter diagrams of (W), (S) and (FW) to facilitate construction of the functions F(.) and $N^0(.)$.

On completion of these computations the total number of occurrences predicted for the Famita summer scatter diagram was 4% in excess of the number required, (equal to the number in the Famita winter data set) and consequently the scatter diagram was modified by an overall 4% reduction in the number of occurrences in each class. Only 0.4% of the occurrences in the (S) data set were omitted from the graphical procedures and it was, therefore, assumed that there were no significant omissions in the predicted scatter diagram.

The scatter diagram derived in the above manner had class intervals of T_z offset by 0.5 seconds from the winter data and was, therefore, redistributed according to the time classes of the latter to enable direct summation for the required 'one-year' wave climate as presented in Fig. 2.3.1.

III.3 THE PERFORMANCE OF THE 'COMPARISON' MODEL OF SUMMER SCATTER DIAGRAM PREDICTION

The marginal probability density histograms of T_z for the measured winter scatter diagram at Famita and for the predicted summer diagram are shown in Fig. III.2a. From these plots it is apparent that the distribution for the summer periods is shifted, by about 0.5 seconds towards lower values of T_z than present in the winter data, whilst the overall shape of the two distributions is similar. This behaviour corresponds to that observed from comparison of the complete data set (W) and (S).

The marginal probability density histograms of $H_{1/3}$ for the Famita winter data and the predicted summer data using both the 'comparison model' of Section III.2 and the empirical methods are presented in Fig. III.2b. The 'comparison model' yields a histogram with ordinates generally lying between those derived from the two empirical models as was found to be the case for the actual summer data (S) compared with its empirical estimates from the (W) data.

The cumulative conditional distributions of $H_{1/3}$ were also plotted for the winter data and for all three predictions of the summer data, a sample of which is shown in Fig. III.3. These plots demonstrated that although the 'comparison model' yields values between those of the empirical models in the marginal distributions, no such general relationship is evident in the conditional distributions of $H_{1/3}$. The

relationships between these predicted conditional distributions showed a distinct similarity to those developed from the (W) and (S) data set.

As a result of the above investigation it was concluded that the 'comparison' model had performed sufficiently well to warrant its selection in preference to the empirical models in this study. However, the tests carried out on the probability structure of the scatter diagrams were by no means exhaustive and it is possible that a modification of the simple empirical type models accounting for the shift in the T_z distribution may be found to perform equally well.

FIG. III.1. PREDICTION OF NUMBER OF OCCURENCES IN FAMITA SUMMER SCATTER DIAGRAM FOR T_z = 7·0 SECONDS.

(I) (W) DATA

T_z = 7·5 SECS.

$H_{1/3} = H_W$

$\sigma = \sigma_W$

(Values cannot be disclosed)

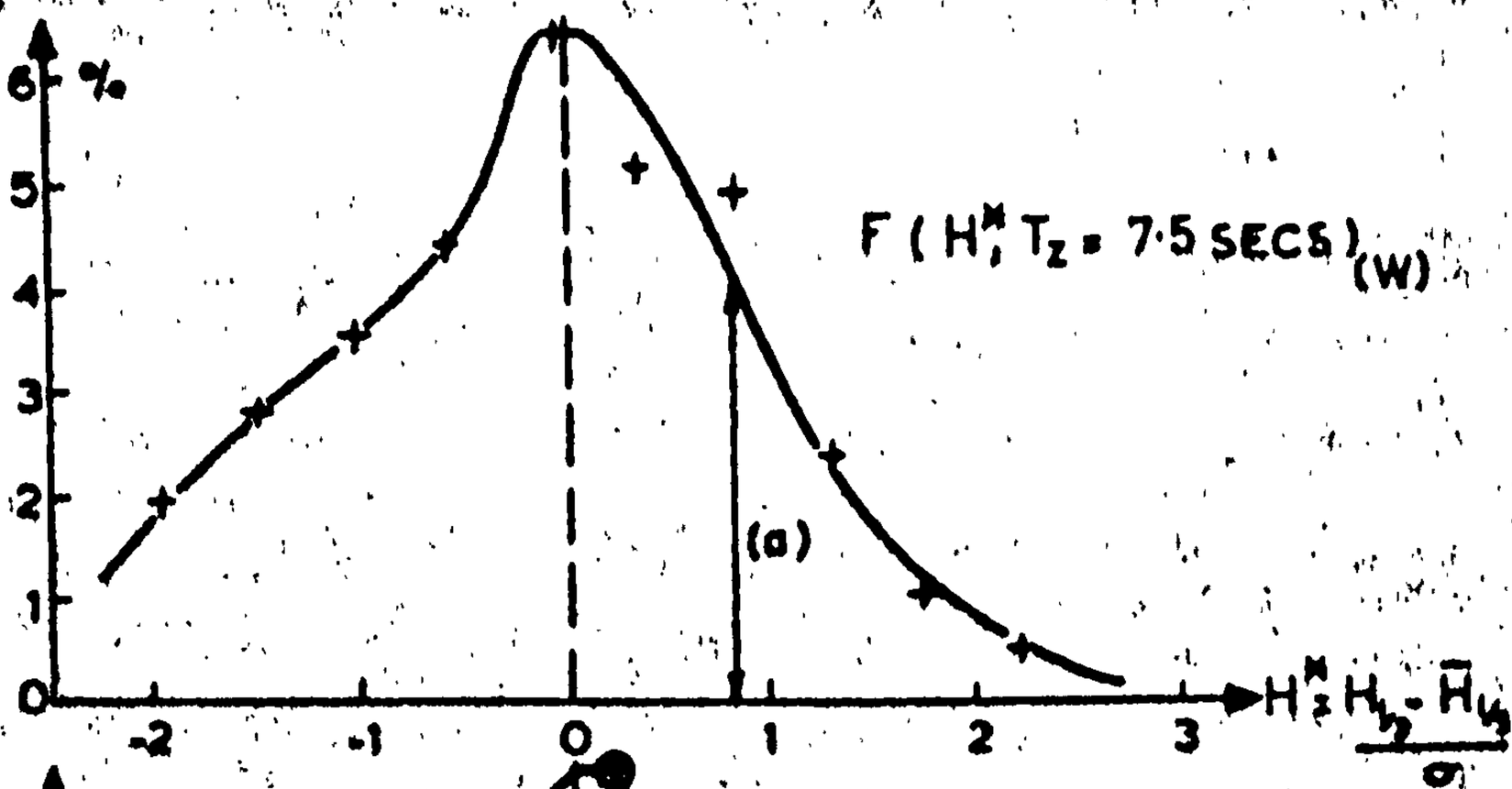

(II) (S) DATA

T_z = 7·0 SECS.

$H_{1/3} = H_S$

$\sigma = \sigma_S$

(Values cannot be disclosed)

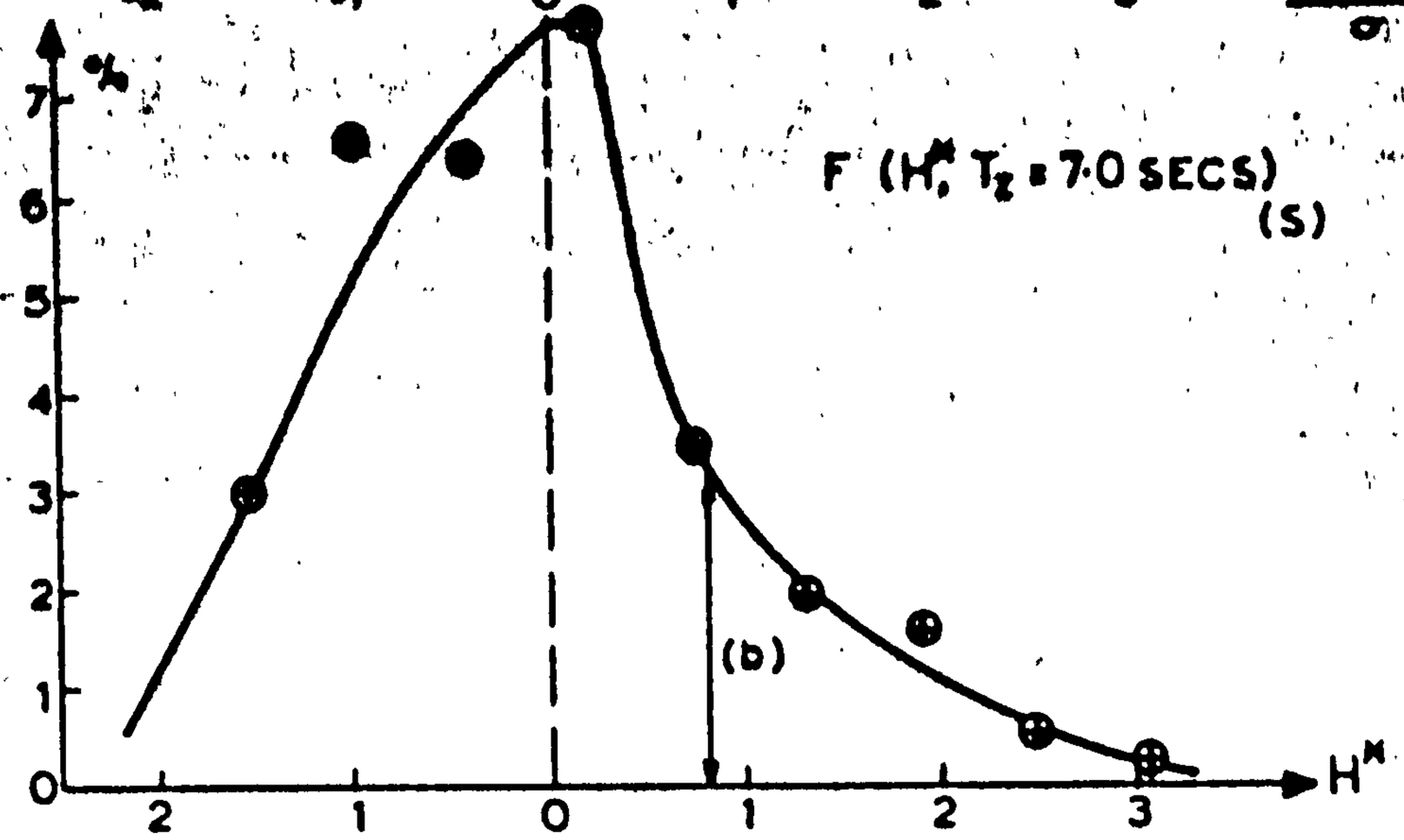

(III) (FW) DATA

T_z = 7·5 SECS

$H_{1/3}$ = 3·094 m

σ = 1·222 m

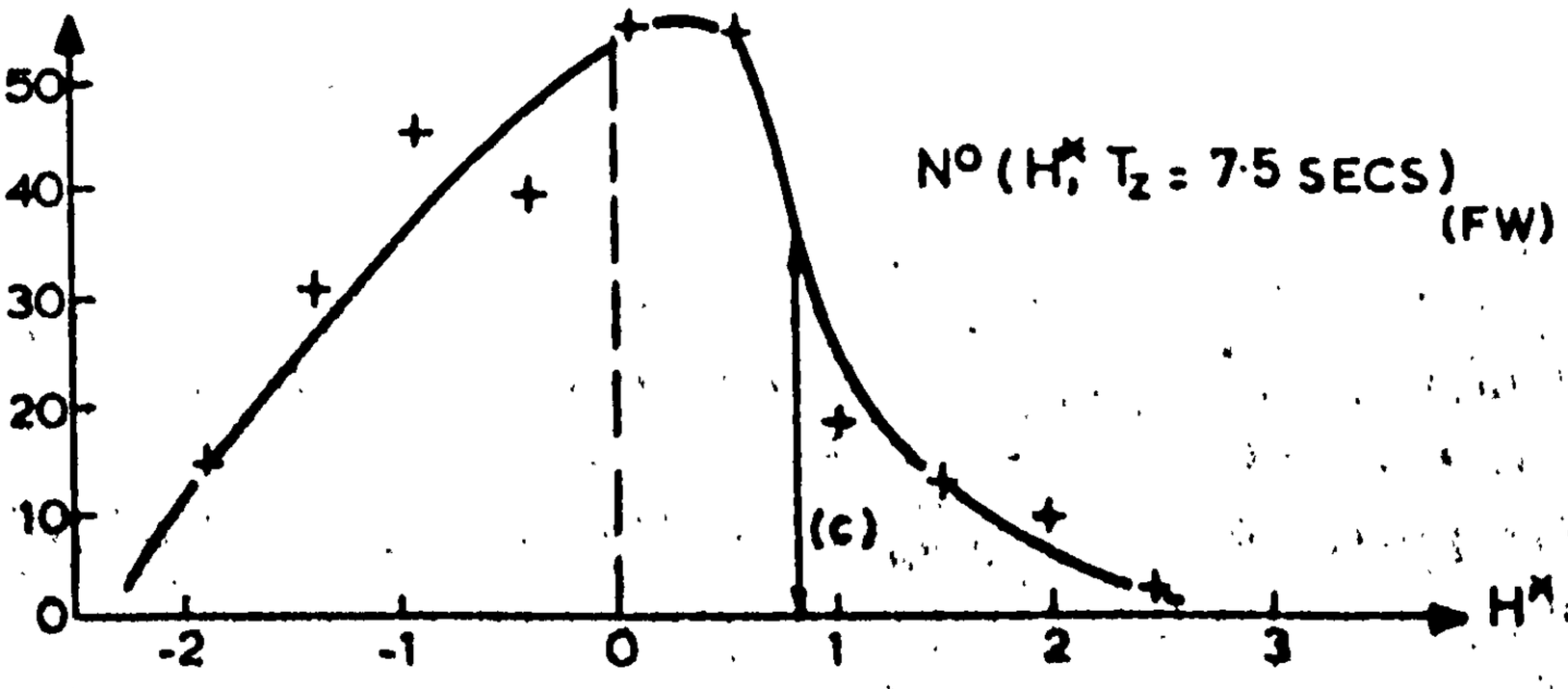

(IV) (FS) PREDICTED

T_z = 7·0 SECS

$\bar{H}_{1/3} = H_S \times \frac{3·094}{\bar{H}_W}$

= 1·916 m

$\sigma = \sigma_S \times \frac{1·222}{\sigma_W}$

= 0·969 m

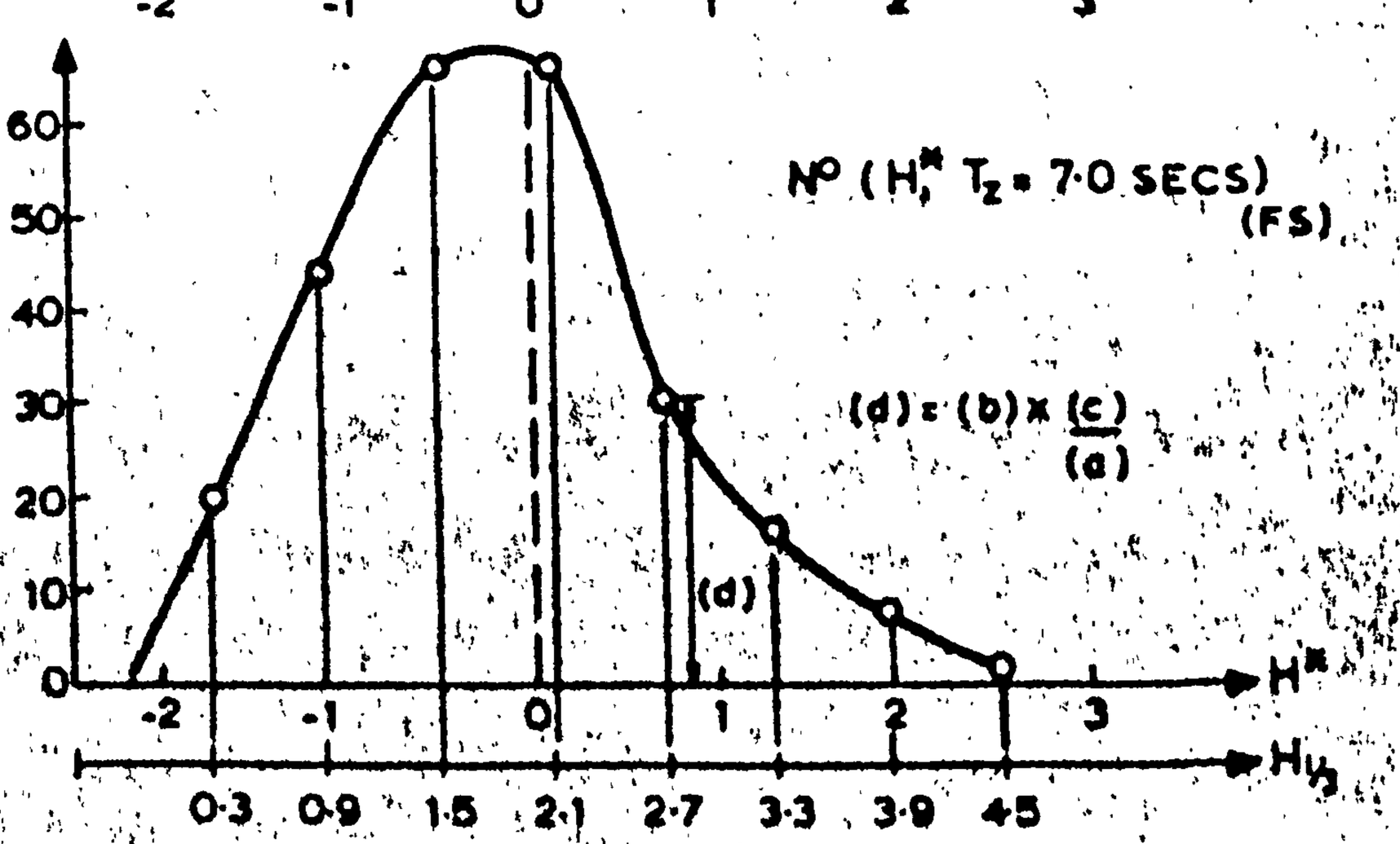

FIG. III. 2A. MARGINAL HISTOGRAMS OF T_z FOR FAMITA SCATTER DIAGRAMS.

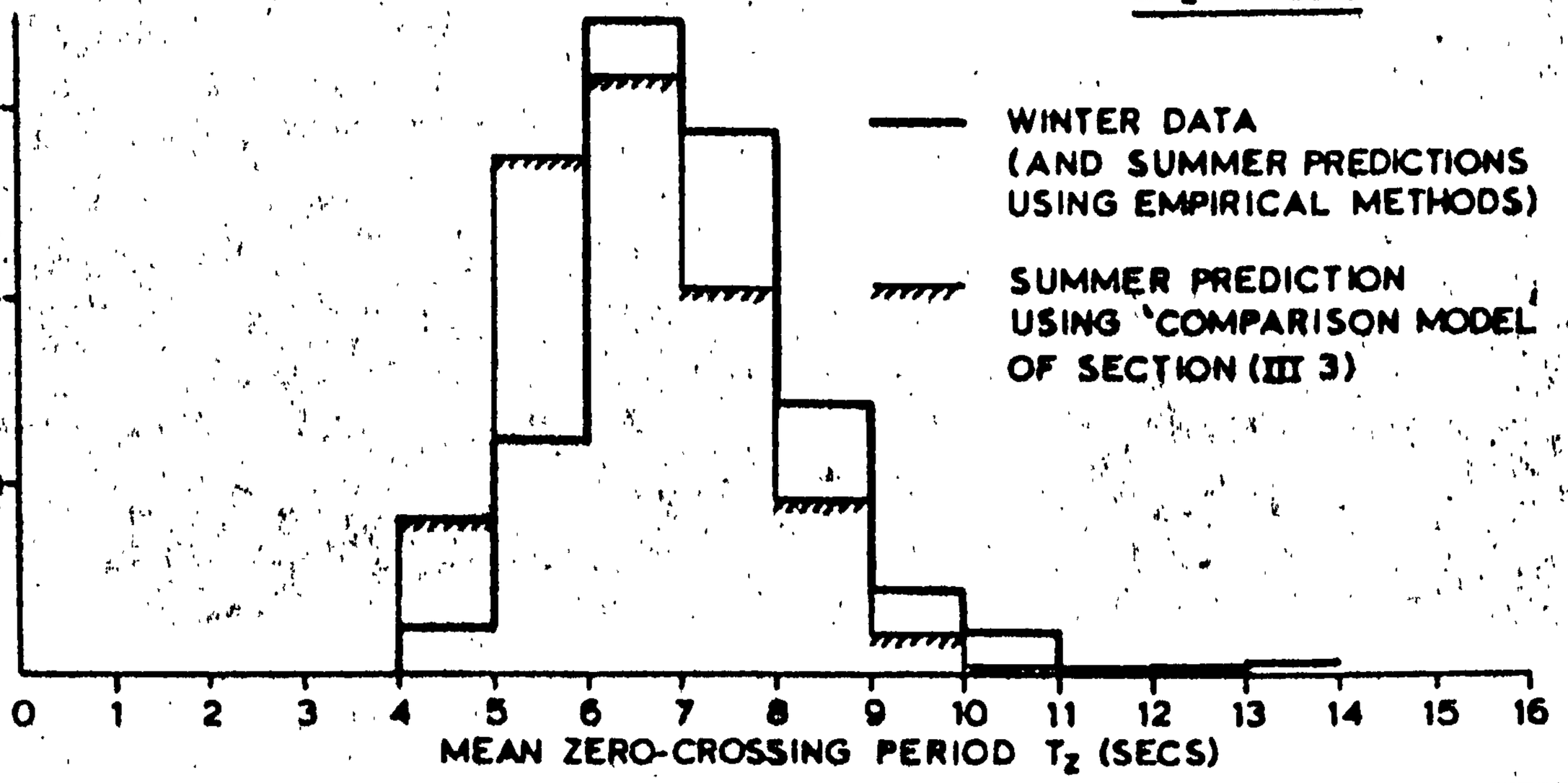

FIG. III.2B. MARGINAL HISTOGRAMS OF $H_{1/3}$ FOR FAMITA SCATTER DIAGRAMS.

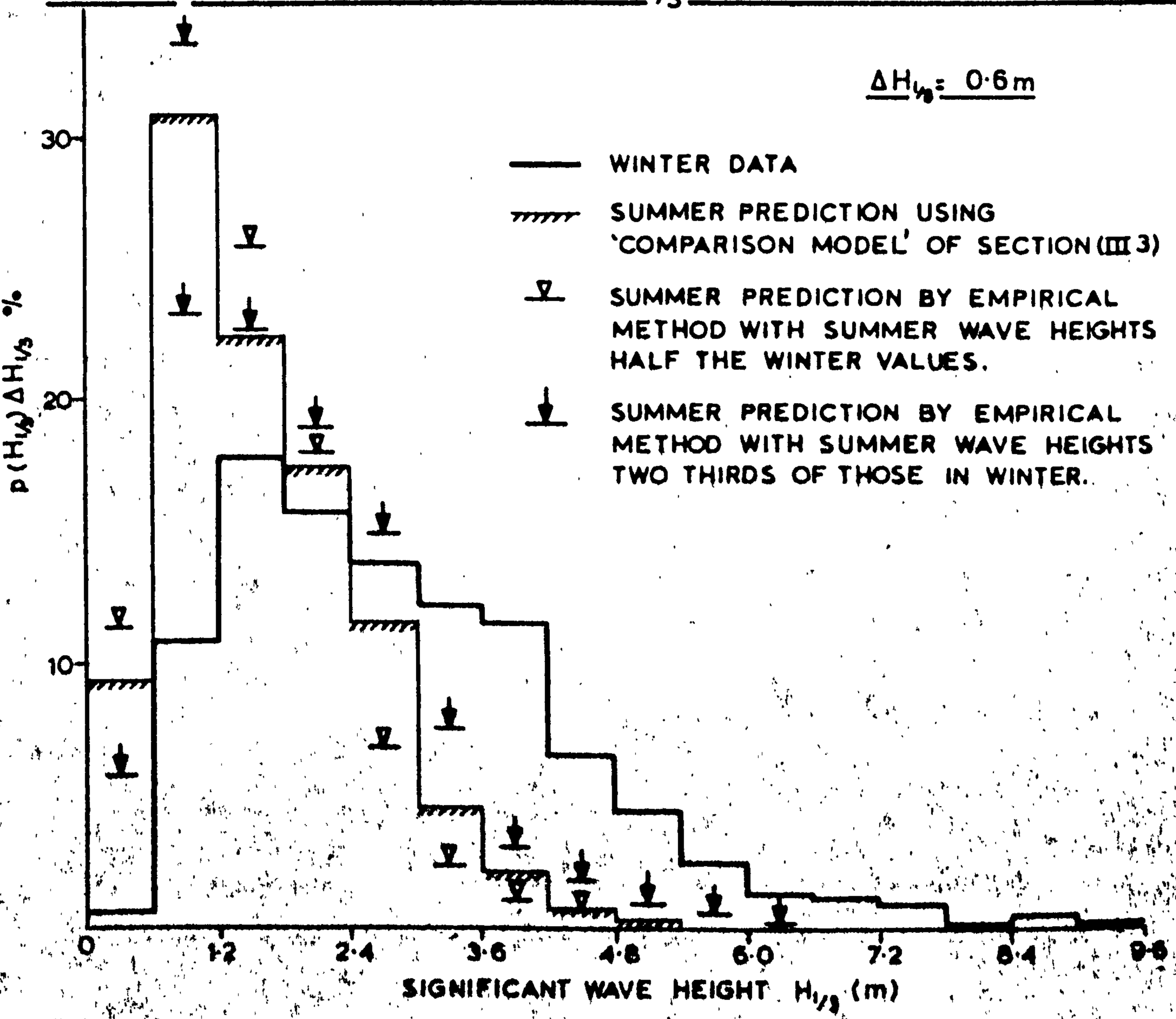

FIG III. 3. CONDITIONAL DISTRIBUTIONS OF SIGNIFICANT WAVE HEIGHT FOR FAMITA SCATTER DIAGRAMS WITH T_Z = 8·5 SECS.

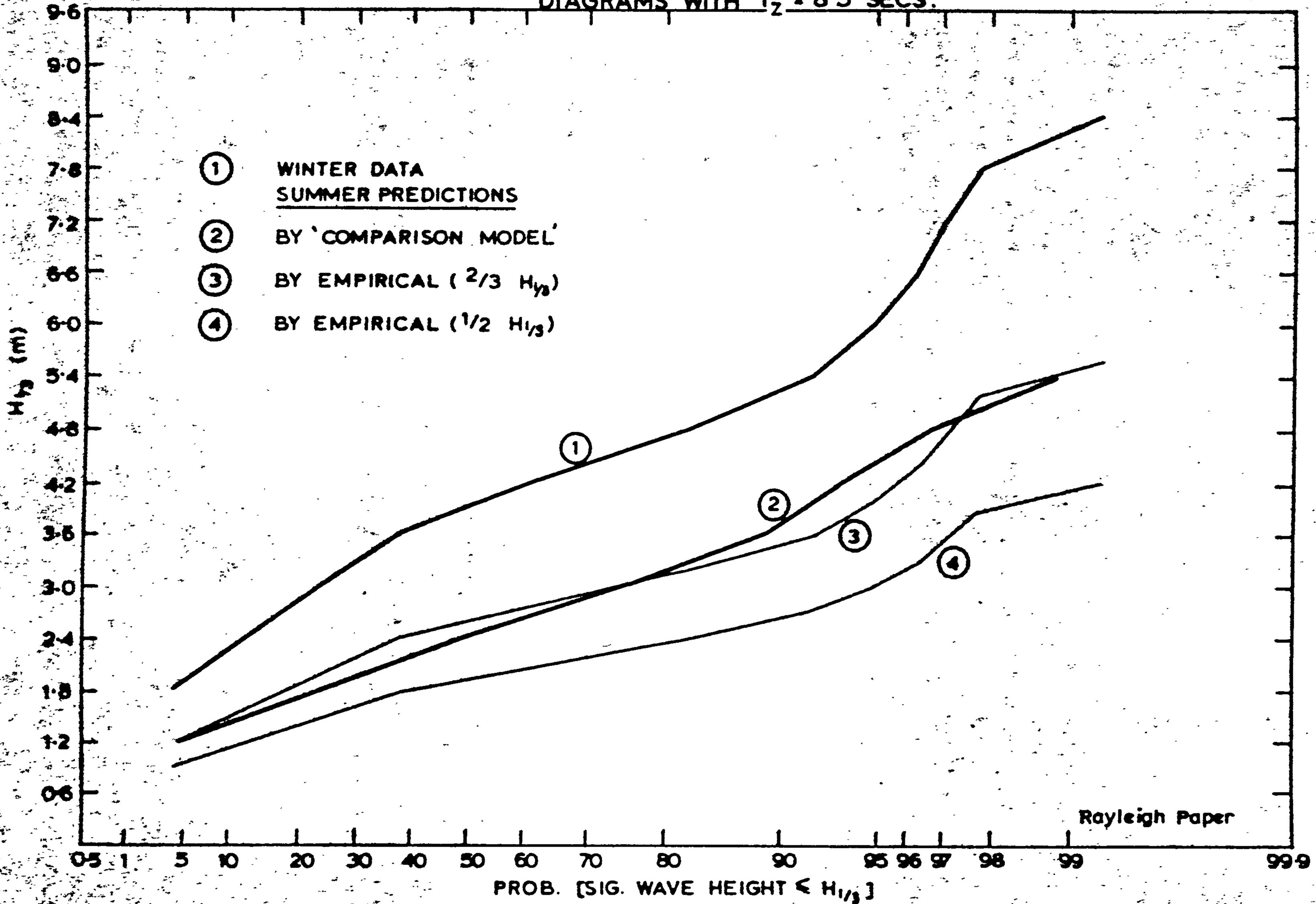

A P P E N D I X F O U R

CHI-SQUARE GOODNESS OF FIT TEST ON THE PROBABILITY DISTRIBUTION OF SIGNIFICANT WAVE HEIGHT

In Section 4.4.2 the distribution of significant wave height for the one-year data set of Fig. 2.3.1 was plotted on various probability papers with the objective of obtaining a reasonable fit to a particular theoretical probability distribution. These graphical techniques suggested that the Gumbel distribution approximated the probability structure quite well and the theoretical Gumbel distribution for the data was obtained by method of moments, using the mean and variance of the data set. The fit is shown on Fig. 4.7 and the probability histograms are given in Tables 4.1 and 4.3. The purpose of this Appendix is to test the hypothesis that the distribution of $H_{1/3}$ is Gumbel by the application of the Chi-square goodness-of-fit test.

The procedure involves the use of a statistic, χ_c^2, with an approximate chi-square distribution[47] which measures the discrepancy between the observed probability density function of the data and the Gumbel density function. The hypothesis of equivalence is tested by investigating the sampling distribution of χ_c^2.

The 1924 samples from the Famita scatter diagram are grouped into the 16 class intervals to form the frequency histogram representing the marginal distribution of $H_{1/3}$ in Table 4.1 and are repeated here in Table IV.1 with the four most extreme wave height classes consolidated into two classes to increase the number of events contained in each group. The general class width of 0.6m. in Table IV.1 represents approximately 2.37 classes per standard deviation, (see Table 4.1) which is sufficiently close to the recommended figure[47] of 2.5. The number of events falling in the i-th class interval is referred to as the observed frequency, f_i. The number of events which would be expected to fall in the i-th class interval if the distribution is 'Gumbel' is called the expected frequency, F_i, and is given in Table IV.1 obtained from $p(H_{1/3})\ \Delta H_{1/3}$ in Table 4.3 for the 'theoretical' Gumbel distribution obtained by method of moments.

The sample statistic, χ_c^2, measures the total discrepancy between the observed and expected frequencies for all classes as:

$$\chi_c^2 = \sum_{\text{all } i} \left(\frac{f_i - F_i}{F_i}\right)^2 \qquad \text{(IV.1)}$$

which is computed in Table IV.1.

The distribution of χ_c^2 is approximately equal to χ_n^2, the chi-square distribution with n degrees of freedom. In this case n is equal to 11, the number of class intervals minus the number of independent restrictions imposed on the data. The three restrictions arise from:

(a) the fact that the frequency associated with the last class interval is defined once the frequencies in the remaining classes are known; and

(b) from the two statistics (mean and variance) of the data set used to define the parameters of the Gumbel distribution.

Defining the small probability α as the level of significance of the test, then the acceptance region of the test is:

$$\chi_c^2 \leq \chi^2_{n=11;\alpha} \qquad \text{(IV.2)}$$

The probability α represents the region of rejection for the hypothesis test thus for small values of α it is unlikely that observed samples will fall in this region if the hypothesis is valid. Conversely if the sample fails to satisfy Eq. (IV.2) there is strong reason to question the hypothesis, its likelihood of validity decreasing as α is reduced.

For the data of Table (IV.1):

$$\chi_c^2 = 85.001$$

and from tables of the chi-square distribution[47]:

$$\chi^2_{n=11;\alpha=0.005} = 26.76$$

These values do not satisfy Eq. (IV.2) and the hypothesis is, therefore, rejected at the $\alpha = 0.005$ level of significance. This may be interpreted as indicating that if the hypothesis is true the probability that a

deviation X_c^2 as large as 26.76 is due to chance only is 0.5%. Consequently, the observed value of $X_c^2 = 85.001$ has a much lower probability of being caused by chance only, this therefore, casts serious doubts on the hypothesis which may be considered unacceptable.

However, the major contribution to the deviation occurs within the first two class intervals, as seen from Table IV.1. If these values are omitted the total deviation becomes:

$$X_c^2 = 16.257$$

and the resulting chi-square distribution, which now has nine degrees of freedom:

$$X^2_{n=9;\alpha=0.05} = 16.92$$

Thus the deviation now falls within the region of acceptance at the $\alpha = 0.05$ level of significance from which it may be inferred that there is no strong evidence to question the hypothesis for values of $H_{1/3}$ in excess of 1.2m, the upper limit of the second class interval. In this range the data may, therefore, be considered to be well approximated by the Gumbel distribution.

In practical terms, for extension of wave climate data in long-term prediction analyses of interest in this study, use of the hypothesis is considered to be acceptable over the entire range of $H_{1/3}$. This follows because the fit in the extremes is of most significance to the wave climate extrapolations and resulting distributions of individual wave height or wave load are relatively insensitive to minor changes in the lower range of $H_{1/3}$, such as those resulting from the Gumbel assumption for significant heights less than 1.2m.

TABLE IV.1

COMPUTATION OF χ_c^2

i	$H_{1/3}$ (m)	f_i	F_i	$\left(\frac{f_i - F_i}{F_i}\right)^2$
1	0.3	96	164	28.195
2	0.9	402	293	40.549
3	1.5	389	377	0.382
4	2.1	321	349	2.246
5	2.7	245	268	1.974
6	3.3	161	181	2.210
7	3.9	132	117	1.923
8	4.5	70	71	0.014
9	5.1	46	44	0.091
10	5.7	23	25	0.160
11	6.3	12	17	1.471
12	6.9	11	7	2.286
13	7.5 8.1	10	8	0.500
14	8.7 9.3	6	3	3.000
	Totals	1924	1924	85.001

$$(\chi_c^2)_{14} = \sum_{i=1}^{14} \left(\frac{f_i - F_i}{F_i}\right)^2 = 85.001$$

$$(\chi_c^2)_{12} = \sum_{i=3}^{14} \left(\frac{f_i - F_i}{F_i}\right)^2 = 16.257$$

A P P E N D I X F I V E

EXPANSION OF $E\{X_i|X_i|X_j|X_j|X_k^3 X_\ell^3\}$

An expression for $E\{X_i|X_i|X_j|X_j|X_k^3 X_\ell^3\}$ in terms of the cross-covariances R_{ij}, etc., is required for solution of expectation E23, and hence the fourth moment of response, by application of the cubic approximation for $X|X|$ as shown in Section 5.4.4.

Using Eqs. (5.4.12) and (5.4.31):

$$E\{X_i|X_i|X_j|X_j|X_k^3 X_\ell^3\} = E\{X_i|X_i|X_j|X_j|X_k^3\, E\{X_\ell^3|X_i\, X_j\, X_k\}\} \quad (V.1)$$

$$\begin{aligned}
&= \Big\{3\sigma_{\ell c}^2[b_i\, E\{|X_i^3|X_j|X_j|X_k^3\} + b_j\, E\{X_i|X_i||X_j^3|X_k^3\} \\
&+ b_j\, E\{X_i|X_i|X_j|X_j|X_k^4\}] + b_i^3\, E\{|X_i^5|X_j|X_j|X_k^3\} \\
&+ 3b_i^2\, b_j\, E\{X_i^3|X_i||X_j^3|X_k^3\} + 3b_i^2\, b_k\, E\{X_i^3|X_i|X_j|X_j|X_k^4\} \\
&+ 3b_i\, b_j^2\, E\{|X_i^3|X_j^3|X_j|X_k^3\} + 6b_i\, b_j\, b_k\, E\{|X_i^3\, X_j^3|X_k^4\} \\
&+ 3b_i\, b_k^2\, E\{|X_i^3|X_j|X_j|X_k^5\} + b_j^3\, E\{X_i|X_i||X_j^5|X_k^3\} \\
&+ 3b_j^2\, b_k\, E\{X_i|X_i|X_j^3|X_j|X_k^4\} + 3b_j\, b_k^2\, E\{X_i|X_i||X_j^3|X_k^5\} \\
&+ b_k^3\, E\{X_i|X_i|X_j|X_j|X_k^6\}\Big\} \qquad (V.2)
\end{aligned}$$

where $\sigma_{\ell c}^2 = R_{\ell\ell} - (b_i\, R_{i\ell} + b_j\, R_{j\ell} + b_k\, R_{k\ell})$ from Eq. (I.57) Appendix One;
and
$b_i\, b_j$, b_k are defined in Eq. (5.4.36).

Considering now the form of the expectations on the r.h.s. of Eq. (V.2):

$E\{|X_i^3|X_j|X_j|X_k^3\}$ - (Eq. (5.4.63)

$E\{X_i|X_i|X_j|X_j|X_k^4\} = E18$

all the remaining terms need to be expanded further for solution, using:

i) Eq. (5.4.12);
ii) the expressions for the third and fourth conditional moments, Eqs. (5.4.31) and (5.4.32); and
iii) the following expressions for the fifth and sixth order conditional moments:

$$E\{X_k^5|X_i\ X_j\} = 15\sigma_{kc}^4\ \bar{x}_{kc} + 10\sigma_{kc}^2\ \bar{x}_{kc}^3 + \bar{x}_{kc}^5 \qquad (V.3)$$

$$E\{X_k^6|X_j\ X_j\} = 15\sigma_{kc}^6 + 45\sigma_{kc}^4\ \bar{x}_{kc}^2 + 15\sigma_{kc}^2\ \bar{x}_{kc}^4 + \bar{x}_{kc}^6 \qquad (V.4)$$

where σ_{kc}^2 is defined with Eq. (5.4.63); and
$\bar{x}_{kc}^2 = a_i\ X_i + a_j\ X_j$ from Eq. (I.55), Appendix One
with a_i, a_j defined with Eq. (5.4.23).

In this manner it can be shown that the required expectation is given by:

$$E\{X_i|X_i|X_j|X_j|X_k^3\ X_\ell^3\} = \sum_{r=1}^{19} EX(r) \qquad (V.5)$$

where terms EX(r) are as follows:

$$EX(1) = E\{|X_i^3|X_j|X_j|X_k^3\}\ [3\sigma_{\ell c}^2\ b_i]$$

$$EX(2) = E\{X_i|X_i||X_j^3|X_k^3\}\ [3\sigma_{\ell c}^2\ b_j]$$

and the above expectations are given by Eq. (5.4.63).

$$EX(3) = E\{X_i|X_i|X_j|X_j|X_k^4\}\ [3\sigma_{\ell c}^2\ b_k]$$

and the expectation is E18.

$$EX(4) = E\{X_i^5|X_i|X_j|X_j|\}\ [3\sigma_{kc}^2\ a_i(b_i^3 + 6a_i\ b_i^2\ b_k + a_i^2\ b_i\ b_k^2 + 5a_i^3\ b_k^3)]$$

$$EX(5) = E\{X_i|X_i|X_j^5|X_j|\}\ [3\sigma_{kc}^2\ a_j(b_j^3 + 6a_j\ b_j^2\ b_k + a_j^2\ b_j\ b_k^2 + 5a_j^3\ b_k^3)]$$

and the expectations are E12.

$$EX(6) = E\{|X_i^5\ X_j^3|\}\ [3\sigma_{kc}^2(a_j\ b_i^3 + 3a_i\ b_i^2\ b_j + 12a_i\ a_j\ b_i^2\ b_k + 12a_i^2\ b_i\ b_j\ b_k + 30a_i^2\ a_j\ b_i\ b_k^2 + 20a_i^3\ a_j\ b_k^3 + 10a_i^3\ b_j\ b_k^2)]$$

$$EX(7) = E\{|X_i^3 X_j^5|\}\ [3\sigma_{kc}^2(a_i b_j^3 + 3a_j b_i b_j^2 + 12a_i a_j b_j^2 b_k + 12a_j^2 b_i b_j b_k + 30a_i a_j^2 b_j b_k^2 + 20a_i a_j^3 b_k^3 + 10a_j^3 b_i b_k^2)]$$

$$EX(8) = E\{X_i^3|X_i|X_j^3|X_j|\}\ [9\sigma_{kc}^2(a_j b_i^2 b_j + 2a_j^2 b_i^2 b_k + 8a_i a_j b_i b_j b_k + 10a_i a_j^2 b_i b_k^2 + 10a_i^2 a_j^2 b_k^3 + 10a_i^2 a_j b_j b_k^2 + 2a_i^2 b_j^2 b_k + a_i b_i b_j^2)]$$

$$EX(9) = E\{X_i^3|X_i|X_j|X_j|\}\ [9\sigma_{kc}^4(b_i^2 b_k + 5a_i b_i b_k^2 + 5a_i^2 b_k^3)]$$

$$EX(10) = E\{X_i|X_i|X_j^3|X_j|\}\ [9\sigma_{kc}^4(b_j^2 b_k + 5a_j b_j b_k^2 + 5a_j^2 b_k^3)]$$

$$EX(11) = E\{|X_i^3 X_j^3|\}\ [9\sigma_{kc}^4(2b_i b_j b_k + 5a_j b_i b_k^2 + 10a_i a_j b_k^3 + 5a_i b_j b_k^2)]$$

$$EX(12) = E\{X_i|X_i|X_j|X_j|\}\ [15\sigma_{kc}^6 b_k^3]$$

The expectations in EX(6) to EX(12) have all been solved in association with E18. However, the remaining terms (E13) to (E19) involve expectations which have not been computed previously and for which solutions have yet to be ascertained.

$$EX(13) = E\{X_i^7|X_i|X_j|X_j|\}\ [a_i^3(b_i^3 + 3a_i b_i^2 b_k + 3a_i^2 b_i b_k^2 + a_i^3 b_k^3)]$$

$$EX(14) = E\{X_i|X_i|X_j^7|X_j|\}\ [a_j^3(b_j^3 + 3a_j b_j^2 b_k + 3a_j^2 b_j b_k^2 + a_j^3 b_k^3)]$$

$$EX(15) = E\{|X_i^7 X_j^3|\}[3a_i^2(a_j b_i^3 + a_i b_i^2 b_j + 4a_i a_j b_i^2 b_k + 2a_i^2 b_i b_j b_k + 5a_i^2 a_j b_i b_k^2 + 2a_i^3 a_j b_k^3 + a_i^3 b_j b_k^2)]$$

$$EX(16) = E\{|X_i^3 X_j^7|\}\ [3a_j^2(a_i b_j^3 + a_j b_i b_j^2 + 4a_i a_j b_j^2 b_k + 2a_j^2 b_i b_j b_k + 5a_i a_j^2 b_j b_k^2 + 2a_i a_j^3 b_k^3 + a_j^3 b_i b_k^2)]$$

$$EX(17) = E\{X_i^5|X_i|X_j^3|X_j|\}\ [3a_i(a_j^2\ b_i^3 + 3a_i\ a_j\ b_i^2\ b_j + 6a_i\ a_j^2\ b_i^2\ b_k + 8a_i^2\ a_j\ b_i\ b_j\ b_k + 10a_i^2\ a_j^2\ b_i\ b_k^2 + 5a_i^3\ a_j^2\ b_k^3 + a_i^2\ b_i\ b_j^2 + a_i^3\ b_j^2\ b_k + 5a_i^3\ a_j\ b_j\ b_k^2)]$$

$$EX(18) = E\{X_i^3|X_i|X_j^5|X_j|\}[3a_j(a_i^2\ b_j^3 + 3a_i\ a_j\ b_i\ b_j^2 + 6a_i^2\ a_j\ b_j^2\ b_k + 8a_i\ a_j^2\ b_i b_j b_k + 10a_i^2\ a_j^2\ b_j\ b_k^2 + 5a_i^2\ a_j^3\ b_k^3 + a_j^2\ b_i^2\ b_j + a_j^3\ b_i^2\ b_k + 5a_i\ a_j^3\ b_i\ b_k^2)]$$

$$EX(19) = E\{|X_i^5\ X_j^5|\}\ [a_j^3\ b_i^3 + 9a_i\ a_j^2\ b_i^2\ b_j + 12a_i\ a_j^3\ b_i^2\ b_k + 36a_i^2\ a_j^2\ b_i\ b_j\ b_k + 30a_i^2\ a_j^3\ b_i\ b_k^2 + 20a_i^3\ a_j^3\ b_k^3 + a_i^3\ b_j^3 + 9a_i^2\ a_j\ b_i\ b_j^2 + 12a_i^3\ a_j\ b_j^2\ b_k + 30a_i^3\ a_j^2\ b_j\ b_k^2]$$

A P P E N D I X V I

LIST OF COMPUTER PROGRAMS

Listings of all programs are contained in a separate document entitled 'Probabilistic Description of Wave Loads and Structural Response: Computer Programs'.

Notes

(1) Programs in FORTRAN language developed for use either on the ICL 1906S computer at the University of Liverpool or on the ICL CDC 7600 computer at the University of Manchester Regional Computer Centre.

(2) All computations based on horizontal 'Morison' wave loading on cylindrical members.

(a) BASIC AND PEAK LOADING DISTRIBUTIONS FOR SINGLE MEMBERS

Program Name	Program Description	Published Information
OSF1	Long-term pdf. of peak force - 'Deterministic' method. (Scatter diagram; pdf. of individual wave height; Stokes 5th).	Theory, results & listings in Ref. 10
OSF2	Long-term pdf.s of basic and peak (narrow band type 2 - F & $\dot{F}$ stat. indept.) loading. (Scatter diagram; P-M ($H_{1/3}$) spectrum; P-H num.int. algorithm).	Theory, results & listings in Ref. 10
OSF3	As OSF2 but using linearised Morison Loading ($u\|u\| \simeq \sqrt{8/\pi}\,\sigma_u u$; const. step. num. int.)	Theory, results & listings in Ref. 10
OSF4	As OSF2 but with P-M (T_z) spectrum.	Results in Ref. 12
OSF5	As OSF2 but excluding basic force variate for run-time reduction.	
OSF6	As OSF5 but for narrow-band type 1 peak pdf. (F, $\dot{F}$ stat. dept.)	Theory outlined & results in Ref. 12
OSF7	As OSF5 but using Gaussian-Hermite Quadrature for num. int. (procedure for run-time reduction).	

Program Name	Program Description	Published Information
OSF8	As OSF5 but with P-M (DNV) spectrum	Results in Ref. 12
OSF9	As OSF3 but with P-M (DNV) spectrum	Results in Ref. 12
OS10	As OSF5 but with P-M ($H_{1/3}/T_z$) spectrum	
OS16	Pierson-Holmes pdf. from 2nd and 4th moments inc. narrow band 'type 2' peak cdf.	Theory summarised in Ref. 17
OS20	Long-term pdf.s of basic and peak (type 2) wave/current loading.	Theory & results in Ref. 11
OS20A	Statistics of short-term wave/current force inc. spectral densities	Theory & results in Ref. 11
OS20ER	As OS20 but with equilibrium range constraint on surface elevn. spect. densities.	
OS21	Long-term pdf.s of basic loading accounting for intermittency in splash zone.	Theory & results in Ref. 11
OS22	As OSF2 but with JONSWAP spectrum.	
OS25	As OSF2 but with wave climate described by cdf. of $H_{1/3}$	Theory & results in Refs. 11, 17.

(b) PEAK AND EXTREME LOADING DISTRIBUTIONS FOR SINGLE MEMBERS

OSF3X OSF5X OSF6X OSF8X	(1) Extreme distribution developed from long-term peak cdf. based on programs OSF3/5/6/8 (indept. peaks; single period of exposure; set of cards available for insertion into programs OSF2-OS10).	Theory & results in Ref. 12
OS5XX	(2) Extreme distribution developed from short-term extreme cdfs. Based on program OSF5 (indept. peaks; single period of exposure).	Theory outlined in Ref. 17
OS6XX	(3) Extreme distribution developed from long-term peak cdf. Based on program OSF6 (indept. peaks; multiple periods of exposure).	
OS26	(4) As OSF5X based on wave climate used in OS25.	

(c) BASIC QUASI-STATIC RESPONSE FOR MULTIPLE FORCE COMPONENT LINEAR SYSTEMS

Program Name	Program Description	Published Information
OS14 OS15	Short-term joint and marginal distributions of response for 2 member systems. 2nd and 4th moments of marginal response, kurtosis and correlation coeff. (various spectra, num. int. by Gauss-Hermite Quadrature, OS15 - floating variable range on response Y_2).	Theory outlined & results in Refs. 11 & 14
OS17 OS18	As above, but with constant step. num. int. (OS18 - floating variable range on response Y_2).	Theory outlined & results in Refs. 11 & 14
OS19A-C	2nd and 4th moments of response (short-term) [various spectra, run-time limitations (30 min max on 1906S at Liverpool) restrict system complexity, A: single response variable; uses external library routines (up to 8 load components) B: multiple response variables; self-contained; optimised (up to 12 components) C: multiple response variables; polynomial approximations for expectations (up to 35 components)]	Theory & results in Refs. 11 and 14
OS23	Response distributions from time-series simulation of water particle kinematics (short-term; various spectra).	Theory outlined in Ref. 79

(b) MISCELLANEOUS

OS24	Long-term cdf. of individual wave height from cdf. of $H_{1/3}$ (with 'associated' T_z).	Theory & Results in Ref. 11